Calhoun: The NPS Institutional Archive

DSpace Repository

Theses and Dissertations 1. Thesis and Dissertation Collection, all items

2000-12

Observation adjoint sensitivity and the adaptive observation-targeting problem

Baker, Nancy L.

Monterey, California. Naval Postgraduate School

http://hdl.handle.net/10945/7748

This publication is a work of the U.S. Government as defined in Title 17, United States Code, Section 101. Copyright protection is not available for this work in the United States.

Downloaded from NPS Archive: Calhoun

Calhoun is the Naval Postgraduate School's public access digital repository for research materials and institutional publications created by the NPS community. Calhoun is named for Professor of Mathematics Guy K. Calhoun, NPS's first appointed -- and published -- scholarly author.

Dudley Knox Library / Naval Postgraduate School
411 Dyer Road / 1 University Circle
Monterey, California USA 93943

http://www.nps.edu/library

NPS ARCHIVE
2000
BAKER, N.

DUDLEY KNOX LIBRAR
NAVAL POSTGRADUAT
MONTEREY CA 93

NAVAL POSTGRADUATE SCHOOL
Monterey, California

DISSERTATION

OBSERVATION ADJOINT SENSITIVITY AND THE ADAPTIVE OBSERVATION-TARGETING PROBLEM

by

Nancy L. Baker

December 2000

Dissertation Chair and Co-Advisor:	Russell L. Elsberry
Dissertation Co-Advisor:	Roger Daley

Approved for public release; distribution is unlimited.

REPORT DOCUMENTATION PAGE

Form Approved OMB No. 0704-0188

Public reporting burden for this collection of information is estimated to average 1 hour per response, including the time for reviewing instruction, searching existing data sources, gathering and maintaining the data needed, and completing and reviewing the collection of information. Send comments regarding this burden estimate or any other aspect of this collection of information, including suggestions for reducing this burden, to Washington headquarters Services, Directorate for Information Operations and Reports, 1215 Jefferson Davis Highway, Suite 1204, Arlington, VA 22202-4302, and to the Office of Management and Budget, Paperwork Reduction Project (0704-0188) Washington DC 20503.

1. AGENCY USE ONLY *(Leave blank)*	**2. REPORT DATE** December 2000	**3. REPORT TYPE AND DATES COVERED** Doctoral Dissertation

4. TITLE AND SUBTITLE:
Observation Adjoint Sensitivity and the Adaptive Observation-Targeting Problem

5. FUNDING NUMBERS

6. AUTHOR(S)
Baker, Nancy Louise

7. PERFORMING ORGANIZATION NAME(S) AND ADDRESS(ES)
Naval Postgraduate School
Department of Meteorology
589 Dyer Road
Monterey, CA 93943-5114

8. PERFORMING ORGANIZATION REPORT NUMBER

9. SPONSORING / MONITORING AGENCY NAME(S) AND ADDRESS(ES)
Naval Research Laboratory
Marine Meteorology Division
7 Grace Hopper Avenue
Monterey, CA 93943-5502

10. SPONSORING / MONITORING AGENCY REPORT NUMBER

11. SUPPLEMENTARY NOTES The views expressed in this thesis are those of the author and do not reflect the official policy or position of the Department of Defense or the U.S. Government.

12a. DISTRIBUTION / AVAILABILITY STATEMENT
Approved for public release; distribution is unlimited.

12b. DISTRIBUTION CODE

13. ABSTRACT

This research introduces the adjoint of the data assimilation system, which together with the classical adjoint sensitivity problem, represents the two fundamental components of the complete forecast adjoint sensitivity problem. This adjoint of the data assimilation system is then used to investigate the sensitivity of the forecast aspect J to the observations and background for idealized analysis problems, and finally a real-data case using the NAVDAS adjoint for a situation with unusually large 72-h forecast errors over the western United States during February 1999.

The observation sensitivity is largest when the observations are relatively isolated, assumed to be more accurate than the background, and the analysis sensitivity gradients are large in amplitude and have a spatial scale similar to the background error covariances. The observation sensitivity is considerably weaker for small-scale analysis sensitivity gradients. The large observation sensitivities suggest that adaptive observations near large-scale analysis sensitivity gradients have a greater potential to change the forecast aspect than observations near small-scale analysis sensitivity gradients. Therefore, targeting decisions based on the adjoint of the data assimilation system may be significantly different from targeting decisions based solely on the analysis sensitivity gradients. These results emphasize the importance of accounting for the data assimilation procedures in the adaptive observation-targeting problem.

14. SUBJECT TERMS
Observation sensitivity, observation adjoint sensitivity, adaptive observations, observation targeting, data assimilation, adjoint methods

15. NUMBER OF PAGES 332

16. PRICE CODE

17. SECURITY CLASSIFICATION OF REPORT Unclassified	**18. SECURITY CLASSIFICATION OF THIS PAGE** Unclassified	**19. SECURITY CLASSIFICATION OF ABSTRACT** Unclassified	**20. LIMITATION OF ABSTRACT** UL

NSN 7540-01-280-5500

Standard Form 298 (Rev. 2-89)
Prescribed by ANSI Std. 239-18

THIS PAGE INTENTIONALLY LEFT BLANK

Approved for public release; distribution is unlimited

OBSERVATION ADJOINT SENSTIVITY AND THE ADAPTIVE OBSERVATION-TARGETING PROBLEM

Nancy L. Baker
B.S., Oregon State University, 1981
M.S., University of Washington, 1985

Submitted in partial fulfillment of the
requirements for the degree of

DOCTOR OF PHILOSOPHY IN METEOROLOY

from the

NAVAL POSTGRADUATE SCHOOL
December 2000

2000
BAKER, N.

C.1

THIS PAGE INTENTIONALLY LEFT BLANK

DUDLEY KNOX LIBRARY
NAVAL POSTGRADUATE SCHOOL
MONTEREY CA 93943-5101

ABSTRACT

This research introduces the adjoint of the data assimilation system, which together with the classical adjoint sensitivity problem, represents the two fundamental components of the complete forecast adjoint sensitivity problem. This adjoint of the data assimilation system is then used to investigate the sensitivity of the forecast aspect J to the observations and background for idealized analysis problems, and finally a real-data case using the NAVDAS adjoint for a situation with unusually large 72-h forecast errors over the western United States during February 1999.

The observation sensitivity is largest when the observations are relatively isolated, assumed to be more accurate than the background, and the analysis sensitivity gradients are large in amplitude and have a spatial scale similar to the background error covariances. The observation sensitivity is considerably weaker for small-scale analysis sensitivity gradients. The large observation sensitivities suggest that adaptive observations near large-scale analysis sensitivity gradients have a greater potential to change the forecast aspect than observations near small-scale analysis sensitivity gradients. Therefore, targeting decisions based on the adjoint of the data assimilation system may be significantly different from targeting decisions based solely on the analysis sensitivity gradients. These results emphasize the importance of accounting for the data assimilation procedures in the adaptive observation-targeting problem.

THIS PAGE INTENTIONALLY LEFT BLANK

TABLE OF CONTENTS

I. INTRODUCTION 1

II. DATA ASSIMILATION ADJOINT THEORY 13
  A. DERIVATION OF OBSERVATION AND BACKGROUND SENSITIVITY 13
  B. MULTIVARIATE OBSERVATION SENSITIVITY 18
  C. MULTIVARIATE BACKGROUND SENSITIVITY 22

III. EXPLORATION OF OBSERVATION ADJOINT SENSITIVITY USING IDEALIZED CASES 23
  A. AN EXAMPLE OF OBSERVATION AND BACKGROUND SENSITIVITY 23
  B. OBJECTIVE MEASURES OF OBSERVATION SENSITIVITY 29
  C. ONE-DIMENSIONAL UNIVARIATE OBSERVATION AND BACKGROUND SENSITIVITY 31
    1. Observation Super-Sensitivity Along a Coastline 31
    2. The Analytical Solution for a Single Observation 34
    3. Understanding Observation Super-sensitivity 38
    4. Exploring the Limits of Observation Sensitivity 43
      a. The Effects of the Background Error Correlation Length Scale *43*
      b. The Effects of the Observation Error Variances *50*
    5. Univariate Wind Observation Sensitivity 52
      a. The Analytical Solution for a Single Wind Observation. *56*
      b. The Effects of the Length Scales L_s *and* L_b *on the Observation Sensitivity* *57*
      c. The Variation of the Observation Sensitivity as a Function of L_b *and the Observation Error* *61*
      d. The Variation of the OSM as a Function of L_s *and Observation Error* *63*
    6. Observation Density and Observation Sensitivity 63
    7. Summary of One-Dimensional Univariate Observation Sensitivity 66
  D. ONE-DIMENSIONAL MULTIVARIATE OBSERVATION SENSITIVITY 68
    1. Theoretical Considerations 68
      a. The Cross-Correlation Contribution to Multivariate Observation Sensitivity *68*
      b. Multivariate Background Sensitivity *71*
      c. Objective Multivariate Observation Sensitivity Measures... .... *72*

2. Wind/Height and Height/Wind Observation Sensitivity along a Coastline 73
3. The Analytical Solutions for a Single Height or Wind Observation 77
4. Exploring the Limits of Observation Sensitivity......85
    a. *The Single Observation Sensitivity Map*......*85*
    b *The Effects of the Background Error Correlation Length Scale*......*91*
    c. *The Effects of the Analysis Sensitivity Length Scale*......*94*
    d. *The Effects of the Observation Error*......*95*
5. Summary of Wind/Height and Height/Wind Observation Sensitivity 98

E. TWO-DIMENSIONAL UNIVARIATE EXAMPLES......104
1. Display of the Observation Sensitivity Vector 105
2. Single Observation Experiments......105
    a. *The Effects of the Background Error Correlation Length Scale on the Observation Sensitivity*......*109*
    b. *The Effects of Observation Error on the Observation Sensitivity*......*111*
3. Multiple Observation Experiments......114
    a. *The Effects of Observation Density on Observation Sensitivity*......*114*
    b. *The Effects of the Background Error Correlation Length Scale on the Observation Sensitivity*......*123*
    c. *The Effects of Observation Error on the Observation Sensitivity*......*127*
4. Summary of Two-Dimensional Univariate Observation Sensitivity 131

F. SIMPLE TWO-DIMENSIONAL MULTIVARIATE EXAMPLES.133
1. The Height-Height, the Height-Wind, and the Wind-Wind Background Error Covariances......133
2. Multivariate Single Observation Sensitivity Maps......134
3. Multivariate Observation Sensitivity using Real Analysis Sensitivity Gradients 142
    a. *Multivariate Single Observation Sensitivity Maps*......*143*
    b. *Limited-Area versus Global Observation Sensitivity Calculations*......*152*
    c. *Multivariate Observation Sensitivity for a Hypothetical Flight Track*......*152*
    d. *Multivariate Observation Sensitivity for a Hypothetical Swath of Satellite Observations*......*155*
    e. *The Marginal Observation Sensitivity Vector*......*159*
4. Summary of Two-Dimensional Multivariate Observation Sensitivity 161

IV. EXPLORATION OF NAVDAS OBSERVATION ADJOINT SENSITIVITY FOR THE NORTH PACIFIC OCEAN ON 7 FEBRUARY 1999 165
- A. A BRIEF DESCRIPTION OF NAVDAS 165
- B. THE NAVDAS ADJOINT 168
  - 1. The NAVDAS Adjoint Solution Method 168
  - 2. The Comparability between the Two-Dimensional Observation Sensitivity and the NAVDAS Adjoint Sensitivity Problem ...169
- C. MEASURES OF POTENTIAL OBSERVATION FORECAST IMPACT 175
- D. OBSERVATION ADJOINT SENSITIVITY RESULTS..................178
  - 1. Experimental Design 183
  - 2. Discussion of NAVDAS Observation Sensitivity Results.......186
- E. TARGETING STRATEGIES USING THE NAVDAS ADJOINT ..192
- F. CHAPTER SUMMARY 214

V. SUMMARY AND CONCLUSIONS 219

LIST OF REFERENCES 235

INITIAL DISTRIBUTION LIST 239

THIS PAGE INTENTIONALLY LEFT BLANK

LIST OF FIGURES

Figure 1.1. An example of the most unstable singular vector during FASTEX IOP-17, for an initial time of 18 UTC 17 February 1997, and optimized for the forecast verification time of 12 UTC 19 February 1997. (a) Horizontal temperature structure at 600 hPa with the forecast verification area given by the box over Great Britain, and (b) vertical cross-section through the temperature structure averaged over the latitude zone of 40-45°N. 4

Figure 1.2. As in Figs. 1.1a and 1.1b, except for the sensitivity of the vertically averaged vorticity from 650 hPa to the surface in the FVA with respect to the initial temperature field during FASTEX IOP-17. The sensitivity gradient is computed for a 72-h nonlinear trajectory ending at 12 UTC 19 February 1997 and an adjoint calculation backwards 42 hours to the initial time of 18 UTC 17 February 1997. 5

Figure 3.1. Simulated sensitivity vectors for a small target (a-d) and a large target (e-h). The imposed analysis sensitivity vectors are shown in (a) and (e), the observation sensitivity vectors in (b) and (f), the background sensitivity vectors in (c) and (g), and the observation sensitivity measures in (d) and (h). 25

Figure 3.2. Examples of one-dimensional univariate height sensitivity for (a-h) coastal, and (i-l) single observation analysis systems. The background error correlation function for an observation at gridpoint 51 for (a,i) $L_b = 3.33\Delta x$, and (e) $L_b = 6.67\Delta x$, (b,f,j) the imposed analysis sensitivity gradients with $L_s = 5.31\Delta x$, (c,g,k) the observation sensitivities, and (d,h,l) the background error sensitivities. 32

Figure 3.3. Values of the parameter B as defined in (3.13) as a function of the specified background error correlation length from 0.1Δx to 12.1Δx (L_b; abscissa) and imposed height analysis sensitivity scale from 2.0Δx to 14.0Δx (L_s; ordinate). The values of B were computed for $n = 1{,}500$. 37

Figure 3.4. Plots of the row of the transposed Kalman gain matrix for the observations at gridpoints (a) 51, (b) 50, (c) 49 and (d) 30 in Fig. 3.2c. Values are plotted as a function of the grid location (abscissa) and amplitude (ordinate). 40

Figure 3.5. Variation of the computed height observation sensitivity measure as a function of the background error correlation length scale from 0.1Δx to 12.1Δx (L_b; abscissa) and the analysis sensitivity length scale from 2.0Δx to 14.0Δx (L_s; ordinate). 44

Figure 3.6. Variation of the height observation sensitivity measure (ordinate) as a function of the background error correlation length scale from 0.25Δx to 25.0Δx (L_b; abscissa) for $L_s = 5.31\Delta x$. 46

Figure 3.7. Variation of the height observation sensitivity measure as a function of L_b (abscissa) and the ratio of the observation error standard deviation ε_r to the background error standard deviation ε_b (ordinate). The analysis sensitivity length scale is fixed at $L_s = 5.31\Delta x$ while $\varepsilon_r/\varepsilon_b$ ranges from 0.0 to 3.0, and L_b varies between 0.1Δx and 12.1Δx. 51

Figure 3.8. Variation of the height observation sensitivity measure as a function of the ratio $\varepsilon_r/\varepsilon_b$ from 0.0 to 3.0 (abscissa) and L_s from 2.0Δx to 14.0Δx (ordinate) for $L_b = 6.0\Delta x$. 53

Figure 3.9. As in Fig. 3.2, except for examples of super-sensitivity for the one-dimensional univariate wind coastal (a-h) and single observation (i-l) analysis system. The background error correlation functions for an observation at gridpoint 51 and (a,i) $L_b = 4.5\Delta x$, and (e) $L_b = 9.0\Delta x$, (b,f,j) the imposed analysis sensitivity gradients with $L_s = 5.31\Delta x$, (c,g,k) the observation sensitivities, and (d,h,l) the background error sensitivities. 54

Figure 3.10. As in Fig. 3.5, except for variation of the wind observation sensitivity measure as a function of the background error correlation length scale (L_b; abscissa) and the analysis sensitivity length scale (L_s; ordinate). 58

Figure 3.11. As in Fig. 3.6, except for variation of the wind observation sensitivity measure (ordinate) as a function of the background error correlation length scale from 0.1Δx to 12.1Δx (L_b; abscissa) for $L_s = 5.31\Delta x$. 60

Figure 3.12. As in Fig. 3.7, except for variation of the wind observation sensitivity measure as a function of L_b (abscissa) and the ratio of the observation error standard deviation (ε_r) to the background error standard deviation (ε_b) (ordinate)... 62

Figure 3.13. As in Fig. 3.8, except for variation of the wind observation sensitivity measure as a function of the ratio of the observation error standard deviation (ε_r) and the background error standard deviation (ε_b) (abscissa) and L_s (ordinate). For this case, $L_b = 6.0\Delta x$ while L_s varies between 2.0Δx and 14.0Δx and $\varepsilon_r/\varepsilon_b$ ranges from 0.0 to 3.0. 64

Figure 3.14. Variation of the height observation sensitivity measure (ordinate) as a function of L_b (abscissa) and the distance between the observations. The curves are for observations placed (a) 1Δx, (b) 2Δx, (c) 3Δx, (d) 5Δx, (e) 10Δx, (f) 15Δx, (g) 16Δx, (h) 17Δx, (i) 18Δx, (j) 20Δx, (k) 30Δx apart. The dotted curve is for the analytical approximation to observation sensitivity measure from (3.6) and (3.16). L_b varies between 0.25Δx and 25.25Δx. 65

Figure 3.15. As in Fig. 3.9, except for the one-dimensional wind/height multivariate coastal (a-f) and single observation (g-i) analysis system. The wind/height background error correlation function for an observation at gridpoint 51 and (a) $L_b = 4.53\Delta x$, and (d,g) $L_b = 9.06\Delta x$, (b,e,h) the imposed height analysis sensitivity gradients with $L_s = 5.31\Delta x$, and (c,f,i) the wind/height observation sensitivities. 74

Figure 3.16. As in Fig. 3.2, except for examples of observation sensitivity for the one-dimensional height/wind multivariate coastal (a-f) and single observation (g-i) analysis system. The height/wind background error correlation function for an observation at gridpoint 51 and (a,g) $L_b = 4.53\Delta x$, and (d) $L_b = 9.06\Delta x$, (b,e,h) the imposed wind analysis sensitivity gradients with $L_s = 5.31\Delta x$, and (c,f,i) the height/wind observation sensitivities. 75

Figure 3.17. As in Fig. 3.4, except for the row of the transposed Kalman gain matrix for wind observations located at gridpoints (a) 4, (b) 3, (c) 2, and (d) 1 in Fig. 3.15c. 83

Figure 3.18. As in Fig. 3.17, except for the row of the transposed Kalman gain matrix for height observations located at gridpoints (a) 4, (b) 3, (c) 2, and (d) 1 in Fig. 3.16c. 84

Figure 3.19. As in Fig. 3.15(g,h,i), except for the wind/height single observation sensitivity map. (a) The wind/height background error correlation model for an observation at gridpoint 51, (b) the imposed height analysis sensitivity gradient, (c) the wind/height sensitivity to a single observation at gridpoint 43, and (d) the single wind/height observation sensitivity map. 87

Figure 3.20. As in Fig. 3.19, except for the height/wind single observation sensitivity map. 89

Figure 3.21. As in Fig. 3.11 except for the variation of the wind/height observation sensitivity measure as a function of the background error correlation length scale from 0.25Δx to 25.0Δx (L_b; abscissa), with $L_s = 5.31\Delta x$. 92

Figure 3.22. As in Fig. 3.6, except for the variation of the height/wind observation sensitivity measure as a function of the background error correlation length scale from 0.25Δx to 25.0Δx (L_b ; abscissa), with $L_s = 5.31\Delta x$ 93

Figure 3.23. As in Fig. 3.10, except for variation of the wind/height observation sensitivity measure as a function of the wind/height background error correlation length scale (L_b; abscissa) and the height analysis sensitivity length scale (L_s; ordinate). 96

Figure 3.24. As in Fig. 3.6, except for variation of the height/wind observation sensitivity measure as a function of the height/wind background error correlation length scale (L_b ; abscissa) and the wind analysis sensitivity length scale (L_s; ordinate). 97

Figure 3.25. As in Fig. 3.12, except for variation of the wind/height observation sensitivity measure as a function of L_b (abscissa) and $\varepsilon_r/\varepsilon_b$ (ordinate). The range of L_b is from 0.1Δx to 12.1Δx, the range of $\varepsilon_r/\varepsilon_b$ is from 0.0 to 3.0, and $L_s = 5.31\Delta x$ 99

Figure 3.26. As in Fig. 3.7, except for variation of the height/wind observation sensitivity measure as a function of L_b (abscissa) and $\varepsilon_r/\varepsilon_b$ (ordinate). The range of L_b is from 0.1Δx to 12.1Δx, the range of $\varepsilon_r/\varepsilon_b$ is from 0.0 to 3.0, and $L_s = 5.31\Delta x$ 100

Figure 3.27. As in Fig. 3.13, except for variation of the wind/height observation sensitivity measure as a function $\varepsilon_r/\varepsilon_b$ (abscissa) and L_s (ordinate). For this case, $L_b = 6.0\Delta x$ while L_s varies between 2.0Δx and 14.0Δx and $\varepsilon_r/\varepsilon_b$ ranges from 0.0 to 3.0. 101

Figure 3.28. As in Fig. 3.8, except for variation of the height/wind observation sensitivity measure as a function $\varepsilon_r/\varepsilon_b$ (abscissa) and L_s (ordinate). For this case, $L_b = 6.0\Delta x$ while L_s varies between 2.0Δx and 14.0Δx and $\varepsilon_r/\varepsilon_b$ ranges from 0.0 to 3.0. 102

Figure 3.29. Two-dimensional univariate single height observation sensitivity example. (a) Imposed analysis sensitivity gradient, (b) single height observation sensitivity, (c) background sensitivity, (d) corresponding analysis, assuming an innovation of 1.0 m for the single height observation at the "+", (e) background error correlation function for the observation at the "+", and (f) row of $\mathbf{K}^T$ for the observation at the "+". 107

Figure 3.30. As in Fig. 3.6, except for variation of the observation sensitivity measure (ordinate) as a function of L_b from 0.25Δx to 25.0Δx (abscissa) for the single height observation in a two-dimensional field. 110

Figure 3.31. As in Fig. 3.7, except for variation of the observation sensitivity measure as a function of L_b (abscissa) and $\varepsilon_r/\varepsilon_b$ (ordinate) for the single height observation in a two-dimensional field. 112

Figure 3.32. Two-dimensional univariate height observation sensitivity example for multiple observations. The target height observation is identified by the circle; the other height observations are given by the "+". In this plot, $L_b = 3.6\Delta x$, and $\varepsilon_r/\varepsilon_b = 0.1$. (a) The imposed analysis sensitivity gradient, (b) the analysis space projection of the observation sensitivity vector, (c) the background sensitivity, (d) the corresponding analysis, assuming an innovation of 1.0 m at each observation location, (e) the background error correlation function corresponding to the target observation, and (f) the row of $\mathbf{K}^T$ for the target observation. 115

Figure 3.33. Plots of the row of $\mathbf{K}^T$ for the 20 observations shown in Fig. 3.32. The row of $\mathbf{K}^T$ corresponds to the circled observation in each panel. The grid domain and color scale corresponds to Fig. 3.32. 118

Figure 3.34. As in Fig. 3.32, except for two-dimensional univariate height observation sensitivity example for multiple observations, with $L_b = 10.7\Delta x$, and $\varepsilon_r/\varepsilon_b = 0.1$. 121

Figure 3.35. Two-dimensional univariate height observation sensitivity example for multiple observations, as in Fig. 3.34, except with $L_b = 1.0\Delta x$, and $\varepsilon_r/\varepsilon_b = 0.1$. 122

Figure 3.36. As in Fig. 3.30, except for variation of the observation sensitivity measure (ordinate) as a function of L_b from 0.1Δx to 300.0Δx (abscissa) for the target observation as indicated by the circle in Fig. 3.32b. 125

Figure 3.37. Two-dimensional univariate height observation sensitivity example for multiple observations as in Fig. 3.32, except with $L_b = 3.6\Delta x$, and $\varepsilon_r/\varepsilon_b = 0.5$. 128

Figure 3.38. Two-dimensional univariate height observation sensitivity example for multiple observations as in Fig. 3.37, except with $L_b = 3.6\Delta x$, and $\varepsilon_r/\varepsilon_b = 1.0$. 129

Figure 3.39. As in Fig. 3.26, except for variation of the observation sensitivity measure as a function of L_b (abscissa) and $\varepsilon_r/\varepsilon_b$ (ordinate) for the target height observation in a two-dimensional field. 130

Figure 3.40. The imposed idealized analysis sensitivity gradient for height, u- and v-wind, as in Fig. 3.29. 137

Figure 3.41. Single observation sensitivity maps for the partial observation sensitivities in (3.50a-i). (a) Univariate height, (b) height/u-wind, (c) height/v-wind, (d) u-wind/height, (e) univariate u-wind, (f) u-wind/v-wind, (g) v-wind/height, (h) v-wind/u-wind, and (i) univariate v-wind observation sensitivities. 138

Figure 3.42. Kalman gain matrices for a single observation denoted by a circle corresponding to the background error correlation functions in (3.49a-i). (a) Univariate height, (b) height/u-wind, (c) height/v-wind, (d) u-wind/height, (e) univariate u-wind, (f) u-wind/v-wind, (g) v-wind/height, (h) v-wind/u-wind, and (i) univariate v-wind background error correlation models. 140

Figure 3.43. NOGAPS analysis sensitivity gradients at 850 hPa for (a) temperature, (b) u-wind, and (c) v-wind. 144

Figure 3.44. As in Fig. 3.41, except for single observation sensitivity maps corresponding to the analysis sensitivity gradients in Fig. 3.43. 146

Figure 3.45. As in Fig. 3.42, except for Kalman gain matrices for a single observation denoted by a circle corresponding to the background error correlation functions in (3.49a-i) and the grid domain in Fig. 3.43. 147

Figure 3.46. Total single observation sensitivity maps from (3.52a-c) corresponding to the analysis sensitivity gradients in Fig. 3.43 for (a) temperature, (b) u-wind, and (c) v-wind 150

Figure 3.47. As in Fig. 3.43, except NOGAPS analysis sensitivity gradients at 850 hPa for a more limited domain for (a) temperature, (b) u-wind, and (c) v-wind. The observation locations for the hypothetical flight track are given by the "+" 153

Figure 3.48. Total observation sensitivity measure from (3.52a-c) and (3.6) for a set of 22 observations indicated by the "+". 154

Figure 3.49. As in Fig. 3.43, except NOGAPS analysis sensitivity gradients at 850 hPa for a more limited domain for (a) temperature, (b) u-wind, and (c) v-wind. 156

Figure 3.50. As in Fig. 3.41, except the observation sensitivity vectors for the hypothetical satellite swath from (3.50a-i) corresponding to the analysis sensitivity gradients in Fig. 3.49. 157

Figure 3.51. Total observation sensitivities for the hypothetical satellite swath from (3.52a-c) for (a) temperature, (b) u-wind, and (c) v-wind. 159

Figure 3.52. The total marginal observation sensitivity vectors for the hypothetical flight track of observations and a single probe observation for (a) temperature, (b) u-wind, and (c) v-wind. 161

Figure 4.1. Sensitivity of the 72-h NOGAPS energy-weighted forecast error with respect to the FNMOC/NOGAPS 850-hPa initial (a) u-wind component, (b) v-wind component, and (c) temperature fields valid at the target time of 00 UTC 7 February 1999. The forecast verification area (not shown) is centered over the western United States and Canada (30 °N – 60°N and 150°W – 100°W). 179

Figure 4.2. As in Fig. 4.1, except for the sensitivity of the 72-h NOGAPS energy-weighted forecast error with respect to the FNMOC/NOGAPS 700-hPa initial (a) u-wind component, (b) v-wind component, and (c) temperature fields valid at the target time of 00 UTC 7 February 1999. 180

Figure 4.3. As in Fig. 4.1, except for the sensitivity of the 72-h NOGAPS energy-weighted forecast error with respect to the FNMOC/NOGAPS 500-hPa initial (a) u-wind component, (b) v-wind component, and (c) temperature fields valid at the target time of 00 UTC 7 February 1999. 181

Figure 4.4. As in Fig. 4.1, except for the sensitivity of the 72-h NOGAPS energy-weighted forecast error with respect to the FNMOC/NOGAPS 400-hPa (a) initial temperature, (b) u-wind component, and (c) v-wind component fields valid at the target time of 00 UTC 7 February 1999. 182

Figure 4.5. Magnitude of the sensitivity of the forecast aspect *J* to the (a) u-wind observation components, (b) v-wind observation components, and (c) temperature observations between 450 and 550 hPa valid at 00 UTC 7 February 1999 for the control plus G-IV adaptive observations (CTL+G-IV) case. 187

Figure 4.6. Magnitude of the sensitivity of the forecast aspect *J* to the TOVS MSU Channel 2 brightness temperatures valid at 00 UTC 7 February 1999 for the control plus G-IV adaptive observations (CTL+G-IV) case. 190

Figure 4.7. Hypothetical driftsonde locations, denoted by the "*", and valid for 00 UTC 7 February 1999. The approximate locations of the 13 launch sites are indicated by a "L". 195

Figure 4.8. Reduction in the expected variance of the change in the 72-h forecast error $\left\langle (\delta J)^2 \right\rangle_o$ computed for all observations for the control (CTL) case, and plotted for the radiosonde observations. 197

Figure 4.9. As in Fig. 4.8, except for the reduction in the expected variance of the change in the 72-h forecast error $\left\langle (\delta J)^2 \right\rangle_o$ computed for all observations for the control plus G-IV targeting (CTL+GIV) case, and plotted for the radiosonde and dropsonde observations. 199

Figure 4.10. As in Fig. 4.8, except for the reduction in the expected variance of the change in the 72-h forecast error $\left\langle (\delta J)^2 \right\rangle_o$ computed for all observations for the control plus hypothetical targeting deployment from Elmendorf AFB (CTL+e1) case, and plotted for the radiosonde and dropsonde observations. 200

Figure 4.11. As in Fig. 4.8, except for the reduction in the expected variance of the change in the 72-h forecast error $\left\langle (\delta J)^2 \right\rangle_o$ computed for all observations for the control plus hypothetical targeting deployment from Shemya/ Eareckson air station (CTL+s1) case, and plotted for the radiosonde and dropsonde observations. 201

Figure 4.12. As in Fig. 4.8, except for the reduction in the expected variance of the change in the 72-h forecast error $\left\langle (\delta J)^2 \right\rangle_o$ computed for all observations for the control plus hypothetical targeting deployment from Tokyo (CTL+t1) case, and plotted for the radiosonde and dropsonde observations. 202

Figure 4.13. As in Fig. 4.8, except for the reduction in the expected variance of the change in the 72-h forecast error $\left\langle (\delta J)^2 \right\rangle_o$ computed for all observations for the control plus hypothetical targeting deployment in Chapter III.F.3.c. (CTL+t1) case, and plotted for the radiosonde and dropsonde observations. 203

Figure 4.14. As in Fig. 4.8, except for the reduction in the expected variance of the change in the 72-h forecast error $\left\langle (\delta J)^2 \right\rangle_o$ computed for all observations for the control plus hypothetical driftsonde-deployed dropsondes (CTL+d1) case, and plotted for the radiosonde and driftsonde-deployed dropsonde observations. 204

Figure 4.15. Relative contributions to the reduction in the variance of the change in the forecast aspect for ten observing platforms for the seven different targeting deployments corresponding to Figs. 4.8-4.14. 207

Figure 4.16. As in Fig. 4.8, except for the reduction in the expected variance of the change in the 72-h forecast error $\left\langle (\delta J)^2 \right\rangle_o$ computed for all observations for the control plus hypothetical first alternate targeting deployment from Shemya/ Eareckson air station (CTL+s2) case, and plotted for the radiosonde and dropsonde observations. 210

Figure 4.17. As in Fig. 4.8, except for the reduction in the expected variance of the change in the 72-h forecast error $\left\langle (\delta J)^2 \right\rangle_o$ computed for all observations for the control plus hypothetical second alternate targeting deployment from Shemya/ Eareckson air station (CTL+s3) case, and plotted for the radiosonde and dropsonde observations. 211

Figure 4.18. As in Fig. 4.15, except for relative contributions to the reduction in the variance of the change in the forecast aspect for ten observing platforms for the control plus driftsonde (CTL+d1) in Fig. 4.14 and three Shemya/Eareckson hypothetical targeting deployments labeled s1, s2, and s3 corresponding to Figs. 4.11, 4.16, and 4.17. 212

Figure 4.19. As in Fig. 4.15, except for relative contributions to the reduction in the variance of the change in the forecast aspect for ten observing platforms for the control (CTL) in Fig. 4.8, control plus driftsonde (CTL+d1) in Fig. 4.14, and hypothetical targeting deployments combining the driftsonde network with the second Shemya and the Tokyo hypothetical deployments labeled (d1+s2) and (d1+t1) corresponding to Figs. 4.16 and 4.12. 214

THIS PAGE INTENTIONALLY LEFT BLANK

LIST OF TABLES

Table 4.1. Change in the univariate sensitivity to a single temperature observation for a specified change in the observation error for the NAVDAS adjoint. Values in columns 2-4 are, respectively, the observation error standard deviations (ε_r), E from (3.11), and the changes in E from EXP1. Values in column 5 are the observation sensitivities and values in column 6 are the changes in the observation sensitivity from EXP1. 173

Table 4.2. As in Table 4.1, except for the change in the univariate sensitivity to a single temperature observation for a specified change in the observation error for the two-dimensional analysis system. 173

Table 4.3. As in Table 4.1, except for the change in the total sensitivity to a single temperature observation for a specified change in the observation error for the NAVDAS adjoint.. 174

Table 4.4. As in Table 4.3, except for the change in the total sensitivity to a single temperature observation for a specified change in the observation error for the two-dimensional analysis system. 174

Table 4.5. Summary of the observations valid for the 6-hour time window centered on 00 UTC 7 February 1999. Column 1 denotes the observing platform; column 2 is the number of observations; column 3 is the number of rejected or thinned observations, and column 4 gives the total number of observations. 185

Table 4.6. Observation counts for the different observing platforms for the different hypothetical targeting experiments. CTL: control or conventional observing networks; CTL+GIV: control plus G-IV flight track; CTL+e1: control plus Elmendorf flight track; CTL+s1: control plus Shemya flight track; CTL+t1: control plus Tokyo flight track; CTL+c4: control plus Chapter III.F.3.c flight path; CTL+d1: control plus driftsonde network...................................... 194

THIS PAGE INTENTIONALLY LEFT BLANK

ACKNOWLEDGMENTS

I wish to thank Professor Russell Elsberry for his scientific guidance and editorial expertise that significantly improved the quality and readability of this dissertation. I would also like to thank Dr. Roger Daley, whose inspiration provided the mathematical foundation for the data assimilation adjoint theory, for his technical guidance on this research. My numerous scientific discussions with Roger over the past five years have significantly increased my understanding of data assimilation. I am grateful to Dr. Ron Errico for encouraging me to pursue this degree. Ron has been a mentor to me for a number of years, and my development as a scientist has been greatly enhanced by our many conversations. I appreciate the time and effort that these committee members, along with Professor Richard Franke, Professor R. Terry Williams and Professor Carlyle Wash, have spent reviewing the research proposals and dissertation.

Progress on this dissertation was aided with a six month Naval Research Laboratory Long Term Training assignment at the Naval Postgraduate School. The opportunity to obtain the doctorate in Meteorology while employed at the Naval Research Laboratory, and the support of my supervisors Dr. Edward Barker, Dr. Jim Goerss, Dr. Richard Hodur, and Dr. Phillip Merilees are gratefully acknowledged. I also wish to thank Professor Carlyle Wash, Chair of the Meteorology Department, for providing office space and support during my stay at the Naval Postgraduate School, and Dr. Rolf Langland for providing the NOGAPS adjoint analysis sensitivity fields.

I could not have completed this dissertation without the constant love, support and encouragement of my husband Michael Smelser. Mike willingly shouldered the majority

of the household responsibilities so that I could concentrate on my research. Finally, I give special thanks to my son Ian, whose laughter and love have provided balance and joy to my life while completing this degree.

This work was supported by the Naval Research Laboratory and the Office of Naval Research under program element 0602435, project number BE-35-2-32; program element 0602435N, project number BE-35-2-19; and program element 0601153N, project number BE-33-03-45.

I. INTRODUCTION

Ongoing improvements to the current numerical weather forecast models and data assimilation systems, combined with the deployment of space-based and other advanced observing systems, have led to a slow, steady reduction in short- and medium-range forecast errors over the past few decades (Hogan *et al.* 1999; ECMWF 2000). Despite these advances, it is still clear that a significant component of medium-range forecast error is due to analysis (initial condition) error in relatively poorly sampled regions such as the mid-Pacific Ocean, the tropics and the Southern Hemisphere Oceans (Rabier *et al.* 1994; Rabier *et al.* 1996). If the regions where additional observations are mostly likely to have a large positive impact on the numerical forecast can be identified in advance, then these regions can hypothetically be sampled with dropsondes from aircraft or unmanned aerial vehicles (UAVs) with the capability to observe the atmosphere. These targeted observations would supplement the conventional or routine observing network and would be adaptive in the sense that the locations of the supplemental observations would vary from day to day.

The concept of targeted or adaptive observations has generated a great deal of interest recently (e.g., Snyder 1996), and several objective targeting techniques have emerged to tackle this problem. Some of the approaches include the singular vector approach (Palmer *et al.* 1998; Gelaro *et al.* 1999; Bergot *et al.* 1999; Buizza and Montani 1999), the gradient sensitivity technique (Langland and Rohaly 1996; Bergot *et al.* 1999), the ensemble spread method (Lorenz and Emanuel 1998), the quasi-inverse technique (Pu *et al.* 1998; Pu and Kalnay 1999), and the ensemble transform approach (Bishop and Toth 1999).

The singular vector (SV) and the gradient sensitivity methods, which make use of the adjoint of the forecast model, are of particular interest for this dissertation. A forecast verification area (FVA), which is a subset of the total domain, and a cost function J, which is a scalar measure of some forecast quantity of interest over the FVA, are defined. The cost function or *forecast aspect* J, must be a differentiable function of the forecast accuracy, and must also be quadratic in the perturbations for the singular vector technique.

The singular vector (SV) or singular value decomposition (svd) method identifies the possible error structures in the analysis field that grow most rapidly as they are propagated forward in time by the forecast model. This procedure uses the linearized forecast model (tangent model) and its matrix transpose (adjoint), together with a normalization or scaling matrix (usually an energy norm) to define a matrix problem, whose largest singular values are associated with the most rapidly amplifying singular vectors of the forecast error. For targeting applications, the norm or metric used in SV calculations should include information about the analysis error covariances. However, Palmer *et al.* (1998) have shown that a metric based on perturbation total energy is a useful approximation to the analysis error covariance metric.

In the gradient sensitivity method, the adjoint of the forecast model is used to calculate the gradient of J with respect to the initial conditions for the forecast. It can be shown that this gradient, which will be referred to as the *analysis sensitivity gradient*, is a linear combination of the corresponding singular vectors and singular values of a compound operator involving products of the adjoint and tangent models with the total energy norm provided that J is specified in terms of the total energy error (Buizza *et al.* 1997; Gelaro *et al.* 1999). Under these conditions, most of the structure of the analysis sensitivity gradient can be explained using only the leading or most unstable singular vectors (Gelaro *et al.* 1998).

An example of the most unstable singular vector during the Fronts and Atlantic Storm Track Experiment (FASTEX) Intensive Observing Period (IOP) number 17 is shown in Fig. 1.1. The 600-hPa temperature structure of the leading singular vector (Fig. 1.1a) was calculated using the total energy norm (Buizza and Palmer 1995; Rabier *et al.* 1996). The FVA over Northern Europe is identified by the box in Fig. 1.1a, and the solid line indicates the center for the vertical cross-section (Fig. 1.1b) for temperature averaged over the latitude zone of 40-45° N.

The corresponding gradient of J with respect to the initial temperature field is shown in Fig. 1.2a, where J is the vertically averaged vorticity from 650 hPa to the surface in the FVA. The vertical cross section averaged over the latitude zone of 40-45° N is shown in Fig. 1.2b. The SV structures and the analysis sensitivity gradients are remarkably similar for this case, which indicates that most of the forecast error growth is associated with the leading SV. In the extratropics, the structures associated with the

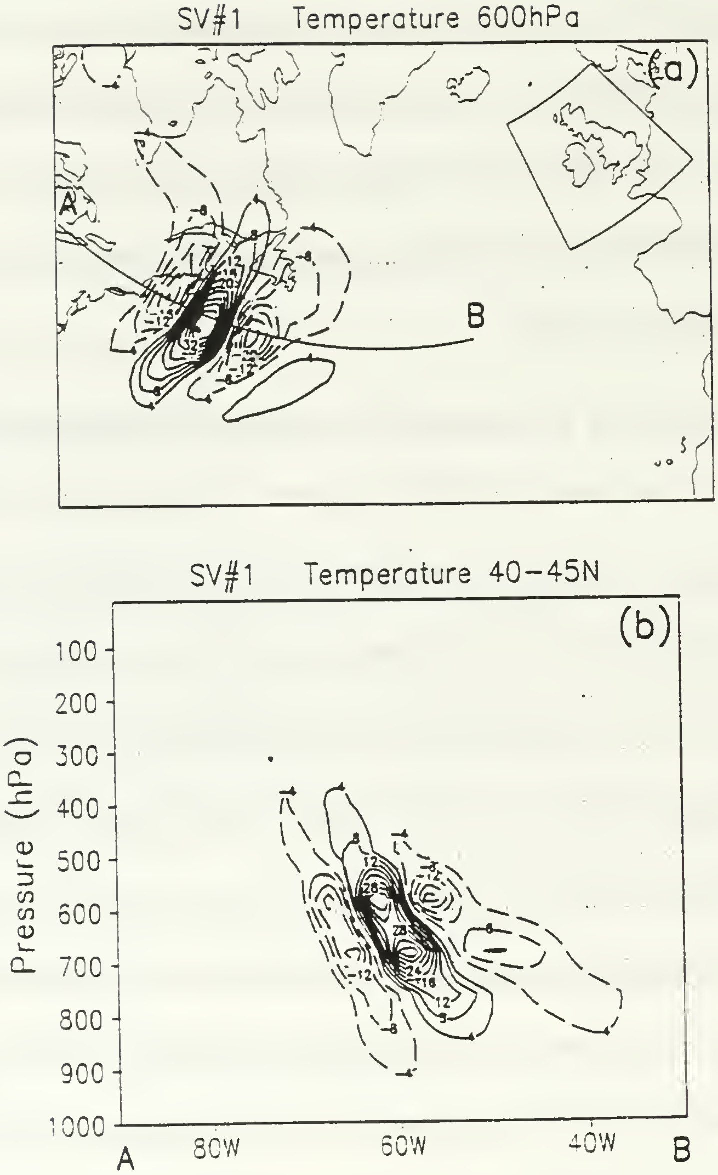
SV#1 Temperature 600hPa
(a)
A
B
SV#1 Temperature 40-45N
(b)
Pressure (hPa)
100
200
300
400
500
600
700
800
900
1000
A
80W
60W
40W
B

Figure 1.1. An example of the most unstable singular vector during FASTEX IOP-17 for an initial time of 18 UTC 17 February 1997, and optimized for the forecast verification time of 12 UTC 19 February 1997. (a) Horizontal temperature structure at 600 hPa with the forecast verification area given by the box over Great Britain, and (b) vertical cross-section through the temperature structure averaged over the latitude zone of 40-45°N. (Figure provided by R. Gelaro, NRL – Monterey.)

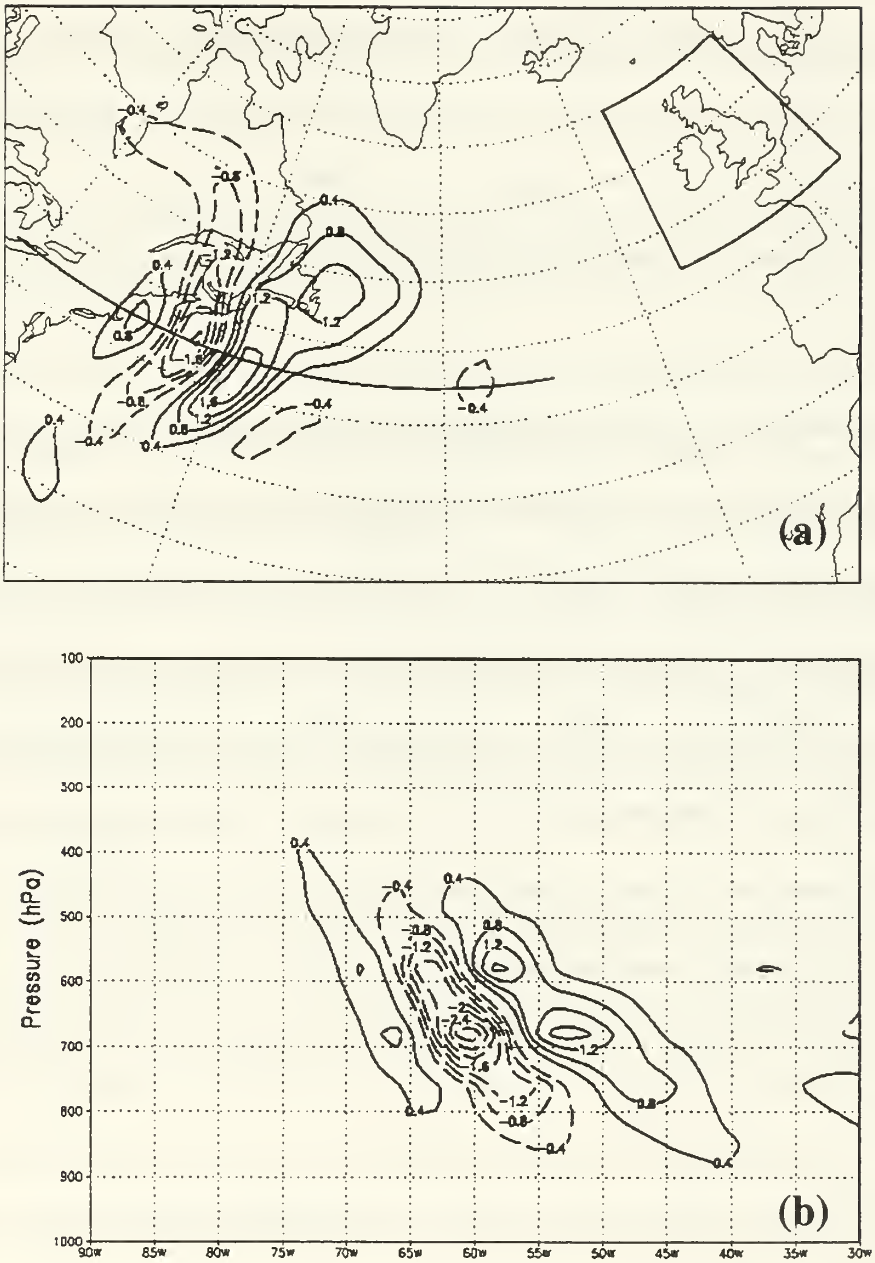

Figure 1.2. As in Figs. 1.1a and 1.1b, except for the sensitivity of the vertically averaged vorticity from 650 hPa to the surface in the FVA with respect to the initial temperature field during FASTEX IOP-17. The sensitivity gradient is computed for a 72-h nonlinear trajectory ending at 12 UTC 19 February 1997 and an adjoint calculation backwards 42 hours to the initial time of 18 UTC 17 February 1997. (a) Horizontal temperature analysis sensitivity gradient at 600 hPa with the forecast verification area given by the box over Great Britain, and (b) vertical cross-section through the temperature analysis sensitivity gradient averaged over the latitude zone of 40-45°N. (Figure provided by R. Langland, NRL – Monterey.)

leading SV or analysis sensitivity gradient usually have maximum amplitude in the lower troposphere, tilt into the prevailing westerlies, and correspond to growing baroclinic disturbances (Rabier *et al.* 1994; Rabier *et al.* 1996). The structures may be quite different in the tropics or when associated with other unstable phenomena (Buizza and Palmer 1995).

It is important to note that structures such as those shown in Figs. 1.1 or 1.2 are not measures of analysis error but indicate the directions along which the analysis error is likely to grow most rapidly. While only a small part of the analysis error may project onto these structures, growth of this component of the analysis error may dominate the forecast error (Gelaro *et al.* 1999). Even though the actual analysis errors may be considerably larger in other regions, it is the dynamically sensitive areas that should be most carefully observed. However, this does not imply that it is not necessary to observe in non-sensitive regions, since the linearization implicit in either the SV or gradient sensitivity techniques requires that the basic state for linearization be reasonably close to the true state.

These singular vectors (Fig. 1.1) and analysis sensitivity gradients (Fig. 1.2) were determined *a posteriori*, using the forecast from an analysis valid at the initial or targeting time. However, real-time targeting requires that the target area be identified in advance to allow time for flight planning and deployment of the observations. It is possible to create a reasonably close facsimile of these unstable structures *a priori* using the singular vectors generated from the 48- or 72-hour forecasts starting from some earlier time

(Gelaro *et al.* 1999). Once the sensitive regions have been identified, a flight track is chosen to sample the sensitive regions given the constraints of aircraft endurance, range, and economic limits.

Several recent field studies have been conducted to test the concept of targeted or adaptive observations. The first, a sub-experiment of FASTEX (Joly *et al.* 1997), was conducted in the North Atlantic during January and February 1997, and had a defined forecast verification area encompassing Great Britain and Northern Europe. The North Pacific Experiment (NORPEX; Langland *et al.* 1999b) was entirely devoted to investigating the impact of targeted observations on the downstream area over the United States. These two experiments were followed by the National Centers for Environmental Prediction (NCEP) Winter Storms Reconnaissance (WSR) missions of 1999 and 2000 (Szunyogh *et al.* 2000).

Some of the targeting sorties carried out during FASTEX (Langland *et al.* 1999a; Bergot 1999; Szunyogh *et al.* 1999) and particularly NORPEX (Langland *et al.* 1999b) and WSR (Szunyogh *et al.* 2000) were successful, in the sense that assimilation of the dropwinsondes resulted in improved forecasts over the verification domain and at the verification time. Other targeting sorties using the same targeting algorithms were unsuccessful (Bergot 1999), which demonstrated that simply presenting additional observations in an arbitrary or highly localized pattern to the data assimilation systems does not guarantee that the subsequent forecasts will be improved. Perhaps this should not be too surprising since, strictly speaking, data assimilation and forecasting are statistical problems in which the minimum variance solutions are obtained in an ensemble sense. Thus, it can never be guaranteed that a minimum variance solution will be obtained by adding observations. Many other reasons are possible for the forecast failures. Reasons related to possible inadequacies in the model or targeting technique include: (i) the adjoint and tangent models may have been linearized about atmospheric states that were too different from the true state; (ii) the forecast model adjoints (which usually do not include all physical processes) may not describe the physical phenomena adequately; (iii) the forecast models may not be accurate or complete enough; or (iv) details of the targeting technique (such as the choice of the energy norm in the singular vector method) might be flawed. Other possible reasons for forecast failure are concerned with the data assimilation process, the observing systems, and the way in which the targets are sampled.

The objective targeting techniques discussed above identify regions or structures where the forecast is sensitive to analysis errors. However, simply deploying a dropwinsonde in a sensitive region does not necessarily change the analysis. The dropwinsonde report must go through a complex data assimilation process before it is allowed to influence the analysis, and potentially affect the forecast. In data assimilation procedures, the reports are first quality controlled and checked against other observations (buddy-checked). The observations that pass the data screening procedures are allowed to interact with the background field (usually a 6-hour forecast from the model) and the other observations. Only then can an observation truly affect the analysis. The effect of an observation on the analysis (and thereby the forecast) depends upon the specified background and observation error statistics, and the distribution and properties of all other observations in the vicinity. None of the above objective targeting techniques provides any guidance on these issues that lie within the realm of the data assimilation step versus the modeling step. Consequently, the placement of the adaptive observations in the sensitive areas has been largely subjective.

One can imagine a number of reasons for the failure of targeting exercises that are inherently related to the data assimilation system. For example, how should structures such as those in Figs. 1.1 and 1.2 be sampled – how many dropwinsondes are needed and where should they be placed? How will other observations in the vicinity affect the outcome, and should the sampling strategy account for their likely presence? What effect does the background error, which is likely to be large and not well known in poorly observed regions, have on targeting results?

A very critical issue is whether the data assimilation system is capable of optimally assimilating the targeted observations. Recent research by Fischer *et al.* (1998), Bergot (2000), Rabier *et al.* (2000), and Bishop *et al.* (2000) suggests that advanced assimilation techniques, such as four-dimensional variational data assimilation (4DVAR), are better able to utilize targeted observations than three-dimensional variational data assimilation systems (3DVAR). Bergot *et al.* (1999) found that the French operational 3DVAR data assimilation system required that all of the analysis sensitivity structure must be sampled, rather than just the extrema. They concluded that the success of adaptive observations will depend on the data assimilation scheme.

The importance of taking into account the characteristics of the data assimilation system and the presence of other observations has been emphasized by Baker and Daley (1999), Doerenbecher *et al.* (2000), Berliner *et al.* (1999), Baker and Daley (2000), Doerenbecher and Bergot (2000), and Bishop *et al.* (2000). Extensions to the present targeting strategies have been proposed to address these limitations, e.g., the observation adjoint sensitivity approach (Baker and Daley 2000; Doerenbecher and Bergot 2000) and the ensemble transform Kalman filter techniques (Bishop *et al.* 2000). The observation adjoint sensitivity approach uses the adjoint of the data assimilation system to compute the sensitivity of the forecast aspect J to the observations and the background, while taking into account the specified background and observation error statistics, and the distribution and properties of the other observations in the area. The Ensemble Transform Kalman Filter (ET KF) approach uses a Kalman filter to predict the reduction in the prediction error variances due to the adaptive observations. This method also accounts for the presence of other observations and, provided the assimilation system uses the background error covariance matrix generated by the ET KF, the error characteristics of the data assimilation system.

The research in this dissertation and in Baker and Daley (2000) was motivated by preparations in late 1996 by scientists at the Naval Research Laboratory in Monterey, CA for then upcoming FASTEX experiment. Although the SV and analysis sensitivity gradients highlight areas of the atmosphere with large sensitivity to the initial conditions, neither method is able to give any information as to whether the initial errors are likely due to the observations (or lack thereof), the background, or the data assimilation system.

For targeting applications, neither method is able to provide guidance on where the targeted observations should be placed, given the presence of other observations and the characteristics of the assimilating algorithm. In view of these limitations, the author and R. Daley discussed the feasibility of determining the sensitivity of the forecast aspect to the observations and the background. Based on these discussions, R. Daley derived the equations for observation and background sensitivity presented in Chapter II, which was the genesis of the following research.

Although the research is focused on the adaptive observation-targeting problem, the potential applicability of the data assimilation adjoint theory is much broader, in that it illustrates how data assimilation works and lends insight into how observations are used by the data assimilation system.

The purpose of the research described in this dissertation is to thoroughly investigate observation adjoint sensitivity, and assess its potential application for the adaptive targeting of observations. The data assimilation adjoint theory is presented in Chapter II. Observation and background sensitivity are investigated in the simplified context of one- and two-dimensional analysis systems in Chapter III. In Chapter IV, the observation sensitivity using the NAVDAS (NRL Atmospheric Variational Data Assimilation System) adjoint (Daley and Barker 2000a) and analysis sensitivity gradients computed using the NOGAPS (Navy Operational Global Atmospheric Prediction System) adjoint (Rosmond 1997) is investigated. The summary and conclusions are presented in Chapter V.

THIS PAGE INTENTIONALLY LEFT BLANK

II. DATA ASSIMILATION ADJOINT THEORY

A. DERIVATION OF OBSERVATION AND BACKGROUND SENSITIVITY

The derivation of the observation and background sensitivity begins with the three-dimensional analysis problem and the analysis equation (Daley 1991),

$$\mathbf{x}_a = \mathbf{x}_b + \mathbf{K}(\mathbf{y} - H\{\mathbf{x}_b\}) \tag{2.1}$$

The vector of observations (of length M) is given by $\mathbf{y}$, the background vector (of length N) is given by $\mathbf{x}_b$, and the analysis vector (of length N) is given by $\mathbf{x}_a$. In general, the application of the observation or forward operator H represents any necessary spatial and temporal interpolations from the forecast model background to the observation location and time. If the observed quantity is not directly related to the model state variables, then H also represents the transformation from the forecast values to the observed quantity. For satellite radiances (or brightness temperatures), $H\{x_b\}$ represents the forward radiative transfer model applied to $\mathbf{x}_b$ and computes forecast or background radiances. The differences between the observation and the background in observation space $(\mathbf{y} - H\{\mathbf{x}_b\})$ is referred to as the *innovation vector*, and the quantity $\mathbf{x}_a - \mathbf{x}_b = \mathbf{K}(\mathbf{y} - H\{\mathbf{x}_b\})$ is the *correction vector.* If one considers linear analysis problems only, then

$$\mathbf{x}_a = \mathbf{x}_b + \mathbf{K}(\mathbf{y} - \mathbf{H}\mathbf{x}_b)\,. \tag{2.2}$$

The matrix **H** is the Jacobian matrix corresponding to the forward operator $H\{x_b\}$ linearized about the background state vector. This approximation is valid for the radiative transfer relationship between temperatures and radiances, but is not valid for moisture retrievals. The Kalman gain (or weight) matrix, **K**, is given by

$$\mathbf{K} = \mathbf{P}_b\mathbf{H}^T(\mathbf{H}\mathbf{P}_b\mathbf{H}^T + \mathbf{R})^{-1}, \tag{2.3}$$

where $\mathbf{P}_b$ is the background error covariance matrix and **R** is the observation error covariance matrix.

Equation (2.2) may be rewritten as

$$\mathbf{x_a} = \mathbf{x_b} - \mathbf{KHx_b} + \mathbf{Ky} = (\mathbf{I} - \mathbf{KH})\mathbf{x_b} + \mathbf{Ky}, \tag{2.4}$$

where **I** is the NxN identity matrix. The sensitivity of the analysis to the observations $\partial\mathbf{x_a}/\partial\mathbf{y}$ and the sensitivity of the analysis to the background $\partial\mathbf{x_a}/\partial\mathbf{x_b}$ is derived first. Following Gelb (1974), the vector gradient of a vector is a matrix and is given by $\partial\mathbf{x}^T/\partial\mathbf{y} = \mathbf{A}$, or $\partial x_i/\partial y_k = a_{ki}$. Using this relationship, the following equations may be derived:

$$\partial\mathbf{x_a}/\partial\mathbf{y} = \mathbf{K}^T, \tag{2.5a}$$

$$\partial\mathbf{x_a}/\partial\mathbf{x_b} = (\mathbf{I} - \mathbf{KH})^T = \mathbf{I} - \mathbf{H}^T\mathbf{K}^T, \tag{2.5b}$$

where

$$\mathbf{K}^T = (\mathbf{H}\mathbf{P_b}\mathbf{H}^T + \mathbf{R})^{-1}\mathbf{H}\mathbf{P}_b. \tag{2.6}$$

One useful application of (2.5a,b) is to the adaptive targeting problem. Suppose that the targeting is based upon the adjoint-based techniques described in Chapter I. The cost function J is a scalar measure of some quantity of interest over the forecast verification domain (which is a subset of the total domain). The gradient of J with respect to the initial conditions for the forecast is given by $\partial J/\partial \mathbf{x}_a$, and is a vector of length N. This is the analysis sensitivity vector described in Chapter I. In the following development, the individual unstable singular vectors or some linear combination of these singular vectors may be used instead of the actual gradient $\partial J/\partial \mathbf{x}_a$, realizing that they are closely related, as described in Chapter I.

Except in theoretical experiments, the forecast error is not known when selecting targets and the cost function J must be based on the forecast alone. During FASTEX, the forecast aspect J for the adjoint sensitivity calculations was defined as the average lower troposphere vorticity in the forecast verification domain since low-level tropospheric vorticity is thought to be highly correlated with the cyclone position forecast error (Langland *et al.* 1999a). This scenario is referred to as an *a priori* (pre-deployment) estimate of J, as opposed to an *a posteriori* (after-the-fact) estimate.

The primary quantity of interest in this dissertation is the sensitivity of the forecast aspect to the observations or $\partial J/\partial \mathbf{y}$, which is a vector of length M and will be referred to as the *observation sensitivity vector.* Also of interest is the sensitivity of the forecast aspect to the background field $\partial J/\partial \mathbf{x}_b$, which is a vector of length N and will be referred to as the *background sensitivity vector.* Using the chain rule and (2.5), the observation and background sensitivity vectors may be written as

$$\partial J/\partial \mathbf{y} = \frac{\partial \mathbf{x}_a}{\partial \mathbf{y}}\frac{\partial J}{\partial \mathbf{x}_a} = \mathbf{K}^T \partial J/\partial \mathbf{x}_a , \tag{2.7a}$$

$$\partial J/\partial \mathbf{x}_b = \frac{\partial \mathbf{x}_a}{\partial \mathbf{x}_b}\frac{\partial J}{\partial \mathbf{x}_a} = (\mathbf{I} - \mathbf{H}^T\mathbf{K}^T)\partial J/\partial \mathbf{x}_a \tag{2.7b}$$

Expanding the terms in the transposed Kalman gain matrix ($\mathbf{K}^T$) in (2.6) using (2.3) gives the following expressions for the observation and background sensitivity vectors,

$$\partial J/\partial \mathbf{y} = (\mathbf{H}\mathbf{P}_b\mathbf{H}^T + \mathbf{R})^{-1}\mathbf{H}\mathbf{P}_b \, \partial J/\partial \mathbf{x}_a , \tag{2.8a}$$

$$\partial J/\partial \mathbf{x}_b = \left[\mathbf{I} - \mathbf{H}^T(\mathbf{H}\mathbf{P}_b\mathbf{H}^T + \mathbf{R})^{-1}\mathbf{H}\mathbf{P}_b\right]\partial J/\partial \mathbf{x}_a . \tag{2.8b}$$

Strictly speaking, the applicability of the chain rule in (2.7) requires that the analysis sensitivity vector $\partial J/\partial \mathbf{x}_a$ be calculated using all the observations that are used in generating $\mathbf{K}$ or $\mathbf{K}^T$. Therefore, the assumption that $\partial J/\partial \mathbf{x}_a$ is specified independently of any additional targeted observations is not entirely correct. The adjoint and singular vectors are determined by the tangent forward propagator based on the nonlinear trajectory. As long as the change to this trajectory (due to the additional observations) evolves linearly over the optimization interval, the adjoint sensitivity gradient vectors and singular vectors should remain basically unchanged (Harrison *et al.* 1999). Thus, the assumption that $\partial J/\partial \mathbf{x}_a$ would not change substantially if additional observations were to be used is reasonable, and under these circumstances the use of the chain rule is appropriate.

In the analysis problem (2.1), $\mathbf{K}$ is the matrix of weights given to the *innovation* or difference between the observation and the background value (in observation space). In an analogous sense, the matrix $\mathbf{K}^T$ is the matrix of weights given to the analysis sensitivity gradient for the observation sensitivity problem (2.7a).

It is also convenient for display purposes to define the *analysis space projection of the observation sensitivity vector,*

$$\mathbf{H}^T\, \partial J/\partial \mathbf{y} = \partial J/\partial \mathbf{x}_a - \partial J/\partial \mathbf{x}_b\,. \tag{2.9}$$

Thus, (2.8a) and (2.8b) give a method of calculating the gradient (or sensitivity) of the forecast aspect with respect to the observations $\partial J/\partial \mathbf{y}$ and the gradient of the forecast aspect with respect to the background field $\partial J/\partial \mathbf{x}_b$. In order to use these expressions, the observation and background error covariances and the positions and types of the observations must be specified. One must also specify any forward operators $\mathbf{H}$ and matrix transposes $\mathbf{H}^T$ required to transform variables between observation to grid space. Assuming that $\partial J/\partial \mathbf{x}_a$ or a suitable proxy for the analysis sensitivity vector has already been computed, the actual observed and background values are not required. Note that this approach (unlike that of Le Dimet *et al.* 1995) does not require a second-order adjoint to determine the forecast aspect sensitivity with respect to the observations.

B. MULTIVARIATE OBSERVATION SENSITIVITY

Equations (2.1) – (2.9) are written is general terms, and the variables are not explicitly specified. For univariate problems, the variables in (2.1) – (2.9) are the same. To understand observation and background sensitivity, it is useful to expand the equations into the three components of the multivariate analysis problem (excluding moisture and indirect observations such as brightness temperatures). The sensitivity of J to a given observation in the multivariate setting includes contributions due to the background error cross-correlations between geopotential height (h), zonal (u) and meridional (v) wind components, and the height and u and v wind analysis sensitivity gradients.

The background error covariance matrix $\mathbf{P}_b$ is now composed of the 3x3 sub-matrices as follows,

$$\mathbf{P}_b = \begin{bmatrix} \mathbf{C}_{hh} & \mathbf{C}_{hu} & \mathbf{C}_{hv} \\ \mathbf{C}_{uh} & \mathbf{C}_{uu} & \mathbf{C}_{uv} \\ \mathbf{C}_{vh} & \mathbf{C}_{vu} & \mathbf{C}_{vv} \end{bmatrix}, \tag{2.10}$$

where $\mathbf{C}_{xy}$ is dimensioned (N x N) and represents the covariance between $x\,(=h,u,v)$ and $y\,(=h,u,v)$.

The *total sensitivity* of J to the height observations may be derived by expanding the terms in (2.8a) into the multivariate components using matrix-vector notation. Using (2.10), let

$$\mathbf{S} = (\mathbf{H}\mathbf{P}_b\mathbf{H}^T + \mathbf{R})^{-1} = \begin{bmatrix} \mathbf{S}_{hh} & \mathbf{S}_{hu} & \mathbf{S}_{hv} \\ \mathbf{S}_{uh} & \mathbf{S}_{uu} & \mathbf{S}_{uv} \\ \mathbf{S}_{vh} & \mathbf{S}_{vu} & \mathbf{S}_{vv} \end{bmatrix}, \quad (2.11)$$

where the subscripts on the (M x M) sub-matrices $\mathbf{S}_{xy}$ indicate that the background error covariance is computed between the locations of observations of type x and type y. The forward operator, which is composed of the three sub-matrices

$$\mathbf{H} = \begin{bmatrix} \mathbf{H}_h \\ \mathbf{H}_u \\ \mathbf{H}_v \end{bmatrix}, \quad (2.12)$$

transforms $\mathbf{P}_b$ into the observation space given by the subscript x on $\mathbf{H}_x$. Finally, the total observation sensitivity and analysis sensitivity gradients are expanded into their three component vectors

$$\partial J/\partial \mathbf{y} = \begin{bmatrix} \partial J/\partial \mathbf{h}_o \\ \partial J/\partial \mathbf{u}_o \\ \partial J/\partial \mathbf{v}_o \end{bmatrix}, \quad (2.13)$$

and

$$\partial J/\partial \mathbf{x}_a = \begin{bmatrix} \partial J/\partial \mathbf{h}_a \\ \partial J/\partial \mathbf{u}_a \\ \partial J/\partial \mathbf{v}_a \end{bmatrix}, \quad (2.14)$$

where the subscripts o and a refer to the observations and analysis, respectively.

Equation (2.8a) may then be written as

$$\begin{bmatrix} \partial J/\partial \mathbf{h}_o \\ \partial J/\partial \mathbf{u}_o \\ \partial J/\partial \mathbf{v}_o \end{bmatrix} = \begin{bmatrix} \mathbf{S}_{hh} & \mathbf{S}_{hu} & \mathbf{S}_{hv} \\ \mathbf{S}_{uh} & \mathbf{S}_{uu} & \mathbf{S}_{uv} \\ \mathbf{S}_{vh} & \mathbf{S}_{vu} & \mathbf{S}_{vv} \end{bmatrix} \begin{bmatrix} \mathbf{H}_h \\ \mathbf{H}_u \\ \mathbf{H}_v \end{bmatrix} \begin{bmatrix} \mathbf{C}_{hh} & \mathbf{C}_{hu} & \mathbf{C}_{hv} \\ \mathbf{C}_{uh} & \mathbf{C}_{uu} & \mathbf{C}_{uv} \\ \mathbf{C}_{vh} & \mathbf{C}_{vu} & \mathbf{C}_{vv} \end{bmatrix} \begin{bmatrix} \partial J/\partial \mathbf{h}_a \\ \partial J/\partial \mathbf{u}_a \\ \partial J/\partial \mathbf{v}_a \end{bmatrix}. \tag{2.15}$$

Multiplying through the terms in (2.15) gives the three equations for the total sensitivity of J to the h, u and v observations,

$$\begin{aligned} \partial J/\partial \mathbf{h}_o = & \mathbf{S}_{hh}\mathbf{H}_h[\mathbf{C}_{hh}\,\partial J/\partial \mathbf{h}_a + \mathbf{C}_{hu}\,\partial J/\partial \mathbf{u}_a + \mathbf{C}_{hv}\,\partial J/\partial \mathbf{v}_a] \\ & +\mathbf{S}_{hu}\mathbf{H}_u[\mathbf{C}_{uh}\,\partial J/\partial \mathbf{h}_a + \mathbf{C}_{uu}\,\partial J/\partial \mathbf{u}_a + \mathbf{C}_{uv}\,\partial J/\partial \mathbf{v}_a], \\ & +\mathbf{S}_{hv}\mathbf{H}_v[\mathbf{C}_{vh}\,\partial J/\partial \mathbf{h}_a + \mathbf{C}_{vu}\,\partial J/\partial \mathbf{u}_a + \mathbf{C}_{vv}\,\partial J/\partial \mathbf{v}_a] \end{aligned} \tag{2.16a}$$

$$\begin{aligned} \partial J/\partial \mathbf{u}_o = & \mathbf{S}_{uh}\mathbf{H}_h[\mathbf{C}_{hh}\,\partial J/\partial \mathbf{h}_a + \mathbf{C}_{hu}\,\partial J/\partial \mathbf{u}_a + \mathbf{C}_{hv}\,\partial J/\partial \mathbf{v}_a] \\ & +\mathbf{S}_{uu}\mathbf{H}_u[\mathbf{C}_{uh}\,\partial J/\partial \mathbf{h}_a + \mathbf{C}_{uu}\,\partial J/\partial \mathbf{u}_a + \mathbf{C}_{uv}\,\partial J/\partial \mathbf{v}_a], \\ & +\mathbf{S}_{uv}\mathbf{H}_v[\mathbf{C}_{vh}\,\partial J/\partial \mathbf{h}_a + \mathbf{C}_{vu}\,\partial J/\partial \mathbf{u}_a + \mathbf{C}_{vv}\,\partial J/\partial \mathbf{v}_a] \end{aligned} \tag{2.16b}$$

and

$$\begin{aligned} \partial J/\partial \mathbf{v}_o = & \mathbf{S}_{vh}\mathbf{H}_h[\mathbf{C}_{hh}\,\partial J/\partial \mathbf{h}_a + \mathbf{C}_{hu}\,\partial J/\partial \mathbf{u}_a + \mathbf{C}_{hv}\,\partial J/\partial \mathbf{v}_a] \\ & +\mathbf{S}_{vu}\mathbf{H}_u[\mathbf{C}_{uh}\,\partial J/\partial \mathbf{h}_a + \mathbf{C}_{uu}\,\partial J/\partial \mathbf{u}_a + \mathbf{C}_{uv}\,\partial J/\partial \mathbf{v}_a]. \\ & +\mathbf{S}_{vv}\mathbf{H}_v[\mathbf{C}_{vh}\,\partial J/\partial \mathbf{h}_a + \mathbf{C}_{vu}\,\partial J/\partial \mathbf{u}_a + \mathbf{C}_{vv}\,\partial J/\partial \mathbf{v}_a] \end{aligned} \tag{2.16c}$$

A compact notation is introduced next. From (2.6),

$$\mathbf{K}^T_{xy,z} = \mathbf{S}_{xy}\mathbf{H}_y\mathbf{C}_{yz}. \tag{2.17}$$

The subscripts x, y and z on $\mathbf{K}^T_{xy,z}$ are defined as follows. The term $(\mathbf{HP}_b\mathbf{H}^T)$ in (2.11) is the projection of the background error covariance matrix into the observation space given by the first two subscripts (x and y). The term $\mathbf{H}_y\mathbf{C}_{yz}$ in (2.16) is the projection of the background error covariances from the analysis sensitivity grid space (as denoted by the third subscript, z) into observation space (as given by the second subscript, y).

The total sensitivity of J to the height observations may then be written as the sum of the nine *partial sensitivities,*

$$\begin{aligned}\partial J/\partial \mathbf{h}_o = {} & \mathbf{K}^T_{hh,h}\,\partial J/\partial \mathbf{h}_a + \mathbf{K}^T_{hh,u}\,\partial J/\partial \mathbf{u}_a + \mathbf{K}^T_{hh,v}\,\partial J/\partial \mathbf{v}_a + \mathbf{K}^T_{hu,h}\,\partial J/\partial \mathbf{h}_a + \mathbf{K}^T_{hu,u}\,\partial J/\partial \mathbf{u}_a \\ & + \mathbf{K}^T_{hu,v}\,\partial J/\partial \mathbf{v}_a + \mathbf{K}^T_{hv,h}\,\partial J/\partial \mathbf{h}_a + \mathbf{K}^T_{hv,u}\,\partial J/\partial \mathbf{u}_a + \mathbf{K}^T_{hv,v}\,\partial J/\partial \mathbf{v}_a .\end{aligned} \qquad (2.18a)$$

The total sensitivity of J to the u-wind observations is,

$$\begin{aligned}\partial J/\partial \mathbf{u}_o = {} & \mathbf{K}^T_{uh,h}\,\partial J/\partial \mathbf{h}_a + \mathbf{K}^T_{uh,u}\,\partial J/\partial \mathbf{u}_a + \mathbf{K}^T_{uh,v}\,\partial J/\partial \mathbf{v}_a + \mathbf{K}^T_{uu,h}\,\partial J/\partial \mathbf{h}_a + \mathbf{K}^T_{uu,u}\,\partial J/\partial \mathbf{u}_a \\ & + \mathbf{K}^T_{uu,v}\,\partial J/\partial \mathbf{v}_a + \mathbf{K}^T_{uv,h}\,\partial J/\partial \mathbf{h}_a + \mathbf{K}^T_{uv,u}\,\partial J/\partial \mathbf{u}_a + \mathbf{K}^T_{uv,v}\,\partial J/\partial \mathbf{v}_a ,\end{aligned} \qquad (2.18b)$$

and the total sensitivity of J to the v-wind observations is,

$$\begin{aligned}\partial J/\partial \mathbf{v}_o = {} & \mathbf{K}^T_{vh,h}\,\partial J/\partial \mathbf{h}_a + \mathbf{K}^T_{vh,u}\,\partial J/\partial \mathbf{u}_a + \mathbf{K}^T_{vh,v}\,\partial J/\partial \mathbf{v}_a + \mathbf{K}^T_{vu,h}\,\partial J/\partial \mathbf{h}_a + \mathbf{K}^T_{vu,u}\,\partial J/\partial \mathbf{u}_a \\ & + \mathbf{K}^T_{vu,v}\,\partial J/\partial \mathbf{v}_a + \mathbf{K}^T_{vv,h}\,\partial J/\partial \mathbf{h}_a + \mathbf{K}^T_{vv,u}\,\partial J/\partial \mathbf{u}_a + \mathbf{K}^T_{vv,v}\,\partial J/\partial \mathbf{v}_a ,\end{aligned} \qquad (2.18c)$$

where $\mathbf{K}^T$ is defined by (2.17). Thus, the total sensitivity to the height observations (2.18a) is composed of nine terms resulting from the interaction of the height observations with other the h, u or v observations, given the initial h, u or v analysis sensitivity gradients.

The first term in (2.18a) involves only the height observations and the height analysis sensitivity gradient, and represents the univariate height observation sensitivity. Similarly, the fifth term in (2.18b) and the last term in (2.18c) are the u- and v-wind component univariate observation sensitivities.

C. MULTIVARIATE BACKGROUND SENSITIVITY

The background sensitivity given by (2.8b) may be expanded into component form using (2.10) – (2.14) as

$$\begin{bmatrix} \partial J/\partial \mathbf{h}_b \\ \partial J/\partial \mathbf{u}_b \\ \partial J/\partial \mathbf{v}_b \end{bmatrix} = \begin{bmatrix} \partial J/\partial \mathbf{h}_a \\ \partial J/\partial \mathbf{u}_a \\ \partial J/\partial \mathbf{v}_a \end{bmatrix} - \begin{bmatrix} \mathbf{H}_h^T & \mathbf{H}_u^T & \mathbf{H}_v^T \end{bmatrix}^T \begin{bmatrix} S_{hh} & S_{hu} & S_{hv} \\ S_{uh} & S_{uu} & S_{uv} \\ S_{vh} & S_{vu} & S_{vv} \end{bmatrix} \begin{bmatrix} \mathbf{H}_h \\ \mathbf{H}_u \\ \mathbf{H}_v \end{bmatrix} \begin{bmatrix} C_{hh} & C_{hu} & C_{hv} \\ C_{uh} & C_{uu} & C_{uv} \\ C_{vh} & C_{vu} & C_{vv} \end{bmatrix} \begin{bmatrix} \partial J/\partial \mathbf{h}_a \\ \partial J/\partial \mathbf{u}_a \\ \partial J/\partial \mathbf{v}_a \end{bmatrix}. \tag{2.19}$$

The rightmost four matrices in (2.19) simply equal the observation sensitivities from (2.15) so that

$$\begin{bmatrix} \partial J/\partial \mathbf{h}_b \\ \partial J/\partial \mathbf{u}_b \\ \partial J/\partial \mathbf{v}_b \end{bmatrix} = \begin{bmatrix} \partial J/\partial \mathbf{h}_a \\ \partial J/\partial \mathbf{u}_a \\ \partial J/\partial \mathbf{v}_a \end{bmatrix} - \begin{bmatrix} \mathbf{H}_h^T & \mathbf{H}_u^T & \mathbf{H}_v^T \end{bmatrix}^T \begin{bmatrix} \partial J/\partial \mathbf{h}_o \\ \partial J/\partial \mathbf{u}_o \\ \partial J/\partial \mathbf{v}_o \end{bmatrix}, \tag{2.20}$$

or

$$\begin{bmatrix} \partial J/\partial \mathbf{h}_b \\ \partial J/\partial \mathbf{u}_b \\ \partial J/\partial \mathbf{v}_b \end{bmatrix} = \begin{bmatrix} \partial J/\partial \mathbf{h}_a \\ \partial J/\partial \mathbf{u}_a \\ \partial J/\partial \mathbf{v}_a \end{bmatrix} - \mathbf{H}_h^T \partial J/\partial \mathbf{h}_o - \mathbf{H}_u^T \partial J/\partial \mathbf{u}_o - \mathbf{H}_v^T \partial J/\partial \mathbf{v}_o. \tag{2.21}$$

where the observation sensitivities are defined according to (2.18a-c).

III. EXPLORATION OF OBSERVATION ADJOINT SENSITIVITY USING IDEALIZED CASES

The purpose of this section is to explore systematically the behavior of the observation sensitivity as a function of the analysis parameter space. These analysis parameters include the background error correlation length scale, analysis sensitivity gradient length scale, and the relative magnitude of the observation error variances to the background error variances. Since observation sensitivity also changes as observations are added to the analysis, the effects of the observation density will also be examined in this section. The simplified context of one- and two-dimensional univariate and multivariate analyses and adjoints are used to facilitate the interpretation and discussion.

A. AN EXAMPLE OF OBSERVATION AND BACKGROUND SENSITIVITY

The adjoint sensitivities to the background and observations in (2.8a,b) are illustrated for a two-dimensional horizontal univariate (e.g., geopotential height) case. The analysis sensitivity vector $\partial J/\partial \mathbf{x}_a$, which is the gradient of J with respect to the initial conditions for the forecast, is assumed to be already calculated on a two-dimensional domain with N equally spaced grid points. The two independent variables of the domain are defined as x and y (not to be confused with the definitions of analysis/background and observation vectors in Chap. II.A). The domain is non-periodic and is given by $-\pi \leq x \leq \pi$ and $-\pi \leq y \leq \pi$. The number of grid points in the x and y directions is $N^{1/2}$ and the grid lengths Δx and Δy are equal.

If there are M observations of the same variable type as the analysis variable (such as height), then the forward observation matrix **H** in (2.8a,b) is simply a linear interpolation operator. The observation errors are assumed to be uncorrelated so that the observation error covariance matrix $\mathbf{R} = \varepsilon_r^2 \mathbf{I}$, where **I** is the M x M identity matrix and ε_r^2 is the (constant) observation error variance. The background error covariance $\mathbf{P}_b$ is an N x N matrix with the element (i,j) given by $\varepsilon_b^2 \rho_b(x_i,x_j,y_i,y_j)$, where ε_b^2 is the (constant) background error variance and ρ_b is the background error correlation between the two analysis grid points. For these examples, the special Second Order Autoregressive Function (SOAR) is used to define ρ_b as

$$\rho_b(x_i,x_j,y_i,y_j) = \left(1 + {}^{r}\!/_{L_b}\right)\exp\left({}^{-r}\!/_{L_b}\right), \tag{3.1}$$

where L_b is the correlation length for the background error, and the distance between two grid points is given by

$$r = \left[\left(x_i - x_j\right)^2 + \left(y_i - y_j\right)^2\right]^{1/2}. \tag{3.2}$$

The analysis sensitivity gradient or vector is simulated with simple trigonometric and exponential functions. Analysis sensitivity vectors for error cost functions tend to be zero or essentially zero over most of the domain. The non-zero regions of the analysis sensitivity gradient are usually small in spatial extent, and are referred to as the target. Two such imposed analysis sensitivity vectors are shown in Fig. 3.1, where Fig. 3.1a is for a small target (small spatial scale) and Fig. 3.1e is for a large target. The two patterns

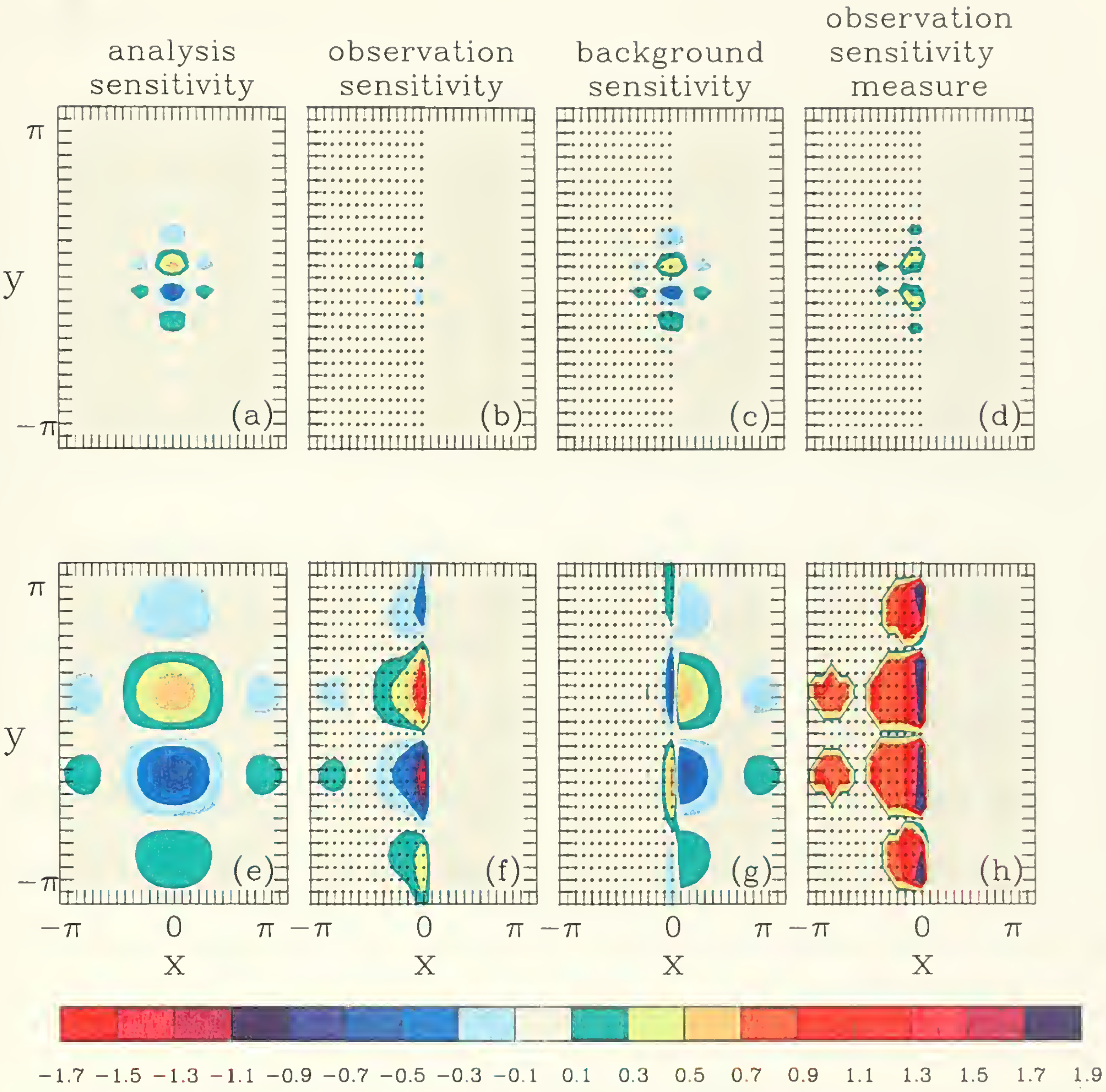

Figure 3.1. Simulated sensitivity vectors for a small target (a-d) and a large target (e-h). The imposed analysis sensitivity vectors are shown in (a) and (e), the observation sensitivity vectors in (b) and (f), the background sensitivity vectors in (c) and (g), and the observation sensitivity measures in (d) and (h). The observation locations are given by the "+". The color scale is indicated along the bottom.

bear some resemblance to the constant pressure projection of the analysis sensitivity gradient shown in Fig. 1.1a.

A hypothetical situation in which the analysis sensitivity gradient straddles a coastline is simulated in Fig. 3.1, where the continent is on the left-hand side of the figure and the ocean is on the right-hand side of the figure. In these figures, $N^{1/2} = 29$ and the grid length is $\pi/14$. The observation locations are shown by the "+" signs in Figs. 3.1b-d and 3.1f-h. An observation is assumed to be available at every gridpoint over the continent ($-\pi \leq x \leq 0$), with no observations over the ocean ($0 < x \leq \pi$). The observations and background values are specified to be equally accurate, or $\varepsilon_r = \varepsilon_b = 1.0$. The background error correlation length is defined as $L_b = \pi/6 = 2.42\Delta x$. The background sensitivity vector $\partial J/\partial \mathbf{x}_b$ (from (2.6b)) corresponding to the small target (small-scale analysis sensitivity vector) of Fig. 3.1a is shown in Fig. 3.1c. The background sensitivity vector corresponding to the large-scale analysis sensitivity vector of Fig. 3.1e is shown in Fig. 3.1g. An objective measure of observation sensitivity is shown in Figs. 3.1d,h. This measure will be discussed in the next sub-section.

Since the background sensitivity is a grid point quantity, it is easily plotted. Because the observation sensitivity vector $\partial J/\partial \mathbf{y}$ (from (2.8a)) is in observation space (defined only at the observation locations), it is more difficult to contour. There are several ways around this difficulty, which will be discussed later. However, one obvious technique is to assume that an observation is located at every grid point. This approach is applied to the present example. Over the continent, the observation error ε_r may be set to

1.0 as above. Over the ocean, setting the observation error ε_r to 1.0×10^6 with a background error variance of 1.0 is equivalent to having no observations over the ocean. The observation sensitivity vector $\partial J/\partial \mathbf{y}$ may then be easily plotted. With these specifications, the observation sensitivity vectors $\partial J/\partial \mathbf{y}$ corresponding to the small and large analysis sensitivity vectors in Figs. 3.1a and 3.1e respectively are shown in Figs. 3.1b and 3.1e.

A number of features in Fig. 3.1 merit comment. First, in the unobserved ocean portion (right half) of the domain, the background sensitivity and analysis sensitivity are the same, and the observation sensitivity is zero (because there are no observations).

Turning now to the left halves of each panel of Fig. 3.1, which is the well-observed continental interior portion far from the coastline, differences are apparent between the small target case (Figs. 3.1a-d) and the large target case (Figs. 3.e-h). For the small target case (Figs. 3.1a-d), even though the analysis sensitivity gradient is well sampled in the continental interior, there is no sensitivity to the observations, only to the background. For the large target case of Fig. 3.1e-h, the observation sensitivity is the same as the analysis sensitivity in the continental interior and there is no sensitivity to the background.

The well-sampled continental interior case can be easily explained following procedures developed in Daley (1991, section 4.5). When the background errors are assumed to have a red spectrum, which implies that the background errors are primarily large scale, analysis algorithms such as (2.1) use the observations primarily to reduce the large-scale errors. Because the small-scale background errors are implicitly assumed to be relatively small, the observations have very little effect on these small spatial scales. For this example, the small-scale features of the analysis are derived primarily from the background and the large-scale features are derived primarily from the observations. In an adjoint context, this means that the background sensitivity will be derived primarily from the small scales of the analysis sensitivity and the observation sensitivity will be derived primarily from the large scales. Consequently, for large targets (Fig. 3.1f) there will be a large observation sensitivity and small background sensitivity over the continent; the opposite will be true for small targets (Fig. 3.1b).

The region along the coastline, which is the boundary between the well sampled and the unsampled regions, is considered next. For the small target analysis sensitivity gradient, the sensitivity to coastal observations is only slightly larger than in the well-sampled continental interior (Fig. 3.1b). For the large target (Fig. 3.1e-h), the situation is completely different. In a narrow region along the coastal boundary, both the sensitivity to the observations (Fig. 3.1f) and the sensitivity to the background (Fig. 3.1g) are greater in magnitude than the analysis sensitivity (Fig. 3.1e) at the same gridpoint. The background sensitivity is of opposite sign to the observation and analysis sensitivities in this coastal region, which is consistent with (2.9). This phenomenon has been defined by Baker and Daley (2000) as observation and background super-sensitivity, respectively.

B. OBJECTIVE MEASURES OF OBSERVATION SENSITIVITY

In Baker and Daley (2000), *observation super-sensitivity* was defined to exist whenever the magnitude of the observation sensitivity exceeded the analysis sensitivity gradient at that location. This measure is strictly valid only for observations located at gridpoints, and for univariate problems (i.e., the observation sensitivity and analysis sensitivity gradients variables are the same). A different objective measure of observation sensitivity is defined to overcome these limitations. This measure allows for observation sensitivity values to be compared for different locations within the domain, or for different analysis sensitivity gradients.

Define the vector **a** as the limit of the observation sensitivity as the background error correlation length $L_b \rightarrow 0$ and the observation error variances $\varepsilon_r \rightarrow 0$, or

$$\mathbf{a} = \lim \partial J / \partial \mathbf{y} \Big|_{\varepsilon_r \rightarrow 0}^{L_b \rightarrow 0} . \tag{3.3}$$

The cross-correlation terms in (2.16) become zero in the limit as $L_b \rightarrow 0$. The off-diagonal univariate correlation terms also become zero in the limit as $L_b \rightarrow 0$, while the diagonal correlation terms equal one in the limit as $L_b \rightarrow 0$. In the limit of $L_b \rightarrow 0$ and $\varepsilon_r \rightarrow 0$, (3.3) reduces to

$$\mathbf{a} = (\mathbf{H}\mathbf{H}^T)^{-1} \mathbf{H}\, \partial J / \partial \mathbf{x}_a . \tag{3.4}$$

For the special case in which the observations are assumed to be located at gridpoints, then $(\mathbf{H}\mathbf{H}^T)^{-1} = \mathbf{I}$ and

$$\mathbf{a} = \mathbf{H}\,\partial J/\partial \mathbf{x}_a . \tag{3.5}$$

Similarly, define the vector of observation sensitivity as $\mathbf{o} = \partial J/\partial \mathbf{y}$. The observation sensitivity measure (OSM) for the mth observation is defined as the observation sensitivity divided by the limit of the observation sensitivity as $L_b \rightarrow 0$ and $\varepsilon_r \rightarrow 0$ (both for the mth observation), or

$$\mathrm{OSM} = \mathrm{o}_m/\mathrm{a}_m , \tag{3.6}$$

where the observation and analysis sensitivity gradient variables in o_m and a_m are the same. Observation super-sensitivity is then defined to exist when |OSM| > 1. The OSM for the examples in Fig. 3.1b,f are plotted in Figs. 3.1d,h, and clearly shows the narrow bands of super-sensitivity along the coastline for the large-scale target.

Similarly, the maximum observation sensitivity measure for all observations may be defined as

$$\mathrm{OSM}_{\max} = \max\left[\mathrm{o}_m/\mathrm{a}_m\right], \qquad 1 \le m \le M. \tag{3.7}$$

Finally, a measure of the observation sensitivity over a network of observations can be defined. This network may be any given set of observations, such as a suite of deployed observations, or all of the observations in a single rawinsonde profile. This measure cannot exceed unity unless super-sensitivity exists for at least one observation in the network. The network observation sensitivity measure is given by

$$\mathrm{OSM}_{\mathrm{net}} = \sum_{m=1}^{M} (\mathrm{o}_m)^2 \Big/ \sum_{m=1}^{M} (\mathrm{a}_m)^2 . \tag{3.8}$$

The measures in (3.6) and (3.7) have one fundamental flaw. When a_m is very small, the OSM will be very large solely for that reason. If a_m is zero, then the OSM measures in (3.6) and (3.7) will be undefined, and the OSM must be carefully applied. The OSM in (3.8) is less likely to be singular under these conditions. Nonetheless, the OSM does allow super-sensitive observations to be easily identified and observation sensitivity values to be compared, provided that care is taken with its use.

C. ONE-DIMENSIONAL UNIVARIATE OBSERVATION AND BACKGROUND SENSITIVITY

1. Observation Super-Sensitivity Along a Coastline

A simpler one-dimensional height univariate analog to the two-dimensional example described above is considered to understand the super-sensitivity found along the coastline in Fig. 3.1. The results from three one-dimensional univariate experiments are presented in Fig. 3.2. In Fig. 3.2 (a-d), the domain contains 101 evenly spaced gridpoints from π to $+\pi$. In the first case, the coastline is located at gridpoint 51, with a height observation located at every point to the left of (and including) gridpoint 51. The background error correlation length scale (L_b), which was chosen empirically to give large observation sensitivity, equals 3.33Δx and is shown for gridpoint 51 in Fig. 3.2a, where the abscissa is grid location (x) and the ordinate is the correlation between the height value at gridpoint 51 and adjacent gridpoints. The specified height analysis sensitivity gradient is shown in Fig. 3.2b, and is given by a simple cosine wave with a scale (L_s) equal to 5.31Δx with an amplitude of 1.0. The length scale L_s is chosen such that the sum of the analysis sensitivity over the grid domain is nearly zero. This choice

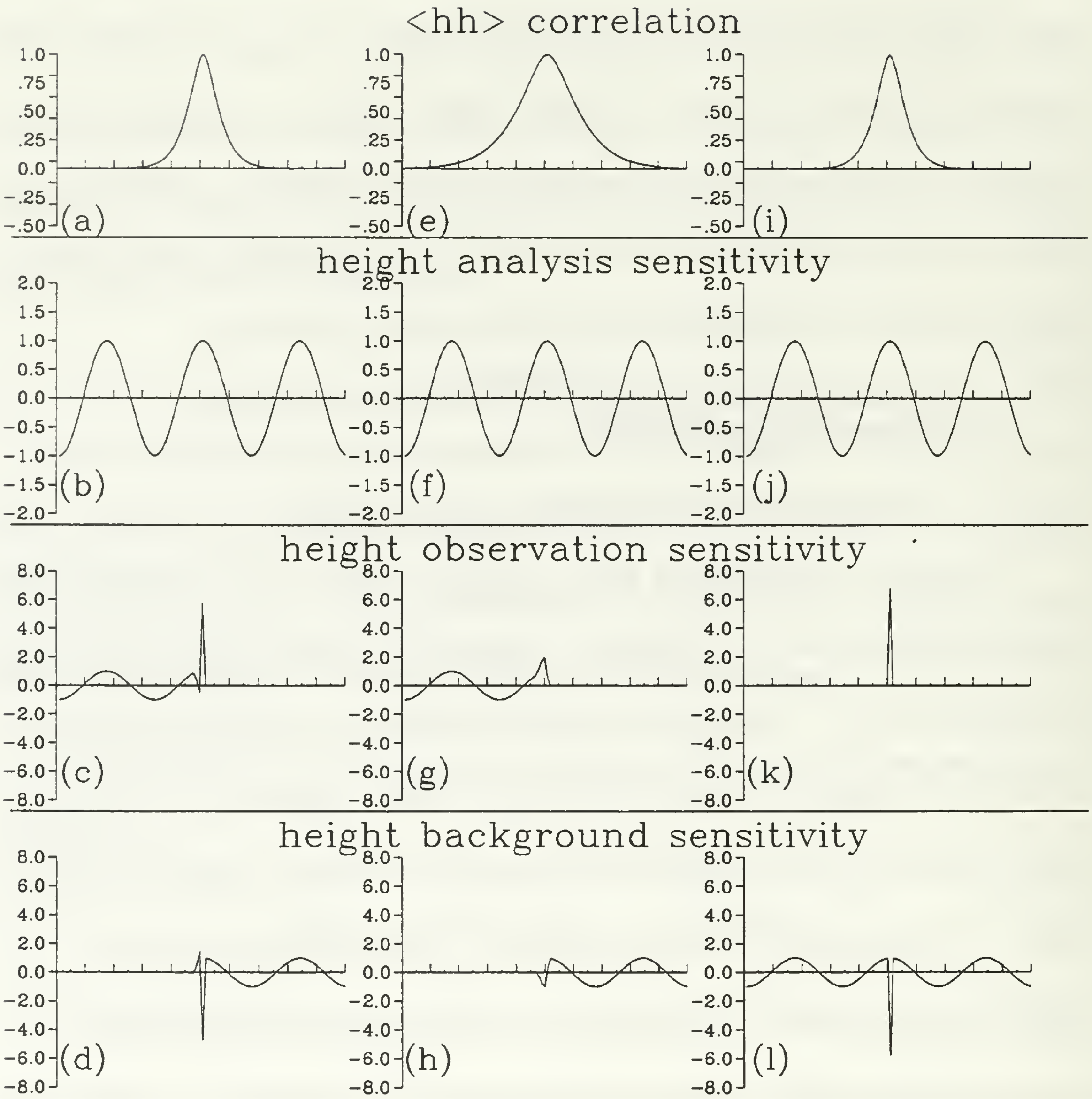

Figure 3.2. Examples of one-dimensional univariate height sensitivity for (a-h) coastal, and (i-l) single observation analysis systems. The background error correlation function for an observation at gridpoint 51 for (a,i) $L_b = 3.33\Delta x$, and (e) $L_b = 6.67\Delta x$, (b,f,j) the imposed analysis sensitivity gradients with $L_s = 5.31\Delta x$, (c,g,k) the observation sensitivities, and (d,h,l) the background error sensitivities. The domain consists of 101 gridpoints, where $\varepsilon_r = 0.1$ and $\varepsilon_b = 1.0$. Values are plotted as a function of the grid location (abscissa) and amplitude (ordinate).

allows the computational results to be compared with analytical calculations for an infinite domain when the analysis sensitivity gradient is defined as a cosine wave. The background error variances are assumed to be spatially uniform and are equal to 1.0. For illustrative purposes only, the height observations are assumed to be nearly perfect (ε_r = 0.1). This small observation error variance prevents the matrix $(\mathbf{HP}_b\mathbf{H}^T + \mathbf{R})^{-1}$ in (2.6) from becoming singular. The resulting observation and background sensitivity vectors are shown in Figs. 3.2c and d, respectively.

These analysis and observation sensitivities are similar to Fig. 3.1e over the continent (left of gridpoint 51). The analysis and background sensitivities are similar to Fig. 3.1f over the ocean (right of gridpoint 51). At the coastline (gridpoint 51) in Fig. 3.2c, the observation sensitivity exceeds the analysis sensitivity and the background sensitivity is large, but is of opposite sign. Notice also the observation sensitivity oscillations immediately adjacent to gridpoint 51 on the inland side of the coastline. Thus, there is evidence of observation super-sensitivity at the coast in Figs. 3.1e,f.

Figures 3.2e-h are similar to Figs. 3.2a-d, except that the background correlation length scale is doubled ($L_b = 6.67\Delta x$). The principal effect is to decrease the observation (Fig. 3.2g) and background (Fig. 3.2h) super-sensitivities at the coastal gridpoint 51. The observation sensitivity oscillations immediately adjacent to gridpoint 51 in Fig. 3.2c do not exist in Fig. 3.2g, where the observation sensitivity at gridpoint 51 blends smoothly with the interior continental values.

The special case of a single perfect ($\varepsilon_r = 0$) observation at gridpoint 51 is shown in Fig. 3.2i-1. The background error correlation and analysis sensitivity (Fig. 3.2i,j) are the same as in Figs. 3.2a,b, respectively. This very pure example again shows that observation sensitivity (Fig. 3.2k) exceeds the analysis sensitivity at the observation point and the background sensitivity at the observation point is large with an opposite sign (Fig. 3.2l). Everywhere else, the observation sensitivity is zero and the background sensitivity is the same as the analysis sensitivity and is therefore relatively small.

The observation super-sensitivity will be further explored in the next section with the help of the analytical solution for a single observation.

2. The Analytical Solution for a Single Observation

The single observation case of Fig. 3.2i - 1 is so simple that it can be explored analytically. Consider a grid defined such that each point, x_n , is given by $n\Delta x$, $-\infty \leq n \leq \infty$. Assume the analysis sensitivity vector is given by

$$\partial J/\partial \mathbf{x}_a = \alpha \cos(n\Delta x/L_s), \tag{3.9}$$

where L_s is the horizontal length scale and α is a constant amplitude factor. A single observation, with an expected observation error variance ε_r^2, is placed at a location x_r. The background error covariance between the observation location and any analysis grid point ($\mathbf{HP}_b$) is assumed to be given by $\varepsilon_b^2\ \rho_b(x_r,x_n)$. The discretized SOAR function for the background error correlation is defined according to (3.1), i.e.

$$\rho_b(x_r,x_n) = (1+|x_r - x_n|/L_b)\exp(-|x_r - x_n|/L_b). \tag{3.10}$$

From (2.7a), the (scalar) observation sensitivity at x_r is then,

$$\partial J/\partial \mathbf{y} = \mathbf{K}^T \partial J/\partial \mathbf{x}_a = \varepsilon_b^2 \left(\varepsilon_b^2 + \varepsilon_r^2\right)^{-1} \alpha \sum_{n=-\infty}^{+\infty} \rho_b(x_r, x_n) \cos(x_n/L_s). \tag{3.11}$$

The analysis sensitivity gradients are restricted to functions resolvable by the grid, or $2\pi L_b \geq 2\Delta x$. After some manipulation, (3.11) may be re-written as

$$\partial J/\partial \mathbf{y} = \alpha\varepsilon_b^2(\varepsilon_b^2 + \varepsilon_r^2)^{-1} \cos(x_r/L_s) B = \alpha\varepsilon_b^2(\varepsilon_b^2 + \varepsilon_r^2)^{-1} B\, \partial J/\partial \mathbf{x}_a \big|_{x=x_r}, \tag{3.12}$$

where

$$B = \left[1 + 2\sum_{n=1}^{\infty}(1 + n\Delta x/L_b)\exp(-n\Delta x/L_b)\cos(n\Delta x/L_s)\right]. \tag{3.13}$$

Here, B is a non-dimensional quantity that depends on three scales: the grid length Δx, the analysis sensitivity length scale L_s, and the background error correlation length scale L_b. For this simple example, the observation sensitivity in (3.12) is proportional to $\cos(x_r/L_s)$ and has the same functional form as the analysis sensitivity. The observation sensitivity $\partial J/\partial \mathbf{y}$, which becomes a scalar for a single observation, increases as the accuracy of the observation improves.

Provided that $2\pi L_b > 2\Delta x$, B is an accurate trapezoidal rule approximation to the definite integral

$$B \approx \frac{2}{\Delta x}\int_0^\infty (1 + x/L_b)\exp(-x/L_b)\cos(x/L_s)\mathrm{d}x, \tag{3.14}$$

and therefore, B may be approximated as

$$B \approx 4\frac{L_b}{\Delta x(1 + L_b^2/L_s^2)^2}, \tag{3.15}$$

and

$$\partial J/\partial y \approx \frac{4\alpha\varepsilon_b^2 L_b \cos(x_r/L_s)}{(\varepsilon_b^2+\varepsilon_r^2)\Delta x(1+L_b^2/L_b^2)^2}. \tag{3.16}$$

The magnitude of B in (3.15) is maximized when $L_b = L_s/\sqrt{3}$, or when the scale of the analysis sensitivity and the background error correlation length are roughly similar. In Fig. 3.3, the B values (from (3.13)) are plotted as a function of $0 \le 2\pi L_b \le 12\Delta x$ (abscissa) and $2\Delta x \le 2\pi L_s \le 14\Delta x$ (ordinate). The maximum B value for a given choice of L_s (i.e., $L_b = L_s/\sqrt{3}$) is shown as the heavy, nearly diagonal line on Fig. 3.3. Provided that $L_s > 2\Delta x$, and $2\pi L_b > 2\Delta x$, it can be seen from (3.15) that when $L_b \ll L_s$, then $B \approx 4L_b/\Delta x$. Furthermore, B (and $\partial J/\partial y$) will tend to zero when $L_b \gg L_s$. These limiting values can be seen in the plot of B in Fig. 3.3.

To relate the B values in Fig. 3.3 to observation super-sensitivity, the definition of the observation sensitivity measure (3.6) is inserted into (3.15) to give

$$OSM = \varepsilon_b^2(\varepsilon_b^2+\varepsilon_r^2)^{-1}B. \tag{3.17}$$

Since super-sensitivity is defined to occur whenever OSM > 1, this will occur when

$$B > 1+\varepsilon_r^2/\varepsilon_b^2. \tag{3.18}$$

If the observations are perfect ($\varepsilon_r = 0$), super-sensitivity occurs for $B > 1$. If observation errors are at least as large as the background errors ($\varepsilon_r \ge \varepsilon_b$), super-sensitivity does not occur until $B > 2$. For observations that are not perfect, but are more accurate than the

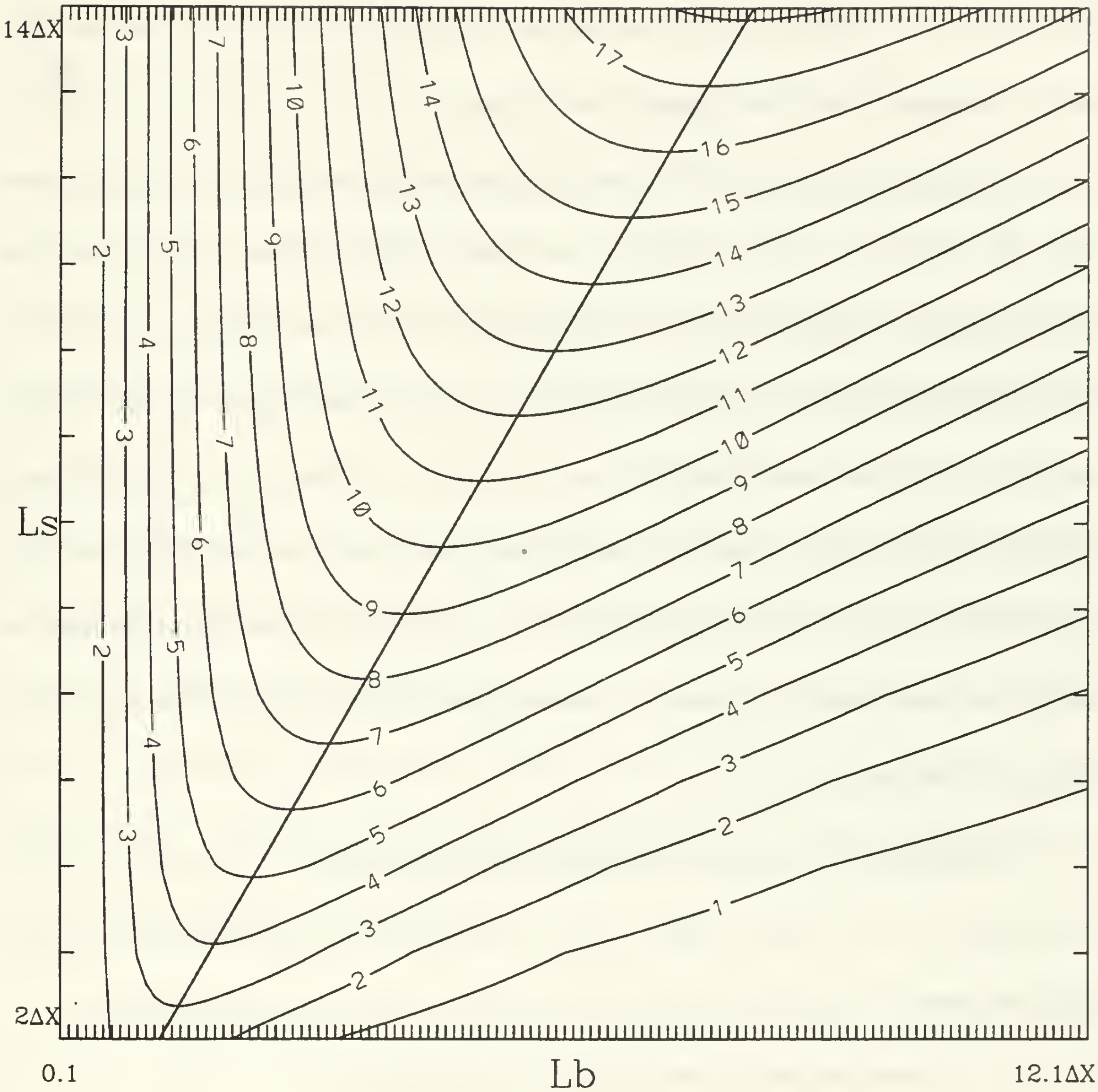

Figure 3.3. Values of the parameter B as defined in (3.13) as a function of the specified background error correlation length from 0.1Δx to 12.1Δx (L_b; abscissa) and imposed height analysis sensitivity scale from 2.0Δx to 14.0Δx (L_s; ordinate). The values of B from (3.13) were computed for $n = 1{,}500$.

background ($\varepsilon_r < \varepsilon_b$), the threshold depends on the relative accuracy, and is somewhere between 1 and 2. For typical targeting applications, B will range between 1 and 2 implying (from Fig. 3.3) that a single observation will be super-sensitive for most choices of L_b and L_s, except when the analysis sensitivity gradient is small-scale and the background error correlation length scale is very long.

It is easy to see from Fig. 3.3 that observation super-sensitivity is more likely to occur for large-scale analysis sensitivity gradients (or large targets). The observation super-sensitivity is enhanced when the observational error is small and the background error characteristic scale (L_b) is close to that of the analysis sensitivity (L_s). Small-scale analysis sensitivities (small targets) may be much less sensitive to observations, depending upon the relative accuracy between the observations and background, and the background error correlation length scale. It is important to note that although the observation super-sensitivity increases monotonically with L_s (provided $L_b = L_s/\sqrt{3}$), the same is not true for L_b.

The super-sensitivity indicated along the coastline in Figs. 3.1e and 3.2c can now be attributed to the similar length scales imposed for the analysis sensitivity and background error correlation combined with an abrupt change in observation density.

3. Understanding Observation Super-sensitivity

The above discussion explains when and where super-sensitivity will occur, but not why. To understand why super-sensitivity occurs, consider the terms in the observation sensitivity equation given by (2.7a) and (2.8a), i.e.,

$$\partial J/\partial \mathbf{y} = \mathbf{K}^T \, \partial J/\partial \mathbf{x}_a = (\mathbf{HP}_b\mathbf{H}^T + \mathbf{R})^{-1}\mathbf{HP}_b \, \partial J/\partial \mathbf{x}_a .$$

The term $\mathbf{HP}_b\mathbf{H}^T$ is the background error covariance between observation locations and is in observation space. The observations are assumed to be uncorrelated so that $\mathbf{R}$ is a diagonal matrix of the observation error variances. The term $\mathbf{HP}_b$ is the background error cross-covariance between the observation locations and every gridpoint. The spatial scale of the transposed Kalman gain matrix $\mathbf{K}^T$ is determined primarily by the background error correlation length scale.

The four rows of $\mathbf{K}^T$ corresponding to the four different observations at gridpoints 51 (located on the coastline), 50 and 49 (the two observations located just inland from the coast), and 30 (located in the well-sampled interior) from Fig. 3.2a-d are shown in Figs. 3.4a-d, respectively. The magnitudes and spatial extents of the row of $\mathbf{K}^T$ are much larger for the observations near the coastline (gridpoint 51) than for the interior observation (gridpoint 30). Moreover, the rows of the matrix are strongly asymmetrical for the observations on and near the coastline. The asymmetry arises due to the term $(\mathbf{HP}_b\mathbf{H}^T + \mathbf{R})^{-1}$, and is most pronounced for abrupt changes in the observation density (e.g., near the coastline in this example).

The sensitivity to J for a given observation is the product of the row of $\mathbf{K}^T$ and the (Nx1) analysis sensitivity vector. This can be visualized by mentally summing, gridpoint by gridpoint, the product of the row of $\mathbf{K}^T$ (Figs. 3.4a-d) and $\partial J/\partial \mathbf{x}_a$ (Fig. 3.2b). The observation sensitivity is greatest when large values of the row of $\mathbf{K}^T$ coincide with large values of the analysis sensitivity with signs such that the contributions to the observation sensitivity are of the same sign.

The large values of observation sensitivity near the coastline are thus explained as being due to large values of analysis sensitivity combined with observations that are

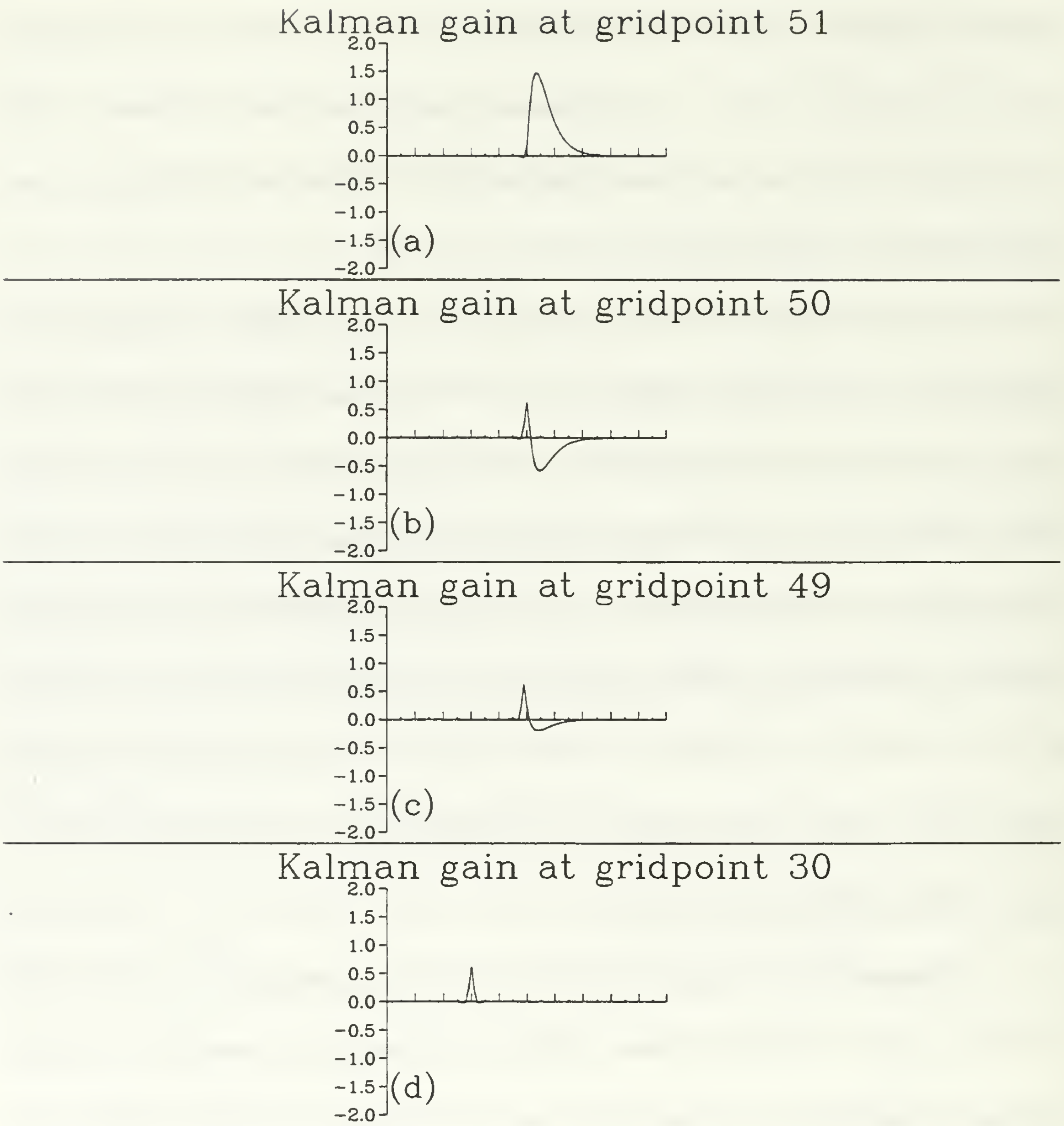

Figure 3.4. Plots of the row of the transposed Kalman gain matrix for the observations at gridpoints (a) 51, (b) 50, (c) 49 and (d) 30 in Fig. 3.2c. Values are plotted as a function of the grid location (abscissa) and amplitude (ordinate).

relatively isolated compared to the observations in the interior of the continent. The change of sign for the observation sensitivity for observation at gridpoint 50 occurs because the largest values in the row of $\mathbf{K}^T$ are negative as opposed to positive (i.e., compare Fig. 3.4b to Figs. 3.4a,c). The observation sensitivity is enhanced when the observation errors are assumed to be small relative to the background errors.

Consequently, the observations along the coastline have larger potential impact than the continental interior observations, because there are no more observations over the ocean. This result is independent of the synoptic flow, and observations along either coast will be equally valuable (given identical assumptions). In reality, $\partial J/\partial \mathbf{x}_a$ is strongly dependent upon the synoptic flow and significant values of analysis sensitivity tend to occur over the oceans for many J of interest. Therefore, if the domain of interest for which J is defined is in the interior of the continent, observations along the upstream coastline would be more valuable than on the downstream coastline. The single observation experiment (Figs. 3.2i-l) can now be interpreted as the limiting case of a "good" coastline observation with very "poor" continental interior observations.

The physical reasoning why the super-sensitivity is maximized when the analysis sensitivity scale is close to the background error correlation length scale may be explained as follows. Analysis sensitivity gradient structures such as those in Figs. 1.1a or 2.1a normally consist of a number of substructures or elements of opposite sign. Maximum sensitivity of the forecast aspect J to an observation occurs when the observation is strongly projected onto the analysis sensitivity by the adjoint of the assimilation algorithm (e.g, $\mathbf{K}^T$). The projection of an observation by the assimilation system (through $\mathbf{K}$) is largely controlled by the background error correlation. If the correlation model is always non-negative (e.g., the SOAR model of (3.1)), then the projection of the innovation for a single observation will have the same sign everywhere that it is non-zero. Suppose the single observation is located at the maximum or minimum of one of the substructures of the analysis sensitivity. If the background correlation length L_b is too small, the influence of the observation will be only felt over part of the substructure. If L_b is too large, the influence of the observation will be spread onto adjacent substructures that may have the opposite sign and thus reduce the projection. Therefore, some intermediate value of L_b will be optimal.

Super-sensitivity is a phenomenon that occurs when the observation density is low. Comparing Fig. 3.2k with Fig. 3.2c suggests that the super-sensitivity is largest for a single observation and diminishes as more observations are taken. It is prudent not to draw too many conclusions from the super-sensitivity phenomenon. Super-sensitivity merely indicates that the forecast aspect will be very sensitive to an observation at a certain location, given that the assimilation system has certain characteristics. It cannot be inferred that no other observations are necessary or a single super-sensitive observation will make a large reduction in the forecast error. In particular, a target in an area of the analysis sensitivity gradient with a number of substructures may require a number of observations to reduce substantially the forecast error.

In conclusion, large observation sensitivity occurs due to the co-location of large adjoint weight ($\mathbf{K}^T$) with significant amplitude analysis sensitivity gradients. In general, observations with large adjoint sensitivity have large (magnitude and spatial scale) adjoint weights that project optimally onto large analysis sensitivity gradients. Since the matrix $\mathbf{K}^T$ is the transpose of the weight matrix $\mathbf{K}$ in the linear analysis equation (2.2), these observations will also be given large weight in the forward analysis. If the innovation is large, these observations will have a strong effect on the analysis. If the projection of $\mathbf{K}^T$ onto $\partial J/\partial \mathbf{x}_a$ is optimal, the observation sensitivity will also be large. However, large observation sensitivity does not guarantee a large effect on the analysis from a given observation because that depends upon the magnitude of the innovation. Therefore, the observation sensitivity is a measure of the potential for an observation to have significant impact on the analysis in a region that is very sensitive to errors in the initial conditions.

4. Exploring the Limits of Observation Sensitivity

The previous section showed where observation super-sensitivity is likely to occur, and explained why it occurs. The goal of this section is to understand how observation sensitivity varies as a function of the analysis parameters. The OSM (3.6) is used as an objective measure to illustrate this variability. The limiting behavior for extreme values of the parameters is also examined.

a. The Effects of the Background Error Correlation Length Scale

This sub-section begins by comparing the analytical results from Fig. 3.3 with the equivalent results from the single observation one-dimensional numerical example from Figs. 3.2i-l. The variation of the observation sensitivity measure (OSM) as a function of L_b and L_s is shown in Fig. 3.5 in the same format as in the analytical example in Fig. 3.3. For the numerical calculation, the background error correlation

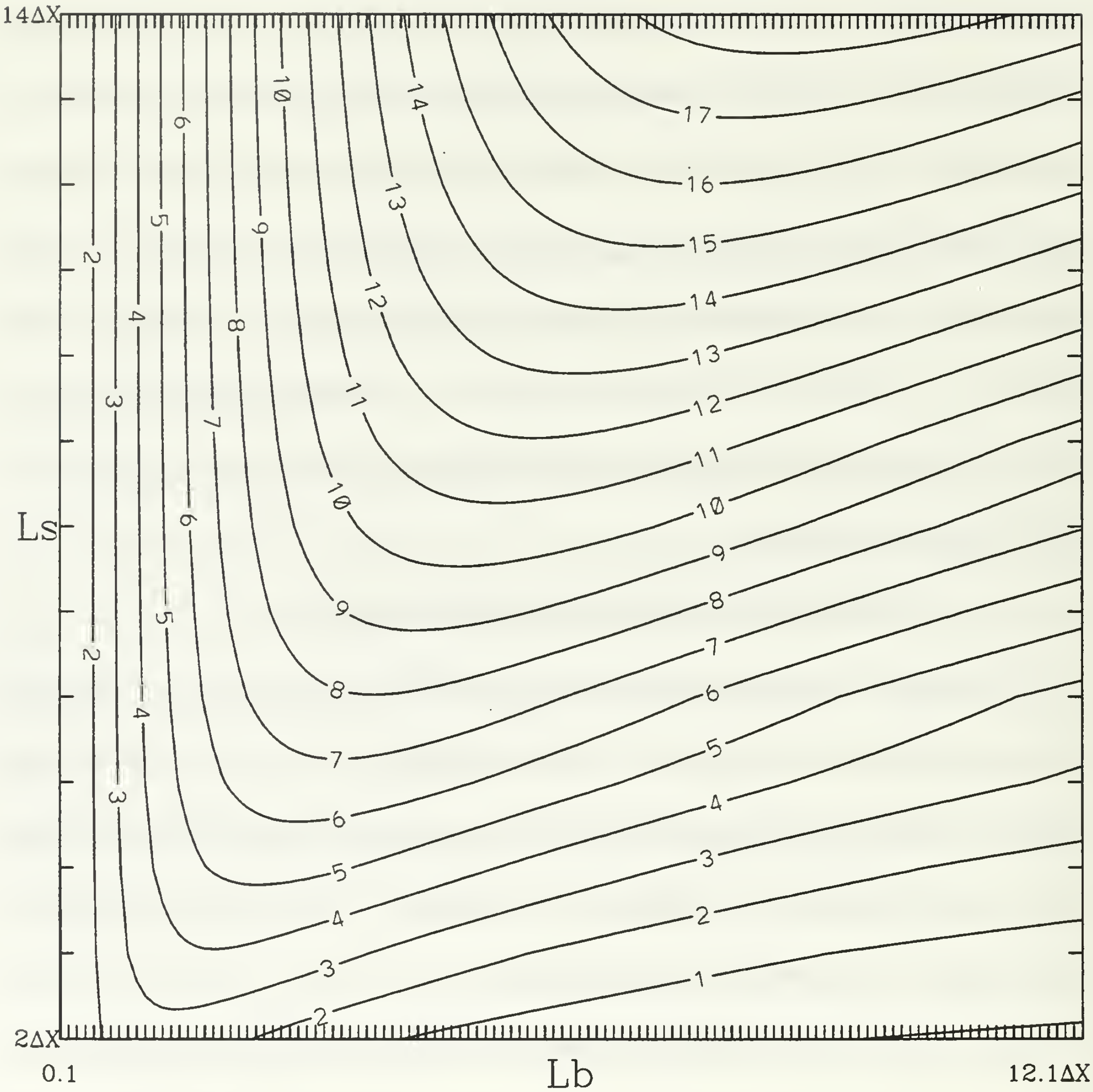

Figure 3.5. Variation of the computed height observation sensitivity measure as a function of the background error correlation length scale from 0.1Δx to 12.1Δx (L_b; abscissa) and the analysis sensitivity length scale from 2.0Δx to 14.0Δx (L_s; ordinate). The domain consists of 101 gridpoints, where $\varepsilon_r = 0.0$ and $\varepsilon_b = 1.0$.

length scale is restricted to vary between 0.1Δx and 12Δx. The analysis sensitivity gradient for any given L_s is restricted to one complete cosine wave, and is set to zero outside this range. The gridlength Δx is the same for all values of L_s. These restrictions were required to minimize the computational effects arising from the finite grid spacing and finite domain. A single observation (which is assumed to be perfect) is placed at the center of the analysis sensitivity gradient maximum.

Overall, the analytical (Fig. 3.3) and computational results (Fig. 3.5) compare very well. The computational relationship between L_s and L_b at the maximum observation sensitivity very closely follows the analytically derived relationship (e.g., $L_b = L_s/\sqrt{3} \approx 0.58L_s$). Minor differences are found for correlation length scales longer than the maximum given by $L_b = L_s/\sqrt{3}$, and are due to the finite grid domain of the computational example. Minor differences are also found for $L_b < 1\Delta x$. Super-sensitivity for the single observation (B>1) exists over most of the domain, except for $L_s = 2\Delta x$ when $L_b = 4\Delta x$.

The variation of the OSM over the larger range of L_b from 0.25Δx to 25.25Δx in increments of 0.25Δx (with L_s = 5.31Δx) is shown in Fig. 3.6. A single observation is placed at a gridpoint in the center of the domain at the local maximum of the analysis sensitivity gradient. The observation is assumed to be perfect, and the background error variances are equal to 1.0. The solid curve in Fig. 3.6 is the computed observation sensitivity measure (from (3.6) and (3.12)), and the dotted line is the analytical approximation to observation sensitivity measure (from (3.6) and (3.16)). The observation sensitivity measure reaches a maximum value near the theoretical maximum

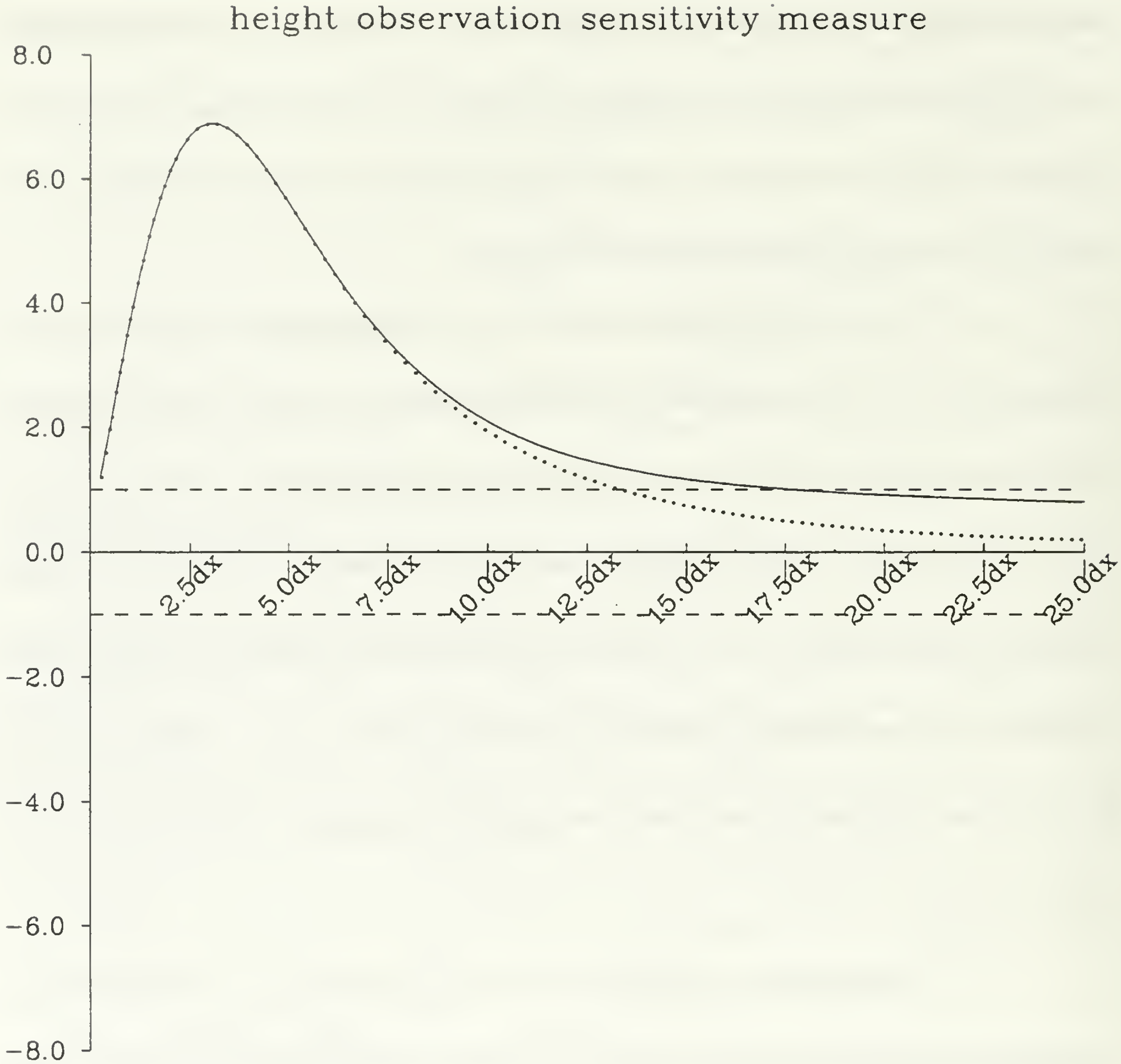

Figure 3.6. Variation of the height observation sensitivity measure (ordinate) as a function of the background error correlation length scale from 0.25Δx to 25.0Δx (L_b; abscissa) for $L_s = 5.31\Delta x$. The solid curve is the computed observation sensitivity measure from (3.6) and (3.12), and the dotted line is the analytical approximation to observation sensitivity measure from (3.6) and (3.16). The dashed lines at ±1.0 are the threshold values for observation super-sensitivity.

of L_b = 3.06Δx, decreases toward zero when L_b is large, and approaches one for small L_b. The computed OSM (solid curve) is larger than the analytical OSM (dashed curve) for L_b greater than about 8.75Δx, where the analytical curve approaches zero faster than the numerical solution. This difference arises because L_b is becoming long compared to the finite grid domain, whereas the analytical solution does not have a boundary effect.

In Fig. 3.6, the single observation is assumed to be perfect, so that OSM = B from (3.17). However, $B \approx 4\, L_b / \Delta x$ when $L_b << L_s$ (but $2\pi\, L_b > 2\Delta x$) and $B \to 0$ when $L_b >> L_s$. The numerical OSM solution in Fig. 3.6 generally follows these limits for the long and short background error correlation length scales.

The limiting case for $L_b \to 0$ and $\varepsilon_r \to 0$ corresponds to the vector **a** in the denominator of the OSM (3.6), and OSM = 1. If the observation is assumed to be imperfect and $L_b \to 0$, then the observation sensitivity parameter $\mathrm{OSM} = \varepsilon_b^2\, (\varepsilon_b^2 + \varepsilon_r^2)^{-1}$. Since ε_r is greater than zero, the OSM is always less than one. Therefore, observation super-sensitivity cannot occur for either perfect or imperfect single observations as $L_b \to 0$.

The OSM limit for $L_b \to \infty$ can be derived analytically as follows. Assume that there are M observations and N gridpoints. The observation error variances ε_r^2 are assumed to be spatially homogeneous so that $\mathbf{R} = \varepsilon_r^2 \mathbf{I}$, where **I** is the M x M identity matrix. Next, assume that $\mathbf{H}\mathbf{P}_b\mathbf{H}^T$ may be expanded using an eigenvector expansion, or $\mathbf{H}\mathbf{P}_b\mathbf{H}^T = \varepsilon_b \mathbf{E}\mathbf{D}\mathbf{E}^T \varepsilon_b$, where **D** is a diagonal matrix, $\mathbf{E}\mathbf{E}^T = \mathbf{I}$, and the background error variances ε_b^2 are assumed to be spatially homogeneous. Thus, the matrix **A** and its inverse $\mathbf{A}^{-1}$ may be defined as

$$\mathbf{A} = (\mathbf{HP}_b\mathbf{H}^T + \mathbf{R}) = \varepsilon_b^2\mathbf{EDE}^T + \varepsilon_r^2\mathbf{I} = \mathbf{E}\left(\varepsilon_b^2\mathbf{D} + \varepsilon_r^2\mathbf{I}\right)\mathbf{E}^T, \tag{3.19a}$$

and

$$\mathbf{A}^{-1} = (\mathbf{HP}_b\mathbf{H}^T + \mathbf{R})^{-1} = \mathbf{E}\left(\varepsilon_b^2\mathbf{D} + \varepsilon_r^2\mathbf{I}\right)^{-1}\mathbf{E}^T, \tag{3.19b}$$

where $\left(\varepsilon_b^2\mathbf{D} + \varepsilon_r^2\mathbf{I}\right)$ is a diagonal matrix. In the limit as $L_b \rightarrow \infty$,

$$\mathbf{D} = \begin{bmatrix} M & \cdots & 0 \\ \vdots & \ddots & \vdots \\ 0 & \cdots & 0 \end{bmatrix}, \tag{3.20a}$$

and

$$\mathbf{E} = \begin{bmatrix} 1/\sqrt{M} & \\ \vdots & \boldsymbol{\alpha} \\ 1/\sqrt{M} & \end{bmatrix} \tag{3.20b}$$

where the leading eigenvalue equals M and the leading eigenvector is given by $\mathbf{e}_1^T = \left(1/\sqrt{M}, 1/\sqrt{M}, \ldots, 1/\sqrt{M}\right)$. The trailing eigenvalues equal zero, and the trailing eigenvectors are given by the (M-1) x M matrix $\boldsymbol{\alpha}$. For a 2x2 problem, $\boldsymbol{\alpha}^T = \left(1/\sqrt{M}, -1/\sqrt{M}\right)$. Thus,

$$\mathbf{A} = \begin{bmatrix} 1/\sqrt{M} & \\ \vdots & \boldsymbol{\alpha} \\ 1/\sqrt{M} & \end{bmatrix} \begin{bmatrix} M\varepsilon_b^2 + \varepsilon_r^2 & \cdots & 0 \\ \vdots & \ddots & \vdots \\ 0 & \cdots & \varepsilon_r^2 \end{bmatrix} \begin{bmatrix} 1/\sqrt{M} & \cdots & 1/\sqrt{M} \\ & \boldsymbol{\alpha}^T & \end{bmatrix} \tag{3.21a}$$

and

$$\mathbf{A}^{-1}=\begin{bmatrix}1/\sqrt{M} & \\ \vdots & \boldsymbol{\alpha} \\ 1/\sqrt{M} & \end{bmatrix}\begin{bmatrix}1/(M\varepsilon_b^2+\varepsilon_r^2) & \cdots & 0\\ \vdots & \ddots & \vdots\\ 0 & \cdots & 1/\varepsilon_r^2\end{bmatrix}\begin{bmatrix}1/\sqrt{M} & \cdots & 1/\sqrt{M}\\ & \boldsymbol{\alpha}^T & \end{bmatrix}. \qquad (3.21b)$$

Equation (3.22) may be rewritten as

$$\mathbf{A}^{-1}=\mathbf{E}\begin{bmatrix}1/(M\varepsilon_b^2+\varepsilon_r^2)-1/\varepsilon_r^2 & \cdots & 0\\ \vdots & \ddots & \vdots\\ 0 & \cdots & 0\end{bmatrix}\mathbf{E}^T+\mathbf{E}\begin{bmatrix}1/\varepsilon_r^2 & \cdots & 0\\ \vdots & \ddots & \vdots\\ 0 & \cdots & 1/\varepsilon_r^2\end{bmatrix}\mathbf{E}^T \qquad (3.22)$$

$$=\left[\frac{1}{M(M\varepsilon_b^2+\varepsilon_r^2)}-\frac{1}{M\varepsilon_r^2}\right]\begin{bmatrix}1 & \cdots & 1\\ \vdots & \ddots & \vdots\\ 1 & \cdots & 1\end{bmatrix}+\frac{1}{\varepsilon_r^2}\mathbf{I}.$$

Because all elements of $\mathbf{HP}_b$ are equal to one in the limit as $L_b \to \infty$,

$$\mathbf{HP}_b\frac{\partial J}{\partial \mathbf{x}_a}=\varepsilon_b^2\left|\begin{matrix}\sum_N \partial J/\partial x_a\\ \vdots\\ \sum_N \partial J/\partial x_a\end{matrix}\right|_M . \qquad (3.23)$$

Moreover, since all the elements of (3.23) are equal, the observation sensitivity vector of length M may be written as

$$\frac{\partial J}{\partial \mathbf{y}}=\frac{\varepsilon_b^2}{(M\varepsilon_b^2+\varepsilon_r^2)}\left|\begin{matrix}\sum_N \partial J/\partial x_a\\ \vdots\\ \sum_N \partial J/\partial x_a\end{matrix}\right|_M . \qquad (3.24)$$

According to (3.24), the observation sensitivity limit (as $L_b \to \infty$) for the m^th^ observation is proportional to the sum of the gridpoint values of the analysis sensitivity gradient over the domain. The imposed analysis sensitivity gradient for the one-dimensional examples in this section was chosen so that the sum of the gridpoint values of the analysis sensitivity gradient is zero. The forecast aspect J used for targeting applications generally produces analysis sensitivity gradients that sum to zero over the global domain. However, some choices of J may not sum to zero over the global domain (R. Langland, NRL–Monterey, personal communication). Thus, observation sensitivity values in the limit as $L_b \rightarrow \infty$ may be quite different depending upon the choice of J. Other important implications of (3.24) will be discussed in Chapter III.E.

b. The Effects of the Observation Error Variances

The analytical approximation to the observation sensitivity (3.17) indicates that super-sensitivity (OSM > 1) for a single observation occurs when $B > 1 + \varepsilon_r^2/\varepsilon_b^2$. The variation of the OSM is shown in Fig. 3.7 as a function of the background error correlation length scale L_b and the ratio of the observation error standard deviation to the background error standard deviation ($\varepsilon_r/\varepsilon_b$) over a range from 0.0 to 3.0. The analysis sensitivity length scale is fixed at $L_s = 5.31\Delta x$ and the range of the background error correlation length scale is from $0.1\Delta x$ and $12.1\Delta x$. The observation sensitivity is maximized for a perfect observation when $L_b = L_s/\sqrt{3} = 3.06\Delta x$. Observation sensitivity decreases as the ratio of the observation error to the background error increases. Perhaps the most interesting result from Fig. 3.7 is the occurrence of super-sensitivity for poor-quality observations. For example, when L_b equals the value that maximizes observation sensitivity, a single observation is super-sensitive even if $\varepsilon_r/\varepsilon_b$ is nearly as large as 2.5.

This troubling result implies that the forecast aspect (for example, forecast error) could be highly sensitive to an isolated poor quality observation in regions with large sensitivity to the initial conditions. This issue will be discussed in detail in Chapter IV.

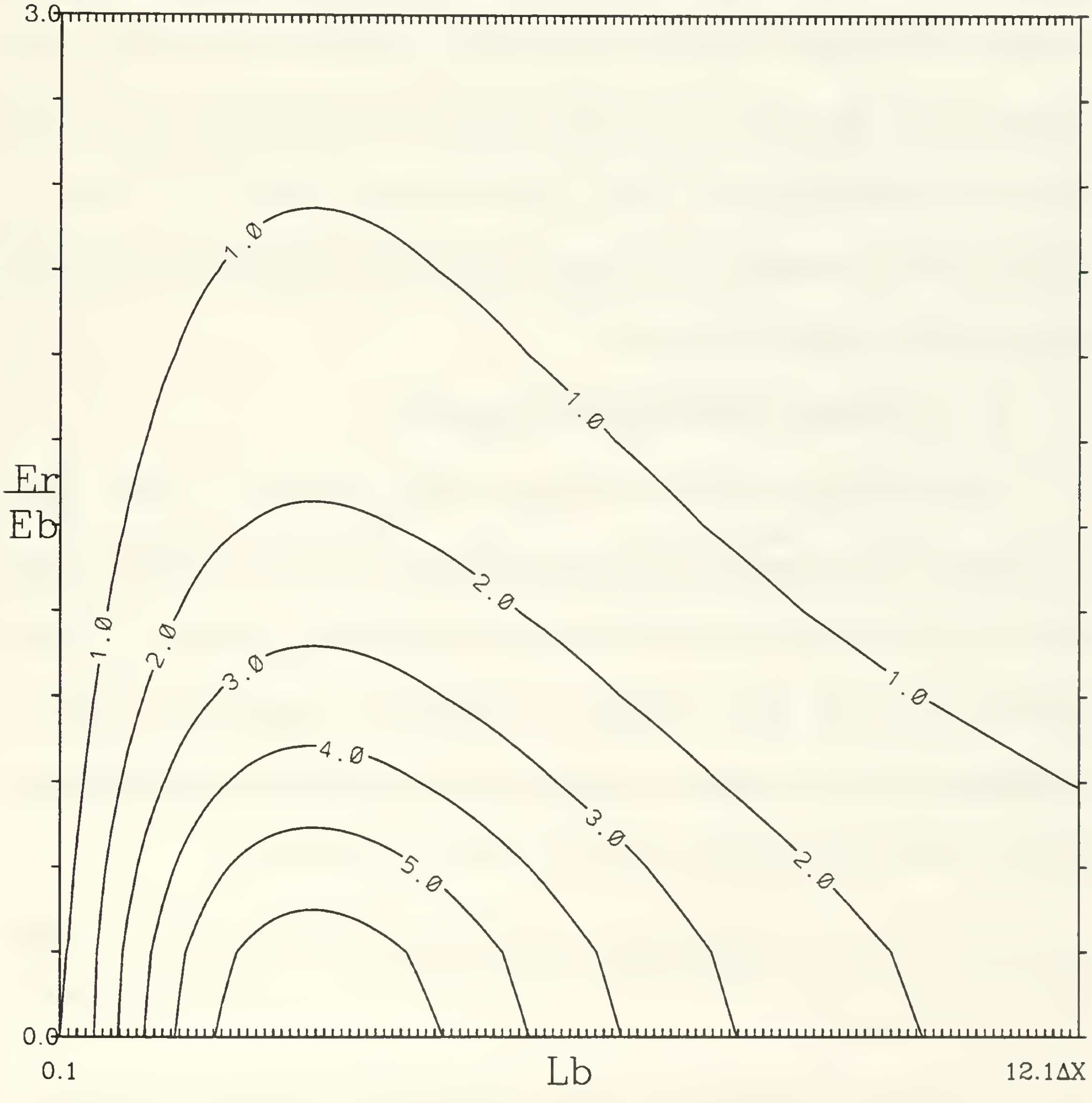

Figure 3.7. Variation of the height observation sensitivity measure as a function of L_b (abscissa) and the ratio of the observation error standard deviation ε_r to the background error standard deviation ε_b (ordinate). The analysis sensitivity length scale is fixed at $L_s = 5.31\Delta x$ while $\varepsilon_r/\varepsilon_b$ ranges from 0.0 to 3.0, and L_b varies between 0.1Δx and 12.1Δx.

The variation of the OSM as a function of L_s and $\varepsilon_r/\varepsilon_b$ over a range from 0.0 to 3.0 is shown in Fig. 3.8, in which the background error correlation length scale is fixed at $L_b = 6.0\Delta x$, while L_s varies from $0.1\Delta x$ and $12.1\Delta x$. The observation sensitivity increases as the analysis sensitivity length scale L_s increases, and decreases as the magnitude of the observation error increases relative to the background error. These results are consistent with (3.16). Thus, super-sensitivity is more likely to occur for observations that are assumed to be accurate relative to the background and when the analysis sensitivity gradient is large-scale.

5. Univariate Wind Observation Sensitivity

The previous sub-sections have examined how the observation sensitivity varies as a function of the background correlation length scale, the analysis sensitivity length scale and the ratio of the observation error to the background error variances. The SOAR function used for the above examples is appropriate for geopotential heights or temperatures, but not for winds. A SOAR correlation function for one-dimensional univariate winds derived following Daley (1991, section 5.2) is given by

$$\rho_{vv}(r) = (1 - r/L_b)\exp(-r/L_b), \tag{3.25}$$

where r is given by (3.2).

The series of experiments conducted for univariate one-dimensional heights is repeated to examine the observation sensitivity for the univariate wind problem. The

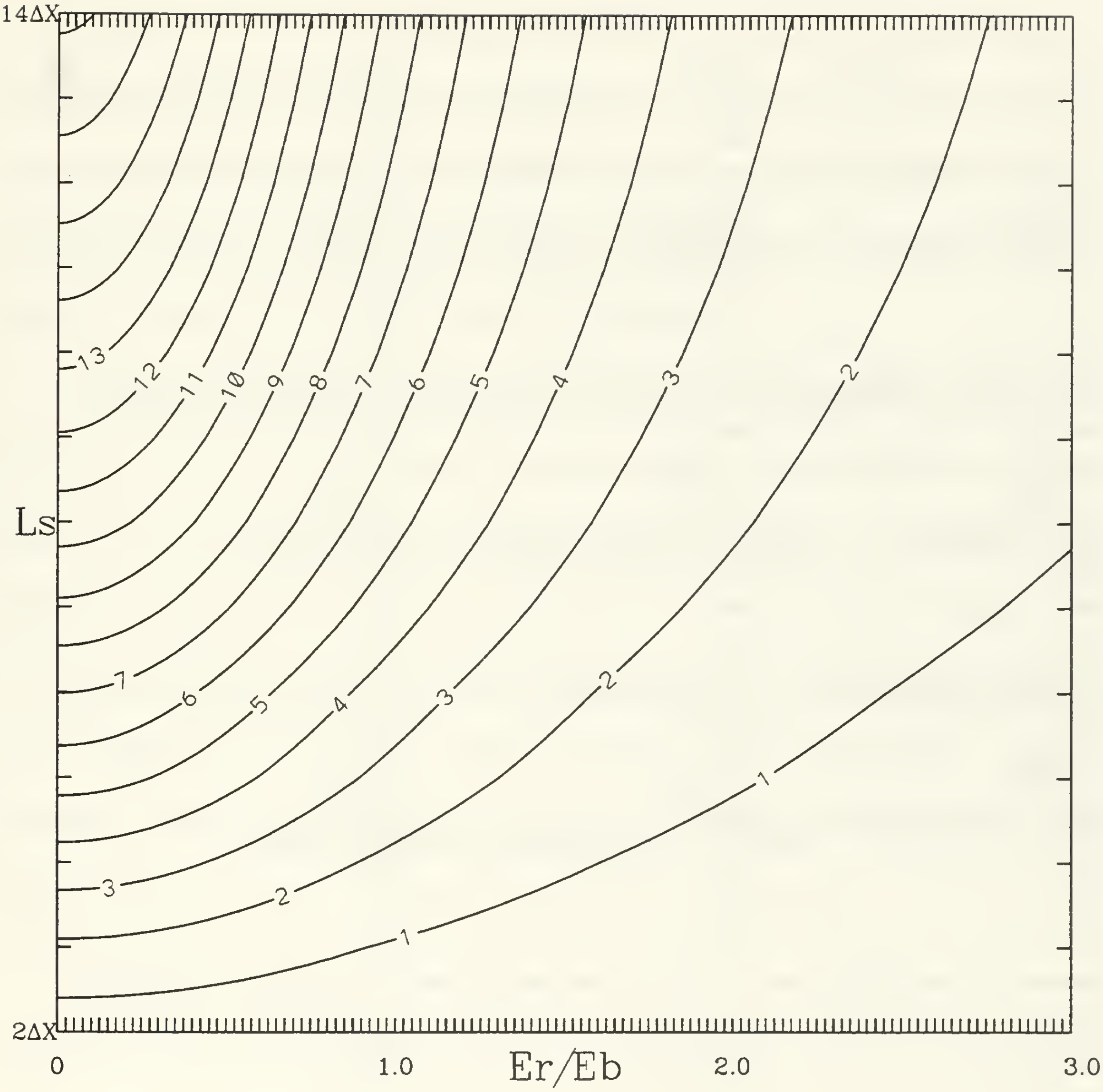

Figure 3.8. Variation of the height observation sensitivity measure as a function of the ratio $\varepsilon_r/\varepsilon_b$ from 0.0 to 3.0 (abscissa) and L_s from 2.0Δx to 14.0Δx (ordinate) for $L_b = 6.0\Delta x$.

one-dimensional coastal case is presented in Fig. 3.9a-d. The wind analysis sensitivity gradient (Fig. 3.9b) is modeled using the cosine function from Fig. 3.2b with $L_s = 5.31\Delta x$. The background error correlation with a length scale L_b of 4.5Δx is plotted in Fig. 3.9a.

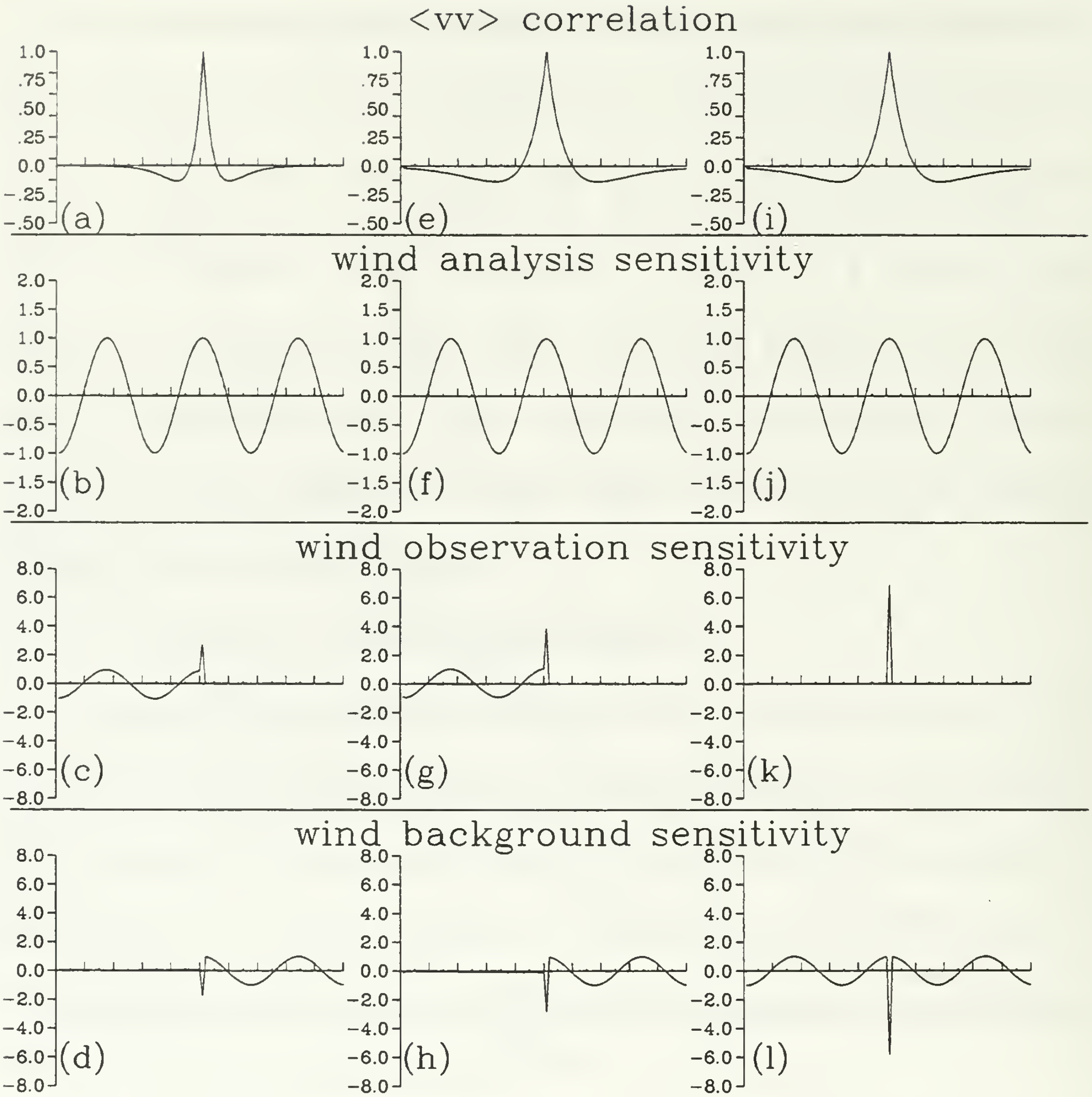

Figure 3.9. As in Fig. 3.2, except for examples of super-sensitivity for the one-dimensional univariate wind coastal (a-h) and single observation (i-l) analysis system. The background error correlation functions for an observation at gridpoint 51 and (a,i) $L_b = 4.5\Delta x$, and (e) $L_b = 9.0\Delta x$, (b,f,j) the imposed analysis sensitivity gradients with $L_s = 5.31\Delta x$, (c,g,k) the observation sensitivities, and (d,h,l) the background error sensitivities. The domain consists of 101 gridpoints, where $\varepsilon_r = 0.0$ and $\varepsilon_b = 1.0$. Values are plotted as a function of the grid location (abscissa) and amplitude (ordinate).

A wind observation is located at every gridpoint left of (and including) point 51. For both the wind and height univariate problems, the observation sensitivity is zero over the oceans (because there are no observations) where the background sensitivity equals the analysis sensitivity. There is no sensitivity to the background over land areas for either the wind (Fig. 3.9d) or height (Fig. 3.2d) examples.

For wind observations, super-sensitivity exists for the observation on the coast and has the same sign as the analysis sensitivity gradient at this location. In contrast, recall the observation sensitivity for height observations (Fig. 3.2c) oscillates from positive to negative and back again for the three observations near the coast. The behavior of the height observation sensitivity at the coastline was shown in Fig. 3.4 to be due to differences in the structure of $\mathbf{K}^T$ for the univariate height example. A similar explanation for the large observation sensitivity in this case (not shown) can be made from examination of the rows of $\mathbf{K}^T$ for the coastal wind observations.

When the background error correlation length is doubled (Fig. 3.9a where $L_b = 9.0\Delta x$), the observation super-sensitivity along the coast is larger (Fig. 3.9g vs. Fig. 3.9c). Likewise, the background sensitivity at the coast (Fig. 3.9h) is larger when L_b is larger. This greater super-sensitivity trend differs from the univariate height example of Fig. 3.2, where the observation sensitivity decreased as L_b increased. Consequently, a different relationship exists between observation sensitivity and L_b for univariate winds and heights.

The observation sensitivity results for a single observation at gridpoint 51 (and $L_b = 9.0\Delta x$) are shown in Figs. 3.9 (i-l). The single observation sensitivity is larger than the sensitivity for the coastal observation (Fig. 3.9g) for the same value of L_b. This single observation experiment can be treated analytically following the procedures used for a single height observation (3.12 – 3.16).

a. The Analytical Solution for a Single Wind Observation

The discretized form of the SOAR correlation function for univariate winds is given by

$$\rho_b(x_r,x_n) = (1-|x_r-x_n|/L_b)\exp(-|x_r-x_n|/L_b). \tag{3.26}$$

The wind correlation model is similar to the height correlation model (3.10) except for a sign change between the first two terms, which produces negative side lobes for the correlation function.

The analysis sensitivity gradient is given by (3.7). The derivation of the analytical approximation to the observation sensitivity follows the procedure in (3.12) – (3.16). The resulting expressions are not the same due to the sign difference in the background error correlation models (3.10) and (3.25).

The analytical approximation to the observation sensitivity analogous to the height observation sensitivity problem in (3.16) may be written

$$\partial J/\partial y = \frac{4\alpha\varepsilon_b^2 L_b^3 \cos(x_r/L_s)}{\left(\varepsilon_b^2+\varepsilon_r^2\right)\Delta x L_s^2 \left(1+L_b^2/L_s^2\right)^2}. \tag{3.27}$$

The magnitude of $\partial J/\partial y$ in (3.27) is maximized when $L_b = \sqrt{3}L_s \approx 1.73L_s$. In contrast, for a single height observation, the magnitude of $\partial J/\partial y$ (from 3.16) is maximized when $L_b = L_s/\sqrt{3}$. This difference is due to the sign change between the height and wind correlation functions (see (3.10) and (3.25), respectively). Assuming that $L_s > 2\Delta x$ and $2\pi L_b > 2\Delta x$, $\partial J/\partial y$ will tend to zero when $L_b \gg L_s$. Also $\partial J/\partial y$ tends to zero when $L_b \ll L_s$.

Applying the definition of the observation sensitivity measure (3.3) to (3.27) gives

$$\mathrm{OSM} = \frac{4\varepsilon_b^2 L_b^3}{\left(\varepsilon_b^2 + \varepsilon_r^2\right)\Delta x L_s^2 \left(1 + L_b^2/L_s^2\right)^2}. \tag{3.28}$$

The observation sensitivity measure is maximized when L_b is approximately twice L_s (i.e., $L_b = \sqrt{3}L_s$), and the observations are assumed to be accurate relative to the background.

b. The Effects of the Length Scales L_b and L_s on the Observation Sensitivity

The computed (not analytical) observation sensitivity measures for a single wind observation placed at the maximum of the analysis sensitivity gradient are plotted in Fig. 3.10 in the same format as Fig. 3.5. The observation error variance is set to zero, while the background error variances are spatially homogeneous and equal to 1.0. The primary difference between the height univariate (Fig. 3.5) and wind univariate (Fig. 3.10) results is that the relationships between the maximum observation sensitivity, and

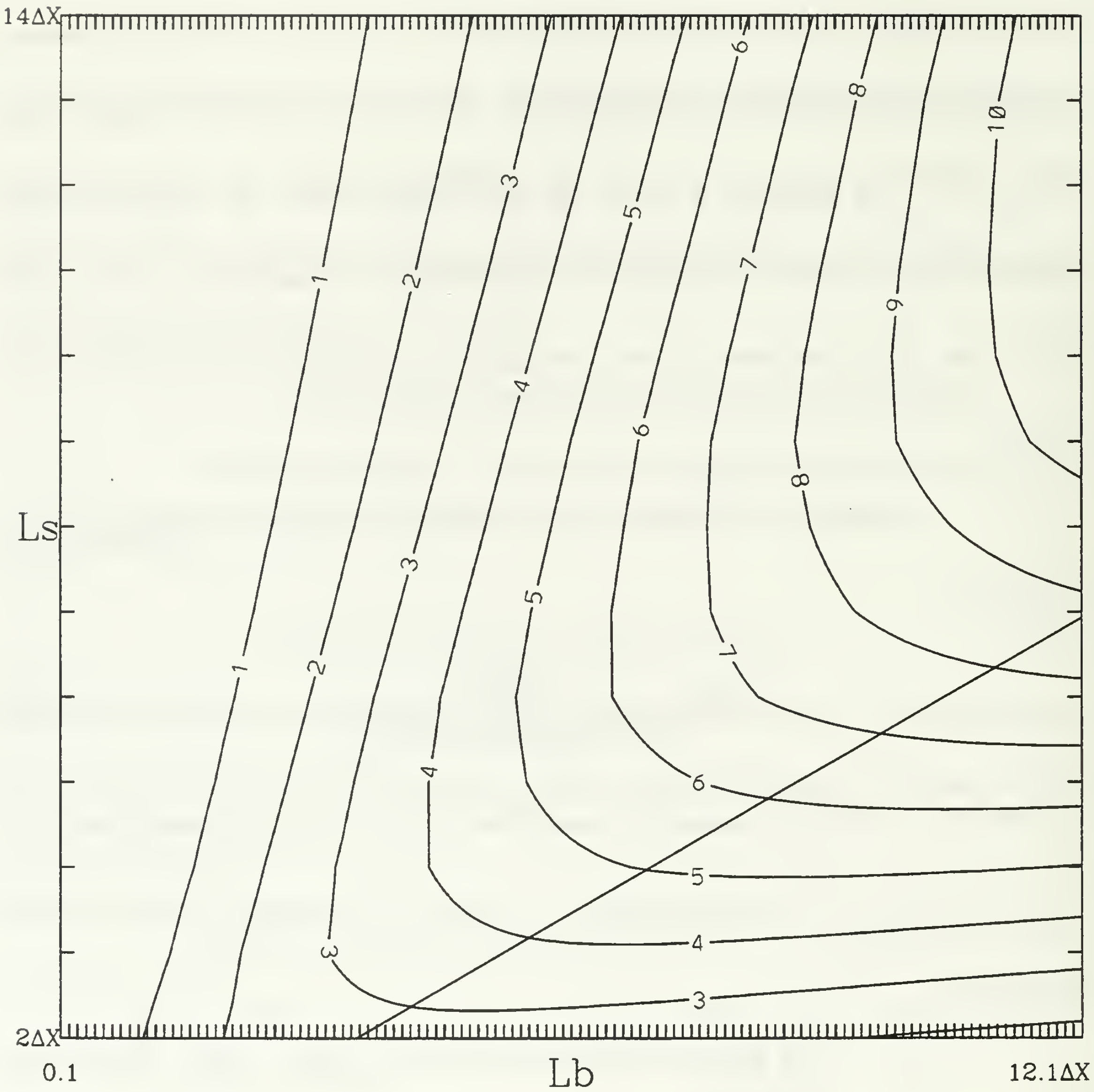

Figure 3.10. As in Fig. 3.5, except for variation of the wind observation sensitivity measure as a function of the background error correlation length scale (L_b; abscissa) and the analysis sensitivity length scale (L_s; ordinate). The length scale L_s varies between 2.0Δx and 14.0Δx, and L_b varies between 0.1Δx and 12.1Δx.

L_b and L_s are not the same. The OSM for a single wind observation (Fig. 3.10) is largest for intermediate values of L_s, while the OSM for a single height observation in Fig. 3.5

increases monotonically with increasing L_s. The analytical relationship between the maximum single wind observation sensitivity and L_b (e.g., $L_b = \sqrt{3}L_s$) is given by the nearly diagonal, heavy line in Fig. 3.10. The computed single wind observation sensitivities compare less favorably with the analytical limit than the single height observation sensitivities (e.g., Fig. 3.3). The differences are likely due to the finite grid resolution, and the narrow central peak for the univariate wind correlation function (e.g, Figs. 3.9a,e,i).

The variation of the single wind observation sensitivity measure as L_b ranges from 0.25 Δx to 25.25 Δx with $L_s = 5.31\Delta x$ is shown in Fig. 3.11. The solid line represents the computed results while the dotted line shows the approximation to the analytical results given by (3.29). The largest discrepancy for the approximation to the analytical results in (3.29) occurs when L_b is small .and the approximation, which required that $2\pi L_b > 2\Delta x$, is no longer valid. When $L_b << L_s$ (and $2\pi L_b > 2\Delta x$), the OSM decreases below 1.0 and tends towards zero, which is consistent with (3.27). This tendency differs from the height example (Fig. 3.6) in which the OSM remains greater than or equal to 1.0 as $L_b \to 0$. When $L_b = 0$, the OSM = 1, for both the single wind and the single height observation, as predicted. The maximum OSM occurs near $L_b = 9.0\Delta x$ as predicted.

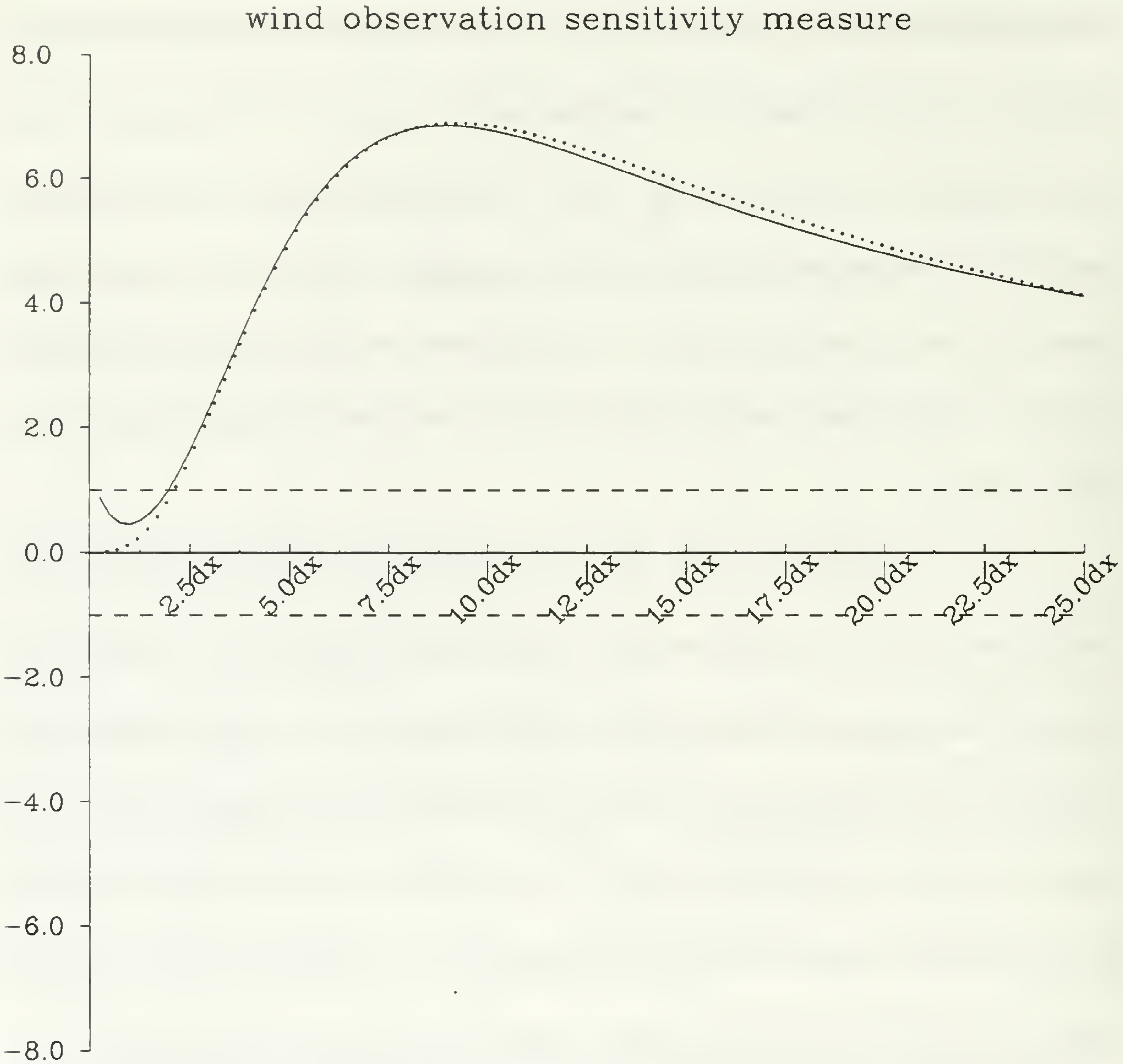

Figure 3.11. As in Fig. 3.6, except for variation of the wind observation sensitivity measure (ordinate) as a function of the background error correlation length scale from 0.1Δx to 12.1Δx (L_b; abscissa) for $L_s = 5.31\Delta x$. The solid line represents the computed observation sensitivity while the dotted line shows the approximation to the analytical value given by (3.28). The dashed lines at ±1.0 are the threshold values for observation super-sensitivity.

The computed result for small L_b can be explained as follows. The SOAR wind correlation function (see Fig. 3.9a) has negative side lobes, unlike that of the height SOAR correlation function (Fig. 3.2a). When L_b is optimal, the negative side lobes of the correlation function (and hence $\mathbf{K}^T$) project efficiently onto the negative side lobes of the analysis sensitivity gradient, which increases the observation sensitivity. When L_b is small, both the main positive and secondary negative side lobes of the wind correlation model (and $\mathbf{K}^T$) project on the main positive maxima of the analysis sensitivity gradient, which reduces the observation sensitivity. If the background error is uncorrelated (L_b = 0) and the observation is perfect, the correlation (and $\mathbf{K}^T$) equal one at the observation location and are zero elsewhere so that the observation sensitivity equals the analysis sensitivity gradient at that location, as given by the vector **a** in (3.6). These results indicate that the approximation given by (3.27) in Fig. 3.11 does not give correct results for small L_b.

According to Chapter III.C.4.a, the OSM should decrease to zero as $L_b \rightarrow \infty$. Experiments (not shown) indicate that this does occur, but that the maximum value $L_b = 25.0\Delta x$ plotted in Fig. 3.11 is too small to show this effect.

c. *The Variation of the Observation Sensitivity as a Function of L_b and Observation Error*

The variation of the wind OSM as a function of L_b and $\varepsilon_r/\varepsilon_b$ is plotted in Fig. 3.12 in the same format as the height OSM in Fig. 3.7. The analysis sensitivity

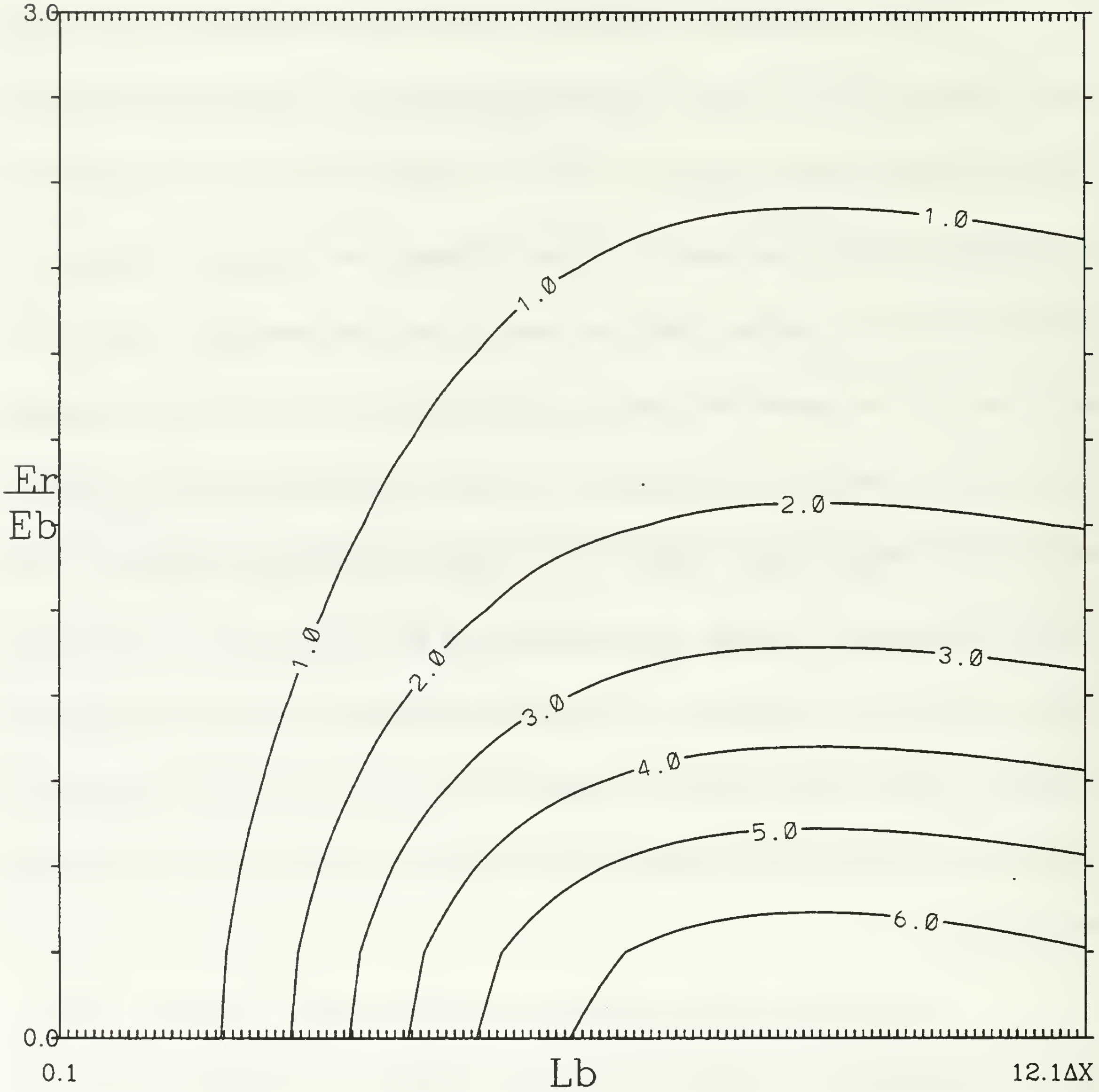

Figure 3.12. As in Fig. 3.7, except for variation of the wind observation sensitivity measure as a function of L_b (abscissa) and the ratio of the observation error standard deviation (ε_r) to the background error standard deviation (ε_b) (ordinate). The analysis sensitivity length scale is fixed at $L_s = 5.31\Delta x$ while $\varepsilon_r/\varepsilon_b$ ranges from 0.0 to 3.0, and L_b varies between 0.1Δx and 12.1Δx.

length scale is fixed at $L_s = 5.31\Delta x$ while $\varepsilon_r/\varepsilon_b$ ranges from 0.0 to 3.0, and L_b varies between $0.1\Delta x$ and $12.1\Delta x$. Notice the observation sensitivity decreases as the observation error increases relative to the background error. Maximum observation sensitivity occurs when the observation is perfect and/or $L_b \approx 9.0\Delta x$ (i.e., L_b is close to the predicted maximum value).

d. The Variation of the Observation Sensitivity as a Function of L_s and Observation Error

This experiment (Fig. 3.13) examines the variations of the OSM for a single wind observation as a function of L_s and $\varepsilon_r/\varepsilon_b$ and is analogous to the height OSM in Fig. 3.8. For this case, $L_b = 6.0\Delta x$ while L_s varies between $2\Delta x$ and $14\Delta x$ and $\varepsilon_r/\varepsilon_b$ ranges from 0.0 to 3.0. The value of L_b was chosen to give as comparable as possible results for both the height and wind correlation models. The observation sensitivity is largest when the observations are perfect ($\varepsilon_r = 0$) and decreases as $\varepsilon_r/\varepsilon_b$ increases. The wind OSM is also maximized when $L_s = L_b$. This result may be derived by setting to zero the derivative of $\partial J/\partial \mathrm{y}$ (from (3.27)) with respect to L_s and solving for L_s.

6. Observation Density and Observation Sensitivity

Thus far, this section has mostly focused on single observation sensitivity. Since observations in atmospheric modeling applications seldom occur in isolation, the behavior of the OSM as a function of observation density and background error correlation length is examined. The experimental design is the same as for the earlier examples, except that the observation density varies from an observation located at every

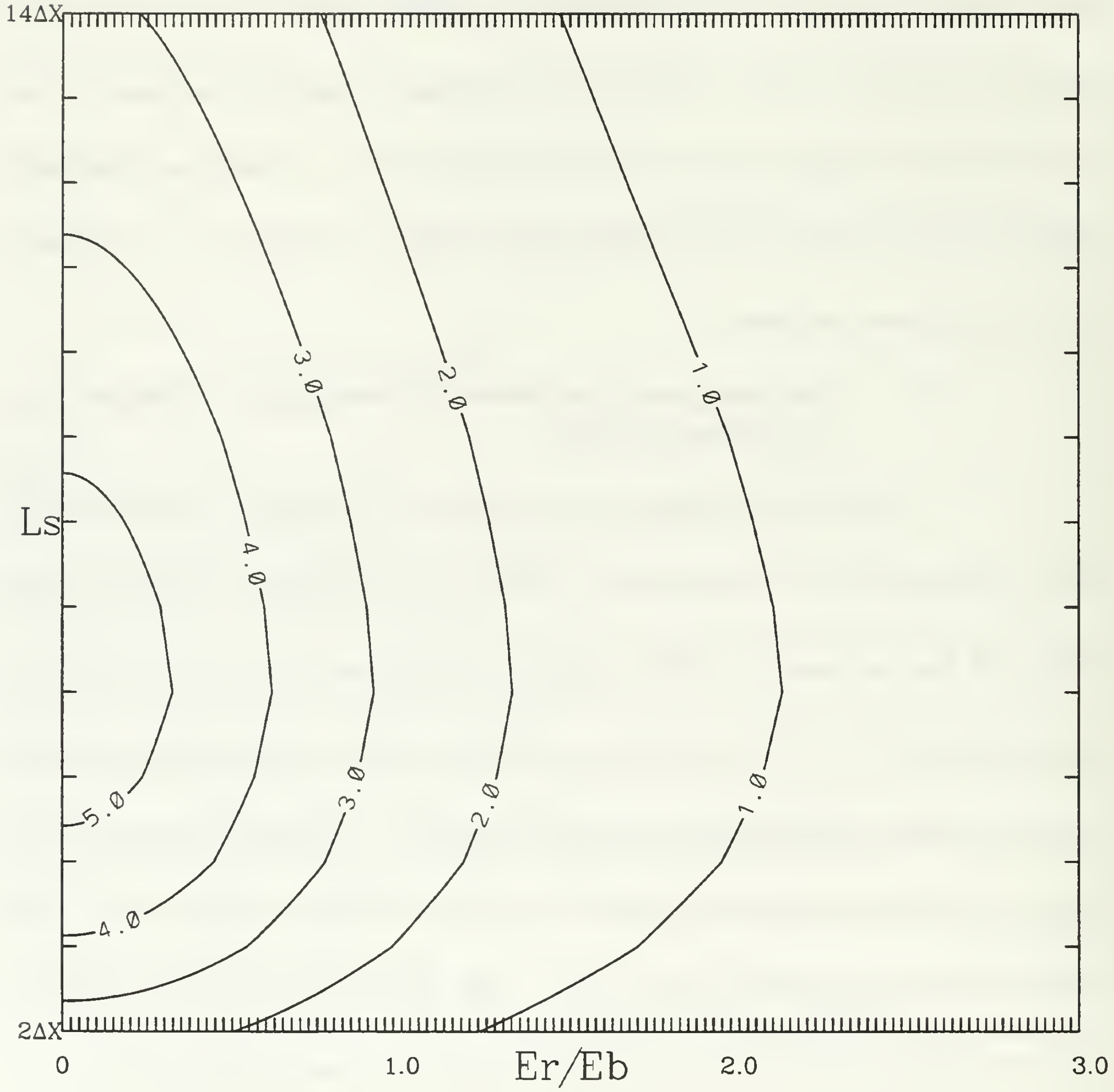

Figure 3.13. As in Fig. 3.8, except for variation of the wind observation sensitivity measure as a function of the ratio of the observation error standard deviation (ε_r) and the background error standard deviation (ε_b) (abscissa) and L_s (ordinate). For this case, $L_b = 6.0\Delta x$ while L_s varies between 2.0Δx and 14.0Δx and $\varepsilon_r/\varepsilon_b$ ranges from 0.0 to 3.0.

gridpoint to observations separated by 30Δx. The observation sensitivity measure for the observation located at gridpoint 51 is shown in Fig. 3.14. The observation sensitivity measure increases until L_b is sufficiently large that the observation begins to interact with

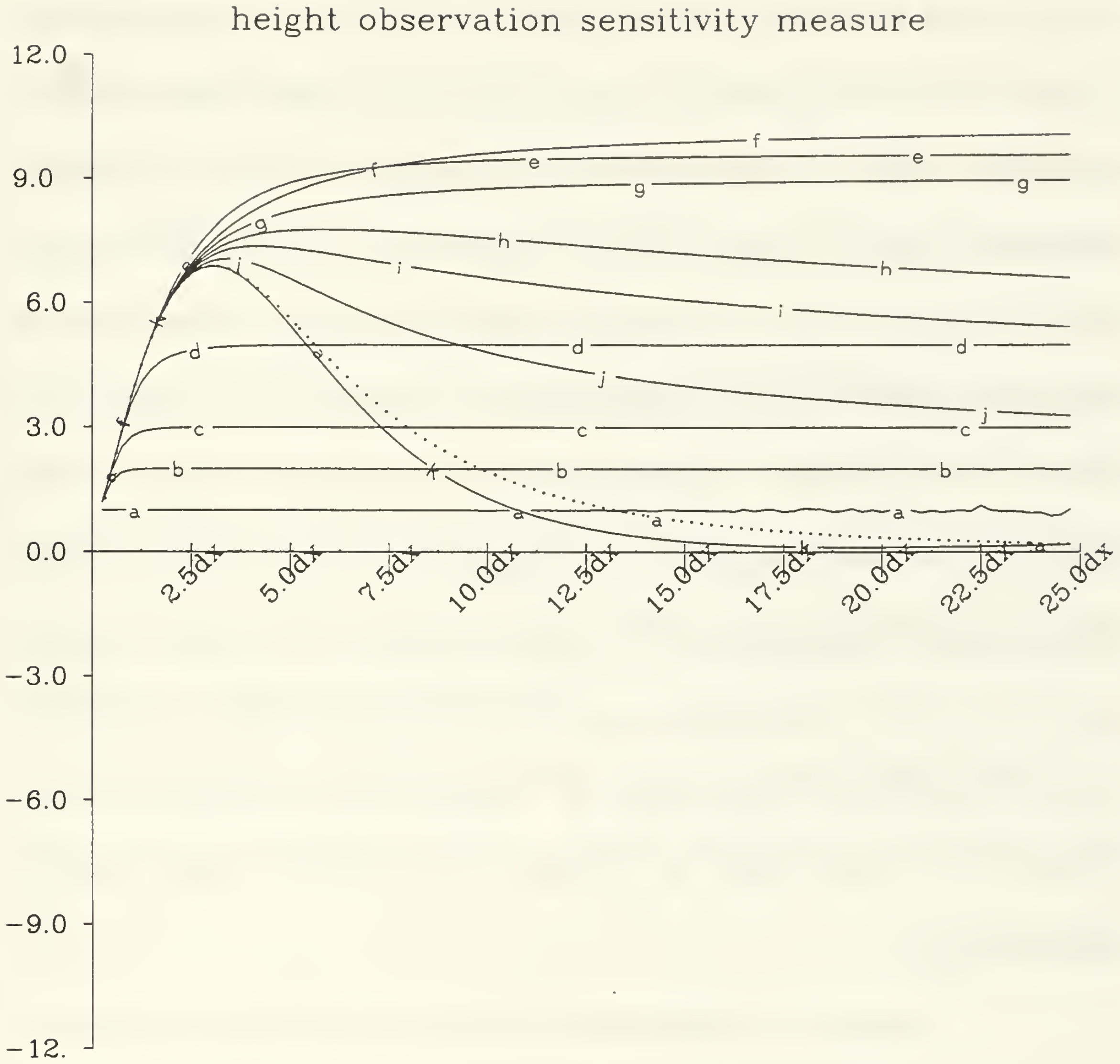

Figure 3.14. Variation of the height observation sensitivity measure (ordinate) as a function of L_b (abscissa) and the distance between the observations. The curves are for observations placed (a) 1Δx, (b) 2Δx, (c) 3Δx, (d) 5Δx, (e) 10Δx, (f) 15Δx, (g) 16Δx, (h) 17Δx, (i) 18Δx, (j) 20Δx, (k) 30Δx apart. The dotted curve is for the analytical approximation to observation sensitivity measure from (3.6) and (3.16). L_b varies between 0.25Δx and 25.25Δx, and $L_s = 5.31\Delta x$.

the neighboring observations and the OSM is maximized. Once the maximum OSM is reached, the behavior of the OSM as L_b continues to increase depends upon the observation density. If an observation is at every gridpoint, the OSM is constant and super-sensitivity does not occur. When the observations are dense, the OSM remains nearly constant for further increases of L_b. When the observation density is low, the OSM curve is similar to that of a single observation (the dashed curve) and the OSM decreases as L_b increases. This difference can be explained as follows. If the observations are widely spaced and L_b is large, the projection of $\mathbf{K}^T$ onto $\partial J/\partial \mathbf{x}_a$ includes negative contributions from the negative side-lobes of the analysis sensitivity gradient (Fig. 3.2b), which thereby reduces the observation sensitivity. Conversely, when the observations are closely spaced, $\mathbf{K}^T$ is localized and the contributions from the projection of $\mathbf{K}^T$ onto $\partial J/\partial \mathbf{x}_a$ are primarily from the positive analysis sensitivity gradient maxima.

7. Summary of One-Dimensional Univariate Observation Sensitivity

The results in this section have demonstrated that the behavior of the observation sensitivity depends upon length scales of the background error correlations and the analysis sensitivity gradients, the ratio of the assumed observation error variance to the assumed background error variance, and the observation density.

Observation sensitivity is maximized when the observation is strongly projected onto the analysis sensitivity gradient by the adjoint of the assimilating algorithm (e.g., $\mathbf{K}^T$). This maximum observation sensitivity occurs when the length scales of the background error correlation and the analysis sensitivity gradient are similar and the observations are assumed to be accurate relative to the background. Thus, when the background error correlation spectrum is assumed to be red (L_b is large), observation sensitivity is greater for large-scale targets than for small-scale targets. Conversely, background sensitivity is greater for small-scale targets.

Observation and background super-sensitivity is a phenomenon that can occur when the density of the observations is low, or there is an abrupt discontinuity in the observation density. It was shown that $\mathbf{K}^T$ is largest (both in spatial scale and magnitude) when an observation is relatively isolated, so that the projection of $\mathbf{K}^T$ onto the analysis sensitivity gradient is maximized.

The observation sensitivity is independent of the observation density when L_b is small, and strongly dependent upon the observation density when L_b is large, which indicates that the general behavior of the OSM as a function of L_b is more complicated than the single observation results (Fig. 3.6) would suggest.

While the results for univariate single wind observation differ in detail from the univariate single height observation results, the same general conclusions can be drawn. The observation sensitivity in both cases is larger for large-scale analysis sensitivity patterns and accurate observations and is smaller for small-scale patterns and poor observations.

D. ONE-DIMENSIONAL MULTIVARIATE OBSERVATION SENSITIVITY

The purpose of this section is to investigate observation sensitivity in a one-dimensional multivariate context. The two variables considered are the geopotential height and the component of the wind perpendicular to the axis defining the one-dimensional grid. For the examples in this section, the grid is defined to be in the x-direction or east-west direction, so that the wind component normal to the axis is the v-wind component.

1. Theoretical Considerations

a. The Cross-Correlation Contribution to Multivariate Observation Sensitivity

The previous section (Chapter III.C) considered univariate examples only, in which sensitivities of J to the observations are given by (2.7a) and the variables $\mathbf{y}$ and $\mathbf{x}_a$ are the same. The sensitivity of J to the observations in a one-dimensional multivariate setting includes contributions due to the cross-correlations between height and v-wind observations and height and v-wind analysis sensitivity gradients.

The *total sensitivity* of J to the height observations is defined as the sum of the *partial sensitivities* and is given by (2.16a). Likewise, the total sensitivity of J to the v-wind observations is given by (2.16c). Only one type of observation (height or wind) will be considered at a time to isolate the cross-correlation contribution to the multivariate observation sensitivity. Under this assumption,

$$\partial J/\partial \mathbf{h}_o = \mathbf{K}_{hh,h}^{T}\,\partial J/\partial \mathbf{h}_a + \mathbf{K}_{hh,v}^{T}\,\partial J/\partial \mathbf{v}_a, \qquad (3.29a)$$

and

$$\partial J/\partial \mathbf{v}_o = \mathbf{K}^T_{vv,h}\,\partial J/\partial \mathbf{h}_a + \mathbf{K}^T_{vv,v}\,\partial J/\partial \mathbf{v}_a. \qquad (3.29b)$$

where the subscript notation from (2.17) is used. The first term in (3.29a) involves only the height observations and the height analysis sensitivity gradient, and is identical to the univariate height relationship in (2.16a). The last term in (3.29a) is the cross-correlation contribution to the total sensitivity. Similarly, the last term in (3.29b) is identical to the univariate wind relationship in (2.16c), and the first term represents the cross-correlation contribution to the total observation sensitivity.

Equations (3.29a) or (3.29b) contain terms involving both the height and wind analysis sensitivity gradients. The use of these equations in an idealized setting would require *a priori* knowledge about the magnitude and phase of $\partial J/\partial \mathbf{h}_a$ relative to $\partial J/\partial \mathbf{v}_a$. While the geostrophic relationship will be used to scale the wind variances relative to the height variances, no such clear-cut relationship exists to define the relative magnitudes of the height and wind analysis sensitivity gradients. Therefore, only the height/wind cross-correlations terms in (3.29) are considered in this section, and the results are intended solely to illustrate the behavior of this cross-correlation component of multivariate observation sensitivity. The total observation sensitivity, as represented by (2.16a-c), will be discussed in Chapter IV using the NAVDAS adjoint. With these restrictions, (3.29a) and (3.29b) are reduced to

$$\partial J/\partial \mathbf{h}_o = \mathbf{K}^T_{hh,v}\,\partial J/\partial \mathbf{v}_a, \qquad (3.30a)$$

$$\partial J/\partial \mathbf{v}_o = \mathbf{K}^T_{vv,h}\,\partial J/\partial \mathbf{h}_a. \qquad (3.30b)$$

The term *height/wind observation sensitivity* (as given by (3.30a)) will be used to indicate the sensitivity of J to height observations, given the wind analysis sensitivity gradient. Likewise, the term *wind/height observation sensitivity* (as given by (3.30b)) is used to indicate the sensitivity of J to wind observations, given the height analysis sensitivity gradient.

Since $\mathbf{HP}_b\mathbf{H}^T$ (from (2.6)) is in observation space, the correlation models used to construct that term are the height-height SOAR and the wind-wind SOAR correlation models as in (3.1) and (3.25), respectively. Let ε_h^2 represent the background geopotential height error variances and ε_v^2 represent the background wind error variances. The covariance functions are given by

$$\langle hh \rangle = \varepsilon_h^2 \rho_{hh}(x), \tag{3.31a}$$

$$\langle vv \rangle = \varepsilon_v^2 \rho_{vv}(x). \tag{3.31b}$$

The coupling between the height and the wind field occurs because of the term $\mathbf{HP}_b$ in $\mathbf{K}^T$, where $\mathbf{P}_b$ represents the background error covariance, and $\mathbf{H}$ is the interpolation operator between observation space and analysis space[1]. The geopotential height-wind background error correlations and proper scaling of the error variances can be derived using the geostrophic assumption and the f-plane assumption, so that

$$v = \gamma \partial h / \partial x, \tag{3.32}$$

---

[1] Cross-correlations between heights and winds also occur due to $(\mathbf{HP}_b\mathbf{H}^T + \mathbf{R})^{-1}$ in the terms not considered in (3.30).

where $\gamma = g/f_o$ (g is the gravitational constant, and f_o is the Coriolis constant defined at 45° N). The background wind error variances may be estimated in terms of the geopotential height error variances, or

$$\varepsilon_v^2 = \gamma^2 \varepsilon_h^2 / L_b^2. \tag{3.33}$$

The height-wind and wind-height covariance functions are derived by substituting the geopotential height correlation function (3.31a) into (3.32), so that

$$\langle hv \rangle = -\gamma \varepsilon_h^2 \rho_{hv} / L_b = -\gamma \varepsilon_h^2 x \exp\left(-|x|/L_b\right)/L_b^2, \tag{3.34a}$$

and

$$\langle vh \rangle = \gamma \varepsilon_h^2 \rho_{vh} / L_b = \gamma \varepsilon_h^2 x \exp\left(-|x|/L_b\right)/L_b^2, \tag{3.34b}$$

where x represents the distance between the two locations of interest. This derivation assumes that the errors are homogeneous, isotropic, and geostrophic.

b. Multivariate Background Sensitivity

The experiments in this section have been restricted to considering only the cross-correlation component of the observation sensitivity and one observation type at a time. With these restrictions, (2.18) and (2.19) reduce to

$$\partial J/\partial \mathbf{h}_b = \partial J/\partial \mathbf{h}_a - \mathbf{H}_v^T \mathbf{K}_{vv,h}^T \, \partial J/\partial \mathbf{h}_a = \partial J/\partial \mathbf{h}_a - \mathbf{H}_v^T \, \partial J/\partial \mathbf{v}_o, \tag{3.35a}$$

$$\partial J/\partial \mathbf{v}_b = \partial J/\partial \mathbf{v}_a - \mathbf{H}_h^T \mathbf{K}_{hh,v}^T \, \partial J/\partial \mathbf{v}_a = \partial J/\partial \mathbf{v}_a - \mathbf{H}_h^T \, \partial J/\partial \mathbf{h}_o. \tag{3.35b}$$

where $\mathbf{K}^T$ has been expanded following the notation introduced in (2.17). The univariate equivalent of (3.35a) is given by

$\partial J/\partial \mathbf{h}_b = \partial J/\partial \mathbf{h}_a - \mathbf{H}_h^T \mathbf{K}_{hh,h}^T \partial J/\partial \mathbf{h}_a = \partial J/\partial \mathbf{h}_a - \mathbf{H}_h^T \partial J/\partial \mathbf{h}_o$. Comparison of the two equations indicates that the behavior of the cross-correlation component of the multivariate background sensitivity should be analogous to the univariate background sensitivity, provided that $\mathbf{H}$ is a simple interpolation operator. For this reason, the cross-correlation component of the background sensitivity is not discussed for these idealized multivariate examples.

c. Objective Multivariate Observation Sensitivity Measures

The observation sensitivity measure (OSM) for the multivariate height/wind problem may be derived by substituting (2.16a) into (3.6). Since the terms involving cross-correlations are zero as $L_b \to 0$, the vector **a** reduces to the univariate component, $\mathbf{K}_{hh,h}^T \partial J/\partial \mathbf{h}_a \big|_{\varepsilon_r \to 0}^{L_b \to 0}$. Under the restrictive assumptions used in this sub-section, the vector **o** from (3.30a) is equal to $\mathbf{K}_{hh,v}^T \partial J/\partial \mathbf{v}_a$ so that the OSM due to the cross-correlation terms is

$$\mathrm{OSM} = \frac{\mathbf{K}_{hh,v}^T \partial J/\partial \mathbf{v}_a}{\mathbf{K}_{hh,h}^T \partial J/\partial \mathbf{h}_a \big|_{\varepsilon_r \to 0}^{L_b \to 0}}. \qquad (3.36)$$

The vector **o** in (3.6) requires the analysis sensitivity gradient for v-component winds, while the vector **a** requires the analysis sensitivity gradient for heights. Use of the OSM in the idealized setting of this sub-section would again require an a priori knowledge of the relationship between height and wind analysis sensitivity gradients. For this reason, the OSM as defined by (3.6) is not used in this section. Since the purpose of this section is to merely illustrate the height/wind and wind/height components of the multivariate observation sensitivity, this is not a serious limitation. In general, there should be no problem in computing the OSM for multivariate problems involving real analysis sensitivity gradients (e.g., those involving the NAVDAS adjoint).

2. Wind/Height and Height/Wind Observation Sensitivity along a Coastline

The experimental framework from the one-dimensional coastal case of Chapter III.C.1 is used here to compute, following (3.30a,b), the sensitivity of J to wind observations given the height analysis sensitivity gradient (Fig. 3.15) and the sensitivity of J to height observations given the wind analysis sensitivity gradient (Fig. 3.16). A few minor changes to the experimental design were made and will be noted where appropriate. The analysis sensitivity gradients for both the height (Fig. 3.15b) and wind (Fig. 3.16b) are given by $\alpha\cos(x/L_s)$ where $L_s = 5.31\Delta x$ and $\alpha = 1$. This value of L_s is chosen to give an odd number of waves across the domain so that the gridpoint values of $\partial J/\partial \mathbf{x}_a$ sum to zero. This choice ensures that the computational results are comparable with the analytical results for an infinite domain.

In contrast to the univariate examples, an observation is placed at every gridpoint to the left of (and including) gridpoint 43. The reason for this new choice of a coastline will become apparent shortly. The observations are either v-component winds or geopotential heights. The observation error variances over land are set to 1% of the background error variances, which prevents the matrix inverse in (2.6) from becoming singular.

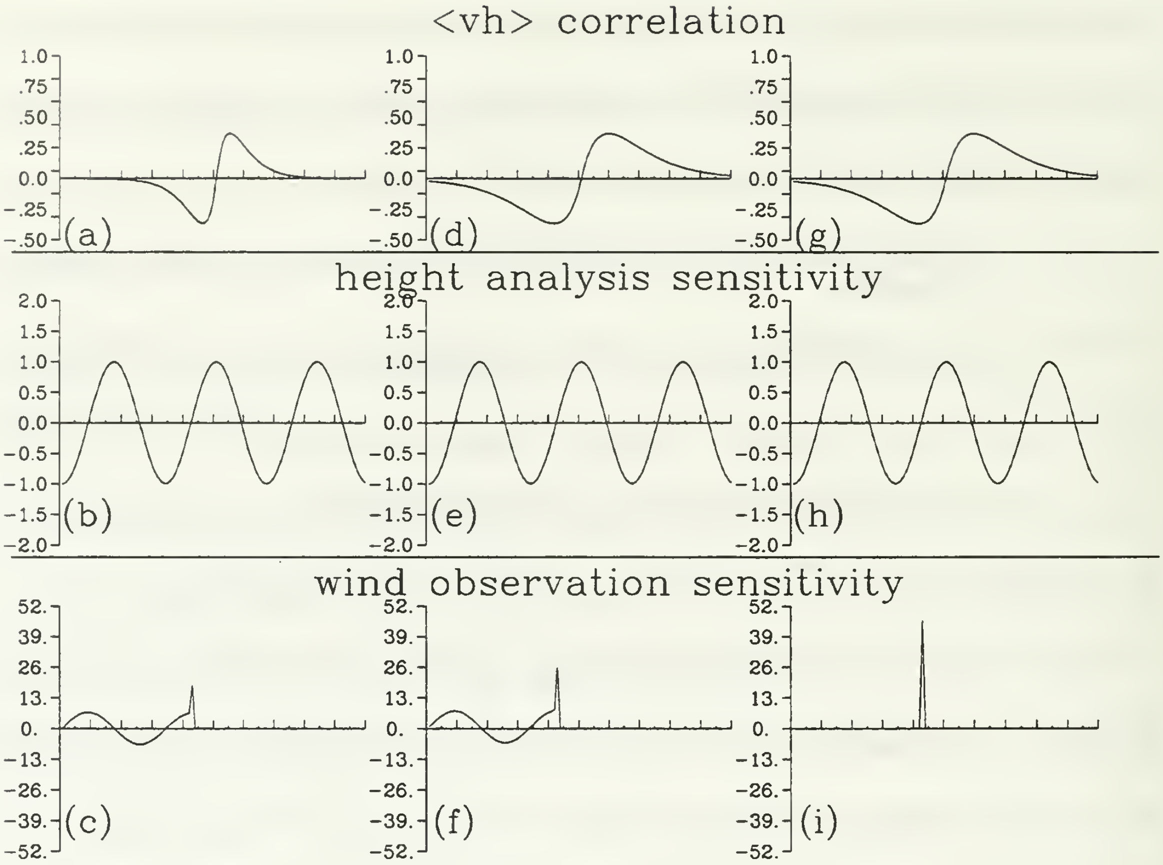

Figure 3.15. As in Fig. 3.9, but for for the one-dimensional wind/height multivariate coastal (a-f) and single observation (g-i) analysis system. The wind/height background error correlation function for an observation at gridpoint 51 and (a) $L_b = 4.53\Delta x$, and (d,g) $L_b = 9.06\Delta x$, (b,e,h) the imposed height analysis sensitivity gradients with $L_s = 5.31\Delta x$, and (c,f,i) the wind/height observation sensitivities. The domain consists of 101 gridpoints, where $\varepsilon_r = 0.01$ and $\varepsilon_b = 1.0$. Values are plotted as a function of the grid location (abscissa) and amplitude (ordinate). Note the special range of ±52.0 for the ordinate in (c,f,i).

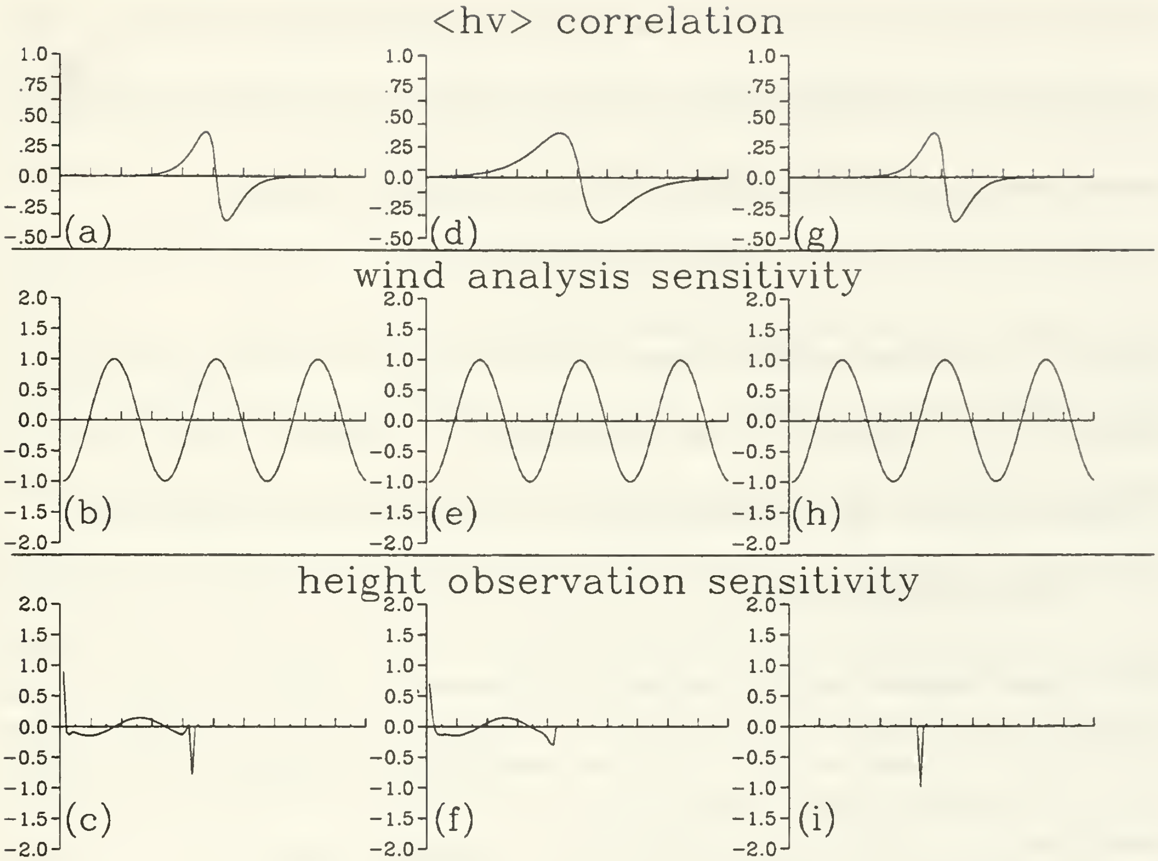

Figure 3.16. As in Fig. 3.2, except for examples of observation sensitivity for the one-dimensional height/wind multivariate coastal (a-f) and single observation (g-i) analysis system. The height/wind background error correlation function for an observation at gridpoint 51 and (a,g) $L_b = 4.53\Delta x$, and (d) $L_b = 9.06\Delta x$, (b,e,h) the imposed wind analysis sensitivity gradients with $L_s = 5.31\Delta x$, and (c,f,i) the height/wind observation sensitivities. The domain consists of 101 gridpoints, where $\varepsilon_r = 0.01$ and $\varepsilon_b = 1.0$. Values are plotted as a function of the grid location (abscissa) and amplitude (ordinate). Note the special range of ±2.0 for the ordinate in (c,f,i).

The background wind error variances are scaled using (3.33) with g = 9.8 m s^{-2}, and the f-plane assumption with f_0 = $1\text{x}10^{-4}$ s^{-1}, and the value for L_b from NAVDAS ($L_b = 3.85 \text{ x } 10^5$ m; see Chapter IV.A), so that

$$\varepsilon_v = 0.25\varepsilon_h. \tag{3.37}$$

A grid spacing of $\Delta x = 8.5 \times 10^4$ m is arbitrarily assumed. Using this grid-spacing along with $L_b = 3.85 \times 10^5$ m implies that $L_b = 4.53\Delta x$. When L_b is allowed to vary, the scaling between the height and wind variances will vary accordingly. In this case,

$$\varepsilon_v = \gamma\varepsilon_h/(C\Delta x) = 1.15\varepsilon_h/C, \qquad (3.38)$$

where C is an arbitrary scaling constant. The background error covariance functions are given by (3.31) and (3.34). The wind-height and height-wind background error correlation functions ($\mathbf{HP}_b$) are shown in Figs. 3.15a,d,g and 3.16a,d,g, respectively.

The wind/height observation sensitivity, with $L_b = 4.53\Delta x$, is shown in Fig. 3.15c. The counter-example for the height/wind observation sensitivity gradient, with $L_b = 4.53\Delta x$, is shown in Fig. 3.16c. The wind/height and height/wind observation sensitivities for a much longer background error correlation length scale ($L_b = 9.06\Delta x$) are shown in Figs. 3.15f and 3.16f, respectively.

The most notable difference between this example (Figs. 3.15, 3.16) and the univariate coastline case (Figs. 3.2, 3.13) is that large values of observation sensitivity (in Figs. 3.15, 3.16) are found along the coastline even though the analysis sensitivity gradients are zero at that point. Closer comparison of Figs. 3.15 and 3.16 indicates that the observation sensitivity is a maximum where the analysis sensitivity gradient is zero, and is zero where the analysis sensitivity gradient is a maximum. In other words, the observation sensitivity is phase-shifted by 90° with the analysis sensitivity gradient. Moreover, the phase shift is in the positive x-direction for height observations and is in the negative-x direction for the wind observations. For the univariate examples, the analysis sensitivity gradient and observation sensitivity are in phase, and the maximum observation sensitivity occurs where the analysis sensitivity gradient is also a maximum. The reasons for these phase shifts will be explained in the next section.

The sensitivities of J to a single wind or height observation placed at gridpoint 43 are shown in Figures 3.15i and 3.16i, respectively. The value of L_b is 4.53Δx in Fig. 3.15i and 9.06Δx in Fig. 3.16i. These two choices for L_b correspond to the examples with the larger observation sensitivity for the coastal cases (Figs. 3.15 and 3.16). In both examples, the observation sensitivity is larger for the single observation than for the observation located at the coastline because $\mathbf{K}^T$ is larger for a single observation (i.e., an isolated observation has more independent information than one with nearby neighbors and is therefore given more weight in an analysis or adjoint sensitivity problem).

3. The Analytical Solutions for a Single Height or Wind Observation

The reason for the phase shift between the maximum values of the wind (height) analysis sensitivity gradient and the height (wind) observation sensitivity can be understood by considering the analytical derivation for a single observation. The procedure follows that of Chapter III.C.2. The sensitivity to a single wind observation, given the height analysis sensitivity gradient, is examined first.

Consider a grid defined such that each point, x_n, is given by nΔx, $-\infty \leq n \leq \infty$. The analysis sensitivity vector is given by (3.9). A single wind observation, with an expected observation error variance ε_{vo}^2, is placed at a location x_r. Using (3.34b), the projection of the background error covariance into observation space ($\mathbf{HP}_b$) for an observation located at x_r may be written as $\gamma\varepsilon_h^2\rho_{vh}(x_r, x_n)/L_b^2$, where $\gamma = g/f_o$. The analytical approximation to the observation sensitivity is derived following the procedures in (3.12) and (3.15), and may be written

$$\partial J/\partial \mathrm{y} \approx \frac{4\gamma\varepsilon_h^2\alpha}{L_b\left[\gamma^2\varepsilon_h^2/L_b^2 + \varepsilon_{vo}^2\right]}\sin(x_r/L_s)\frac{L_b^2}{\Delta x L_s}\frac{1}{(1 + L_b^2/L_s^2)^2}, \tag{3.39}$$

The most striking difference between the wind observation sensitivity given the height analysis sensitivity gradient (3.39), and univariate wind observation sensitivity (3.27) is that $\partial J/\partial \mathrm{y}$, which is proportional to $\sin(x_r/L_s)$, has the same functional form as the analysis sensitivity gradient (3.9), but is phase-shifted by 90°. The analysis sensitivity gradient and the univariate wind observation sensitivity were in phase. This phase shift explains why the wind observation sensitivity is a maximum when the height analysis sensitivity gradient is zero, and also provides the motivation to place the coastline at gridpoint 43 (at a zero crossing of the height analysis sensitivity gradient) instead of gridpoint 51 (at a local analysis sensitivity gradient maximum).

The magnitude $\partial J/\partial \mathrm{y}$ in (3.39) is maximized when $L_b = \sqrt{3}L_s \simeq 1.73L_s$. The relationship between maximum observation sensitivity, L_b and L_s is the same as was derived for the wind-wind correlation model, even though the expression for $\partial J/\partial \mathrm{y}$ is not the same (*cf.* (3.27)). Assuming that the scale of the analysis sensitivity is greater than two grid-lengths, it can be seen that when $L_b \gg L_s$, then $\partial J/\partial \mathrm{y}$ will tend to zero. In addition, $\partial J/\partial \mathrm{y}$ will also tend to zero when $L_b \ll L_s$.

Consider the simple example when $\partial J/\partial y$ is maximized (i.e., $L_b = \sqrt{3}L_s$). Then,

$$\partial J/\partial y \approx \frac{\sqrt{3}\gamma\varepsilon_h^2\alpha}{4\Delta x\left[\gamma^2\varepsilon_h^2/L_b^2 + \varepsilon_{vo}^2\right]}\sin\left(x_r/L_s\right), \tag{3.40}$$

If the wind observation is perfect ($\varepsilon_{vo}^2 = 0$),

$$\partial J/\partial y \approx \frac{3\sqrt{3}\alpha L_s^2}{4\gamma\Delta x}\sin\left(x_r/L_s\right). \tag{3.41}$$

For a given Δx and L_s, $\partial J/\partial y$ is proportional to $\sin\left(x_r/L_s\right)$ and the magnitude of $\partial J/\partial y$ will be a maximum when $\sin\left(x_r/L_s\right)$ is ± 1. This occurs when the observation at location x_r is placed 90° out of phase from the maximum value for the analysis sensitivity gradient.

The same procedure may be used to derive the relationship between L_b and L_s that maximizes the *total* sensitivity to a *single* wind observation as given by (2.16c). The derivation (not shown) is relatively simple if the analysis sensitivity gradients length scales are assumed to be the same. Under those assumptions, the *total* sensitivity to a single wind observation is also maximized when $L_b = \sqrt{3}L_s$.

The same procedure is used to derive the analytical solution for the sensitivity to a single height observation, given the wind analysis sensitivity gradient. Using (3.30a), (3.34a) and (3.9), the approximation to the (scalar) observation sensitivity at x_r may be written

$$\partial J/\partial y \approx -\frac{4\gamma\varepsilon_h^2\alpha}{L_b\left[\varepsilon_h^2 + \varepsilon_{ho}^2\right]}\sin\left(x_r/L_s\right)\frac{L_b^2}{\Delta x L_s}\frac{1}{(1+L_b^2/L_s^2)^2}. \tag{3.42}$$

The single height observation sensitivity, given a wind analysis sensitivity gradient, is maximized when $L_b = L_s/\sqrt{3} \approx 0.58L_s$, which is the same relationship obtained for a univariate, single height observation, even though the expressions for $\partial J/\partial \mathrm{y}$ are not the same (*cf.* (3.16)). According to (3.42), the height observation sensitivity is 90° out of phase with the wind analysis sensitivity gradient field given by (3.9), and 180° out of phase with the wind observation sensitivity given by (3.39). The maximum value for $\partial J/\partial \mathrm{y}$ (when $L_b = L_s/\sqrt{3}$) can be written as

$$\partial J/\partial \mathrm{y} \approx -\frac{3\sqrt{3}\alpha\gamma\varepsilon_h^2}{4\Delta x\left[\varepsilon_h^2 + \varepsilon_{vo}^2\right]}\sin\left(x_r/L_s\right). \tag{3.43}$$

If the height observation is assumed to be perfect ($\varepsilon_{vo}^2 = 0$),

$$\partial J/\partial \mathrm{y} \approx -\frac{3\sqrt{3}\alpha\gamma}{4\Delta x}\sin\left(x_r/L_s\right). \tag{3.44}$$

The maximum single height/wind observation sensitivity given by (3.44) does not depend directly upon L_s (other than through $\sin\left(x_r/L_s\right)$), whereas the maximum single wind/height observation sensitivity (3.41) is proportional to L_s^2.

The above discussion explains why the maximum wind (height) observation sensitivity occurs 90° out of phase with the maximum height (wind) analysis sensitivity gradient for the coastline examples in Figs. 3.15 and 3.16. Other features of note in Figs. 3.15 and 3.16 are the large observation sensitivity along the coast, the large observation sensitivity at the left boundary for height but not wind observations, and the apparent presence of large sensitivity for wind (but not height) observations in the well-observed interior.

In Fig. 3.15c, the wind/height observation super-sensitivity is single-valued along the coastline, whereas the height/wind observation super-sensitivity (Fig. 3.16c) oscillates from positive to negative and back to positive for the coastal observation and the two points immediately inland. The super-sensitivity along the coast follows the same pattern as in the univariate examples in Fig. 3.2 and Fig. 3.13, namely that the super-sensitivity is single-valued for univariate wind observations and oscillates between positive and negative for univariate height observations. In Chapter III.C.2, the super-sensitivity along the coastline was shown to be due to an abrupt change in the density of the observations in a region of large amplitude of the analysis sensitivity gradient. Closer inspection of the row of $\mathbf{K}^T$ (Fig. 3.4) for each observation showed that the largest values of $\mathbf{K}^T$ occurred for the coastal observations. Consequently, the projection of the row of $\mathbf{K}^T$ onto $\partial J/\partial \mathbf{x}_a$ is maximized for the coastal observations. The same situation (not shown) occurs for the wind/height and height/wind cases in Figs. 3.15 and 3.16, even though the analysis sensitivity gradient is zero at the coastline. The projection of $\mathbf{K}^T$ onto $\partial J/\partial \mathbf{x}_a$ is a maximum due to the asymmetrical cross-correlation functions (Figs. 3.15a and 3.16a) that match the similar structure in the analysis sensitivity gradient near the zero crossing.

One feature of interest in Fig. 3.15 is the apparent presence of super-sensitivity for most of the wind observations over the land interior, but not for the height observations in the same location (Fig. 3.16). Since the units for the height analysis sensitivity gradient and the wind/height observation sensitivity are not the same, super-sensitivity cannot simply be determined by comparing the magnitude of the observation sensitivity to the analysis sensitivity gradient.

Another notable difference between Figs. 3.15 and 3.16 is the large sensitivity at the left-most boundary for the height observations, but not for the wind observations. This difference occurs because of the very different structure of $\mathbf{K}^T$ for the height (wind) observation sensitivity problems, given only the wind (height) analysis sensitivity gradients. The rows of $\mathbf{K}^T$ corresponding to the four observations nearest to the left boundary are shown in Fig. 3.17 (for wind observations) and Fig. 3.18 (for height observations). The row of $\mathbf{K}^T$ for the wind observation on the left boundary (Fig. 3.17d) has nearly constant amplitude over the well-observed continental part of the domain. When this row of $\mathbf{K}^T$ is projected onto the height analysis sensitivity gradient (Fig. 3.15b), the wind observation sensitivity is nearly zero. By comparison, the row of $\mathbf{K}^T$ corresponding to the height observation at the left boundary has maximum (negative) amplitude at gridpoint 1 and rapidly increases to zero away from the boundary. The projection of the row of $\mathbf{K}^T$ onto the wind analysis sensitivity gradient (Fig. 3.16b) produces large positive height observation sensitivity for the observation at the left boundary. The row of $\mathbf{K}^T$ corresponding to the height observation at gridpoint 2 is shown in Fig. 3.18c. In this case, the row of $\mathbf{K}^T$ is nearly symmetrical (both positive and negative) about gridpoint 2 so that the resulting height observation sensitivity is close to zero.

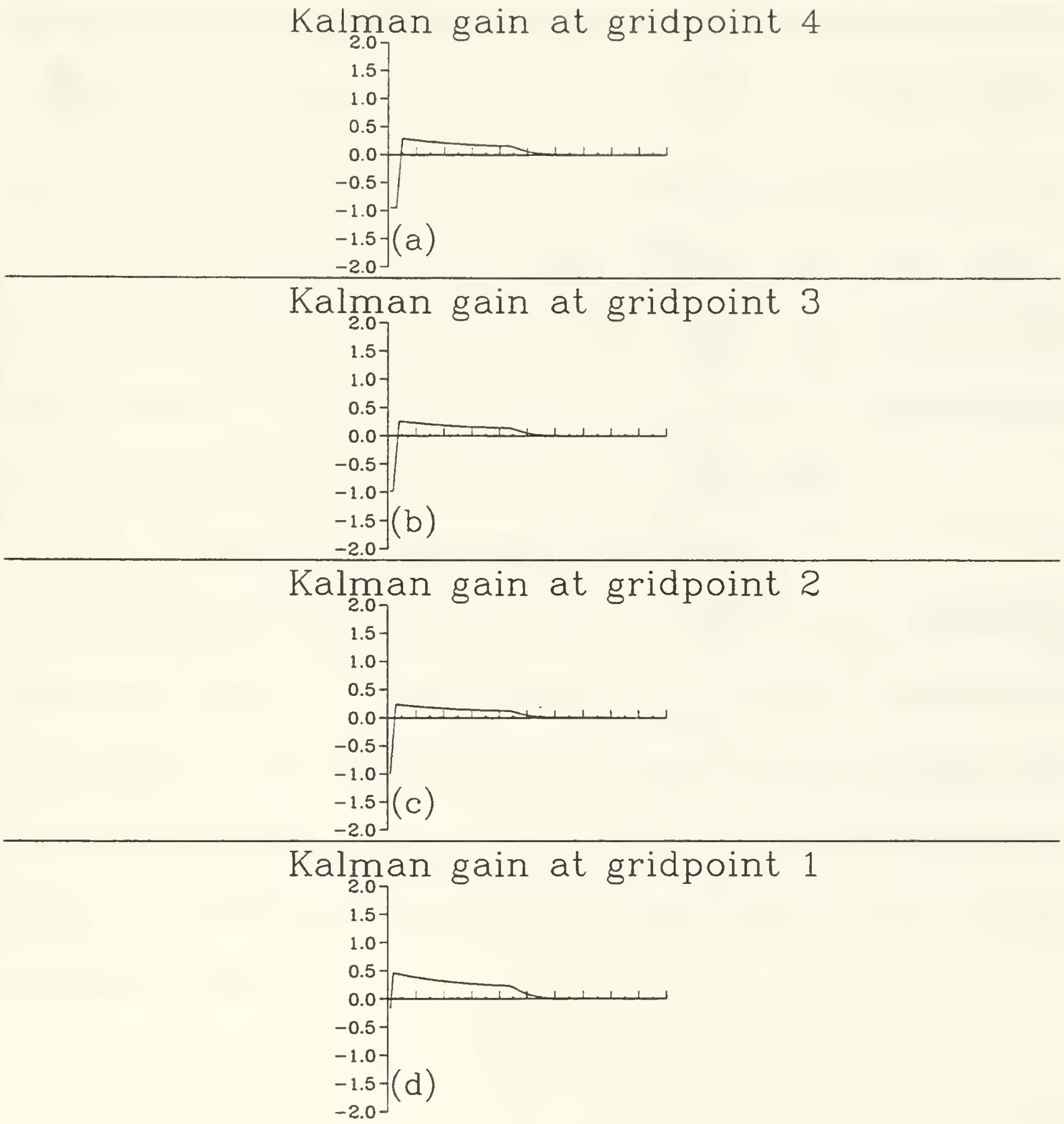

Kalman gain at gridpoint 4

Kalman gain at gridpoint 3

Kalman gain at gridpoint 2

Kalman gain at gridpoint 1

Figure 3.17. As in Fig. 3.4, except for the row of the transposed Kalman gain matrix for wind observations located at gridpoints (a) 4, (b) 3, (c) 2, and (d) 1 in Fig. 3.15c. Values are plotted as a function of the grid location (abscissa) and amplitude (ordinate).

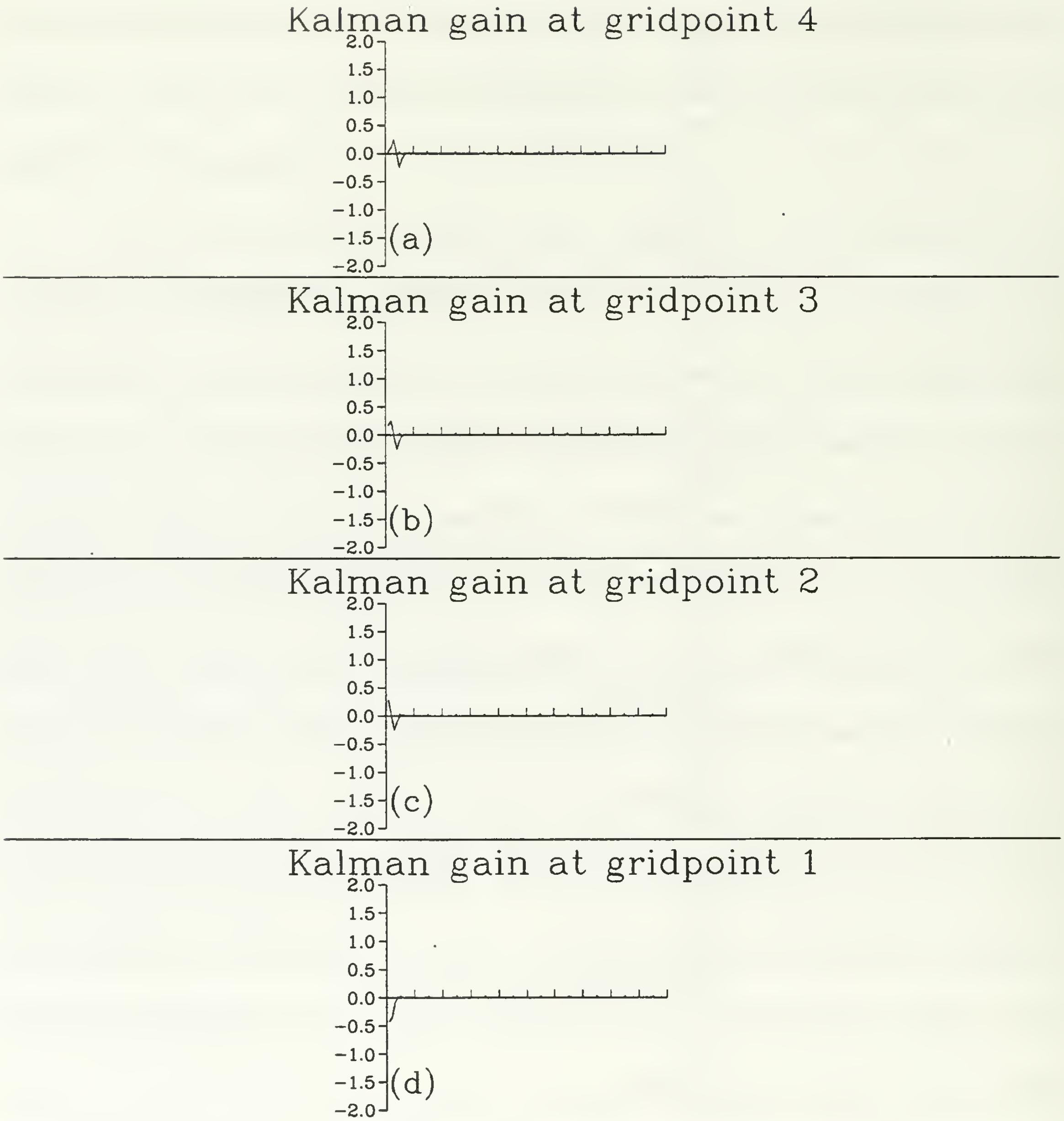

Figure 3.18. As in Fig. 3.17, except for the row of the transposed Kalman gain matrix for height observations located at gridpoints (a) 4, (b) 3, (c) 2, and (d) 1 in Fig. 3.16c. Values are plotted as a function of the grid location (abscissa) and amplitude (ordinate).

Why is the structure of the (transposed) Kalman gain matrix so different for the wind/height and height/wind observation sensitivity problems? Even though the $\langle vh \rangle$ and $\langle hv \rangle$ covariance functions used to compute $\mathbf{HP}_b$ in (2.6) are identical except for the sign difference between (3.34a) and (3.34b), the background error covariance functions used to compute the term $(\mathbf{HP}_b\mathbf{H}^T + \mathbf{R})^{-1}$ are not the same. The $\langle vv \rangle$ covariance function (Fig. 3.9a) is used for wind observations, while the $\langle hh \rangle$ covariance function (Fig. 3.2a) is used for height observations. This difference accounts for the vastly different appearance of $\mathbf{K}^T$ for wind and height observations. These results suggest that large height observation sensitivities could occur along the boundary of a limited domain problem if the analysis sensitivity gradient is non-zero at the boundary.

4. Exploring the Limits of Observation Sensitivity

The purpose of this section is to explore the variations of the observation sensitivity as a function of the analysis parameters L_b, L_s, ε_r, and ε_b. The experimental design follows that used for the one-dimensional univariate computations (Chapter III.C) and the coastal case from this section. Each experiment computes the sensitivity to a height or wind observation given the wind or height analysis sensitivity gradient according to (3.30a,b).

a. The Single Observation Sensitivity Map

A new tool is introduced that may be used to find the location where the sensitivity to a single observation is a maximum. The *single observation sensitivity map* is generated by placing a single probe observation, one at a time, at each gridpoint and solving for the observation sensitivity. In this way, a map showing the sensitivity to a single observation is generated. The probe observation has the error characteristics of some observing system of interest – for example, aircraft temperatures or winds taken during a targeting experiment.

The single observation experiment serves as the framework for the examples in the section. The amplitudes for both the height and wind analysis sensitivity gradients are set to one. The value of Δx is selected so that the height/wind observation sensitivity is maximized when L_b equals the NAVDAS value of $L_b = 3.85x10^5$ m. Maximum observation sensitivity for a single height observation occurs when $L_b = L_s/\sqrt{3} = 3.06\Delta x$, where a value of $L_s = 5.31\Delta x$ is assumed, so that $\Delta x = 1.25x10^5$ m. The relationship between the wind and height background error variances is given by (3.33) or $\varepsilon_v = g\varepsilon_h / f_0 L_b \approx 0.25\varepsilon_h$. The height and wind background error variances are assumed to be spatially homogeneous with $\varepsilon_h = 1.0$. The observations are assumed to be perfect.

The single wind observation sensitivity results, given the height analysis sensitivity gradient, are shown in Fig. 3.19. The wind-height correlation model for an observation at gridpoint 51 using the value of L_b that maximizes the observation sensitivity ($L_b = \sqrt{3}L_s$) is shown in Fig. 3.19a. A single wind observation, which is assumed to be perfect, is placed in the center of the domain at the zero crossing of the height analysis sensitivity gradient (Fig. 3.19b). The maximum wind/height observation sensitivity corresponding to the correlation function in Fig. 3.19a is shown in Fig. 3.19c. The single wind/height observation sensitivity map (SOSM) is shown in Fig. 3.19d. The maximum observation sensitivity in Fig. 3.19d is 90° out of phase with the height

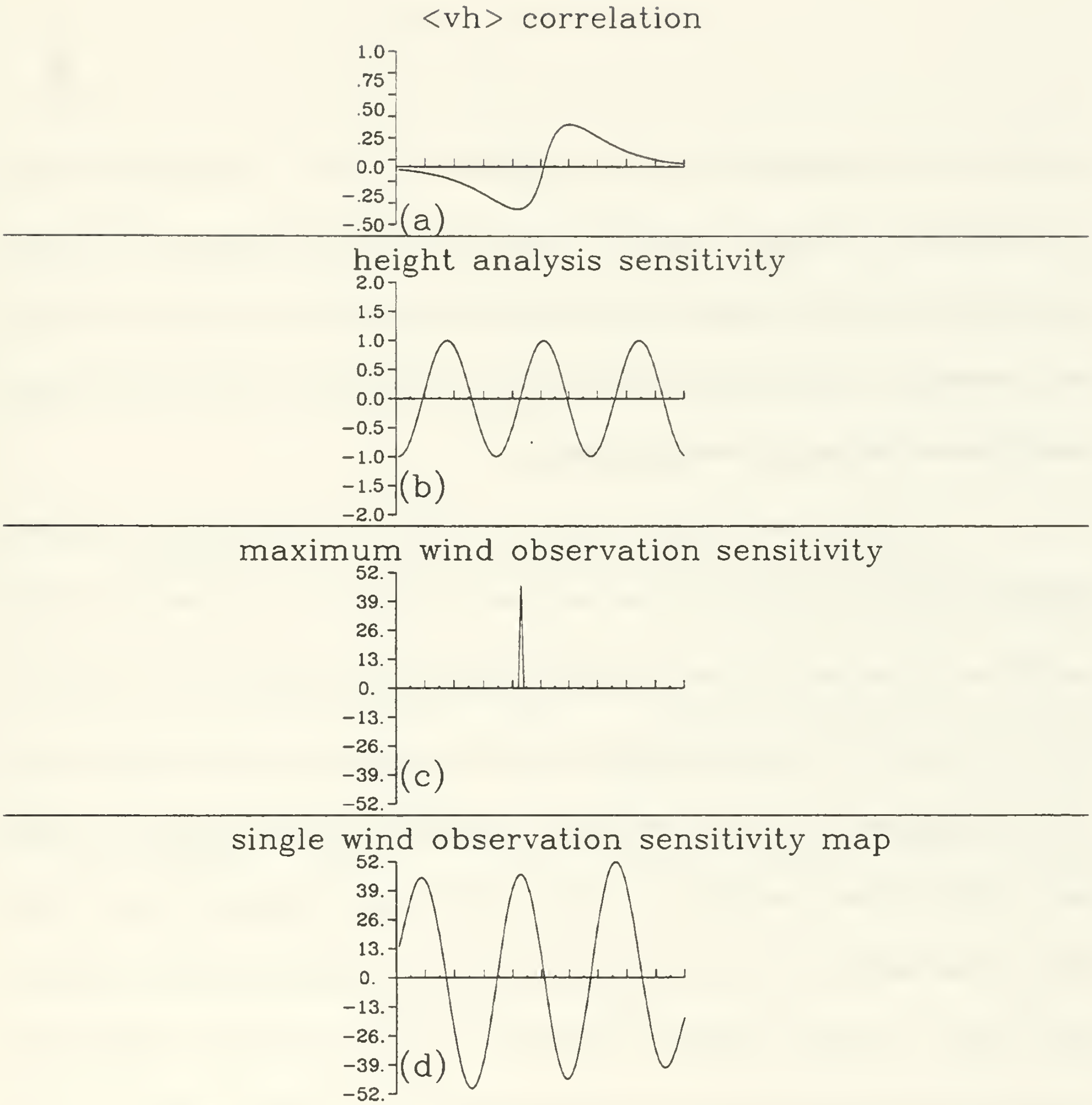

Figure 3.19. As in Fig. 3.15(g,h,i), except for the wind/height single observation sensitivity map. (a) The wind/height background error correlation model for a wind observation at gridpoint 51, (b) the imposed height analysis sensitivity gradient, (c) the wind/height sensitivity to a single wind observation at gridpoint 43, and (d) the single wind/height observation sensitivity map.

analysis sensitivity gradient (Fig. 3.19b) as predicted by (3.39). This 90° phase shift for the maximum wind/height observation sensitivity occurs because of the assumed geostrophic relationship between the height and wind background errors (where the winds are proportional to the derivative of the height field gradient), and the trigonometric specification of the analysis sensitivity gradient.

The results for a single height observation given a wind analysis sensitivity gradient are shown in Fig. 3.20 in the same format as Fig. 3.19. The background error correlation for the value of L_b that maximizes the observation sensitivity ($L_b = L_s/\sqrt{3}$) is shown in Fig. 3.20a. The mathematical form of the analysis sensitivity gradient (Fig. 3.20b) is the same, except it now represents a wind sensitivity gradient and has different units. The maximum sensitivity to a single, perfect height observation placed in the center of the domain at the zero crossing of the analysis sensitivity gradient is shown in Fig. 3.20c. The single height/wind observation sensitivity map (Fig. 3.20d) has the expected 90° phase shift between the height observation sensitivity and wind analysis sensitivity gradient. The observation sensitivity is largest when the analysis sensitivity gradient is a zero, and is zero when the analysis sensitivity gradient is a maximum/minimum.

The most striking differences between the height/wind and wind/height observation sensitivities (Figs. 3.19c, 3.20c) are that they are opposite in sign and that the magnitude of the height/wind observation sensitivity is much smaller. The sign

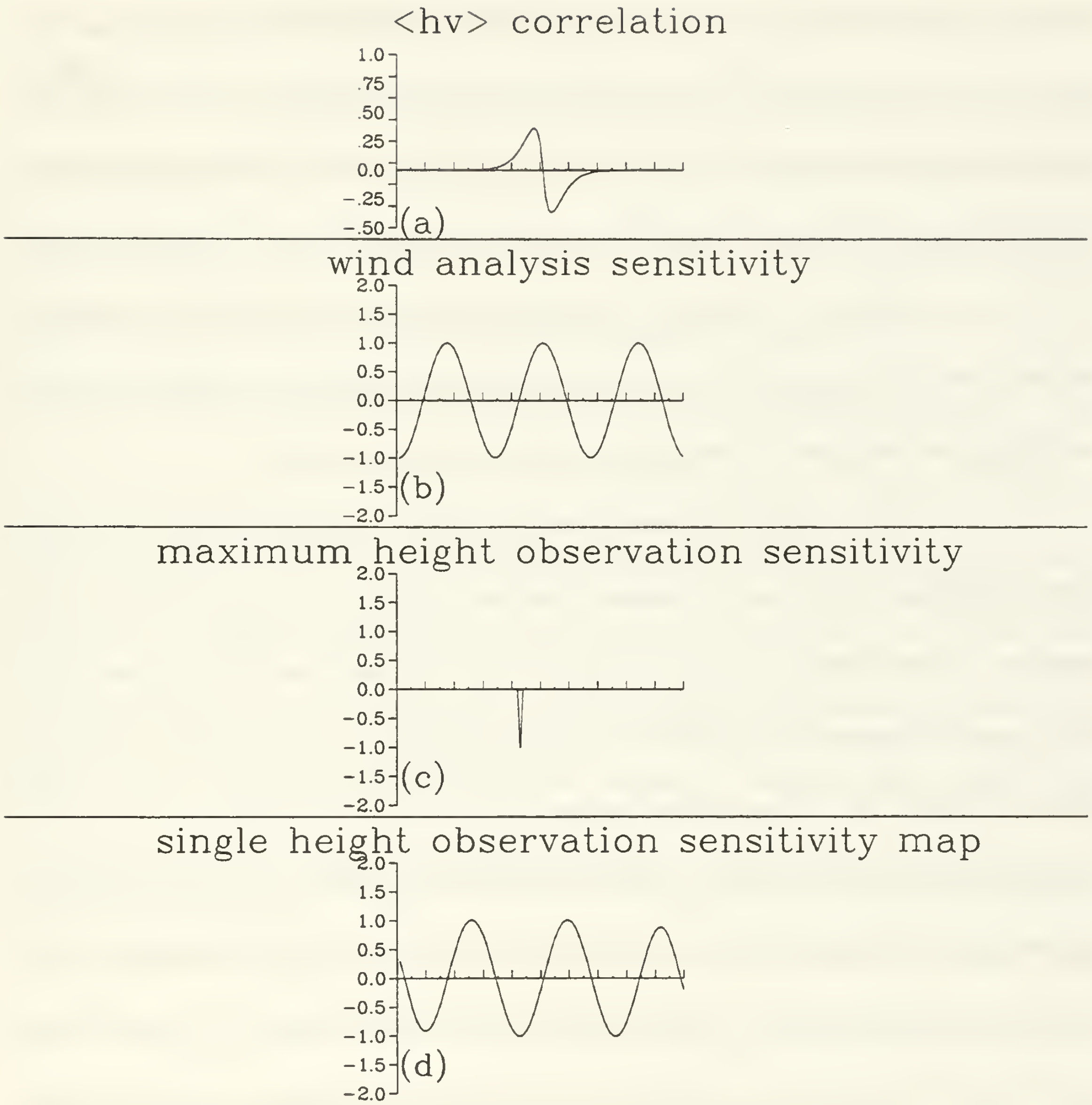

Figure 3.20. As in Fig. 3.19, except for the height/wind single observation sensitivity map. (a) The height/wind background error correlation model for a height observation at gridpoint 51, (b) the imposed wind analysis sensitivity gradient, (c) the height/wind sensitivity to a single height observation at gridpoint 43, and (d) the single height/wind observation sensitivity map.

difference between the height/wind and wind/height observation sensitivities is due to the signs of the correlation functions (3.35a) and (3.35b), and shows up as a 180° phase shift in the single observation sensitivity maps (Figs. 3.19d and 3.20d). The magnitudes of the height/wind and wind/height observation sensitivities are not directly comparable since the units are different. Moreover, since the magnitudes of the analysis sensitivity gradients were both assumed to be one, strict comparisons between the magnitudes of the wind/height and height/wind observation sensitivities cannot be made.

For a single observation, the structure of the Kalman gain is determined by the appropriate multivariate correlation function (cf. Figs. 3.18a and 3.19a), and the magnitude is determined by the error variances. One can easily see why the phase shifts are in opposite directions for height and wind observations by examining the correlation functions (Figs. 3.19a, 3.20a) and the analysis sensitivity gradients (Figs. 3.19b, 3.20b). It is readily apparent that maximum observation sensitivity occurs when the positive and negative lobes of the correlation function match up with the analysis sensitivity gradient structures of the same sign. The correlation function for heights and winds are of opposite sign, and therefore the maximum wind (height) observation sensitivities are 180° out of phase, and 90° out of phase (but in opposite directions) with the height (wind) analysis sensitivity gradients. This exercise also suggests why (in order to maximize observation sensitivity) it is necessary to have similar length scales for the background error correlation and the analysis sensitivity gradient.

b. The Effects of the Background Error Correlation Length Scale

This experiment examines the effect of the background error correlation length scale L_b on the observation sensitivity, where L_b is allowed to vary between 0.25Δx to 25.25Δx in increments of 0. 25Δx. Two experiments are conducted, one for a single wind observation, given the height analysis sensitivity gradient (Fig. 3.21), and the other for a single height observation, given the wind analysis sensitivity gradient (Fig. 3.22). The peak observation sensitivity occurs for shorter L_b for the height observation than for the wind observation, which is consistent with the derived relationships in (3.44) and (3.41). The limiting wind/height observation sensitivity for $L_b \gg L_s$ and $L_b \ll L_s$ can be determined from (3.39), and from (3.42) for the height/wind observation sensitivity. When $L_b \gg L_s$, the height/wind observation sensitivity decreases much faster with increasing L_b than the wind/height observation sensitivity (the decrease is proportional to $1/L_b^3$ for heights and $1/L_b$ for winds). When $L_b \ll L_s$, the wind/height observation sensitivity decreases more rapidly with decreasing L_b (the decrease is proportional to L_b^3 for winds and L_b for heights).

The maximum sensitivity to the wind observation occurs at 9.0Δx with a value of 46.26 (J/ms^{-1}), where the units for J are arbitrary for this idealized case. The theoretical maximum wind observation sensitivity is given by (3.41) and equals 46.63 when $L_b = 9.19\Delta x$. The maximum sensitivity to the height observation (Fig. 3.22) is 1.01

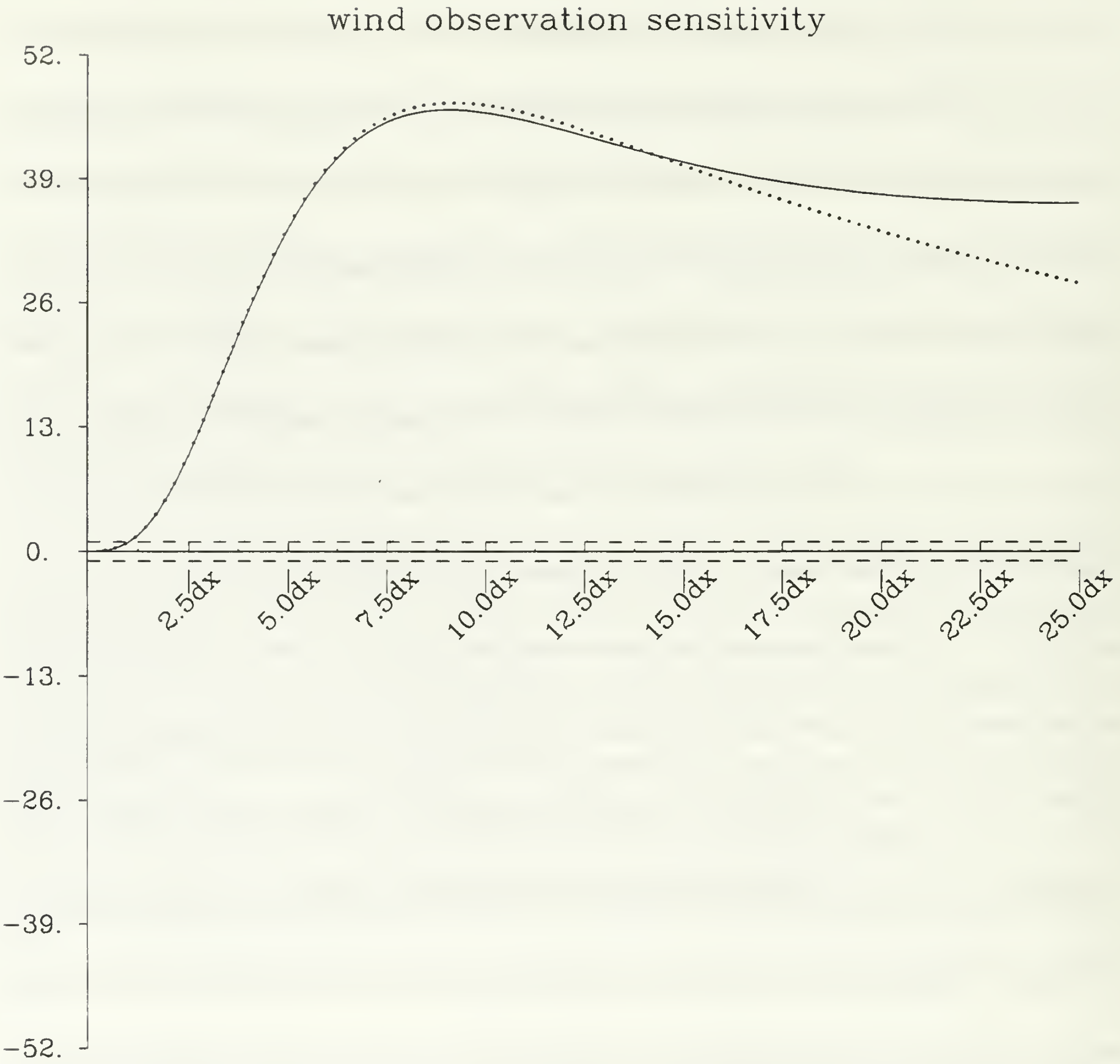

Figure 3.21. As in Fig. 3.11 except for the variation of the wind/height observation sensitivity as a function of the background error correlation length scale from 0.25Δx to 25.0Δx (L_b; abscissa), with $L_s = 5.31\Delta x$. The solid curve is the computed observation sensitivity from (3.6) and (3.29b), and the dotted line is the analytical approximation to observation sensitivity from (3.6) and (3.39). The dashed lines at ±1.0 are the threshold values for observation super-sensitivity.

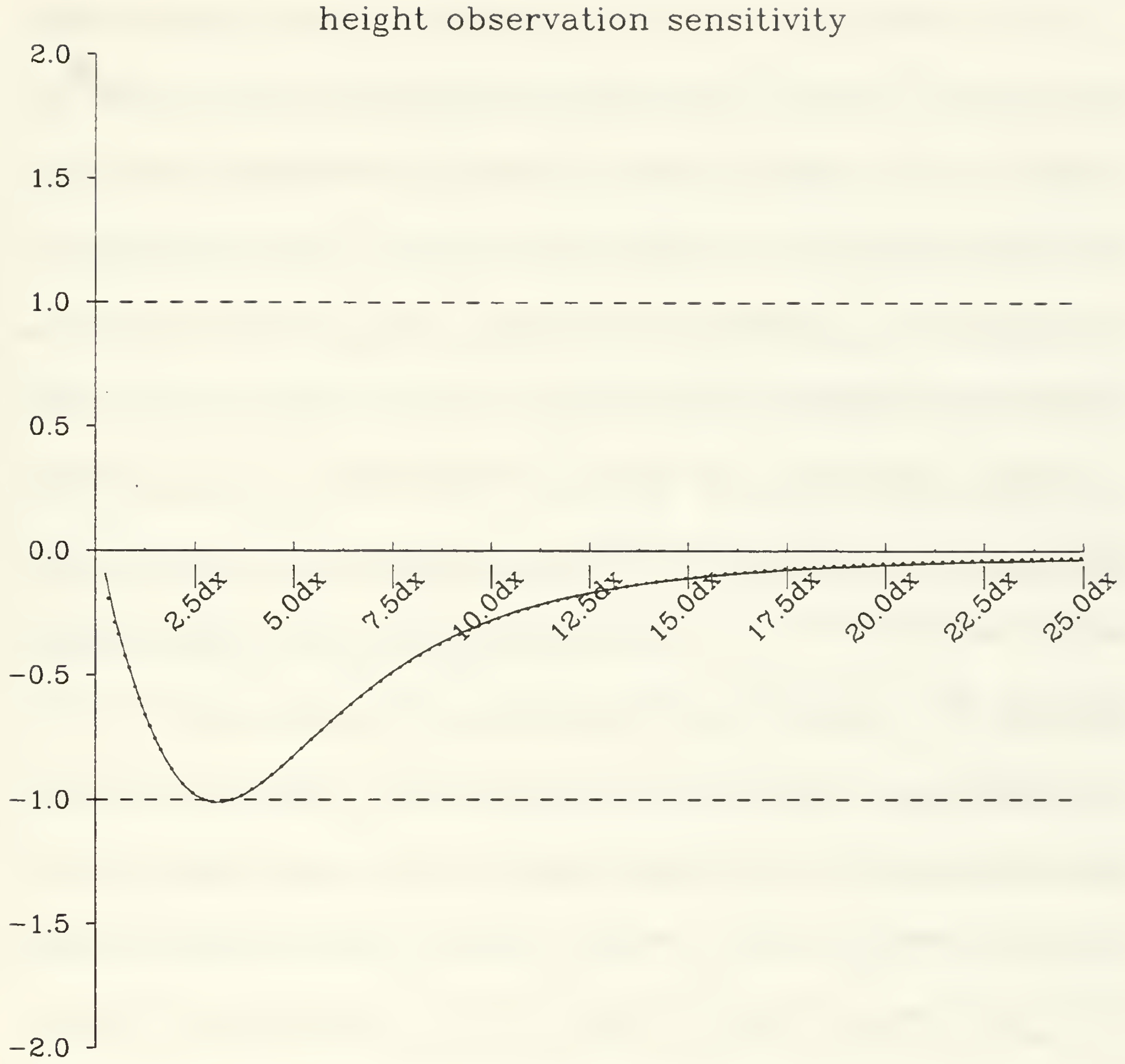

Figure 3.22. As in Fig. 3.6, except for the variation of the height/wind observation sensitivity as a function of the background error correlation length scale from 0.25Δx to 25.0Δx (L_b; abscissa), with $L_s = 5.31\Delta x$. The solid curve is the computed observation sensitivity from (3.6) and (3.29a), and the dotted line is the analytical approximation to observation sensitivity from (3.6) and (3.42). The dashed lines at ±1.0 are the threshold values for observation super-sensitivity.

J/m for $L_b = 3.0\Delta x$, which in excellent agreement with the analytical value from (3.44) of $\partial J/\partial y = 1.02$ J/m for $L_b = 3.06\Delta x$.

The theoretical observation sensitivities computed using the integral approximation (3.39) and (3.42) are plotted as the dotted line in Figs. 3.21 and 3.22. Comparison of the computed (solid) and theoretical approximation (dashed) wind observation sensitivities (Fig. 3.21) shows that the two curves begin to deviate when L_b is larger than 15Δx. This difference occurs because a finite grid domain is used for the numerical example whereas an infinite domain is used for the analytical example. When L_b becomes long relative to the length of the grid domain, then the asymmetrical placement of the observation in the domain (e.g., at point 43) becomes apparent, due to unequal contributions from the positive and negative lobes of the correlation function (and hence $\mathbf{K}^T$). This implies that the upper limit of the useful range for L_b for this experimental design is around 15Δx for wind observations. The computed (solid) and theoretical approximation (dashed) single height/wind observation sensitivity curves in Fig. 3.22 are remarkably similar. The main difference is that the computed observation sensitivity decreases more rapidly towards zero when L_b is less than 1Δx. While these differences appear to be small in Fig. 3.22, they will become more apparent in the next set of figures. This difference implies that the lower limit for valid range for L_b is around 1Δx. Since the approximation used to derive (3.42) required that $2\pi L_b > 2\Delta x$, this result is consistent with the theory.

c. The Effects of the Analysis Sensitivity Length Scale

These experiments parallel those performed for the one-dimensional univariate examples in Chapter III.C.2 and Chapter III.C.5. The analysis sensitivity gradient is given by a single cosine wave and the length scale L_s ranges from 2Δx to 14Δx. The background error correlation length scale varies from 0.1Δx to 12.1Δx. The variation of the sensitivity to a single wind observation as a function of L_b and L_s, given the height analysis sensitivity gradient, is shown in Fig. 3.23. Overall, the pattern of the curves in Fig. 3.23 is similar to the variation of the OSM for the single univariate wind example in Fig. 3.10. This result is as expected, since the relationship for the maximum observation sensitivity (i.e., $L_b = \sqrt{3}L_s$) is the same. The main difference between the two figures arises from the additional factor of $1/L_s$ that appears in the univariate wind observation sensitivity equation (3.27) versus (3.39).

The equivalent results for a single height observation, given the wind analysis sensitivity gradient, are shown in Fig. 3.24, and may be compared to the univariate height example in Fig. 3.5. Both figures have the predicted relationship between maximum observation sensitivity, L_b and L_s (i.e., $L_b = L_s/\sqrt{3}$), but otherwise bear only a vague resemblance to one another. The main difference between the univariate height and the height/wind single observation sensitivity is that the height/wind observation sensitivity differs by an additional factor of $1/L_s$ in (3.42) versus (3.16).

d. The Effects of the Observation Error

The next set of experiments examines the variation of the observation sensitivity as a function of L_b and the ratio of the observation to the background error standard deviation. The sensitivity to a single wind observation, given the height analysis

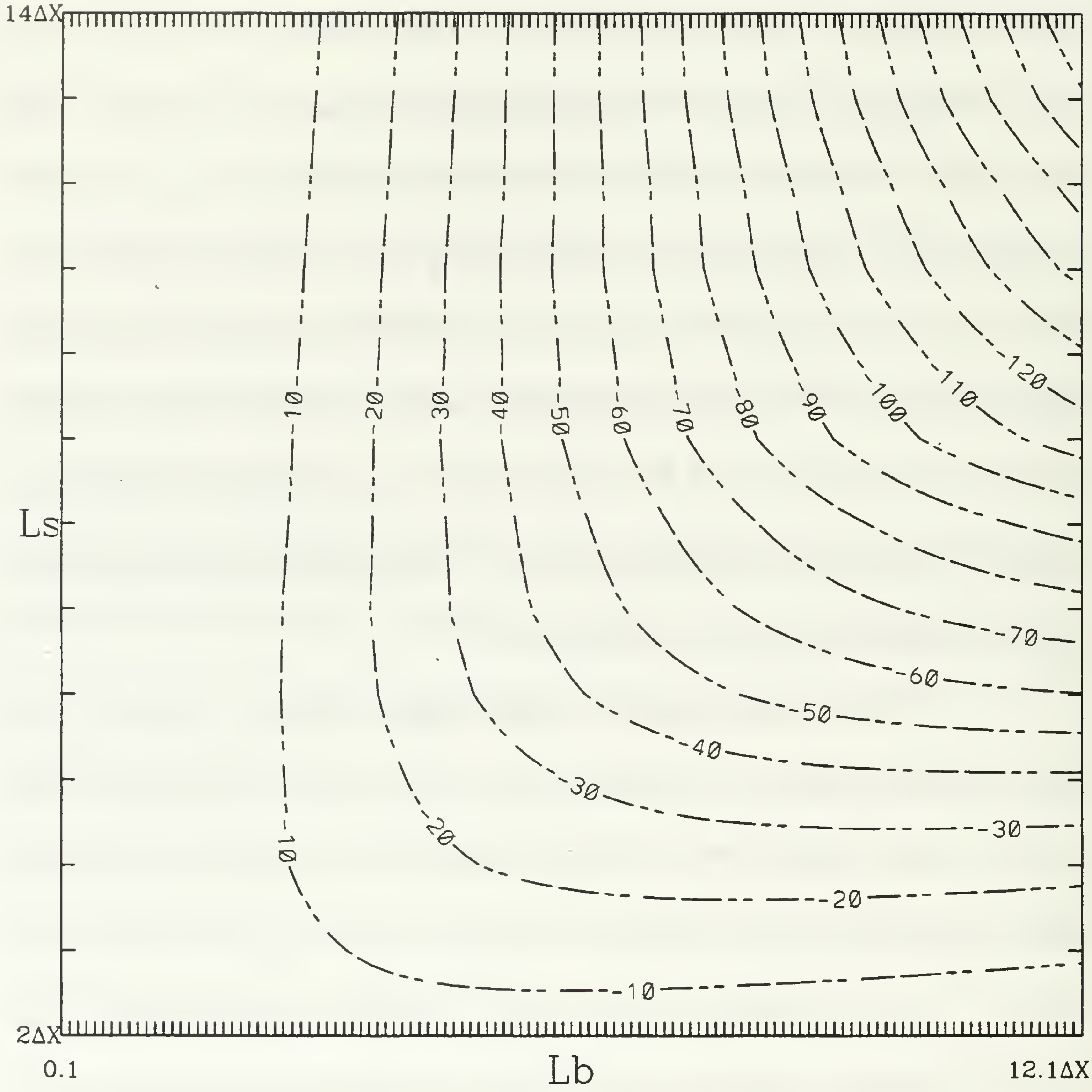

Figure 3.23. As in Fig. 3.10, except for variation of the wind/height observation sensitivity as a function of the wind/height background error correlation length scale (L_b ; abscissa) and the height analysis sensitivity length scale (L_S; ordinate). The length scale L_s varies between 2.0Δx and 14.0Δx, and L_b varies between 0.1Δx and 12.1Δx.

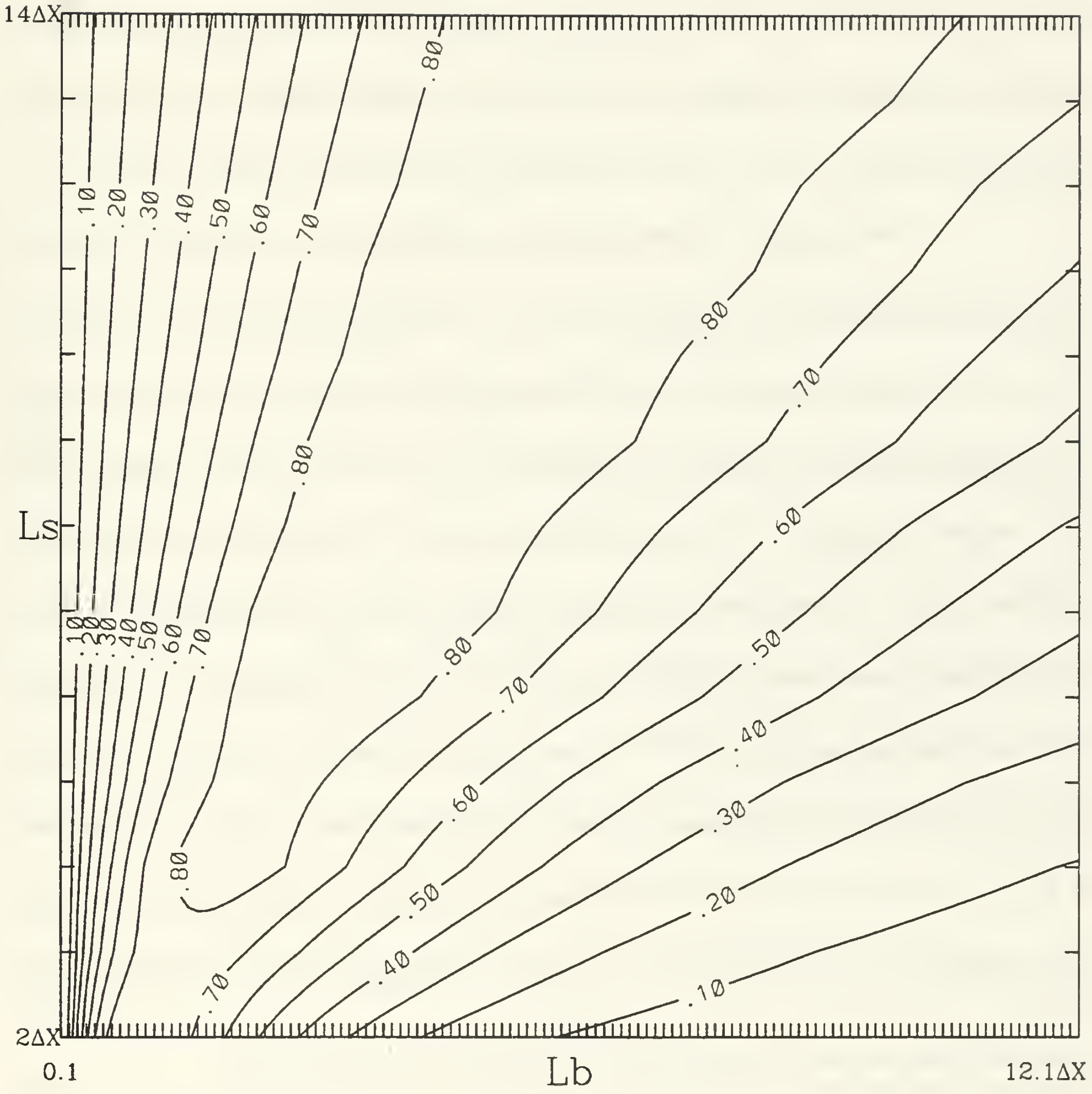

Figure 3.24. As in Fig. 3.5, except for variation of the height/wind observation sensitivity as a function of the height/wind background error correlation length scale (L_b ; abscissa) and the wind analysis sensitivity length scale (L_s; ordinate). The length scale L_s varies between 2.0Δx and 14.0Δx, and L_b varies between 0.1Δx and 12.1Δx.

sensitivity gradient, is in Fig. 3.25, while the sensitivity to a single height observation, given the wind analysis sensitivity gradient is in Fig. 3.26. In each case, the observation sensitivity decreases as the observation becomes less accurate relative to the background. These plots compare very well with the analogous univariate cases (Figs. 3.12 and 3.7).

The final set of figures shows the variation of the observation sensitivity for fixed L_b (= 6Δx) when L_s ranges from 2Δx to 14Δx and error ratio $\varepsilon_r/\varepsilon_b$ varies from 0.0 to 3.0. The single wind/height and single height/wind observation sensitivity results are presented in Figs. 3.27 and 3.28, respectively. The two figures differ mainly by the error variance scaling of the observation sensitivity. The height/wind observation sensitivity (Fig. 3.28) resembles the analogous height univariate example (Fig. 3.8), while the wind/height observation example (Fig. 3.27) bears less resemblance to the analogous wind univariate example (Fig. 3.13). In each case, the observation sensitivity decreases as the observations become inaccurate relative to the background. For a specified value of $\varepsilon_r/\varepsilon_b$, the observation sensitivity increases as the analysis sensitivity gradient length scale increases up to the point where L_s and L_b are roughly similar. The observation sensitivity remains relatively constant as L_s increases beyond that point.

5. Summary of Wind/Height and Height/Wind Observation Sensitivity

This section explored the contribution to total height observation sensitivity from the cross-correlation between height observations and the wind analysis sensitivity gradient, and the contribution to the total wind observation sensitivity from the cross-correlation between wind observations and the height analysis sensitivity gradient.

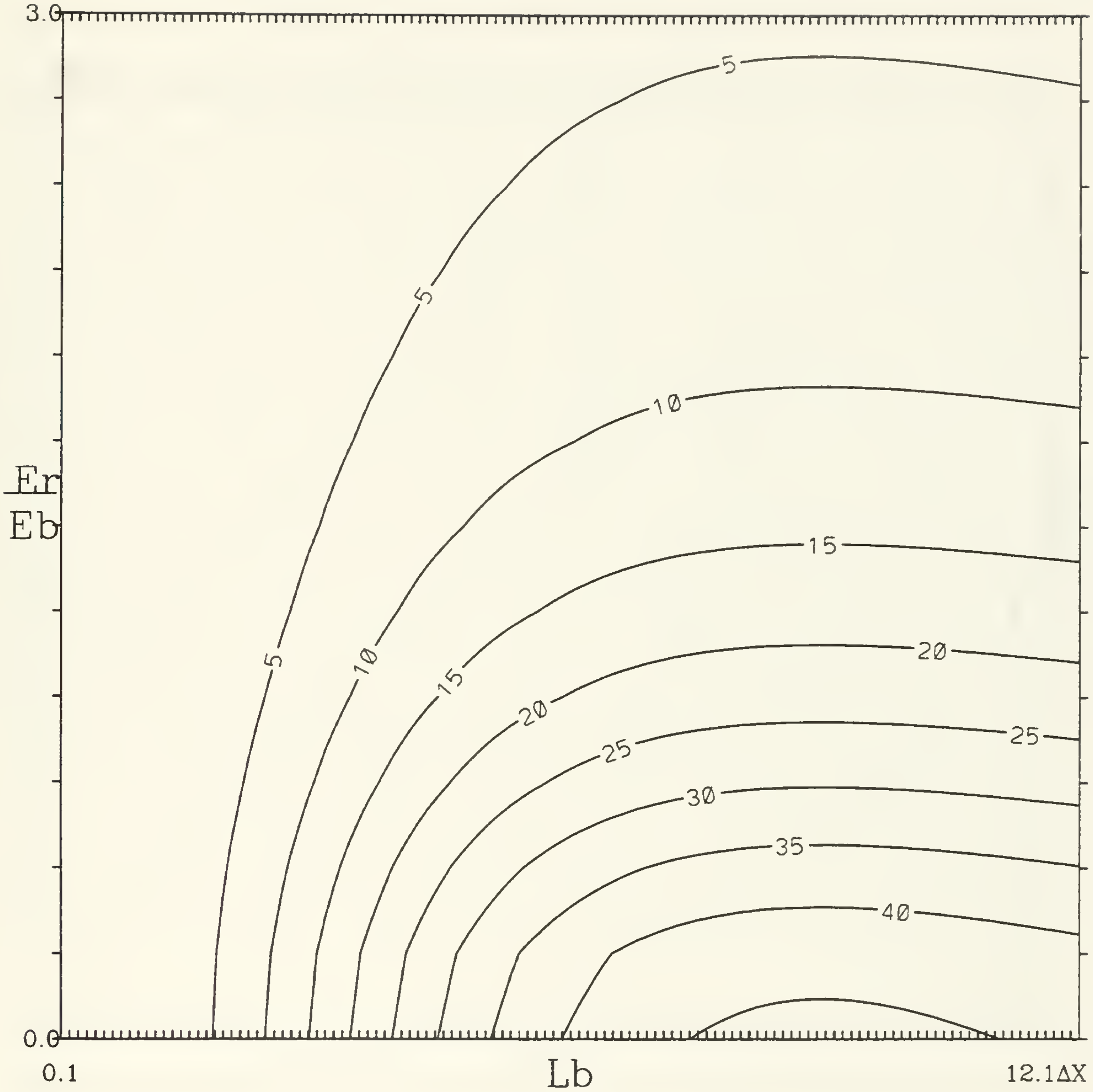

Figure 3.25. As in Fig. 3.12, except for variation of the wind/height observation sensitivity as a function of L_b (abscissa) and $\varepsilon_r/\varepsilon_b$ (ordinate). The range of L_b is from 0.1Δx to 12.1Δx, the range of $\varepsilon_r/\varepsilon_b$ is from 0.0 to 3.0, and $L_s = 5.31\Delta x$.

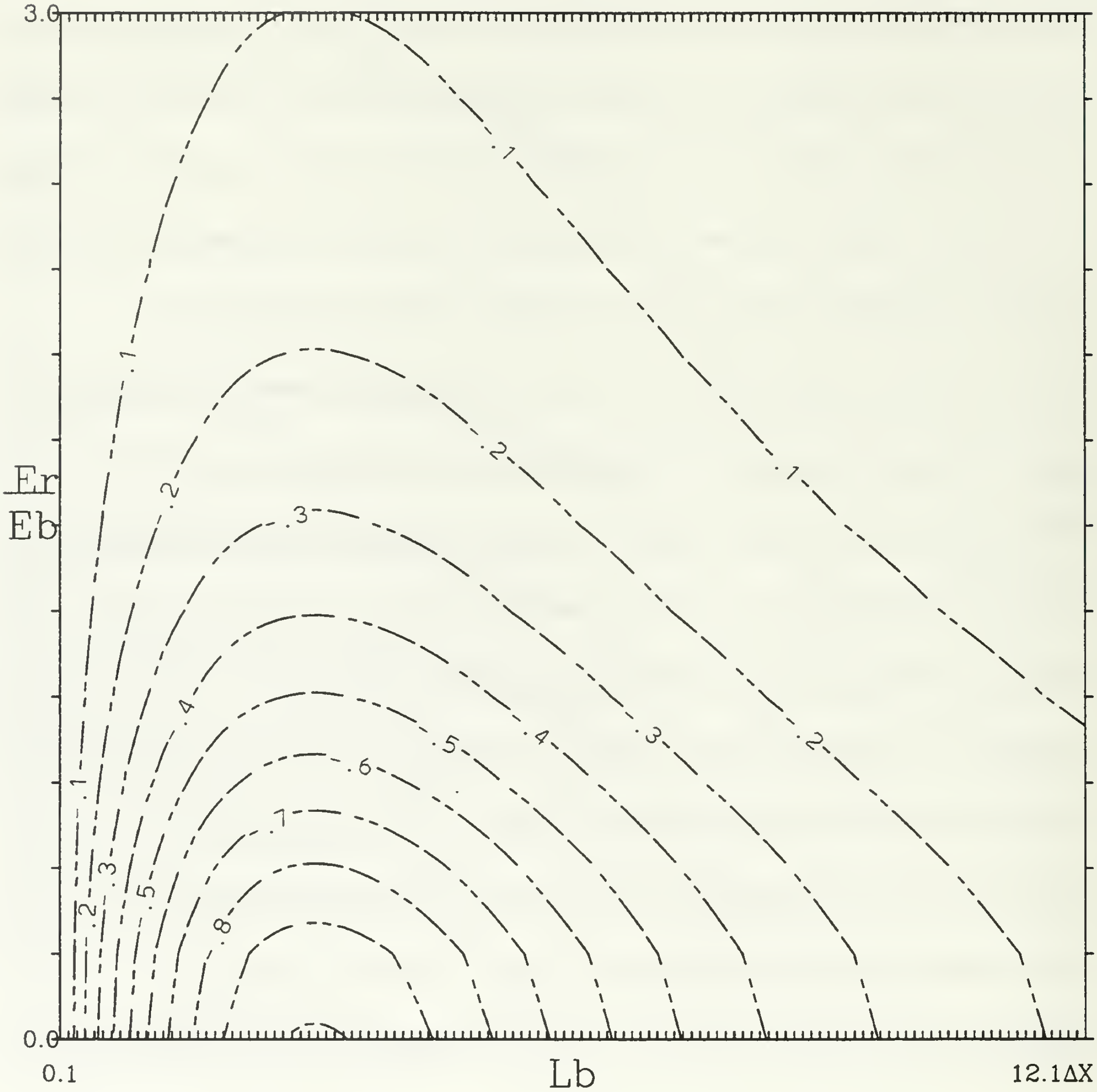

Figure 3.26. As in Fig. 3.7, except for variation of the height/wind observation sensitivity as a function of L_b (abscissa) and $\varepsilon_r/\varepsilon_b$ (ordinate). The range of L_b is from 0.1Δx to 12.1Δx, the range of $\varepsilon_r/\varepsilon_b$ is from 0.0 to 3.0, and $L_s = 5.31\Delta x$.

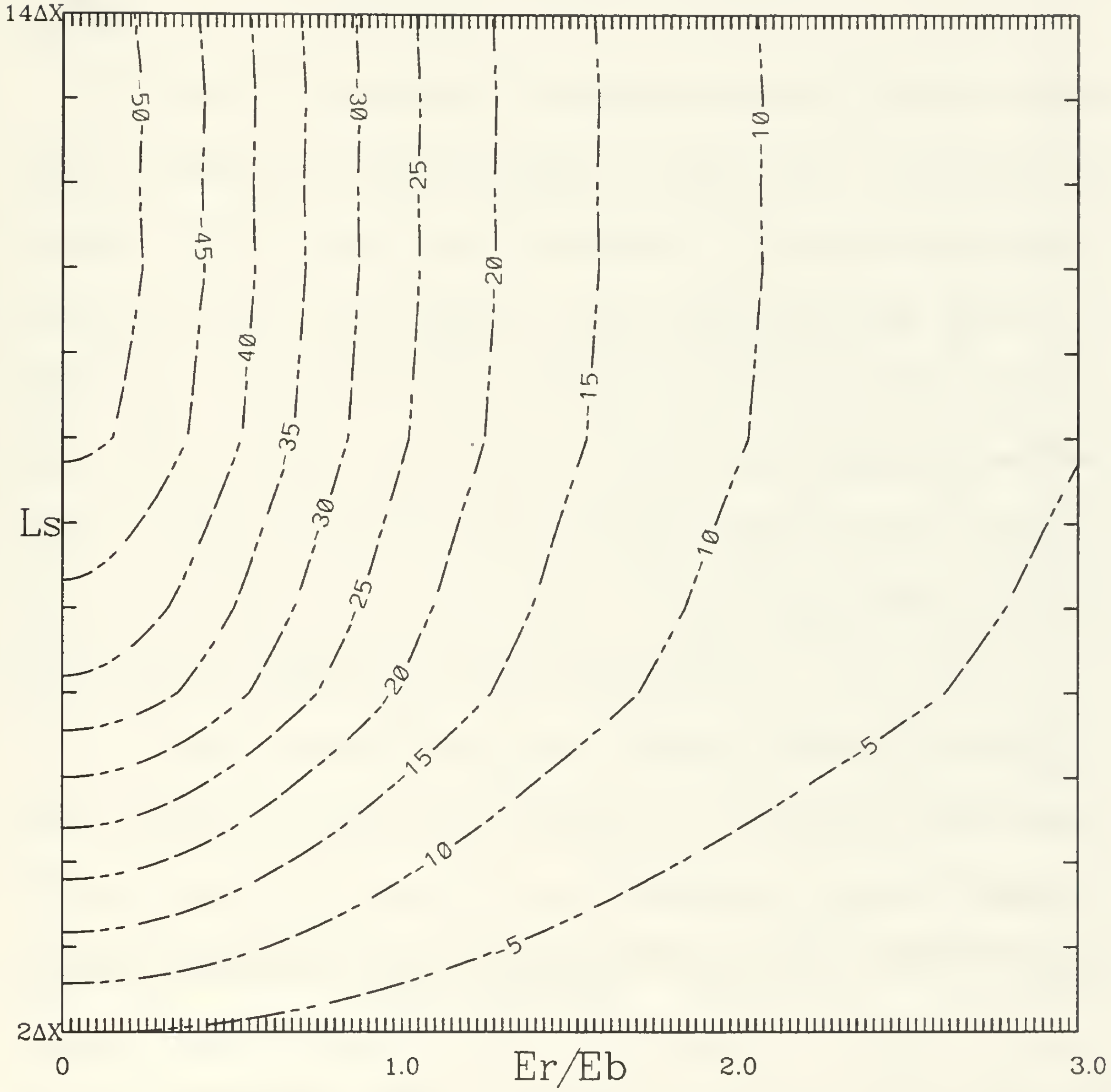

Figure 3.27. As in Fig. 3.13, except for variation of the wind/height observation sensitivity as a function $\varepsilon_r/\varepsilon_b$ (abscissa) and L_s (ordinate). For this case, $L_b = 6.0\Delta x$ while L_s varies between 2.0Δx and 14.0Δx and $\varepsilon_r/\varepsilon_b$ ranges from 0.0 to 3.0.

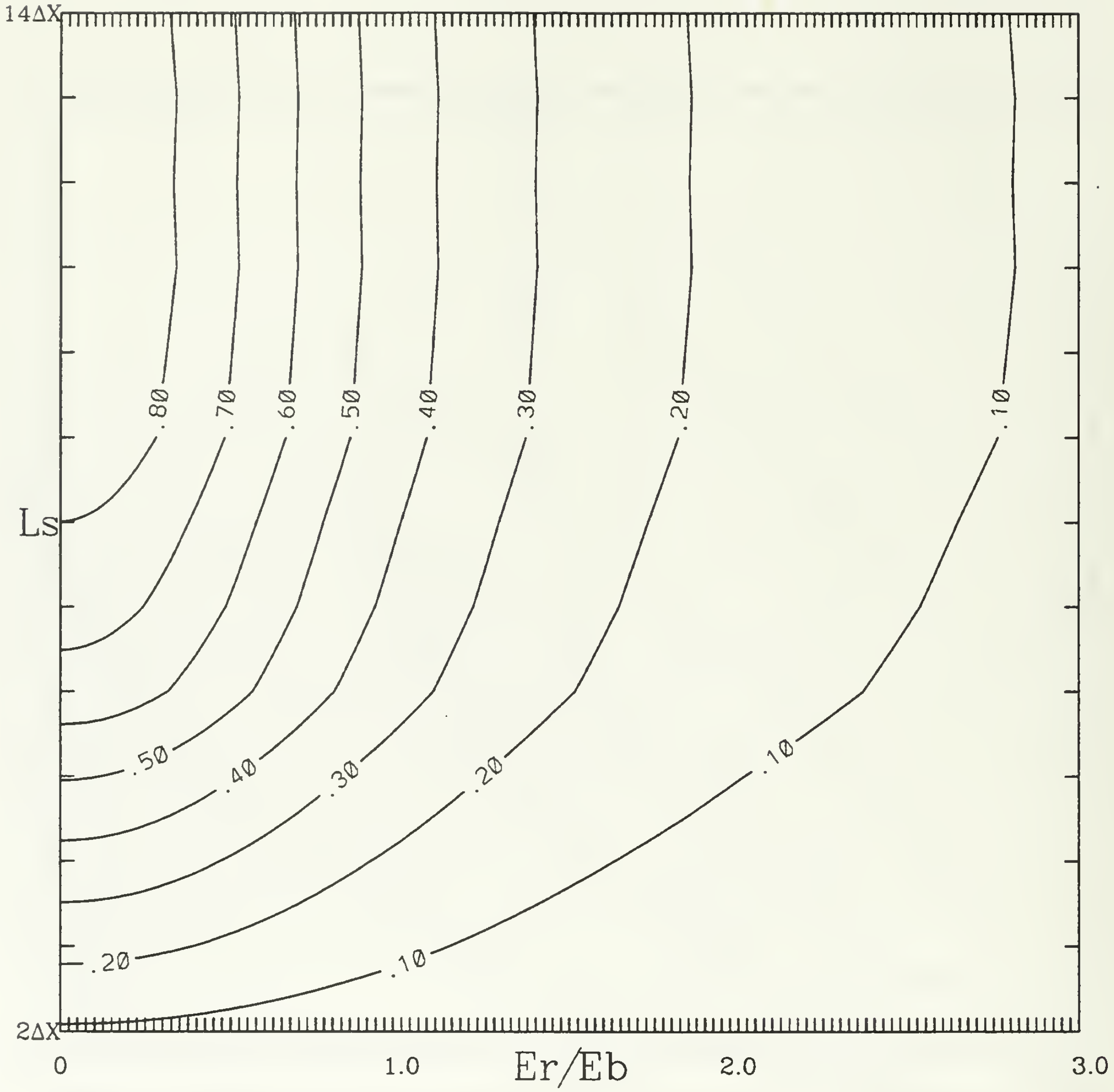

Figure 3.28. As in Fig. 3.8, except for variation of the height/wind observation sensitivity as a function $\varepsilon_r/\varepsilon_b$ (abscissa) and L_s (ordinate). For this case, $L_b = 6.0\Delta x$ while L_s varies between 2.0Δx and 14.0Δx and $\varepsilon_r/\varepsilon_b$ ranges from 0.0 to 3.0.

The simplifying assumptions of a single observation variable and a single analysis sensitivity gradient were applied so that the multivariate contributions due to the geostrophic coupling of the height and wind background error covariances could be isolated. The terms height/wind and wind/height observation sensitivity were introduced to refer to the contribution from these two terms to the total height and wind observation sensitivity.

The behavior of the height/wind and wind/height observation sensitivity is similar to the one-dimensional univariate examples of Chapter III.C. In both cases, the observation sensitivity is largest when the length scales of the analysis sensitivity gradient and background error correlation are similar, and the observations are accurate relative to the background. Super-sensitivity occurs when the observations are isolated or an abrupt discontinuity in the density of the observations occurs. Large height/wind observation sensitivity also occurs at the domain boundary of the well-sampled interior. This implies that large observation sensitivity may occur for limited domain problems when the analysis sensitivity gradient is non-zero along the boundary.

The Single Observation Sensitivity Map (SOSM) was introduced as a technique to identify locations in the domain where the sensitivity to a single observation is largest. The SOSM shows that maximum (minimum) height/wind and wind/height observation sensitivity occurs when the observation is placed 90° out of phase with the maximum (minimum) analysis sensitivity gradient. By comparison, the largest univariate observation sensitivity occurs at the maxima (minima) of the analysis sensitivity gradient. Consequently, the optimal location for an adaptive height observation may not be the optimal location for an adaptive wind observation.

The one-dimensional observation sensitivity results from Chapter III.C and Chapter III.D will be used to interpret the two-dimensional observation sensitivity investigated in Chapter III.E and Chapter III.F.

E. TWO-DIMENSIONAL UNIVARIATE EXAMPLES

The purpose of this section is to explore the behavior of the observation and background sensitivity for the two-dimensional univariate problem, and to determine the extent to which the one-dimensional univariate analytical and computational results of Chapter III.C apply to the two-dimensional problems. An example of a simple, idealized two-dimensional height analysis sensitivity gradient and a single height observation is considered first. The effects of multiple observations on the observation sensitivity are then evaluated. The analysis sensitivity gradient used for these examples differs from the one-dimensional analysis sensitivity gradients in one important respect. The one-dimensional analysis sensitivity gradients were defined to be a simple cosine wave, and the grid domain was defined such that the analysis sensitivity gradient summed gridpoint by gridpoint over the domain is zero. Many choices of J used for adjoint sensitivity research also yield sensitivities that sum to zero over the global domain (R. Langland, NRL– Monterey, personal communication). The analysis sensitivity gradient used in this section is composed of a combination of sine and exponential functions, and the *sum of the gridpoint values of* $\partial J/\partial \mathbf{x}_a$ *is non-zero over the domain.* In this respect, the analysis sensitivity gradient assumed for these experiments is representative of an analysis sensitivity gradient for a limited domain, or for certain cost functions such as precipitation (R. Langland, NRL–Monterey, personal communication). The differences between these two analysis sensitivity gradients leads to surprising results that will be shown in this section.

1. Display of the Observation Sensitivity Vector

Observation sensitivity is defined in observation space and is more difficult to display on a two-dimensional map than standard gridpoint fields, such as the analysis sensitivity vector. The example in Fig. 3.1 avoided this problem by placing an observation at every gridpoint, and assigning a very large observation error standard deviation to those observations over the ocean, which effectively removed the observations from the adjoint problem. While this is a useful trick for simple examples, such as the one illustrated in Fig. 3.1, practical considerations prohibit its use in real applications. The *analysis space projection of the observation sensitivity vector*, which is defined in (2.9), may be used to display observation sensitivity as a contoured field. This field is obtained by applying the adjoint of the forward observation operator to the observation sensitivity vector. The adjoint observation operator ($\mathbf{H}^T$) projects the observation sensitivity vector from observation space into analysis grid space, where it can be displayed as a contoured field. However, the analysis space projection does not provide an unambiguous interpretation of the observation sensitivity in that large values of the analysis space projection (at a gridpoint) cannot directly be related to any particular observation (i.e., more that one observation may contribute to the analysis space projection at a gridpoint). This ambiguity is avoided in this section by assuming that the observations are located at gridpoints.

2. Single Observation Experiments

The experiment design is as follows. The analysis sensitivity gradient (Fig. 3.29a) is composed of a combination of the large- and small-scale sensitivity patterns from Fig.

3.2 with L_s chosen so that only the large-scale patterns are super-sensitive to a *single observation* for an appropriate choice of L_b. This analysis sensitivity gradient is the same as used in Fig. 6 of Baker and Daley (2000). The background error correlation is modeled using the SOAR function for heights from (3.1) with $L_b = 3.60\Delta x$, which is slightly larger than the value of $L_b = 2.07\Delta x$ used in Baker and Daley (2000). However, a single observation placed near the maxima of the large-scale analysis sensitivity gradient will be super-sensitive for either choice of L_b. It will be shown later in this section that the observation sensitivity for multiple observations is maximized when $L_b = 3.60\Delta x$. The background error standard deviation is set to 1.0 and the observation error standard deviation is set to 0.1.

When a single height observation is placed at a gridpoint near the center of one of the positive analysis sensitivity gradient maxima, the analysis space projection of the observation sensitivity (Fig. 3.29b) appears as a very localized response around the gridpoint. In the corresponding background sensitivity vector in Fig. 3.29c, the background sensitivity equals the analysis sensitivity everywhere except at the observation location. The values for the analysis space projection of the observation sensitivity and background sensitivity at this single observation location are 4.45 and –3.84, respectively, which are much larger that the analysis sensitivity gradient value of 0.31 at the same gridpoint.

The background error correlation between the observation location and all other grid locations (i.e., the term $\mathbf{HP}_b$ in (2.8a)) is shown in Fig. 3.29e. Because only the

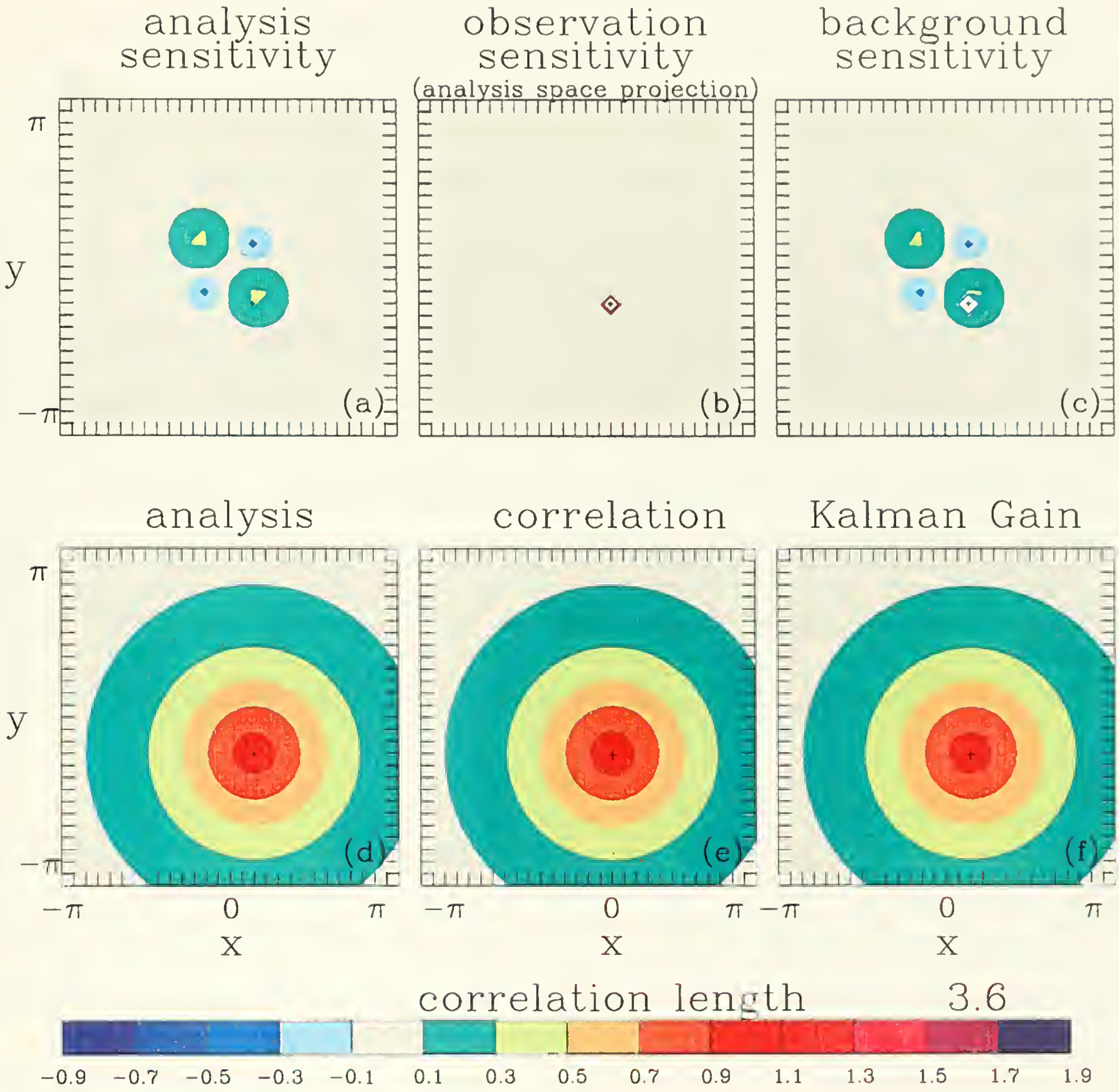

Figure 3.29. Two-dimensional univariate single height observation sensitivity example. (a) Specified analysis sensitivity gradient, (b) single height observation sensitivity, (c) background sensitivity, (d) corresponding analysis, assuming an innovation of 1.0 m for the single height observation at the "+", (e) background error correlation function for the observation at the "+", and (f) row of $\mathbf{K}^T$ for the observation at the "+". The color scale is at the bottom.

single observation exists, the row of the Kalman gain matrix (Fig. 3.29f) corresponding to that (single) observation is nearly identical to the correlation function (Fig. 3.29e). As explained in Chapter III.D, observation sensitivity can be visualized by mentally summing, gridpoint by gridpoint, the product of the row of $\mathbf{K}^T$ (Fig. 3.29f) with the analysis sensitivity gradient (Fig. 3.29a). This mental exercise will be used extensively in this section.

The adjoint sensitivity field can be compared to the (forward) analysis if the background field is assumed to be zero, and the observation is assumed to be one. The actual background and observations are not required for the observation adjoint sensitivity calculations. Under these assumptions, the analysis is given by

$$\mathbf{x}_a = \mathbf{K}\mathbf{y}. \tag{3.45}$$

The analysis "spreads" the information from the observation(s) to the surrounding gridpoints through the background error correlation or the Kalman gain matrix. For a single observation, the resulting analysis (Fig. 3.29d) has the same pattern as the correlation function (Fig. 3.29e) and the appropriate row of $\mathbf{K}^T$ (Fig. 3.29f), and illustrates how the information contained in the single observation is spread to the surrounding observations. In contrast, the adjoint process "gathers" the analysis sensitivity gradient information from the surrounding gridpoints to the observation location according to the background error correlation or Kalman gain matrix.

a. *The Effects of the Background Error Correlation Length Scale on the Observation Sensitivity*

This section examines how the observation sensitivity changes as the background error correlation length scale is varied from 0.25Δx to 25.25Δx. The maximum value of the observation sensitivity measure (Fig. 3.30) is obtained if the specified value of L_b is sufficiently large so that the correlation is essentially one between the observation location and every gridpoint contained within the positive regions of the analysis sensitivity gradient. For this example, the analysis sensitivity gradient at the observation location equals 0.31, and $\sum_{n=1}^{N}(\partial J/\partial \mathbf{x}_a)_n = 7.48$, so that the predicted observation sensitivity limit as $L_b \to \infty$ is 7.41 (from (3.24)) with a corresponding observation sensitivity measure (from (3.6)) of 24.54. The observation sensitivity measure in Fig. 3.30 equals 24.00 when $L_b = 25.25\Delta x$, with a corresponding observation sensitivity of 7.24. These values are in excellent agreement with the predicted limits.

This result may be compared to the single height observation case for the one-dimensional univariate domain (see Fig. 3.6). The observation sensitivity for the one-dimensional height example (cf., Fig. 3.6) is largest when the projection between the (transposed) Kalman gain matrix and the observation sensitivity vector is maximized, which occurs when $L_b = 3.06\Delta x$. As the correlation length increases beyond its maximum value, the contributions from the negative sub-structures of the analysis sensitivity gradient tend to decrease the overall observation sensitivity. In the limit as

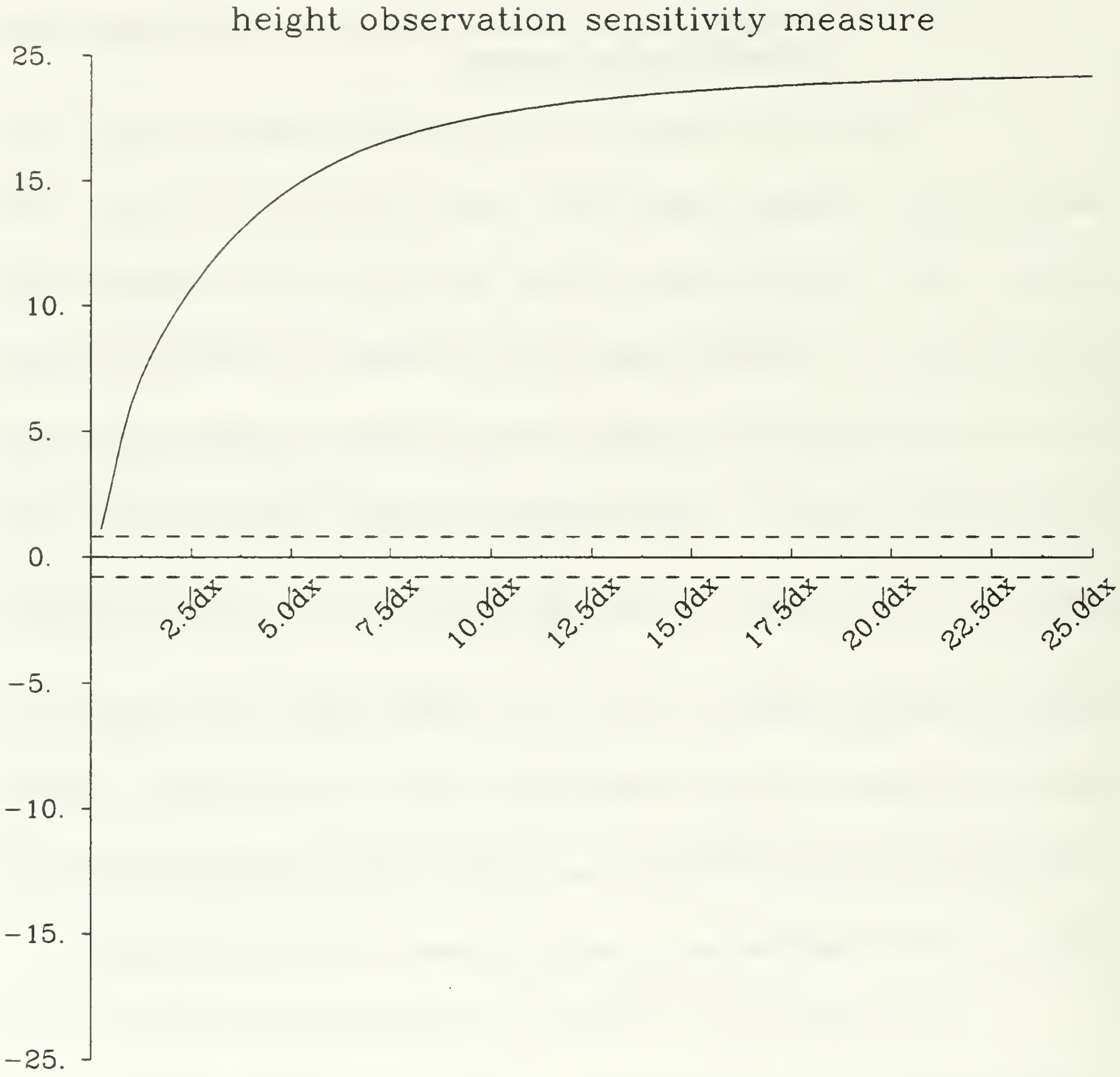

Figure 3.30. As in Fig. 3.6, except for variation of the observation sensitivity measure (ordinate) as a function of L_b from 0.25Δx to 25.0Δx (abscissa) for the single height observation in a two-dimensional field. The dashed lines at ±1.0 are the threshold values for observation super-sensitivity.

$L_b \rightarrow \infty$, the observation sensitivity tends to zero since the sum of the analysis sensitivity gradient was defined to be zero over the domain.

In comparison, the largest observation sensitivity for the two-dimensional univariate example (Fig. 3.29) occurs when both positive sub-structures of the analysis sensitivity gradient contribute maximally to the observation sensitivity vector. This occurs when L_b is sufficiently long so that the observation location is essentially fully correlated with all gridpoints contained within the positive regions of the analysis sensitivity gradient. Once this point is reached, any further increases to L_b cannot change the observation sensitivity. For the two-dimensional univariate height example (Fig. 3.30), the observation sensitivity continues to increase for the entire plotted range of L_b.

b. The Effects of Observation Error on the Observation Sensitivity

The variation of the observation sensitivity measure as a function L_b and the ratio of the observation error standard deviation (ε_r) to the background error standard deviation (ε_b) is plotted in Fig. 3.31. Since $\varepsilon_b = 1.0$ everywhere, ε_r effectively ranges from zero to $3.0\varepsilon_b$. Two effects dominate the observation sensitivity measure in Fig. 3.31. First, the observation sensitivity measure decreases as the observation error standard deviation increases, i.e., with poorer observations. Second, the observation sensitivity measure increases as the background error correlation length scale increases. Overall, these variations may be interpreted that the observation sensitivity is largest for an accurate observation and for long background error correlation length scales.

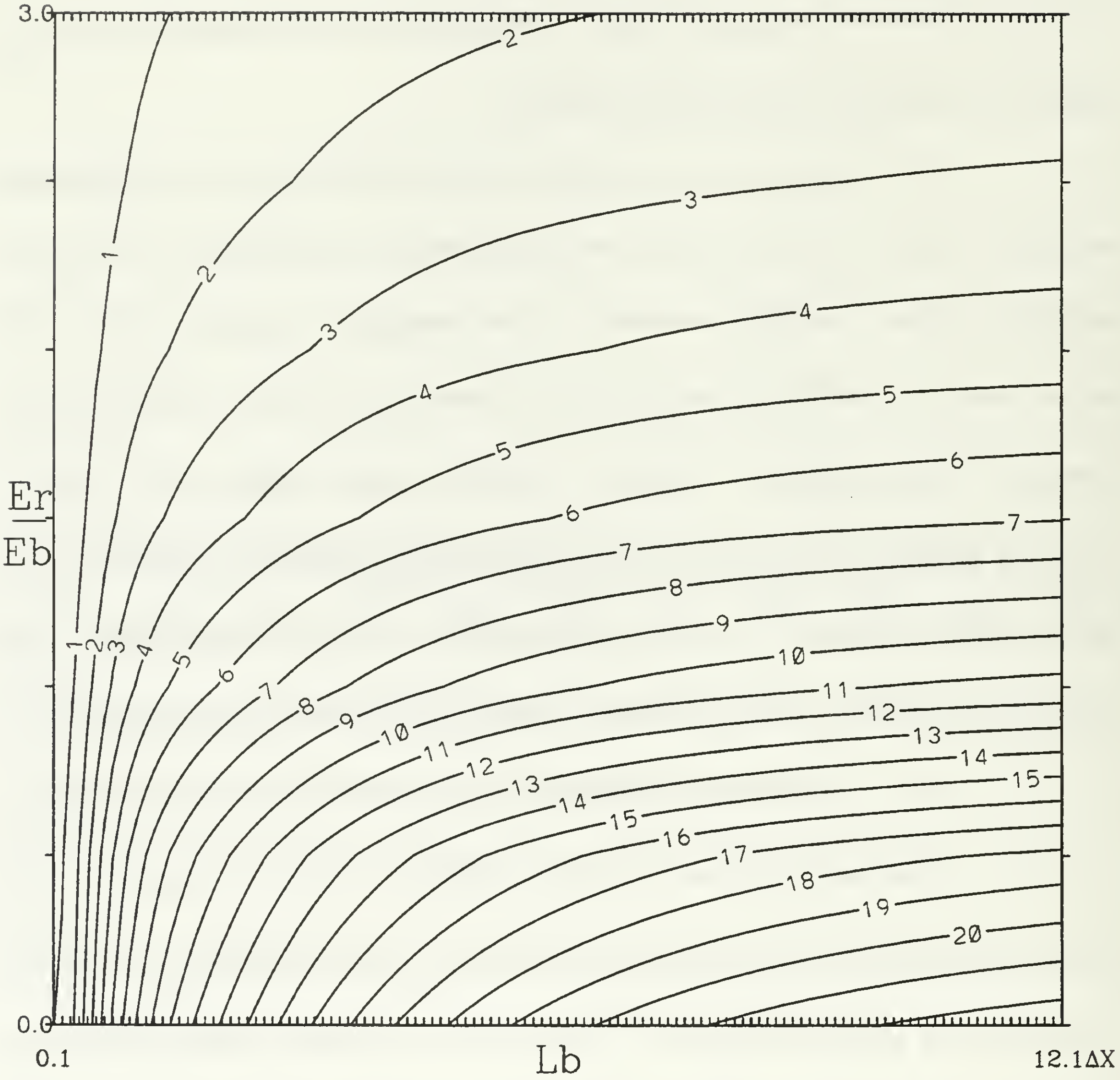

Figure 3.31. As in Fig. 3.7, except for variation of the observation sensitivity measure as a function of L_b (abscissa) and $\varepsilon_r/\varepsilon_b$ (ordinate) for the single height observation in a two-dimensional field. The background error correlation length scale L_b ranges from 0.1Δx to 12.1Δx, while $\varepsilon_r/\varepsilon_b$ varies from 0.0 to 3.0.

This result may be compared to the single height observation case for the one-dimensional univariate domain (see Fig. 3.7). The observation sensitivities in Fig. 3.31 and Fig. 3.7 decrease as the observation error standard deviation increases relative to the background error standard deviation. The primary difference between the two figures occurs because the one-dimensional analysis sensitivity gradient used to generate Fig. 3.7 sums to zero over the domain, whereas the two-dimensional analysis sensitivity gradient used to generate Fig. 3.31 does not sum to zero. Therefore, as discussed above, the asymptotic behavior of the observation sensitivity for long background error correlation lengths is different for the two examples.

The results from these two-dimensional single observation univariate experiments indicate that the general decrease in observation sensitivity with an increase in the ratio of the assumed observation error variances to the background error variances is consistent for all examples and can thus be considered a general observation sensitivity property. However, the behavior of the observation sensitivity as a function of correlation length (i.e., Figs. 3.7 and 3.30) cannot be as readily generalized to other cases. However, this is due to differences between the one- and two-dimensional analysis sensitivity gradients (as explained at the beginning of Chapter III.E) rather than a fundamental difference between one- and two-dimensional observation sensitivity. In both examples, the observation sensitivity increases as the background error correlation length scale increases. Large observation sensitivity occurs when the length scales of the background error correlation and the analysis sensitivity gradient are similar. The observation sensitivity behavior for large values of L_b depends upon the details of the imposed analysis sensitivity gradient. Specifically, if the sum of the analysis sensitivity gradient is zero over the domain, the observation sensitivity will tend to zero as $L_b \rightarrow \infty$.

Conversely, if the sum of the analysis sensitivity gradient over the domain is non-zero, then the observation sensitivity will tend to a non-zero constant value as $L_b \to \infty$.

3. Multiple Observation Experiments

a. The Effects of Observation Density on Observation Sensitivity

The purpose of this section is to determine how the presence of multiple observations changes the behavior of the observation sensitivity vector. The analysis sensitivity gradient is the same one used for the single observation example in Fig. 3.29. However, twenty observations are now placed at gridpoints in a "Z" shape across the centers of the analysis sensitivity gradient pattern (Fig. 3.32a). The background error standard deviation is set to 1.0 and the observation error standard deviation is set to 0.1 to prevent the matrix inversion $(\mathbf{HP}_b\mathbf{H}^T + \mathbf{R})^{-1}$ from becoming computationally singular for very long background correlation length scales.

The first step, experimentally, was to find the value of L_b between nearly 0Δx to 300Δx that maximized the analysis space projection of the observation sensitivity in Fig. 3.32b. The gridpoint (observation) with the maximum analysis space projection of the observation sensitivity for that value of L_b is indicated by the circled observation in Fig. 3.32b,e,f. The background error correlation length scale that maximizes the observation sensitivity is computed to be $L_b = 3.6\Delta x$.

Given the analysis sensitivity gradient in Fig. 3.32a, the resulting analysis space projection of the observation sensitivity vector and the background sensitivity

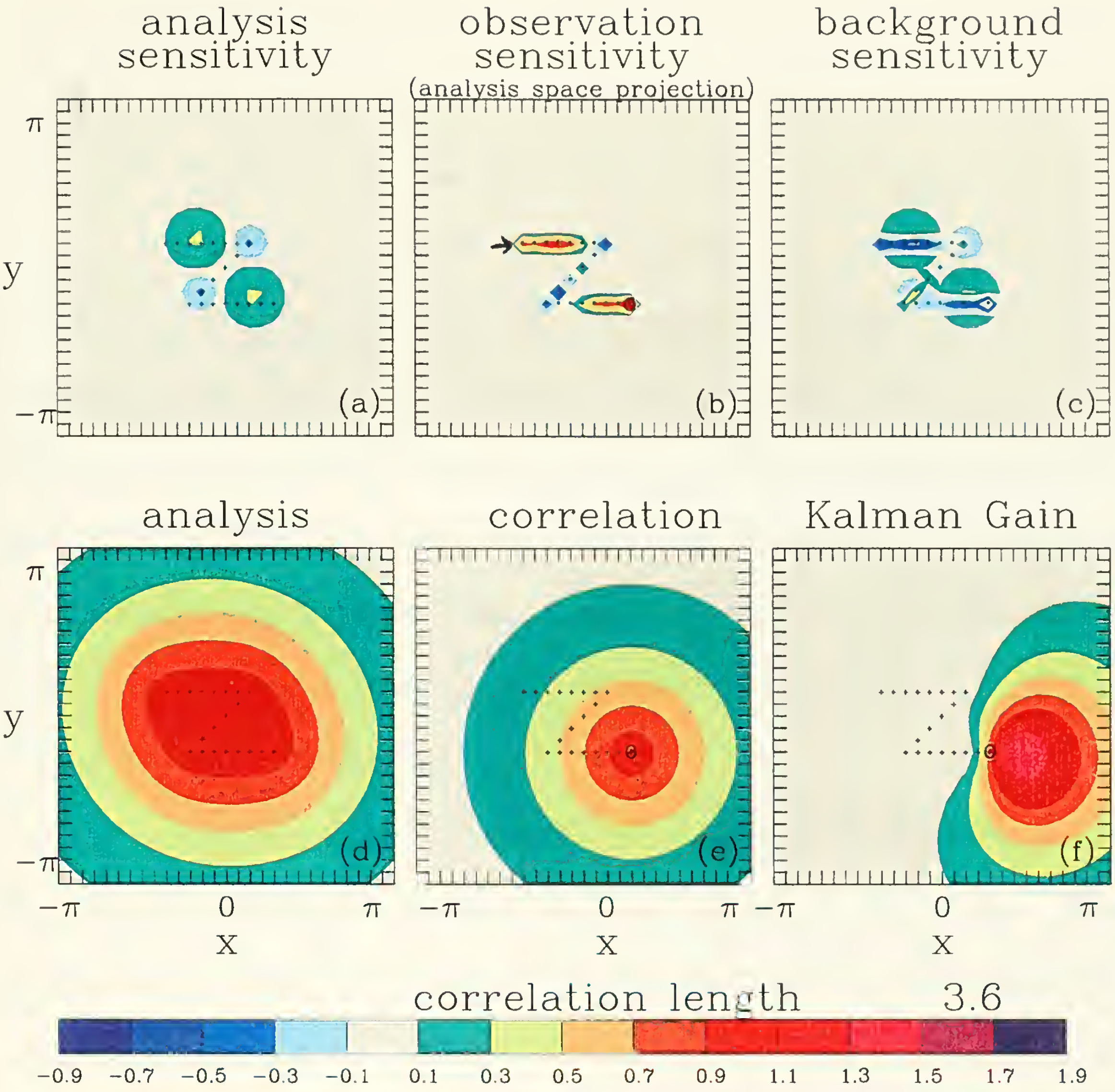

Figure 3.32. Two-dimensional univariate height observation sensitivity example for multiple observations. The largest sensitivity occurs for the height observation identified by the circle; the other height observations are given by the "+". In this plot, $L_b = 3.6\Delta x$, and $\varepsilon_r/\varepsilon_b = 0.1$. (a) The imposed analysis sensitivity gradient, (b) the analysis space projection of the observation sensitivity vector, (c) the background sensitivity, (d) the corresponding analysis, assuming an innovation of 1.0 m at each observation location, (e) the background error correlation function corresponding to the circled observation, and (f) the row of $\mathbf{K}^T$ for the circled observation. The color scale is at the bottom.

vector are displayed in Figs. 3.32b,c respectively. The largest observation sensitivity occurs for the circled observation at the lower right end of the "Z" in Fig. 3.32b. The effect of the observation density gradient is more pronounced when the density change occurs in a region of significant analysis sensitivity gradient amplitude (e.g., for the circled observation). When the observations extend all of the way across the analysis sensitivity gradient, the amplitude of the observation sensitivity is less (for example, for the observation indicated by the arrow). Thus, the largest observation sensitivity (Fig. 3.32b) does not necessarily occur where the analysis sensitivity gradient is a maximum, but where there is a large change in observation density and the analysis sensitivity gradient is both large scale and sufficiently large in magnitude. This result is analogous to the coastal example in Fig. 3.1.

Assuming that the background field is zero and the observations equal one, the resulting two-dimensional analysis from (3.45) is given in Figure 3.32d. The homogenous, isotropic nature of the correlation function relative to the circled location (Fig. 3.32e) is evident and only a hint of the "Z" configuration of the observations can be seen.

The dependence of the univariate observation sensitivity on the observation density can be understood by graphically examining the various terms in the observation sensitivity equation, e.g.,

$$\partial J/\partial \mathbf{y} = \mathbf{K}^T \partial J/\partial \mathbf{x}_a = (\mathbf{HP}_b\mathbf{H}^T + \mathbf{R})^{-1}\mathbf{HP}_b \partial J/\partial \mathbf{x}_a .$$

The term $\mathbf{HP}_b$ is the background error correlation between the observation locations and every gridpoint. The dimensions of this matrix are given by the number of observations

and the number of gridpoints. The row of this matrix corresponding to the circled observation is shown in Fig. 3.32e. It is symmetric in appearance and is essentially the same for every observation location (given the constraints of a finite domain). The inverse error covariance matrix $(\mathbf{HP}_b\mathbf{H}^T + \mathbf{R})^{-1}$ is in observation space and is not plotted. The term $\mathbf{HP}_b\mathbf{H}^T$ is the background error correlation between observation locations. Since the observation errors are assumed to be spatially uncorrelated, the matrix $\mathbf{R}$ is simply the diagonal matrix of the observation error variances ε_r^2. The row of the transpose of the Kalman gain matrix ($\mathbf{K}^T$) corresponding to the circled observation is plotted in Fig. 3.32f. The resulting pattern is not symmetric, but has large values adjacent to the circled observation.

Plots of the appropriate row of $\mathbf{K}^T$ for all of the 20 observations are shown in Fig. 3.33. The most striking features are the very large lobes (in both size and magnitude) that occur for observations that are relatively isolated from their neighbors. Observations that are located near the center of the pattern have much smaller maxima and minima of the Kalman gain (in both size and magnitude). These variations in $\mathbf{K}^T$ are due to the matrix $(\mathbf{HP}_b\mathbf{H}^T + \mathbf{R})^{-1}$. Observations that are farther from the other observations are less correlated with them and this leads to the large asymmetry in the Kalman gain. For the forward analysis problem, this implies that isolated observations contain more independent information than observations with close neighbors and are

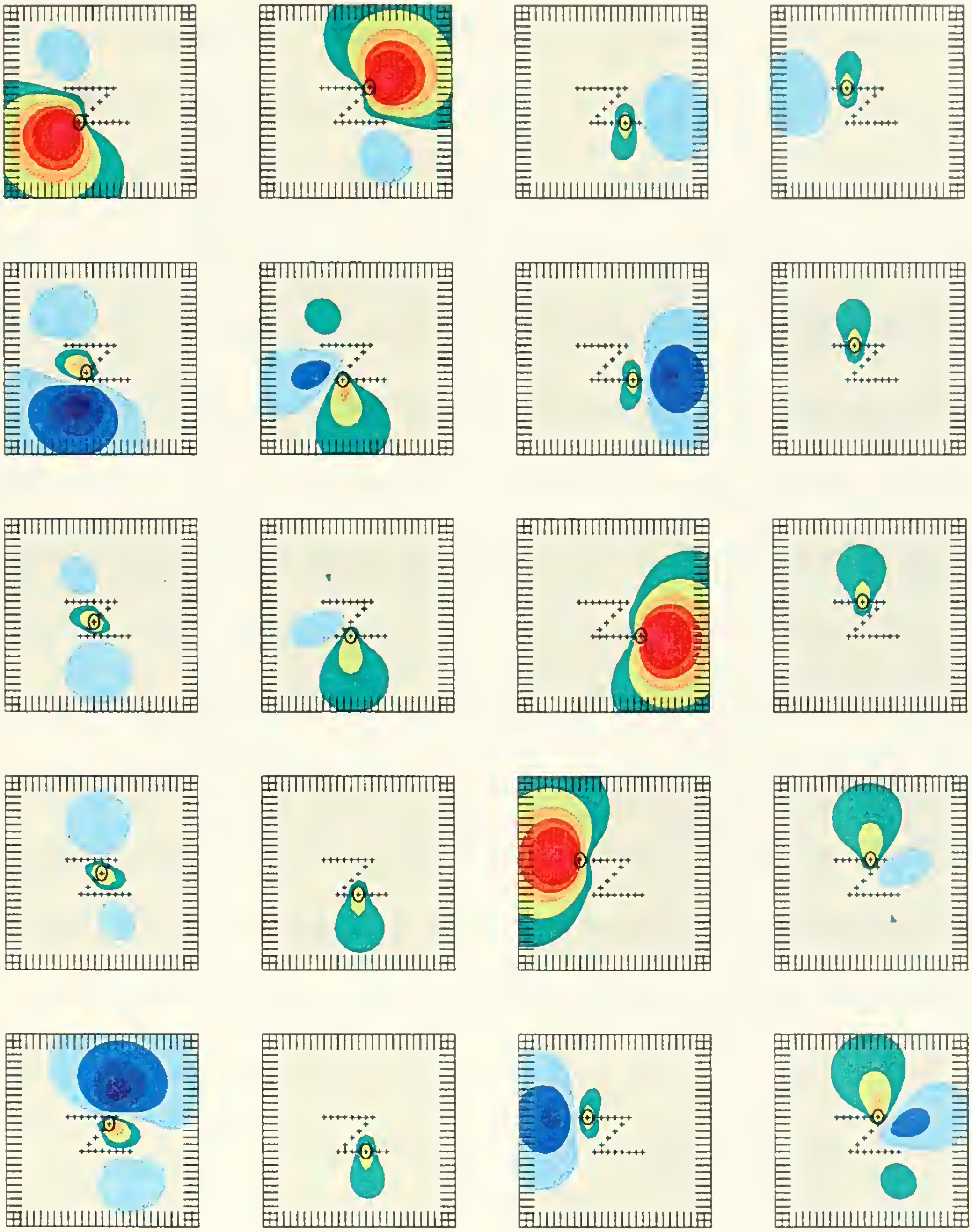

Figure 3.33. Plots of the row of $\mathbf{K}^T$ for the 20 observations shown in Fig. 3.32. The row of $\mathbf{K}^T$ corresponds to the circled observation in each panel. The grid domain and color scale corresponds to Fig. 3.32.

thus given greater weight in the analysis. In the adjoint sense, this indicates that isolated observations have larger "adjoint weights" ($\mathbf{K}^T$) and potentially greater observation sensitivity.

The resulting observation sensitivity vector (2.8a) is the result of the matrix-vector multiplication between $\mathbf{K}^T$ and $\partial J/\partial \mathbf{x}_a$. As explained earlier, this can be visualized for any given observation by mentally summing, gridpoint by gridpoint over the domain, the product of $\partial J/\partial \mathbf{x}_a$ (Fig. 3.32a) and the row of the $\mathbf{K}^T$ corresponding to that observation (Fig. 3.32e or Fig. 3.33). This exercise can be used to explain the larger observation sensitivity value for the observation at the lower-right end of the "Z" (indicated by the circle) when compared to the observation at the upper-left end of the "Z" (indicated by an arrow). The magnitude and shape of the row of $\mathbf{K}^T$ is the same for both observations. However, the circled observation is located in a region with larger values of the analysis sensitivity gradient, so that the non-zero portions of $\mathbf{K}^T$ overlap larger values of the analysis sensitivity gradient. Hence, the circled observation has the larger observation sensitivity.

It is evident that the sensitivity for a given observation depends upon the overlap between the amplitude and spatial extent (length scale) of the appropriate row of $\mathbf{K}^T$, and the amplitude and spatial extent (length scale) of the analysis sensitivity gradient $\partial J/\partial \mathbf{x}_a$. The observation sensitivity is maximized when the maxima or minima of the analysis sensitivity gradient coincide with the maxima or minima of the row of $\mathbf{K}^T$ such that the overall observation sensitivity contributions from the projection of $\mathbf{K}^T$ onto $\partial J/\partial \mathbf{x}_a$ are of the same sign.

The Kalman gain or weight matrix is arguably the most important term for both the linear analysis and observation adjoint sensitivity problems. The properties (amplitude, sign, and length scale) of this matrix are a function of several factors, with the background error correlation length scale being the dominant factor. The scale of $\mathbf{K}^T$ decreases as L_b decreases, and the influence of the analysis sensitivity gradient in the immediate vicinity of the observation becomes more marked (with correspondingly less influence from the adjacent sub-structures of the analysis sensitivity gradient). In addition, neighboring observations will not contribute to the observation sensitivity at a particular location if the correlation length scale is too small. If L_b is too long, then the maximum amplitude of $\mathbf{K}^T$ may not coincide with either the observations or analysis sensitivity gradient extrema (particularly for the more isolated observations).

Similar examples for longer ($L_b = 10.7\Delta x$) and shorter ($L_b = 1.0\Delta x$) background error correlation length scales are shown in Figs. 3.34 and 3.35, respectively, and are in the same format as Fig. 3.32. Although the spatial scale of the row of $\mathbf{K}^T$ is larger (smaller) for longer (shorter) L_b, the amplitude of the row of $\mathbf{K}^T$ for the circled observation is smaller (larger), as shown in Fig. 3.34f (Fig. 3.35f). However, the larger spatial scale of $\mathbf{K}^T$ for $L_b = 10.7\Delta x$ does not give the best overlap between the row of $\mathbf{K}^T$ and the analysis sensitivity gradient, which occurs for $L_b = 3.6\Delta x$ (Fig. 3.32f).

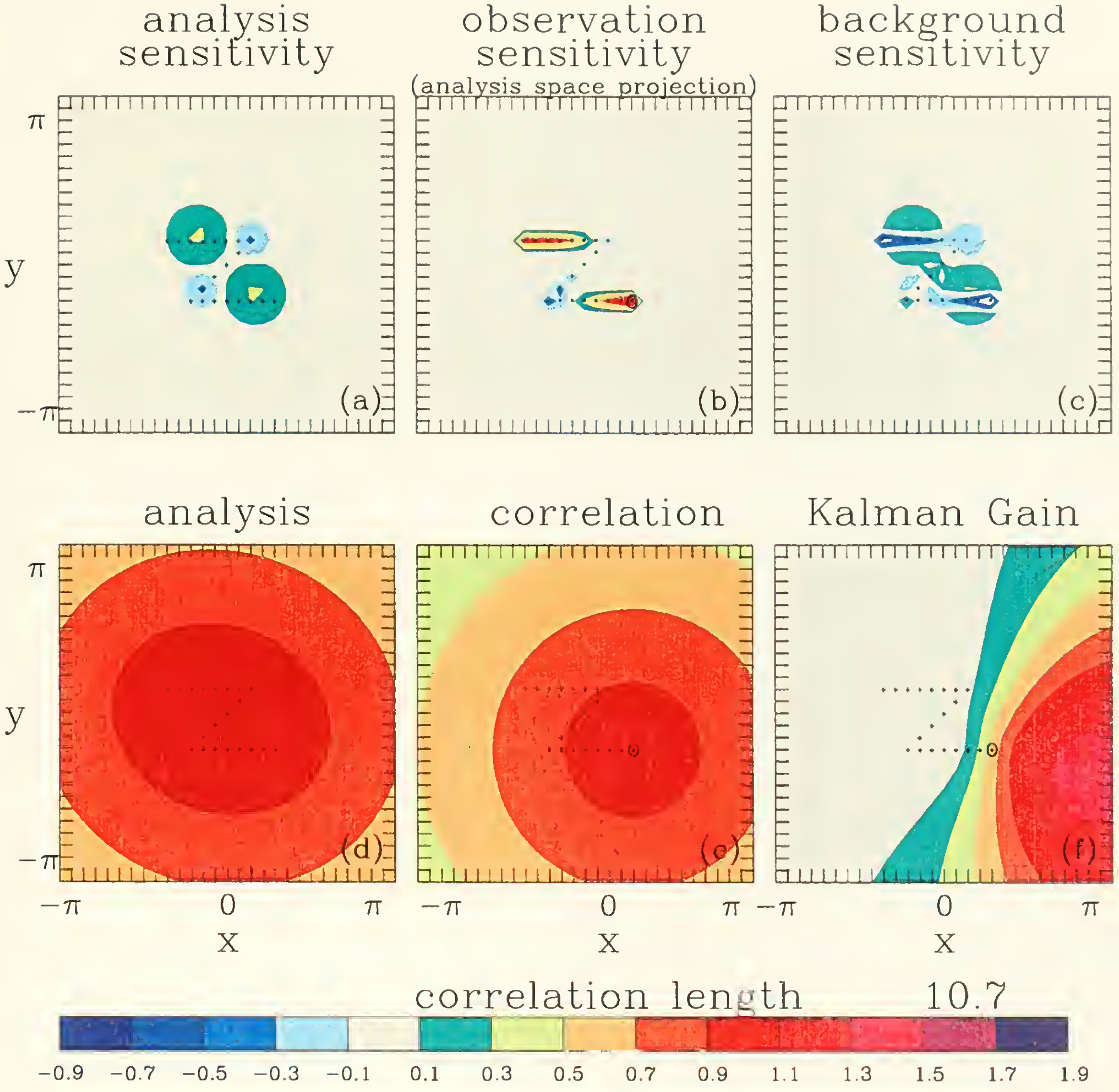

Figure 3.34. As in Fig. 3.32, except for two-dimensional univariate height observation sensitivity example for multiple observations, with $L_b = 10.7\Delta x$, and $\varepsilon_r/\varepsilon_b = 0.1$. (a) The imposed analysis sensitivity gradient, (b) the analysis space projection of the observation sensitivity vector, (c) the background sensitivity, (d) the corresponding analysis, assuming an innovation of 1.0 m at each observation location, (e) the background error correlation function corresponding to the circled observation, and (f) the row of $\mathbf{K}^T$ for the circled observation. The color scale is at the bottom.

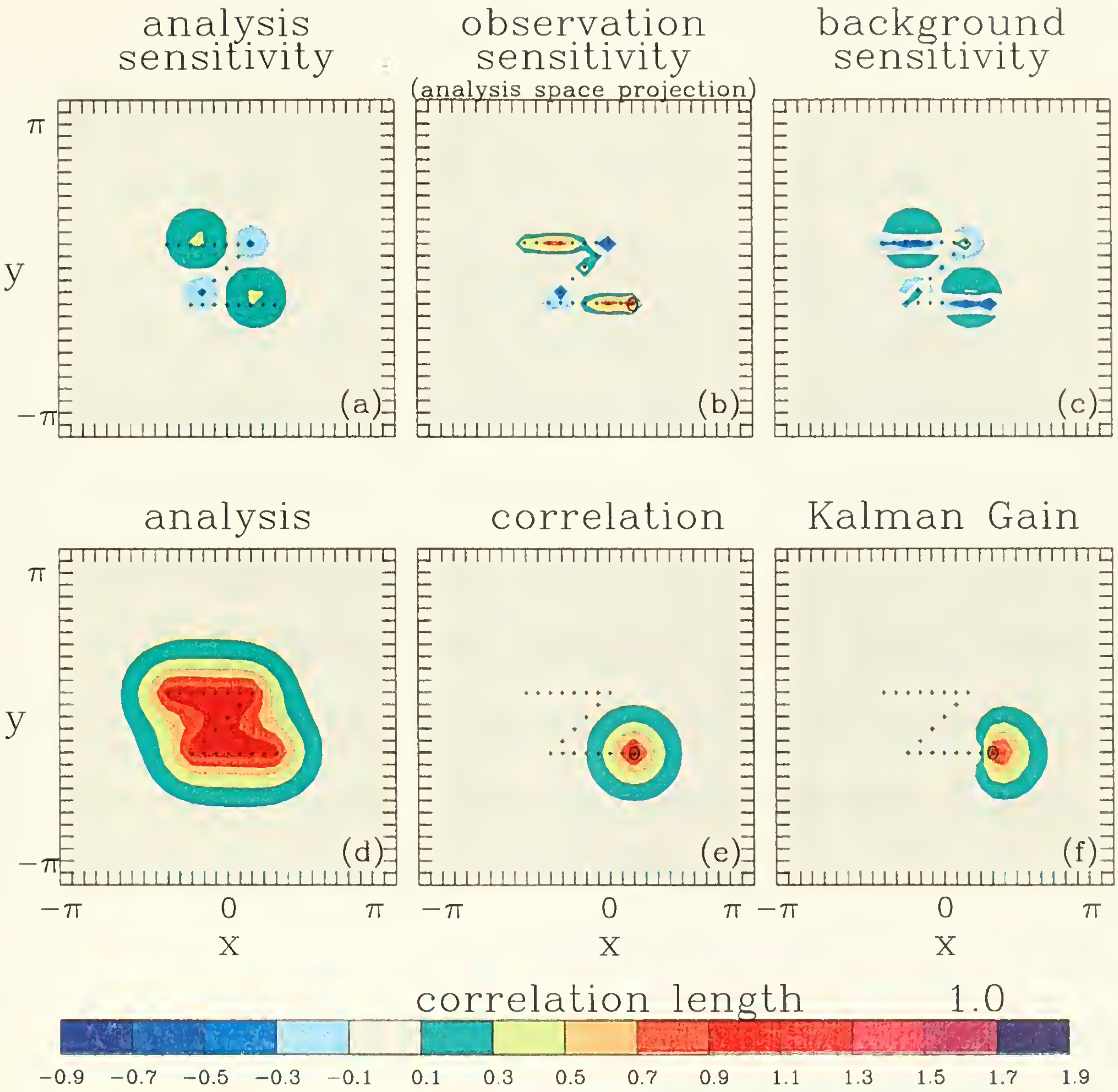

Figure 3.35. Two-dimensional univariate height observation sensitivity example for multiple observations, as in Fig. 3.34, except with $L_b = 1.0\Delta x$, and $\varepsilon_r/\varepsilon_b = 0.1$. (a) The imposed analysis sensitivity gradient, (b) the analysis space projection of the observation sensitivity vector, (c) the background sensitivity, (d) the corresponding analysis, assuming an innovation of 1.0 m at each observation location, (e) the background error correlation function corresponding to the circled observation, and (f) the row of $\mathbf{K}^T$ for the circled observation. The color scale is at the bottom.

The effect of the background error correlation length scale on the analysis is also quite marked. The limited horizontal spreading of the observation information into the adjacent region is evident for the short L_b (Figs. 3.34d) where the 0.9 contour level closely outlines the “Z” shape. By contrast, the 0.9 contour level in Fig. 3.34d is nearly circular when $L_b = 10.7\Delta x$, and the observation distribution is barely perceptible (as evidenced by the slight oval shape to the analysis field). The more optimum $L_b = 3.6\Delta x$ specification leads to an analysis distribution (Fig. 3.32d) that is intermediate between Fig. 3.34d and Fig. 3.35d.

The properties of $\mathbf{K}^T$ depend on two additional factors: the distance between the observations and the specific background error correlation model used. The observation sensitivity behavior is similar (not shown) when the Gaussian (versus the SOAR from (3.1)) background error correlation model given by

$$\rho_{vv}(r) = (1 - r/L_b)\exp(-r/L_b), \tag{3.46}$$

is used, although subtle differences occur. The distance between the observations is relative to L_b and determines, in a sense, how much independent information is contained in each observation. This issue was discussed using the one-dimensional univariate examples in Chapter III.C.

b. The Effects of the Background Error Correlation Length Scale on the Observation Sensitivity

As explained above, the circled location corresponds to the observation (from the set of 20 observations) with the largest sensitivity when $L_b = 3.6\Delta x$. The variation of the observation sensitivity measure for the circled location as a function of background correlation length scale (from nearly 0Δx to 300Δx) is shown in Fig. 3.36, which may be compared to the single observation example in Fig. 3.30. The resulting observation sensitivity behavior is similar for small L_b, when the observations tend to contribute more as individual, single observations. However, the behavior for larger L_b values is quite different when multiple observations are present. For a single observation (Fig. 3.30), the observation sensitivity measure rapidly increases to a maximum value near 25Δx and increases asymptotically as L_b continues to increase. For multiple observations, the observation sensitivity measure for the circled location peaks at 3.6Δx, and then decreases to a small, nonzero value for very large L_b. This behavior can be understood by referring back to Fig. 3.32 (with $L_b = 3.6\Delta x$), Fig. 3.34 (with $L_b = 10.7\Delta x$), and Fig. 3.35 (with $L_b = 1.0\Delta x$). When the background error correlation length is either longer or shorter than the value that maximizes the observation sensitivity at the circled location, the row of $\mathbf{K}^T$ is either small in spatial scale and magnitude (Fig. 3.35f) or sufficiently large in spatial scale (Fig. 3.34f) that the maximum amplitude does not coincide with large values of $\partial J/\partial \mathbf{x}_a$. In either alternative, the observation sensitivity is less than when $L_b = 3.6\Delta x$ (Fig. 3.32). Similar behavior (not shown) is observed for the other observations that are located near the large-scale analysis sensitivity gradient maxima. If an observation has nearby neighbors, maximum observation sensitivity occurs when the background error correlation length scale is relatively short and the observation does not interact with the other observations. When this occurs, the row of

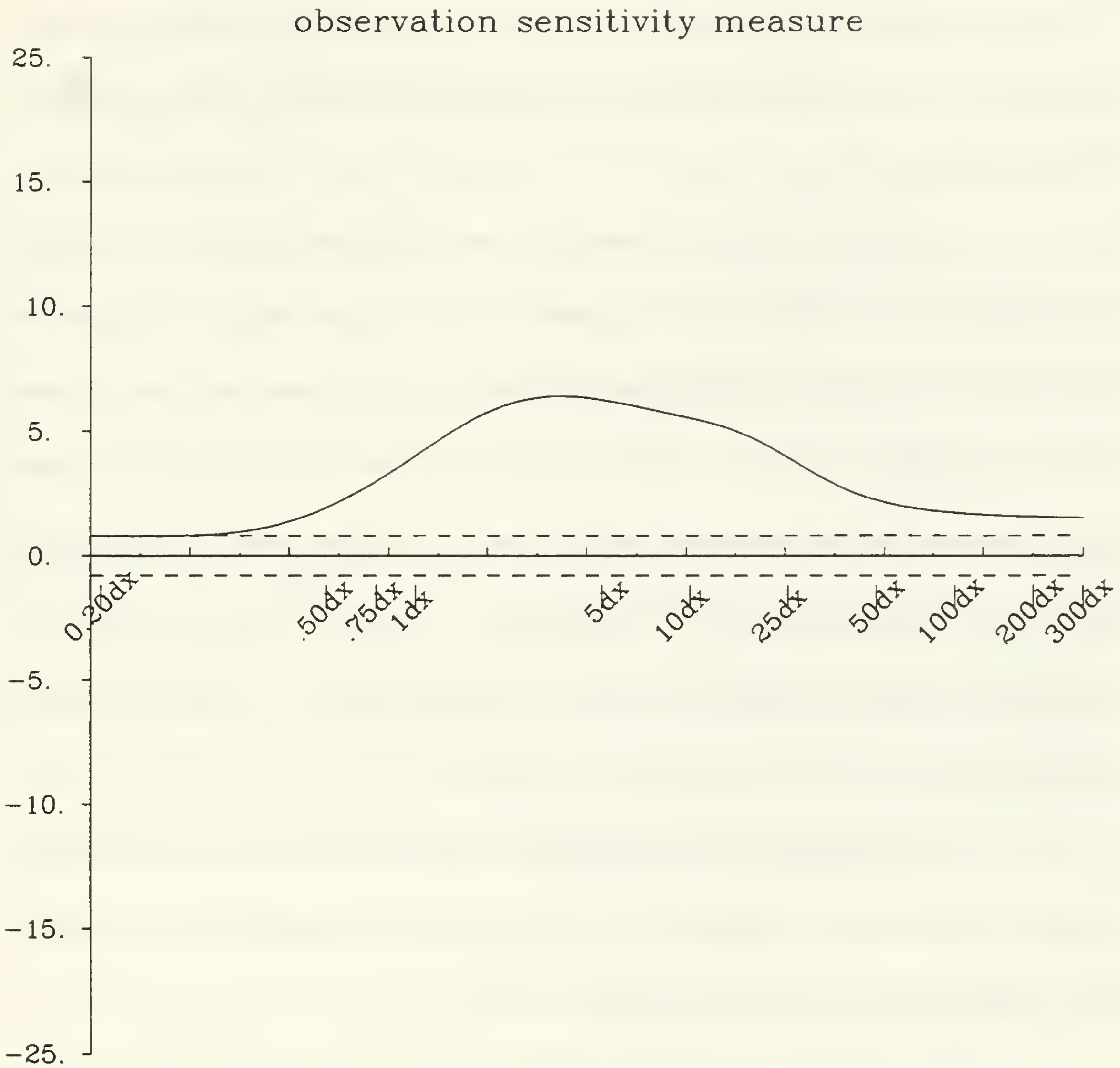

Figure 3.36: As in Fig. 3.30, except for variation of the observation sensitivity measure (ordinate) as a function of L_b from 0.1Δx to 300.0Δx (abscissa) for the circled observation as indicated by the circle in Fig. 3.32b. The dashed lines at ± 1.0 are the threshold values for observation super-sensitivity.

$\mathbf{K}^T$ corresponding to the observation is large (as in the corresponding weight given to the observation in the analysis), and the observation sensitivity is maximized. As L_b increases, the observation interacts more with the other observations and the row of

$\mathbf{K}^T$ (and the corresponding weight given to the observation in the analysis) decreases. The behavior was illustrated for the one-dimensional univariate example in Chapter III.C.6 (see Fig. 3.14).

Provided that the observation and background errors are spatially homogeneous, the arguments used to derive (3.24) may be used to infer that the observation sensitivity for multiple, imperfect observations will also be the same at each location in the limit as $L_b \rightarrow \infty$. However, the observation sensitivity measure changes from location to location because the analysis sensitivity gradient varies from gridpoint to gridpoint. The observation sensitivity measure limit for an infinite L_b for the circled observation in Fig. 3.32 from (3.24) equals 1.86, which is very close to the observation sensitivity measure of 1.90 for $L_b = 300.0\Delta x$ in Fig. 3.36.

The derivation of the observation sensitivity limit as $L_b \rightarrow 0$ for multiple, imperfect observations is straightforward if $\mathbf{H}$ involves the interpolation operator only, and the observations are located at gridpoints. In that case,

$$\partial J/\partial \mathbf{y} = \left(\mathbf{H}\mathbf{H}^T + \mathbf{R}\right)^{-1} \mathbf{H}\,\partial J/\partial \mathbf{x}_a = \left(\mathbf{I} + \mathbf{R}\right)^{-1} \mathbf{H}\,\partial J/\partial \mathbf{x}_a\,, \tag{3.47}$$

and the observation sensitivity is proportional to the analysis sensitivity gradient interpolated to the observation location, and inversely proportional to the observation error variances. For the example in Fig. 3.36, $\varepsilon_r = 0.1$, so that the OSM limit for small L_b will be nearly 1.0.

c. The Effects of Observation Error on Observation Sensitivity

The adjoint weight matrix $\mathbf{K}^T$ also depends on the assumed accuracies of the observations relative to the background. The effects of increasing the observation error standard deviation for all observations from 0.1 to 0.5 and 1.0 are displayed in Figs. 3.37 and 3.38, respectively, and may be compared to Fig. 3.32. The background error standard deviation in each case is spatially homogeneous and equal to 1.0, so that the ratios of $\varepsilon_r/\varepsilon_b$ are 0.1, 0.5 and 1.0 in Figs. 3.32, 3.37, and 3.38, respectively. The spatial extent and the magnitude of the rows of $\mathbf{K}^T$ corresponding to the circled observation (Figs. 3.32f, 3.37f, 3.38f) decrease as the relative observation error magnitude increases. Consequently, the observation sensitivity for that circled location decreases (Figs. 3.32b, 3.37b, 3.38b). The analyzed values near the observation location equal the observed value of 1.0 when the observations are nearly perfect (Fig. 3.32d), but decrease to slightly less than 1.0 near the more isolated observations when the observations and background are of equal assumed accuracy, and the influence of the background field (which equals zero everywhere) becomes stronger (Fig. 3.38d).

The variations of the observation sensitivity measure as a function of L_b (from 0.1Δx to 12.1Δx) and the ratio $\varepsilon_r/\varepsilon_b$ (from 0.1 to 3.0) are plotted in Fig. 3.39. The maximum value of observation sensitivity measure occurs when $L_b = 3.6\Delta x$ and $\varepsilon_r/\varepsilon_b = 0.1$. Two factors dominate the pattern in Fig. 3.39. First, the observation sensitivity decreases as the error ratio increases, which implies that relatively poor observations contribute less to the observation sensitivity. The rate of decrease in

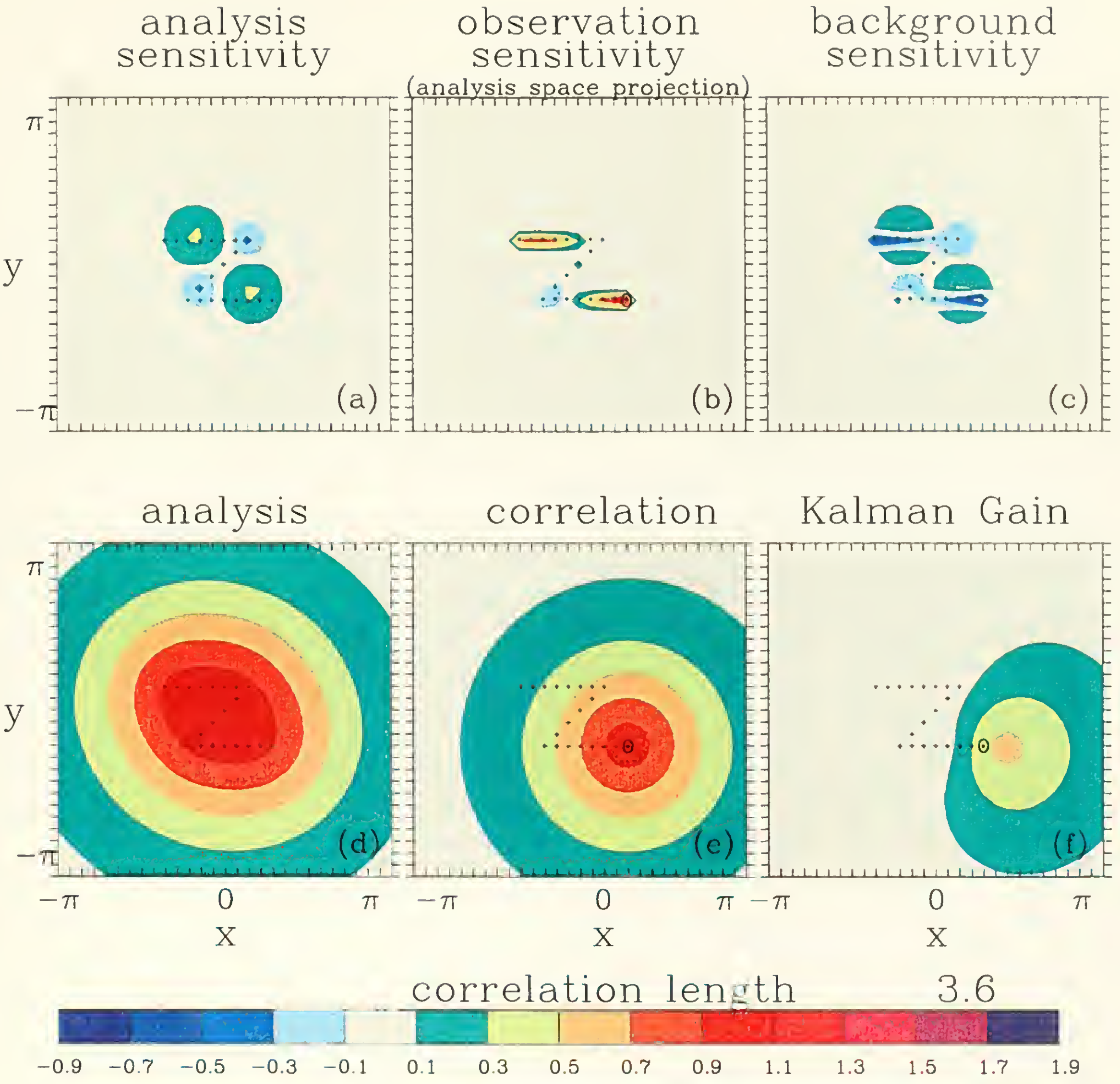

Figure 3.37. Two-dimensional univariate height observation sensitivity example for multiple observations, as in Fig. 3.32, except with $L_b = 3.6\Delta x$, and $\varepsilon_r/\varepsilon_b = 0.5$. (a) The imposed analysis sensitivity gradient, (b) the analysis space projection of the observation sensitivity vector, (c) the background sensitivity, (d) the corresponding analysis, assuming an innovation of 1.0 m at each observation location, (e) the background error correlation function corresponding to the circled observation, and (f) the row of $\mathbf{K}^T$ for the circles observation. The color scale is at the bottom.

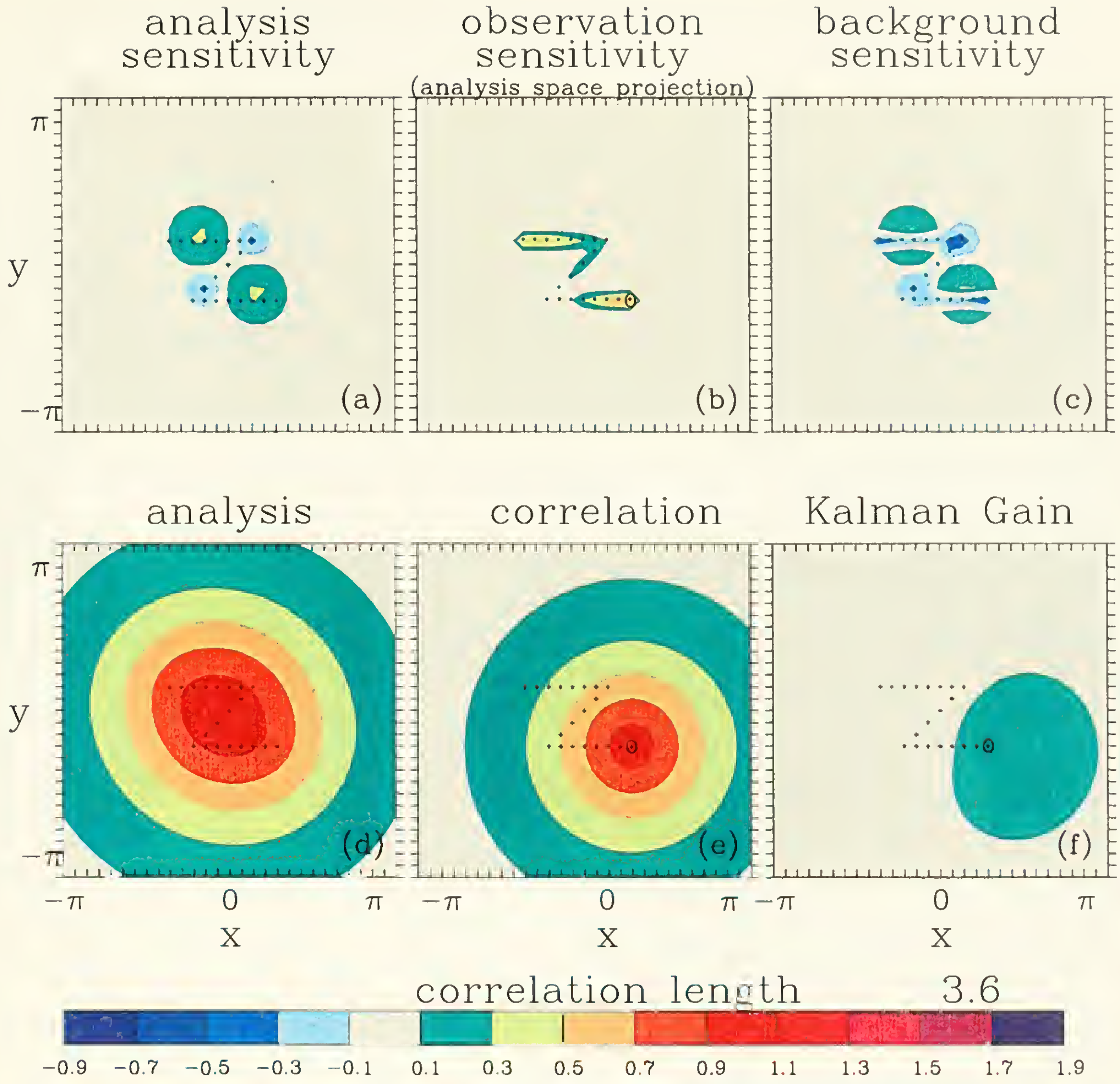

Figure 3.38. Two-dimensional univariate height observation sensitivity example for multiple observations as in Fig. 3.37, except with $L_b = 3.6\Delta x$, and $\varepsilon_r/\varepsilon_b = 1.0$. (a) The imposed analysis sensitivity gradient, (b) the analysis space projection of the observation sensitivity vector, (c) the background sensitivity, (d) the corresponding analysis, assuming an innovation of 1.0 m at each observation location, (e) the background error correlation function corresponding to the circled observation, and (f) the row of $\mathbf{K}^T$ for the circled observation. The color scale is at the bottom.

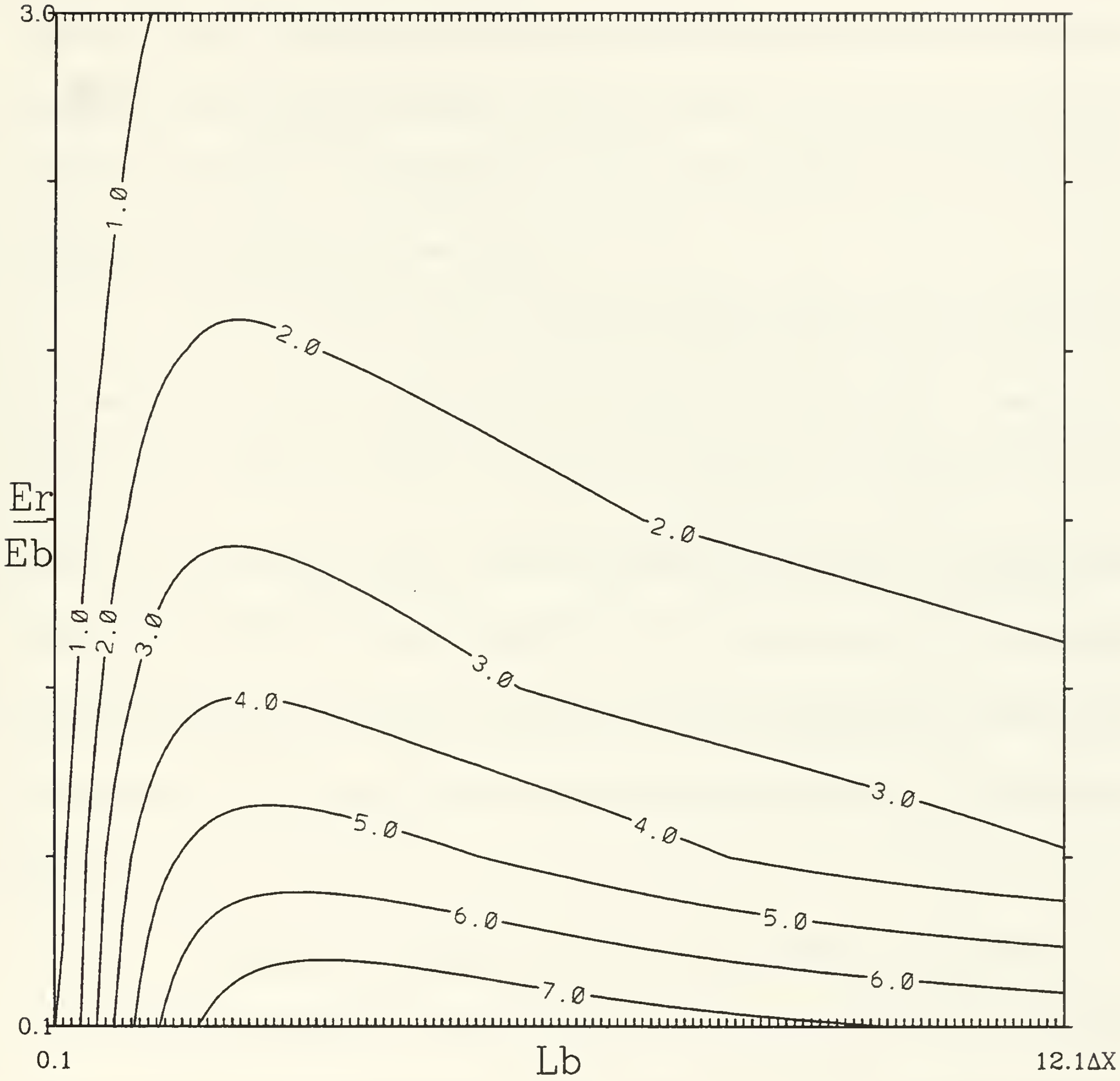

Figure 3.39. As in Fig. 3.26, except for variation of the observation sensitivity measure as a function of L_b (abscissa) and $\varepsilon_r/\varepsilon_b$ (ordinate) for the circled height observation in a two-dimensional field. The background error correlation length scale L_b ranges from 0.1Δx to 12.1Δx, while $\varepsilon_r/\varepsilon_b$ varies from 0.1 to 3.0.

observation sensitivity as the error ratio ($\varepsilon_r/\varepsilon_b$) increases is strongest when L_b is large. As the error ratio ($\varepsilon_r/\varepsilon_b$) increases, the value of L_b with the maximum observation sensitivity measure decreases. In the forward analysis problem, this is equivalent to

stating that "poor" observations have relatively little influence at any gridpoint unless the background error correlation lengths scales are very short. In the adjoint sense, this implies that relatively poor observations have little sensitivity except when the background correlation length scale is small.

These two effects occur because the amplitude and spatial extent of $\mathbf{K}^T$ decreases as the observation error increases (e.g., Fig. 3.29 vs. Fig. 3.38). One way to counteract the resulting decrease in $\partial J/\partial \mathbf{y}$ is to decrease L_b so that $\mathbf{K}^T$ no longer projects onto the adjacent analysis sensitivity gradient sub-structures of opposite sign (thereby decreasing the observation sensitivity). This effect does not occur for a single observation (e.g., Fig. 3.31 or Fig. 3.7) because $\mathbf{K}^T$ does not depend upon the ratio of the error variances ($\varepsilon_r^2/\varepsilon_b^2$). Instead, the observation sensitivity is scaled by $\varepsilon_b^2/\left(\varepsilon_b^2+\varepsilon_r^2\right)$ (see (3.16)).

4. Summary of Two-Dimensional Univariate Observation Sensitivity

The two-dimensional univariate observation sensitivity examples agree well with the one-dimensional univariate results, which implies that the one-dimensional results scale well to two dimensions and are consistent with the theory developed in Chapter III.C. Any differences that occur are readily explained through a careful examination of the matrix-vector multiplication of the (transposed) Kalman gain matrix and the analysis sensitivity gradient.

The two-dimensional univariate observation sensitivity is maximized when an observation is placed near the center of the analysis sensitivity gradient, and the observations are assumed to be accurate relative to the background. The observation sensitivity is also maximized when the length scales of the background error correlation and the analysis sensitivity gradient are similar. Super-sensitivity occurs when the observation density changes abruptly, and is most pronounced when the observation density change occurs where the analysis sensitivity gradient is large in both scale and magnitude.

The one-dimensional single observation univariate OSM (Fig. 3.6) reaches a maximum near the predicted value of $L_b = 3.0\Delta x$, and decreases for larger or smaller L_b. In contrast, the two-dimensional univariate OSM (Fig. 3.29) increases as L_b increases. These apparently misleading results suggest that the behavior of the observation sensitivity as a function of L_b is quite different for one- and two-dimensional analysis systems. However, this is not the case. According to (3.24), the observation sensitivity limit as $L_b \to \infty$ equals the sum of the gridpoint values of the analysis sensitivity gradient over the domain. For the one-dimensional example, the sum of the gridpoint values of the analysis sensitivity gradient is zero, and the observation sensitivity tends to zero as $L_b \to \infty$. For the two-dimensional example, the sum of the gridpoint values of the analysis sensitivity gradient is non-zero, and the observation sensitivity limit approaches the value of the sum as $L_b \to \infty$. Thus, the OSM behavior as a function of L_b depends strongly on the specified analysis sensitivity gradient. For many observation-targeting applications, the sum of the analysis sensitivity gradient over the domain is nearly zero, and the OSM tends to zero as behavior $L_b \to \infty$.

F. SIMPLE TWO-DIMENSIONAL MULTIVARIATE EXAMPLES

The purpose of this section is to examine observation sensitivity in the simple two-dimensional (horizontal) multivariate context. The multivariate relationship allows for interactions between geopotential height and the u and v wind components. This section expands upon the one-dimensional multivariate observation sensitivity examples in Chapter III.D, and the two-dimensional univariate observation sensitivity examples in Chapter III.E. These three sections provide the framework needed to understand the full three-dimensional observation sensitivity that will be discussed in Chapter IV.

1. The Height-Height, the Height-Wind, and the Wind-Wind Background Error Covariances

The wind-wind covariances and height-wind background error covariances were derived following sections 5.2 and 5.3 of Daley (1991), respectively. The derivations (not shown) use the special Second Order Autoregressive (SOAR) function (3.1) for the height-height background error correlation function.

The background geopotential height error variances are given by ε_h^2. The u- and v-wind background error variances are geostrophically related to ε_h^2, and are given by

$$\varepsilon_u^2 = \varepsilon_v^2 = \gamma^2 \varepsilon_h^2 / L_b^2 = g^2 \varepsilon_h^2 / f_0^2 L_b^2 . \tag{3.48}$$

The constant $\gamma = g/f_0$, where g is the gravitational constant and the f_o is the Coriolis parameter at 45 °N. The characteristic length scale L_b is used for both heights and winds.

The nine multivariate covariance functions in (2.10) may be written as

$$C_{hh} = \varepsilon_h^2 (1 + r/L_b) \exp(-r/L_b), \tag{3.49a}$$

$$C_{hu} = \left(\mu\gamma\varepsilon_h^2 r / L_b^2\right) \exp(-r/L_b) \sin\phi, \tag{3.49b}$$

$$C_{hv} = -\left(\mu\gamma\varepsilon_h^2 r/L_b^2\right)\exp(-r/L_b)\cos\phi, \tag{3.49c}$$

$$C_{uh} = -C_{hu} = -\left(\mu\gamma\varepsilon_h^2 r/L_b^2\right)\exp(-r/L_b)\sin\phi, \tag{3.49d}$$

$$C_{vh} = -C_{hv} = \left(\mu\gamma\varepsilon_h^2 r/L_b^2\right)\exp(-r/L_b)\cos\phi, \tag{3.49e}$$

$$C_{uv} = \frac{\gamma^2\varepsilon_h^2}{L_b^3}\left(1-2\nu^2\right)\exp(-r/L_b)\, r\cos\phi\sin\phi, \tag{3.49f}$$

$$C_{vu} = C_{uv} = \frac{\gamma^2\varepsilon_h^2}{L_b^3}\left(1-2\nu^2\right)\exp(-r/L_b)\, r\cos\phi\sin\phi, \tag{3.49g}$$

$$C_{uu} = \frac{\gamma^2\varepsilon_h^2}{L_b^2}\exp(-r/L_b)\left[\left(1-\nu^2 r/L_b\right)\cos^2\phi + \left(1 - r/L_b + \nu^2 r/L_b\right)\sin^2\phi\right], \tag{3.49h}$$

$$C_{vv} = \frac{\gamma^2\varepsilon_h^2}{L_b^2}\exp(-r/L_b)\left[\left(1-\nu^2 r/L_b\right)\sin^2\phi + \left(1 - r/L_b + \nu^2 r/L_b\right)\cos^2\phi\right], \tag{3.49i}$$

where ν^2 is a measure of the divergence. The flow is nondivergent when $\nu^2 = 0$, and irrotational when $\nu^2 = 1$. The geostrophic coupling parameter μ is positive in the Northern Hemisphere, negative in the Southern Hemisphere and zero at the Equator. Observational evidence suggests that μ varies between 0.75 and 0.95 in the Northern Hemisphere mid-latitudes (Lönnberg and Hollingsworth 1986).

The distance (r) between any two locations is given by (3.2). The angle between the x-axis and the line r is given by ϕ, and increases in a counter-clockwise sense from the positive x-axis.

2. Multivariate Single Observation Sensitivity Maps

The one-dimensional multivariate results from Chapter III.D.4.a showed that the maximum sensitivity to a single wind observation is 90° out of phase with the maximum height analysis sensitivity gradient field (which is defined to be a cosine wave). Likewise, the maximum sensitivity to a single height observation is phase-shifted by 90^0 with respect to the wind analysis sensitivity gradient. This phase shift occurs because the geopotential height and wind background errors are geostrophically related so that the geostrophic winds errors are proportional to the gradient of the geopotential height errors. These phase shifts were verified using analytical calculations (Chapter III.D.3). The single observation sensitivity map will be used in this section to determine whether a similar phase shift occurs for two-dimensional multivariate observation sensitivity.

The observation sensitivity vectors for the two-dimensional multivariate configuration are defined according to (2.16a) – (2.16c). The simplifying assumptions used for the one-dimensional multivariate problem (Chapter III.D.1.a) are applied here, namely only one observation type and one analysis sensitivity gradient variable are considered in each example. The relevant partial observation sensitivities are obtained from (2.16a) – (2.16c) and may be written as

$$\partial J/\partial \mathbf{h}_o \approx \mathbf{K}_{hh,h}^T \, \partial J/\partial \mathbf{h}_a \,, \tag{3.50a}$$

$$\partial J/\partial \mathbf{h}_o \approx \mathbf{K}_{hh,u}^T \, \partial J/\partial \mathbf{u}_a \,, \tag{3.50b}$$

$$\partial J/\partial \mathbf{h}_o \approx \mathbf{K}_{hh,v}^T \, \partial J/\partial \mathbf{v}_a \,, \tag{3.50c}$$

$$\partial J/\partial \mathbf{u}_o \approx \mathbf{K}_{uh,h}^T \, \partial J/\partial \mathbf{h}_a \,, \tag{3.50d}$$

$$\partial J/\partial \mathbf{u}_o \approx \mathbf{K}_{uu,u}^T \, \partial J/\partial \mathbf{u}_a \,, \tag{3.50e}$$

$$\partial J/\partial \mathbf{u}_o \approx \mathbf{K}_{uu,v}^T \, \partial J/\partial \mathbf{v}_a \,, \tag{3.50f}$$

$$\partial J/\partial \mathbf{v}_o \approx \mathbf{K}_{vv,h}^T \, \partial J/\partial \mathbf{h}_a \,, \tag{3.50g}$$

$$\partial J/\partial \mathbf{v}_o \approx \mathbf{K}^T_{vv,u}\,\partial J/\partial \mathbf{u}_a\,, \tag{3.50h}$$

$$\partial J/\partial \mathbf{v}_o \approx \mathbf{K}^T_{vv,v}\,\partial J/\partial \mathbf{v}_a\,, \tag{3.50i}$$

The subscripts on the matrix $\mathbf{K}^T$ follow the convention defined in (2.17) and $\mathbf{K}^T$ is defined by (2.6). The nomenclature introduced in Chapter III.D.1.a is used; for example, (3.50b) gives the partial sensitivity to the height observations given the u-wind analysis sensitivity gradient, and is referred to as the height/wind observation sensitivity.

The idealized analysis sensitivity gradient pattern and the grid domain from the experiments in Chapter III.E are used for the heights and winds (Fig. 3.40). The geostrophic coupling parameter μ is set to 1.0, which is equivalent to fully coupled Northern Hemisphere flow. Since the observational study by Hollingsworth and Lönnberg (1986) found that the wind divergence factor ν^2 ranges between 0.1 and 0.2 for background error covariances generated from a forecast background, ν^2 will be set to 0.15. The error variances for the background and the single, probe observation are both assumed to equal 1.0.

The background error correlation length scale L_b equals 2.07Δx, which is the value used in Baker and Daley (2000), and is used here solely for graphical reasons. If $L_b = 3.6\Delta x$ (which corresponds to the maximum univariate height observation sensitivity), the maximum sensitivity to a single height observation exceeds the range plotted for the other figures in this section. Otherwise, the results are qualitatively similar.

A single observation sensitivity map, similar to that in Chapter III.D.4.a, is used here. A probe observation is placed sequentially at each grid point and the observation

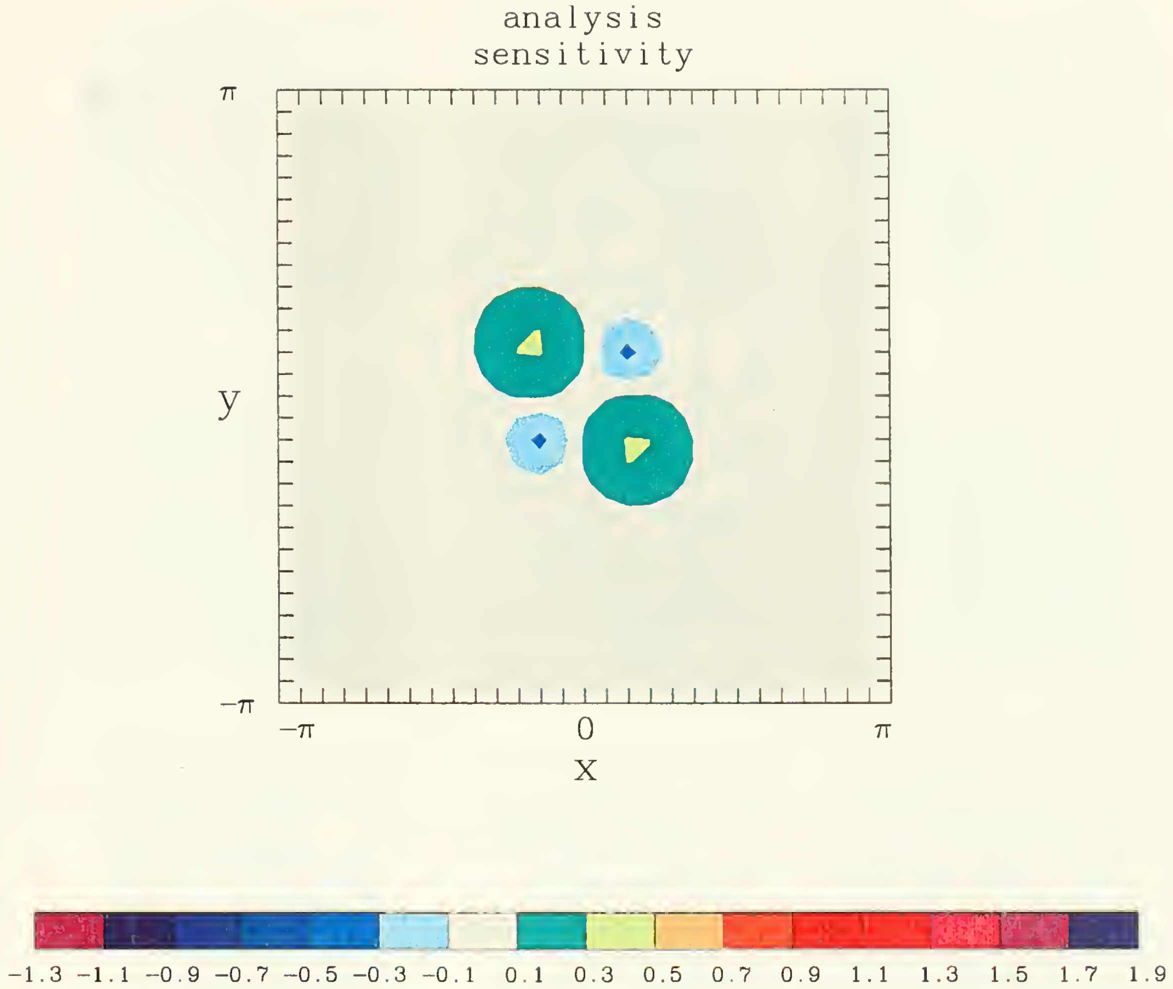

Figure 3.40. The imposed idealized analysis sensitivity gradient for height, u- and v-wind, as in Fig. 3.29. The color scale is at the bottom.

sensitivity is calculated from (3.50a-i). In this way, a map of the sensitivity to a single observation is generated. The single observation sensitivity maps for the nine cases corresponding to the three observation types (h, u, and v) and the three analysis sensitivity gradients (h, u, and v) are shown in Fig. 3.41. In Fig. 3.41a, which is identical to Fig. 6e from Baker and Daley (2000), the maximum sensitivity of J to a single height observation, given the height analysis sensitivity gradient in Fig. 3.40, occurs where the analysis sensitivity gradient is a maximum. The single height/u-wind and height/v-wind

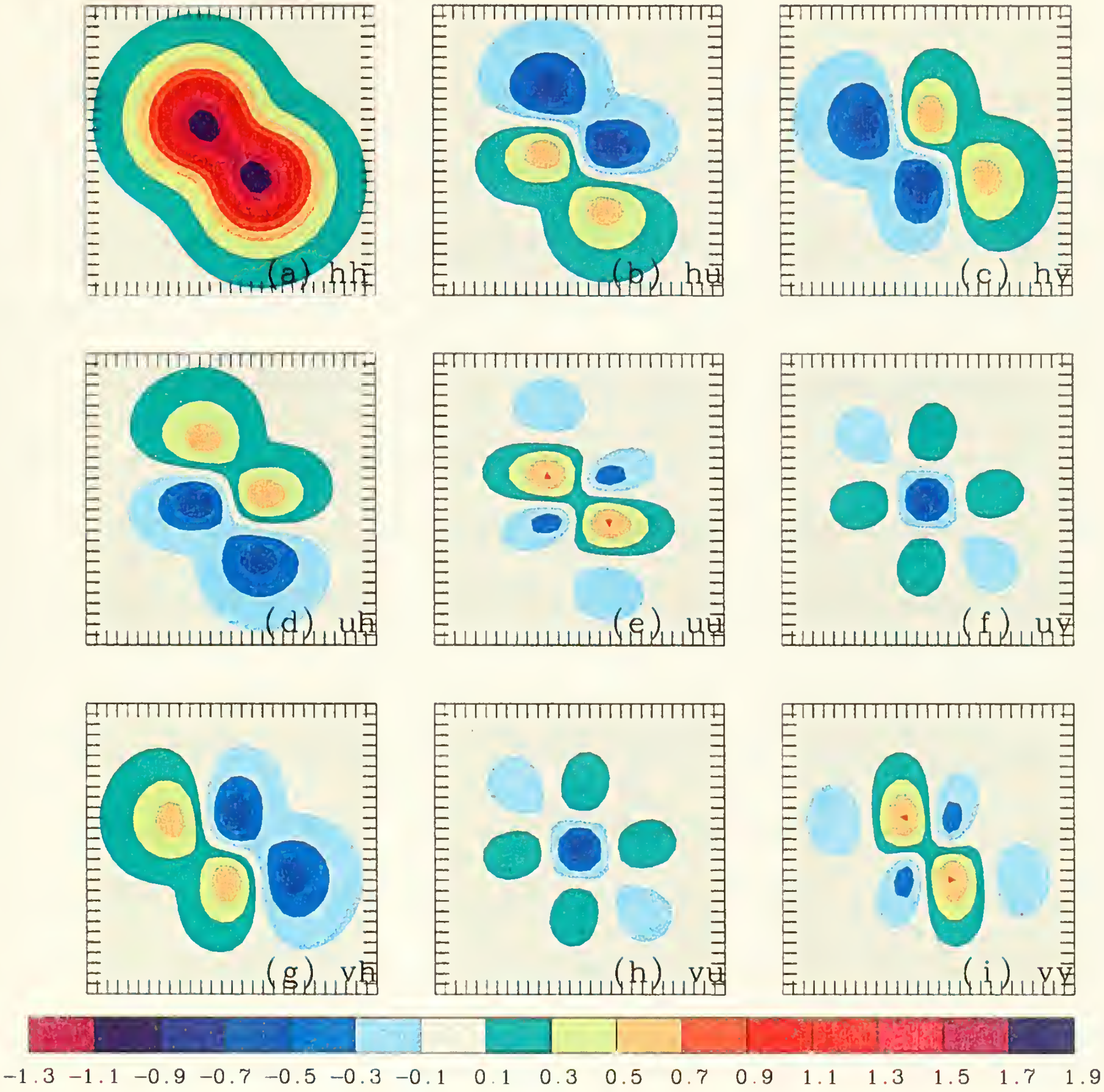

Figure 3.41. Single observation sensitivity maps for the partial observation sensitivities in (3.50a-i). (a) Univariate height, (b) height/u-wind, (c) height/v-wind, (d) u-wind/height, (e) univariate u-wind, (f) u-wind/v-wind, (g) v-wind/height, (h) v-wind/u-wind, and (i) univariate v-wind observation sensitivities. See text for explanation of the nomenclature.

observation sensitivity maps corresponding to the analysis sensitivity gradient in Fig. 3.40 are shown in Figs 3.41b and 3.41c, respectively. The maximum sensitivity to a single height observation is phase-shifted relative to the large-scale u or v analysis sensitivity gradient maxima in Fig. 3.40. These phase-shifts are consistent with the one-

dimensional results (Figs. 3.19, 3.20) from Chapter III.D.4.a. In Fig. 3.41b, positive height/u-wind observation sensitivities occur to the south, and negative sensitivities occur to the north, which implies that a positive height observation perturbation to the south, or a negative height observation perturbation to the north, of the u-wind analysis sensitivity gradient maxima increases J. Likewise, positive height observation perturbations to the east or to the north also increase J (Fig 3.41c). Height observation perturbations of the opposite signs to those described above decrease J.

These results may be understood by considering the analysis equation (2.1). The observation information is spread to the surrounding gridpoints according to the Kalman gain or weight matrix. For a single observation (with $\varepsilon_b = \varepsilon_r = 1.0$), the structure of the Kalman gain matrix is determined by the correlation function. The Kalman gain matrices (or equivalently $\mathbf{K}^T$ for a single observation) corresponding to the nine different background error correlation functions from (3.49a-i) are shown in Fig. 3.42. A single height observation either increases or decreases the height analysis in a circular pattern around the observation (Fig. 3.42a). Since the height analysis is increased or decreased depending upon the sign of the innovation, a positive innovation is always assumed in the following arguments. According to Fig. 3.42b, a single height observation increases the u-winds to the north and decreases the u-winds to the south. A positive increment in height has the net effect of increasing the meridional shear of the zonal wind. This in turn increases the negative vorticity according to

$$\zeta = \partial v/\partial x - \partial u/\partial y. \tag{3.51}$$

A negative vorticity change is consistent with an increase in the analyzed heights near the observation. Similarly, a single height observation decreases the v-winds to the

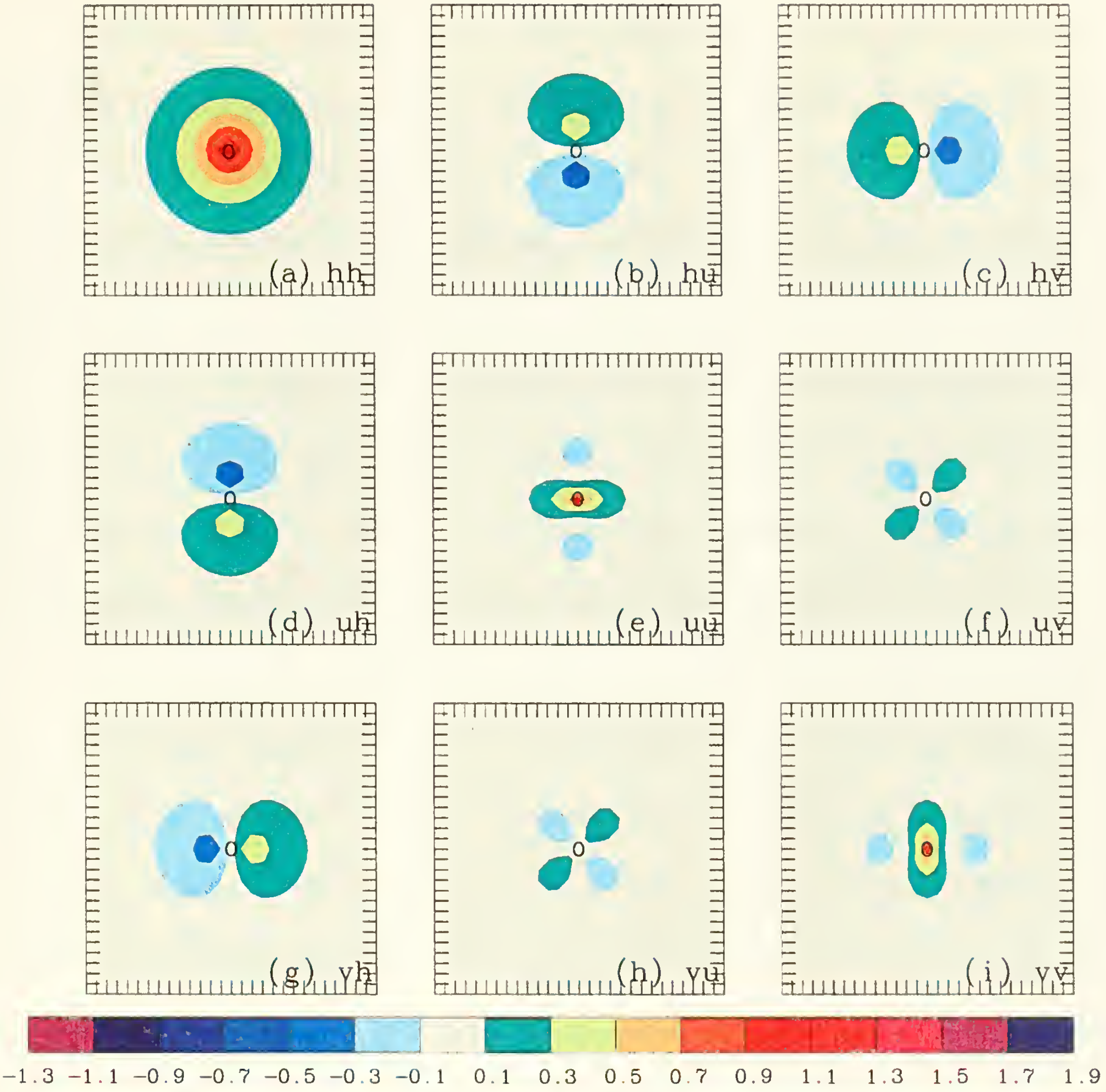

Figure 3.42. Kalman gain matrices for a single observation denoted by a circle corresponding to the background error correlation functions in (3.49a-i). (a) Univariate height, (b) height/u-wind, (c) height/v-wind, (d) u-wind/height, (e) univariate u-wind, (f) u-wind/v-wind, (g) v-wind/height, (h) v-wind/u-wind, and (i) univariate v-wind background error correlation models.

east (of the observation) and increases the v-winds to the west (Fig. 3.42c). This increase in the analyzed height decreases both the meridional wind gradient and the vorticity.

Figure 5.12. Kalman gain matrices for a single object-class trained on a [illegible] corresponding to the background and successive iterations of [illegible]

each of the [illegible]

increase in the [illegible]

vectors.

The regions of maximum observation sensitivity in Fig. 3.41 occur where $\mathbf{K}^T$ is large and projects strongly onto the analysis sensitivity gradient. In Fig. 3.41a, the regions of large height/height observation sensitivity coincide with the large-scale height analysis sensitivity gradients (recall that the scales of the analysis sensitivity gradients are chosen so that only the large-scale patterns are sensitive to a single height observation). In Figs. 3.41b,c, the largest height/wind observation sensitivities are adjacent to the large-scale u- and v-wind analysis sensitivity gradients in accordance with the $\mathbf{K}^T$ distribution (Figs. 3.42b,c). Similar arguments can be employed to explain the u-wind/height and v-wind/height observation sensitivities in Figs. 3.41d,g, respectively.

The four wind-wind correlation functions are derived under the constraint that the flow is quasi-nondivergent ($\nu^2 = 0.15$). The maximum single observation univariate sensitivities (i.e., uu and vv in Figs. 3.41e,i)) occur in phase with the large-scale analysis sensitivity gradients in Figs. 3.40, while the maximum u-wind/v-wind and v-wind/u-wind observation sensitivities (Figs. 3.41f,h) are phase-shifted with the large-scale analysis sensitivity gradient in Fig. 3.40. These patterns show the influence of the $\mathbf{K}^T$ matrix (Fig. 3.42e-i). The weak, negative observation sensitivity patterns in Figs. 3.41e,i are due to the negative side-lobes of the $\langle uu \rangle$ and $\langle vv \rangle$ wind correlation functions (and are reflected in the corresponding $\mathbf{K}^T$ plots of Fig. 3.42e,i). The large negative observation sensitivities in the centers of Figs. 3.41f,h are a consequence of the overlapping observation sensitivities corresponding to the two large-scale analysis sensitivity gradients in Fig. 3.40.

The restrictive assumptions used to generate the single observation sensitivity maps (i.e., that the height and wind observation and background error variances are equal to 1.0, and that the analysis sensitivity gradients have the same functional form and amplitude) prevent any conclusions being made regarding the relative magnitudes of the resulting single observation sensitivity maps (SOSM). Rather, the purpose of this experiment has been to identify the locations of the largest cross-correlation components of the observation sensitivity and to determine whether the phase shifts relative to the analysis sensitivity gradient occur in the two-dimensional context. These assumptions will be relaxed in the following section.

This experiment demonstrates that the maximum cross-correlation components of the multivariate wind and height observation sensitivities are phase-shifted relative to their respective analysis sensitivity gradients. These phase-shifts occur as a result of the background error cross-correlation terms. By contrast, the maximum univariate partial observation sensitivities occur in phase with the maximum analysis sensitivity gradients (for the same variable).

3. Multivariate Observation Sensitivity using Real Analysis Sensitivity Gradients

In this section, two of the limiting assumptions from Chapter III.F.2 are relaxed. First, analysis sensitivity gradients are derived from fields generated using the NOGAPS adjoint rather than idealized trigonometric functions. Second, realistic observation and background error variances, and background error correlation length scales are used. The observation and analysis sensitivity gradient variables are now temperature (instead of geopotential height) and the u- and v- wind components.

The previous examples in Chapter III used idealized analysis sensitivity gradients. While these problems are much simpler than the full three-dimensional observation sensitivities computed using the NAVDAS adjoint, they still represent physically possible problems. The NOGAPS analysis sensitivity gradients were introduced because the results from earlier sections in this chapter demonstrate that the observation sensitivity strongly depends upon the location of the observation in relationship to the spatial distribution of the analysis sensitivity extrema, and the structure of the background error covariances. Moreover, it is easier to understand observation sensitivity in the simpler context of the two-dimensional system than the three-dimensional NAVDAS adjoint that will be introduced in the next chapter.

However, the two-dimensional examples discussed in this sub-section no longer represent physically realistic problems because temperature is being used as a proxy for heights. The geostrophic assumption used to generate the background error covariances relates geopotential height and winds, not temperature and winds. The proper relationship between the temperature and wind fields is given by the thermal wind equation, which relates the horizontal temperature gradients to the vertical wind shear, and thereby requires three dimensions. Nonetheless, the examples are still instructive provided caution is used when relating the results of this section to the full three-dimensional NAVDAS adjoint sensitivity results.

a. Multivariate Single Observation Sensitivity Maps

The two-dimensional analysis sensitivity gradients used for this example (Fig. 3.43) correspond to the 850-hPa temperature and wind (u and v) NOGAPS adjoint analysis sensitivity gradients that will be described in greater detail in Chapter IV. The

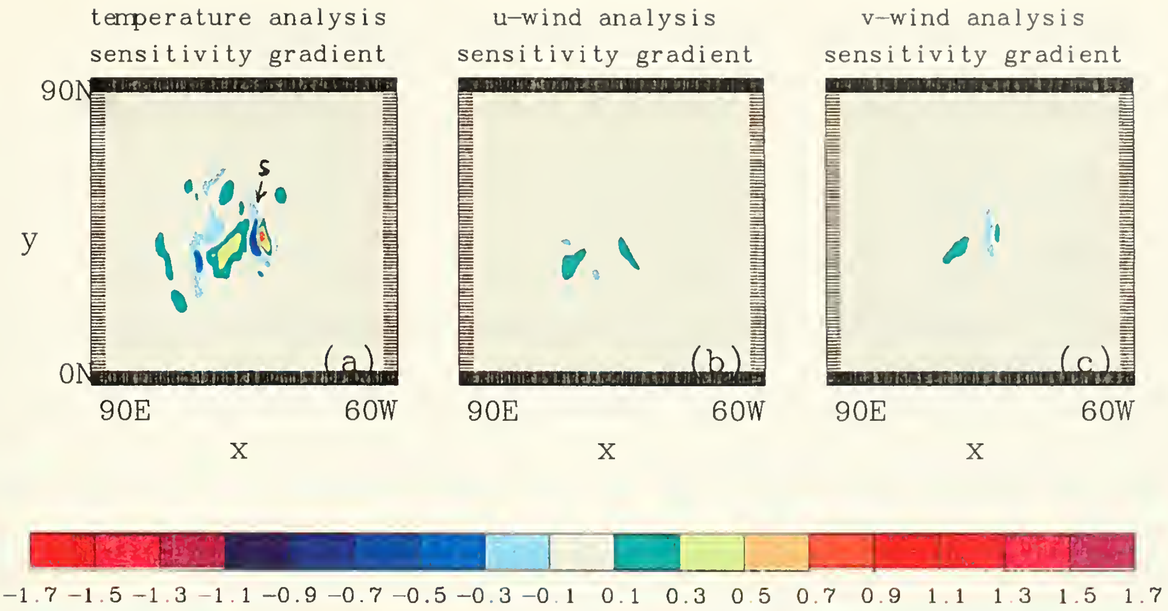
temperature analysis sensitivity gradient
u–wind analysis sensitivity gradient
v–wind analysis sensitivity gradient
90N
y
0N
S
(a)
(b)
(c)
90E
60W
x
−1.7 −1.5 −1.3 −1.1 −0.9 −0.7 −0.5 −0.3 −0.1 0.1 0.3 0.5 0.7 0.9 1.1 1.3 1.5 1.7

Figure 3.43. NOGAPS analysis sensitivity gradients at 850 hPa for (a) temperature, (b) u-wind, and (c) v-wind. The color scale is at the bottom. See text for more details.

cost function J for these calculations is the energy-weighted forecast error (J/kg). The grid domain for this experiment is from 0°N - 90°N and 90°E – 60°W with a grid spacing of one-degree latitude and longitude (Δx = 1.0).

The background error standard deviations are assumed to be spatially homogeneous and equal to 2.5 °K for temperature and 4.2 m s^{-1} for both u- and v-wind components. These values correspond to the background error variances used in NAVDAS at 850 hPa for midlatitude ocean areas. The error standard deviations for the single probe observations correspond to the values assumed by NAVDAS for an aircraft observation at 850 hPa, which are 1.3 °K for temperature, and 2.2 m s^{-1} for u and v. The NAVDAS background error correlation length scale of 3.85 x 10^5 m is used. At 45°N (with Δx = 1° lon.), $L_b = 4.91\Delta x$. For simplicity, a constant L_b is assumed over the domain.

The single observation sensitivity maps for the nine partial sensitivities corresponding to (3.50a-i) are shown in Fig. 3.44. The (transposed) Kalman gain matrices for a single observation (and corresponding to the nine partial sensitivities as in Fig. 3.41) are shown in Fig. 3.45. The univariate components of the observation sensitivity are discussed first (Figs. 3.44a,e,i). In general, the sensitivity of J to a single observation is largest when the analysis sensitivity gradient is large both in spatial scale and in magnitude. The observation sensitivity is negligible when the analysis sensitivity is small both in spatial extent and in magnitude. Several surprising results occur for the univariate temperature observation sensitivity (Fig. 3.44a). The temperature analysis sensitivity gradient sub-structure near the center of the domain is large in amplitude (nearly -1.0 J/kg K), but is relatively small in spatial extent and is flanked by positive sub-structures that are either large in magnitude or spatial extent. The corresponding univariate single observation temperature sensitivity map (Fig. 3.44a) shows that the largest sensitivity occurs for the temperature analysis sensitivity gradient sub-structure that is large in spatial extent, but relatively weak in amplitude (< 0.5 J/kg K). The single observation sensitivity is significantly weaker for the strong positive sub-structure and is non-existent for the negative sub-structure.

These results can be explained based on the results from Chapter III.C-E. The observation sensitivity is maximized when the projection of $\mathbf{K}^T$ (Fig. 3.45a) onto $\partial J/\partial \mathbf{x}_a$ (Fig. 3.43a) is maximized, which is when the spatial scales of $\mathbf{K}^T$ and $\partial J/\partial \mathbf{x}_a$ are roughly similar. Univariate observation sensitivity is also maximized when the observation is placed near the center of the analysis sensitivity gradient maxima. If the

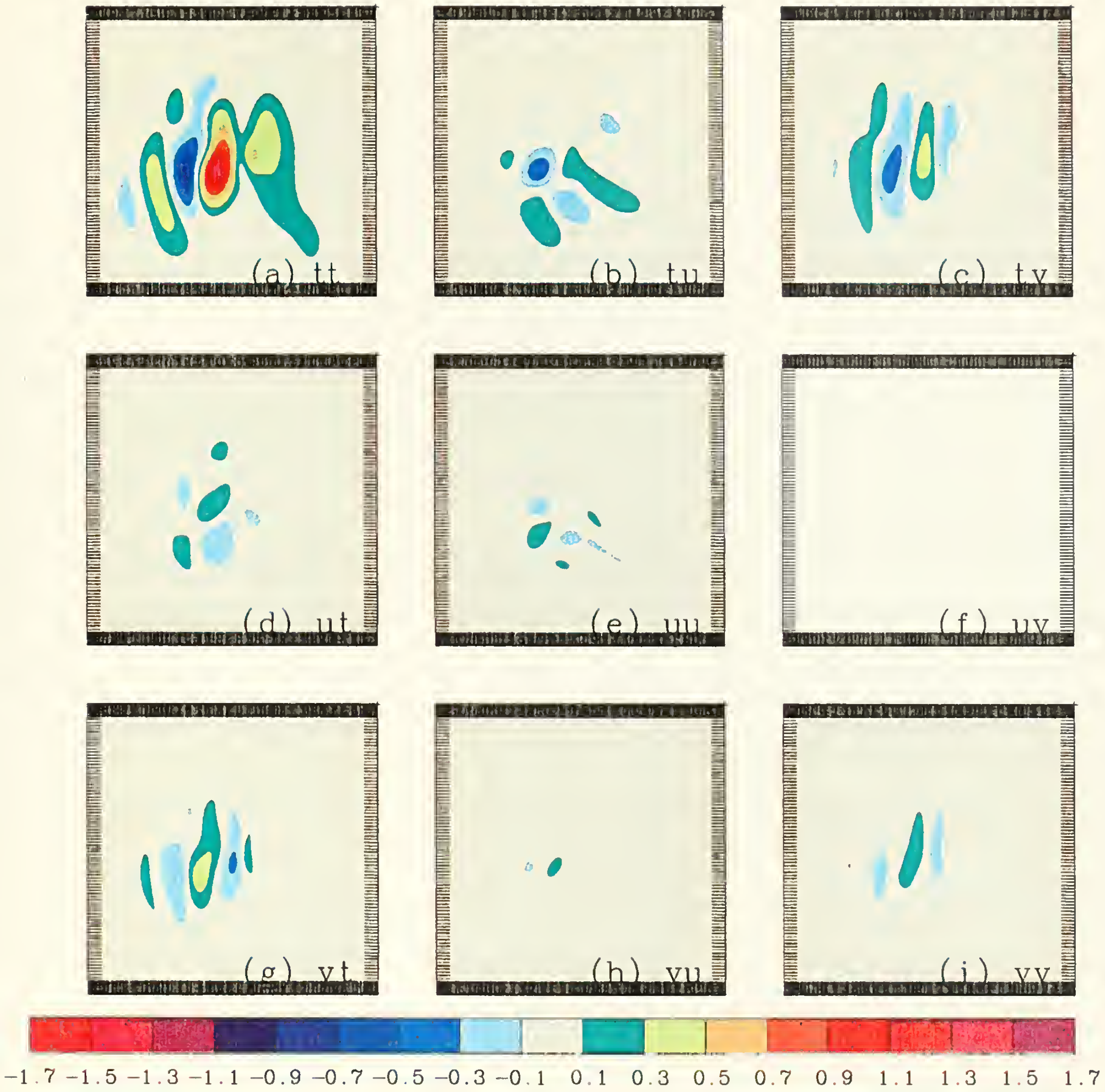

Figure 3.44. As in Fig. 3.41, except for single observation sensitivity maps corresponding to the analysis sensitivity gradients in Fig. 3.43. (a) Univariate temperature, (b) temperature/u-wind, (c) temperature/v-wind, (d) u-wind/temperature, (e) univariate u-wind, (f) u-wind/v-wind, (g) v-wind/temperature, (h) v-wind/u-wind, and (i) univariate v-wind observation sensitivities. See text for explanation of the nomenclature. The values have been multiplied by 0.056. Panel (f) appears blank because the values are less than the minimum contour intervals of ±1.0.

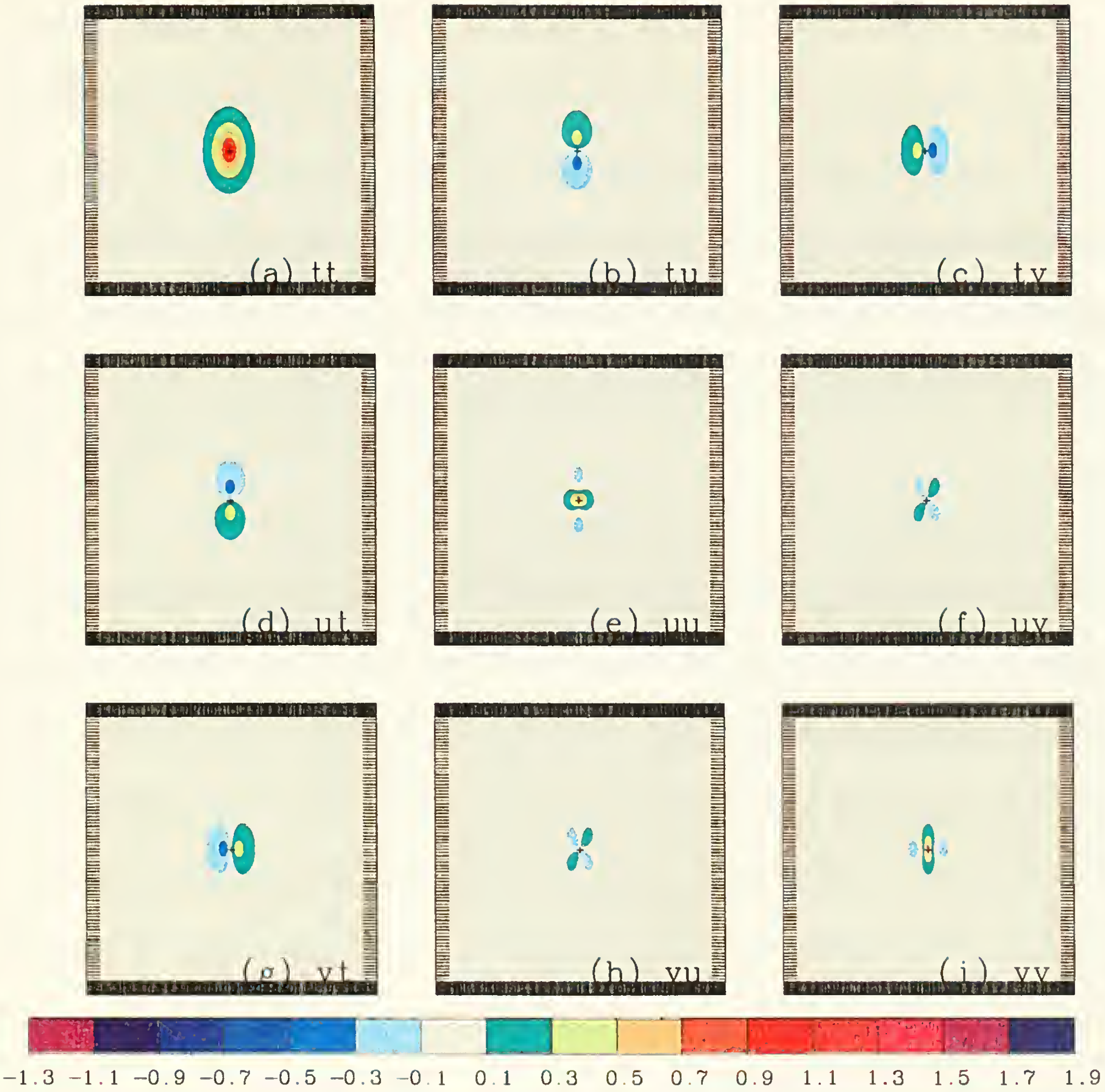

Figure 3.45. As in Fig. 3.42, except for Kalman gain matrices for a single observation denoted by a "+" corresponding to the background error correlation functions in (3.49a-i) and the grid domain in Fig. 3.43. (a) Univariate temperature, (b) temperature/u-wind, (c) temperature/v-wind, (d) u-wind/temperature, (e) univariate u-wind, (f) u-wind/v-wind, (g) v-wind/temperature, (h) v-wind/u-wind, and (i) univariate v-wind background error correlation models.

observation is placed near the center of the large (spatial) scale analysis sensitivity gradient, the contributions to $\partial J/\partial \mathbf{y}$ tend to be the same sign and the observation sensitivity is maximized. If the observation is placed near the center of the negative

analysis sensitivity gradient, the contributions to $\partial J/\partial \mathrm{y}$ are both positive and negative and a large degree of cancellation occurs due to the presence of the nearby analysis sensitivity gradient substructures of opposite sign. Similarly, an observation placed near the center of the small (spatial) scale positive analysis sensitivity gradient substructure will have smaller observation sensitivity due to significant cancellation from the adjacent negative analysis sensitivity gradient (particularly if the observation is placed close to the adjacent substructure of opposing sign).

The cross-correlation contributions to the multivariate observation sensitivities involving either temperature observations or temperature analysis sensitivity gradients (Figs. 3.44b,c,d,g) show evidence of the phase-shift of the maximum observation sensitivity relative to the corresponding analysis sensitivity gradient maxima/minima in Fig. 4.43. Finally, the two components of the observation sensitivity computed using the u-v cross-covariances are shown in Figs. 3.44f,h. The observation sensitivities are very weak. The u-wind/v-wind observation sensitivity is smaller than the minimum contour interval of ±0.1 J/(kg m s^{-1}) (Fig. 3.44f). The small observation sensitivities are a consequence of the weak projection of $\mathbf{K}^T$ onto $\partial J/\partial \mathbf{x}_a$ (for example, compare Fig. 3.44h with Fig. 3.45h).

This experiment demonstrates that the observation sensitivities are strongest for the large-scale analysis sensitivity gradient sub-structures. The observation sensitivity also tends to be maximized when the analysis sensitivity gradient is large in magnitude. These results are consistent with the one-dimensional multivariate results and the two-dimensional multivariate results using idealized analysis sensitivity gradients.

The observation sensitivity is reduced when an observation is located close to analysis sensitivity gradient sub-structures with opposite sign.

The total observation sensitivities corresponding to the nine partial observation sensitivities (3.50a-i) are obtained from (2.16a-c) and may be written as

$$\partial J/\partial \mathbf{T}_o = \mathbf{K}_{TT,T}^{T}\, \partial J/\partial \mathbf{T}_a + \mathbf{K}_{TT,u}^{T}\, \partial J/\partial \mathbf{u}_a + \mathbf{K}_{TT,v}^{T}\, \partial J/\partial \mathbf{v}_a\,, \tag{3.52a}$$

$$\partial J/\partial \mathbf{u}_o = \mathbf{K}_{uu,T}^{T}\, \partial J/\partial \mathbf{T}_a + \mathbf{K}_{uu,u}^{T}\, \partial J/\partial \mathbf{u}_a + \mathbf{K}_{uu,v}^{T}\, \partial J/\partial \mathbf{v}_a\,, \tag{3.52b}$$

$$\partial J/\partial \mathbf{v}_o = \mathbf{K}_{vv,T}^{T}\, \partial J/\partial \mathbf{T}_a + \mathbf{K}_{vv,u}^{T}\, \partial J/\partial \mathbf{u}_a + \mathbf{K}_{vv,v}^{T}\, \partial J/\partial \mathbf{v}_a\,, \tag{3.52c}$$

where the terms involving cross-correlations between observations of different variables have been neglected since only one observation (of one type) is considered at a time. The total single observation sensitivity maps for a single temperature, u- and v-wind observation are shown in Fig. 3.46.

Comparing Fig. 3.46a with Figs. 3.44a,b,c, it is clear that the total temperature observation sensitivity is dominated by the term in (3.52a) involving the temperature analysis sensitivity gradient. The weaker contributions from the other two terms are due to their weaker projections of $\mathbf{K}^T$ onto $\partial J/\partial \mathbf{x}_a$. Likewise, the total u- and v- wind observation sensitivities in Figs. 3.46b,c are dominated by the terms in (3.52b,c) that involve the temperature analysis sensitivity gradient. The overall effect of the multivariate phase shift on the total observation sensitivity is to subtly modify the dominant pattern (i.e., that due to the temperature observation sensitivity gradient). Thus, the predominant patterns are that the maximum total temperature observation sensitivity

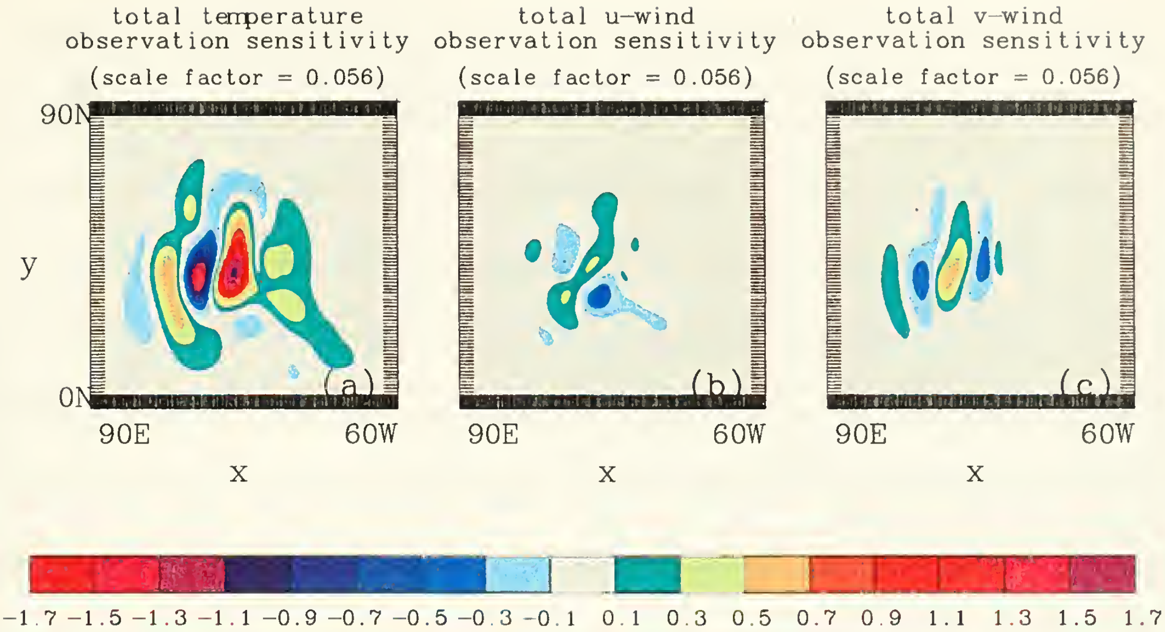

Figure 3.46. Total single observation sensitivity maps from (3.52a-c) corresponding to the analysis sensitivity gradients in Fig. 3.43 for (a) temperature, (b) u-wind, and (c) v-wind. The values have been multiplied by 0.056.

is in phase with the temperature analysis sensitivity gradient, and the maximum total u- and v-wind observation sensitivities are subtly phase-shifted relative to the maxima of the temperature analysis sensitivity gradient. Finally, comparisons among the three total sensitivities demonstrate that the maximum sensitivity to a single temperature, u- or v-wind observation tends to occur in different locations.

These results may be related to the forward analysis problem as follows. The weak sensitivity to a single observation placed near the center of the small-scale analysis sensitivity gradients implies that a single observation cannot resolve these small-scale analysis features. The information from a single observation is spread horizontally according to the weight matrix **K** (which is equivalent to $\mathbf{K}^T$ for any given observation). It is clear from Fig. 3.45 that a single observation cannot provide the analysis changes needed to resolve the small-scale analysis sensitivity gradient sub-structure indicated by

the label "S" in Fig. 3.43a. Note that small observation sensitivity does not imply that the change to the analysis by that observation will be small. Rather, it implies that the analysis will not be changed in the direction needed to change the cost function J. Conversely, strong observation sensitivity implies that the single observation has the *potential* to change the analysis in the direction that will significantly affect J. For a single observation, this occurs when the information from the observation is spread (according to **K**) in such a manner that the *potential* analysis changes are in a direction that changes J, which happens when $\mathbf{K}^T$ and the analysis sensitivity gradient are both large scale and of similar shape (*cf.*, Figs. 3.43a, 3.45a, and 3.46a).

These results have several important implications for adaptive targeting. The most important implication is that there may be little sensitivity to a single observation placed near the center of a small-scale, large amplitude analysis sensitivity gradient, but very large sensitivity to an observation placed near the center of a large-scale, but much weaker analysis sensitivity gradient. Therefore, one may not wish to target only the largest amplitude analysis sensitivity gradients. Because of the phase-shifts due to the multivariate contributions to the observation sensitivity, the results suggest that the best location for a temperature observation may not be the best location for a wind observation. The results discussed in this sub-section are strictly applicable for single observations. The more general case with multiple observations is discussed in following sub-sections.

b. Limited-Area versus Global Observation Sensitivity Calculations

One obvious technique to reduce the computational expense is to perform the observation sensitivity calculations over a limited domain centered on the region of interest. However, the results in Fig. 3.16 and other experiments (not shown) indicate that the observation sensitivity can differ significantly between calculations made for a limited area and global computations. The reason for this discrepancy is that the projection of $\mathbf{K}^T$ for a given observation onto $\partial J / \partial \mathbf{x}_a$ will not be the same if the grid boundaries intersect significant values of $\partial J / \partial \mathbf{x}_a$. For unequivocal results, it would seem that any observation with significant sensitivity must lie well within the grid domain, which in turn requires that the analysis sensitivity gradient must be nearly zero on the boundary.

c. Multivariate Observation Sensitivity for a Hypothetical Flight Track

The 850-hPa analysis sensitivity gradients generated using the NOGAPS adjoint (Fig. 1.2) are also used for this experiment. The domain has been limited to 20°N – 60°N, and 153°E – 142°W, which is sufficiently large to produce results that are equivalent to the larger domain in the previous example. The temperature, u- and v-wind analysis sensitivity gradients for this domain are plotted in Fig. 3.47. Twenty-two observations of either temperatures or u- or v-winds are placed in a backwards "N" pattern across the analysis sensitivity gradient extrema in the eastern part of the domain (i.e., eastern North Pacific). The observation and background error standard deviation values from the previous example are used here as well. The background error correlation length scale value from NAVDAS (applied at 45° N) is used so that

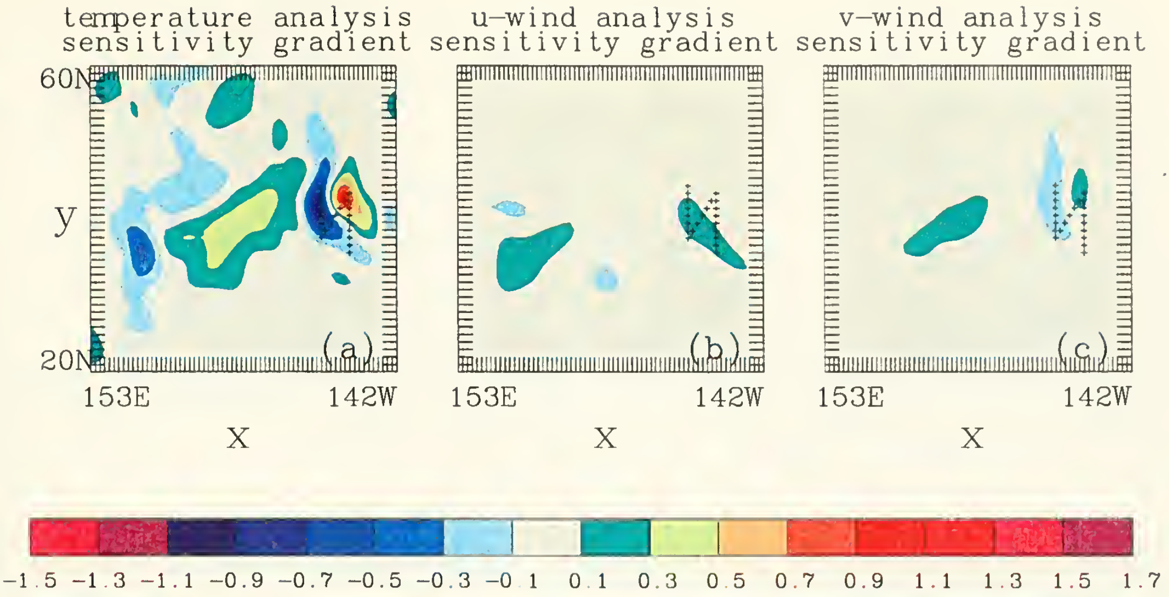
temperature analysis sensitivity gradient
u–wind analysis sensitivity gradient
v–wind analysis sensitivity gradient
60N
20N
y
153E
142W
X
(a)
(b)
(c)
–1.5 –1.3 –1.1 –0.9 –0.7 –0.5 –0.3 –0.1 0.1 0.3 0.5 0.7 0.9 1.1 1.3 1.5 1.7

Figure 3.47. As in Fig. 3.43, except NOGAPS analysis sensitivity gradients at 850 hPa for a more limited domain for (a) temperature, (b) u-wind, and (c) v-wind. The observation locations for the hypothetical flight track are given by the "+". See text for more details.

$L_b = 4.91\Delta x$ (where $\Delta x = 1^\circ$ lat.). The geostrophic coupling parameter $\mu = 1.0$, and the wind divergence factor is set to $\nu^2 = 0.15$.

The total observation sensitivity measures for the temperature, u- and v-wind observations are obtained by applying (3.6) to (3.52a-c), and are plotted for a smaller domain of 161°W – 142°W and 35°N – 50° N in Fig. 3.48. In general, the results follow the general principles highlighted in earlier sections. The observation sensitivity measure is large where the analysis sensitivity gradient is also large in magnitude and spatial scale. Unlike the SOSM results of Fig. 3.46, the observation sensitivity is not dominated by contributions due to the temperature analysis sensitivity gradient. Consequently, it may be more difficult to understand the behavior of the total observation sensitivities.

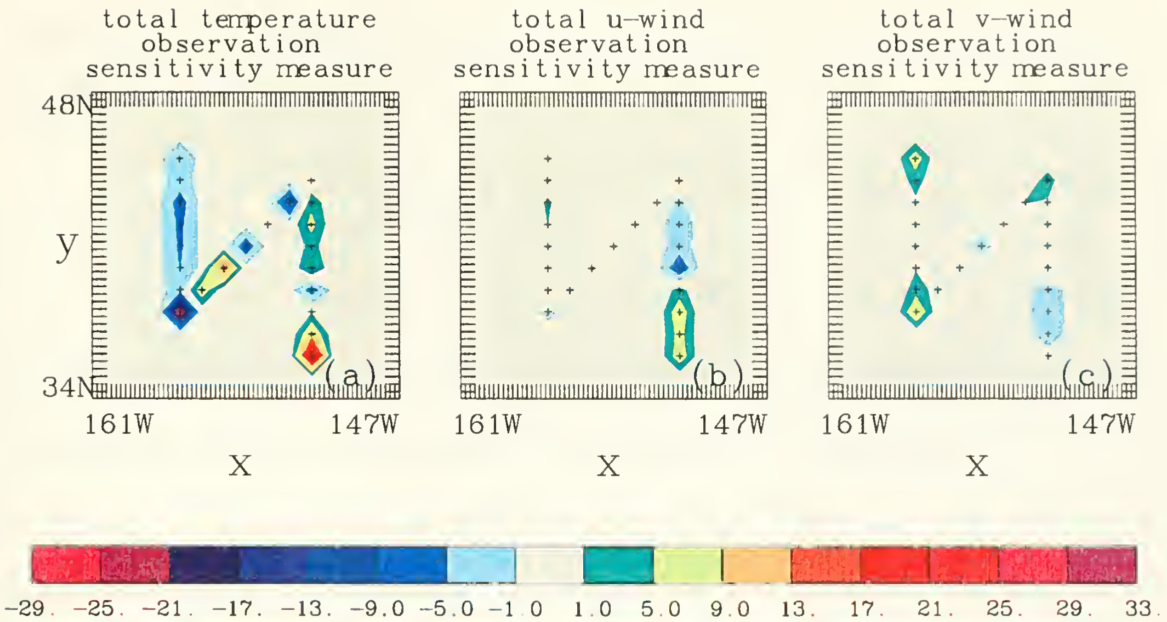

Figure 3.48. Total observation sensitivity measure from (3.52a-c) and (3.6) for a set of 22 observations indicated by the "+". The color scale is at the bottom; note the different scale.

According to Fig. 3.48, relatively isolated observations can have large observation super-sensitivity (OSM > 1), even when the analysis sensitivity gradient is weak at that particular location. In addition, because of the multivariate phase shifts, the observation sensitivity measure can be large where the analysis sensitivity gradient is very small between two adjacent analysis sensitivity gradient sub-structures. Large observation sensitivity implies that the observation has the potential to make large changes to the analysis. When the observation is relatively isolated, the information from the observation will be spread to the surrounding gridpoints according to the structure of $\mathbf{K}^T$ and the background error covariances (see Fig. 3.33). Thus, it may not be desirable to have the few, more isolated observations contributing most to the analysis. These results suggest that simply taking observations along a flight path through the extrema is insufficient, and that it may be necessary to sample larger areas of the analysis sensitivity

gradient pattern to avoid abrupt observation density discontinuities in highly sensitive areas.

d. Multivariate Observation Sensitivity for a Hypothetical Swath of Satellite Observations

The basic design of this experiment follows the previous experiment. In this example, 840 observations are distributed along a swath that bisects the two large-amplitude temperature analysis sensitivity gradient sub-structures (Fig. 3.49a). An observation of T, u, or v is located at every gridpoint within the swath, so that the horizontal resolution is 1° longitude or 78.5 km at 45°N. The width of the swath is 20° longitude or approximately 1600 km at 45°N. This gives a horizontal resolution similar to that available with the current polar-orbiting satellites. This swath would mimic a set of satellite observations if satellites directly measured temperature and if atmospheric winds were available from polar-orbiting satellites. The analysis sensitivity gradients for T, u, and v (with the observation locations indicated by a "+") are shown in Figs. 3.49a,b, and c, respectively.

The nine partial observation sensitivities corresponding to (3.50a-i) are presented in Fig. 3.50. These patterns show that the observation sensitivity for the satellite swath follows the general principles discussed in earlier sections. For the three univariate components of the observation sensitivity (Figs. 3.50a,e,i), the observation sensitivity is nearly equal to the analysis sensitivity in the well-observed interior portions of the swath. However, some observation super-sensitivity occurs along the edges of the swath. The super-sensitivity is strongest when the spatial scale of the analysis sensitivity gradient is large, as for the temperature analysis sensitivity gradient (Fig. 3.50a). The

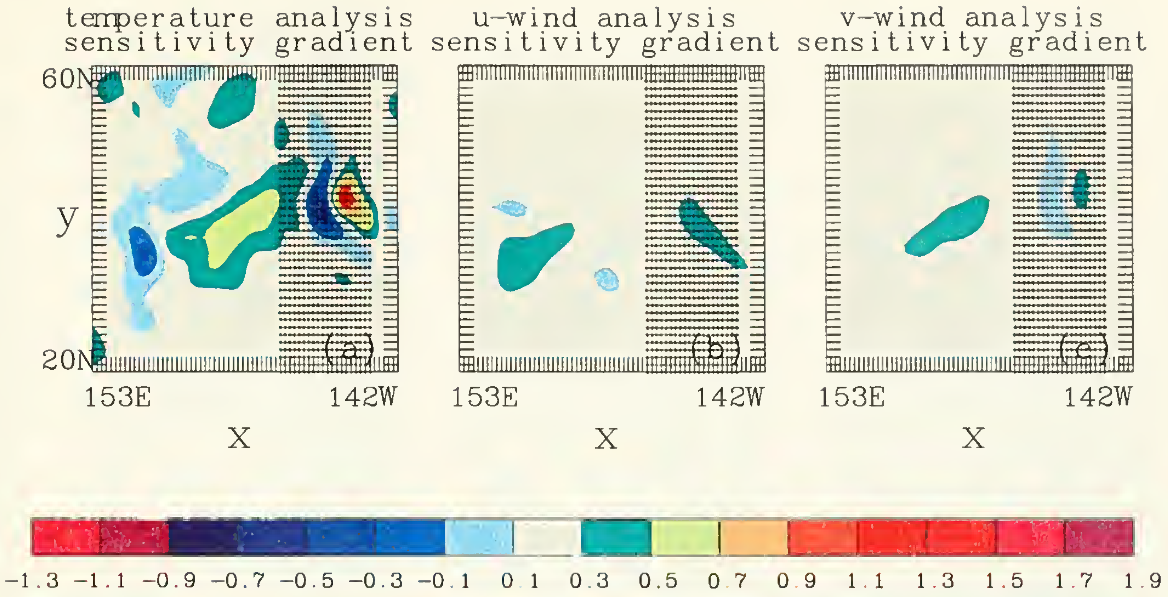
temperature analysis sensitivity gradient
u-wind analysis sensitivity gradient
v-wind analysis sensitivity gradient
60N
20N
y
153E
142W
X
(a)
(b)
(c)
−1.3 −1.1 −0.9 −0.7 −0.5 −0.3 −0.1 0.1 0.3 0.5 0.7 0.9 1.1 1.3 1.5 1.7 1.9

Figure 3.49. As in Fig. 3.43, except NOGAPS analysis sensitivity gradients at 850 hPa for a more limited domain for (a) temperature, (b) u-wind, and (c) v-wind. The observation locations for the hypothetical satellite swath are given by the "+". See text for more details.

cross-correlation components of the multivariate observation sensitivity (Figs. 3.40b-d,f-h) demonstrate the phase shifts between the observation and analysis sensitivities noted in earlier sections. The maximum temperature/u-wind observation sensitivity is displaced to the north and south of the u-wind analysis sensitivity gradient (Fig. 3.50b), which is consistent with the $\langle tu \rangle$ background error correlation model (Fig. 3.45b). Similarly, the maximum temperature/v-wind observation sensitivity is displaced to the east and west of the v-wind analysis sensitivity gradient (Fig. 3.50c), which is consistent with the $\langle tv \rangle$ background error correlation model (Fig. 3.45c). Similar phase shifts, which are due to the geostrophically-coupled background error covariances, can be seen in Figs. 3.50d,g as well. Weaker phase shifts, which show the influence of the $\langle uv \rangle$ and $\langle vu \rangle$ background error correlations (Figs. 3.45f,h), are noted in Fig. 3.50f,h.

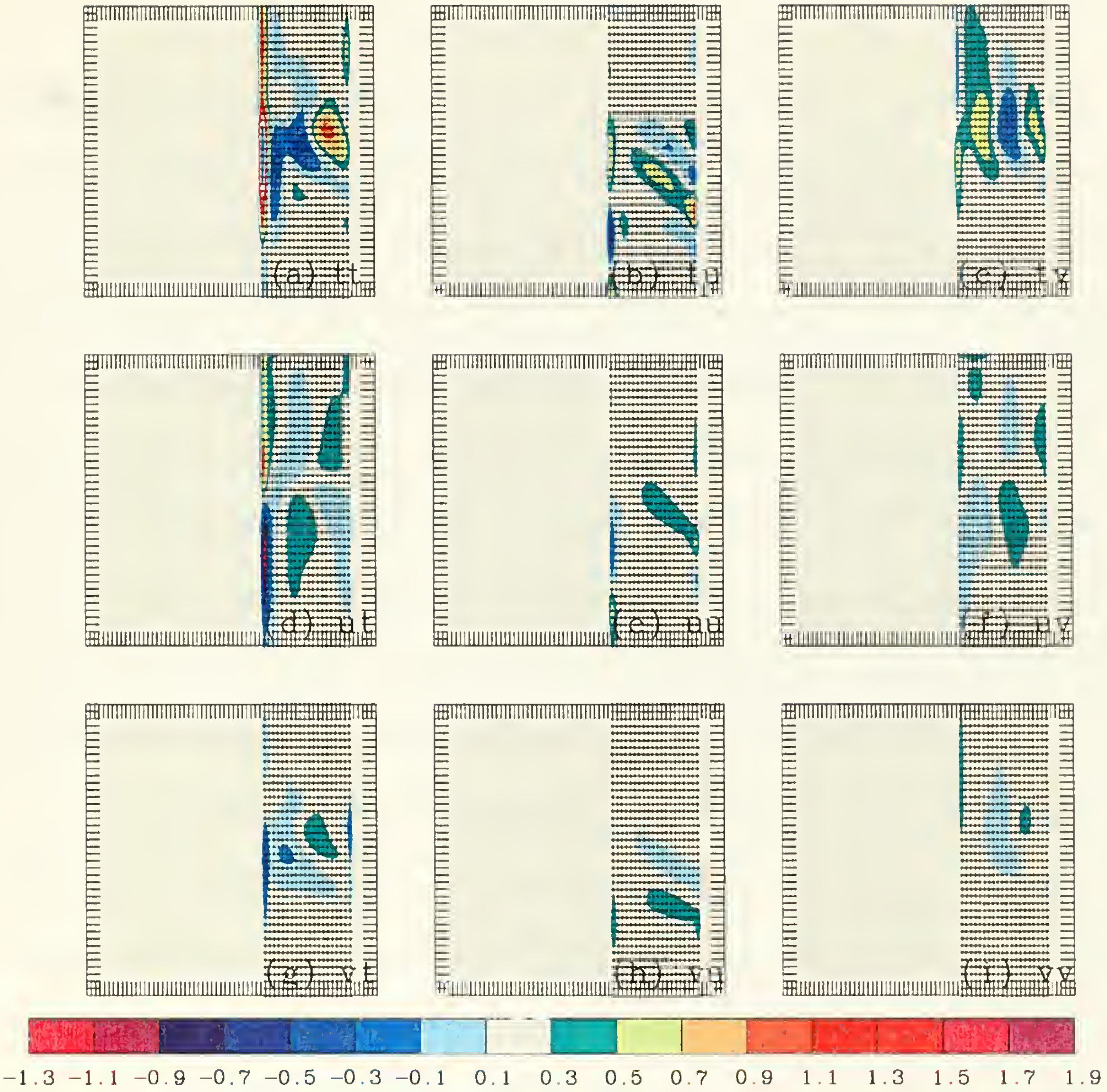

Figure 3.50. As in Fig. 3.41, except the observation sensitivity vectors for the hypothetical satellite swath from (3.50a-i) corresponding to the analysis sensitivity gradients in Fig. 3.49. (a) Univariate temperature, (b) temperature/u-wind, (c) temperature/v-wind, (d) u-wind/temperature, (e) univariate u-wind, (f) u-wind/v-wind, (g) v-wind/temperature, (h) v-wind/u-wind, and (i) univariate v-wind observation sensitivities.

The total observation sensitivities are shown in Fig. 3.51, and are dominated by the partial sensitivities to T, u, and v, given the temperature analysis sensitivity gradient. The total sensitivity of J to the temperature observations (Fig. 3.51a) is similar in appearance to the temperature analysis sensitivity gradient in the well-observed interior of the swath. The multivariate phase shifts are clearly visible in Fig. 3.51 and dominate the total u and v observation sensitivities. It is apparent from comparing Figs. 3.51a, 3.51b, and 3.51c that the largest sensitivities of J to a temperature observation do not occur in the same location as the largest u- or v-wind observation sensitivities. Likewise, the largest u- and v-wind observation sensitivities do not occur at the same location. For targeting, this implies that the optimal location for a temperature observation may not be the optimal location for wind observations.

The observation super-sensitivity along the edges of the swath is clearly visible in Fig. 3.51. The edges of the satellite swath have an analogous effect as the coastline in Fig. 3.1. The largest row of $\mathbf{K}^T$ (not shown) in both magnitude and spatial extent corresponds to the observations along the edges of the swath, and this gives a strong projection of $\mathbf{K}^T$ onto the large-scale analysis sensitivity gradients. The resulting observation super-sensitivity implies that the observations along the edge of a satellite swath, because of their large sensitivity, have much larger potential to significantly influence the analysis. This result is significant because observations at the edges of satellite swaths tend to be less accurate than the nadir observations for a number of reasons (not discussed here). As discussed earlier, the information from an observation is spread to the surrounding observations according to the Kalman gain matrix $\mathbf{K}$.

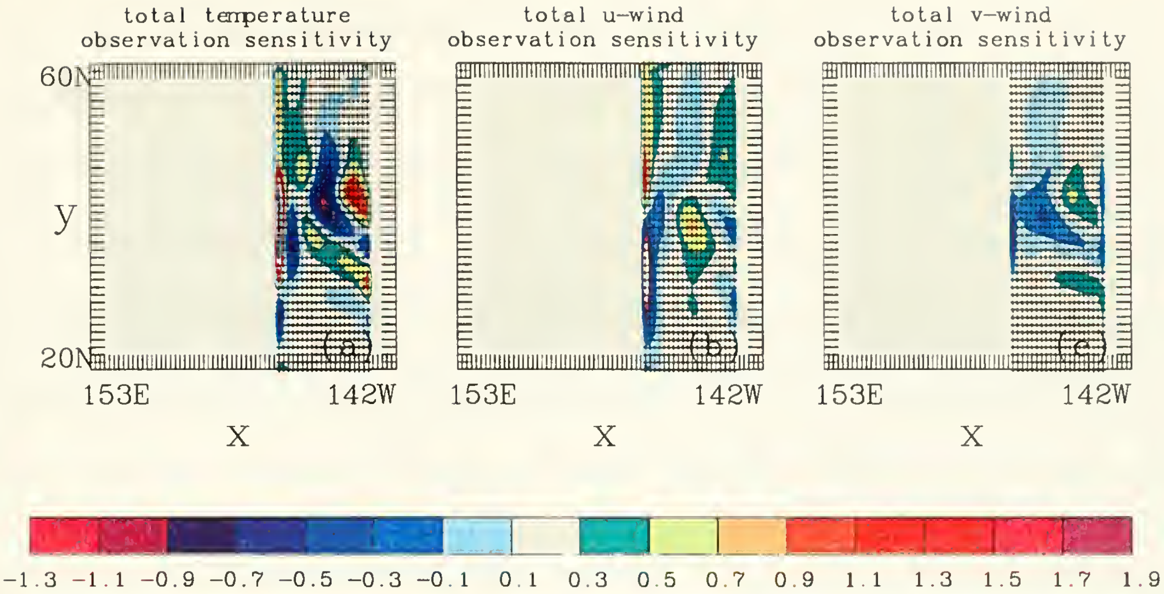

Figure 3.51. Total observation sensitivities for the hypothetical satellite swath from (3.52a-c) for (a) temperature, (b) u-wind, and (c) v-wind. The color scale is at the bottom.

Consequently, the information from the less accurate observations at the edge of the scan will be extrapolated to the data-void regions of the domain, while the more accurate observations at the center of the domain will have only a local effect. These results argue for observation errors that vary as a function of the scan (swath) position.

e. The Marginal Observation Sensitivity Vector

The single observation sensitivity map (SOSM) was used in earlier examples to compute the sensitivity to a single observation at each gridpoint in the domain. Such a map may then be used to find the location where a single targeted observation would have the greatest potential impact. However, the SOSM assumes that targeting occurs in a region with no other observations. In reality, truly data-void regions are probably non-existent because of good global data coverage by polar-orbiting satellites.

The marginal observation sensitivity vector takes into consideration the presence of other observations. Suppose that M pre-existing observations are available in a domain with N gridpoints. The probe observation, which has the error characteristics of the targeted observing system, is placed sequentially at each grid point and the observation sensitivity for the probe observation is computed, taking into account the other M observations. Computationally, this requires the observation sensitivity (2.8a) to be computed N times, and each solution requires (effectively) inverting the $(M+1)\,\mathrm{x}\,(M+1)$ matrix $(\mathbf{HP}_b\mathbf{H}^T+\mathbf{R})^{-1}$.

An example of the marginal (total) observation sensitivity for the hypothetical flight track (the pre-existing observations) of Fig. 3.48 is shown in Fig. 3.52, and may be compared to the single observation sensitivity map of Fig. 3.46 (although those plots are for the larger domain). The temperature, u- and v- wind analysis sensitivity gradients are the same as in Fig. 3.47. The sensitivity to the single probe observation (Fig. 3.52) is substantially reduced when other observations are present. In particular, the total sensitivity to a single temperature observation (Fig. 3.52a) is much less to the east and west of the pre-existing flight track. Furthermore, the small-scale negative temperature analysis sensitivity gradient substructure (Fig. 3.47a) is now sensitive to a single temperature observation (as indicated by the light blue shading in the center of the flight track), whereas it was not when the pre-existing observations were not present (e.g., Fig. 3.46a). These results clearly demonstrate the importance of taking into account the presence of other observations in the targeting region, and how those observations are used by the analysis.

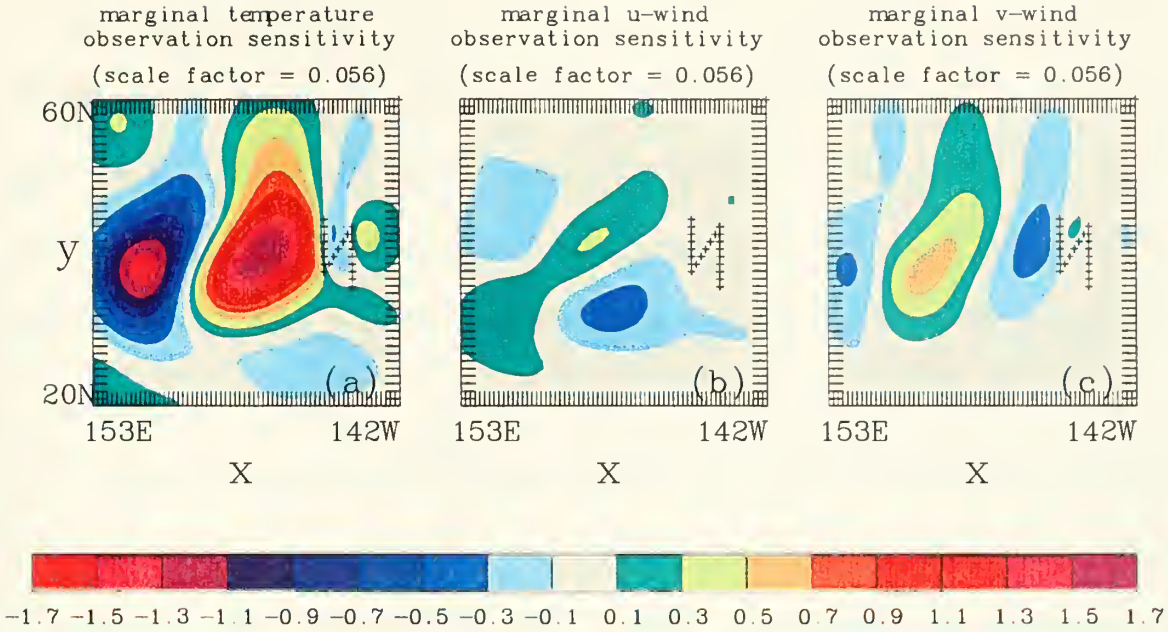

Figure 3.52. The total marginal observation sensitivity vectors for the hypothetical flight track of observations and a single probe observation for (a) temperature, (b) u-wind, and (c) v-wind. The color scale is at the bottom. The values have been multiplied by 0.056.

4. Summary of Two-Dimensional Multivariate Observation Sensitivity

The two-dimensional multivariate observation sensitivity results are consistent with the one-dimensional univariate (Chapter III.C) and multivariate (Chapter III.D) results. The largest univariate component of the observation sensitivity occurs where the analysis sensitivity gradient is also a maxima/minima. The largest cross-correlation components of the observation sensitivity tend to be phase shifted relative to the analysis sensitivity gradient extrema. Both the phase shifts and the signs of the observation sensitivity were shown to be consistent with the background error correlation model that assumes that the background errors are geostrophic and non-divergent. In general, the total observation sensitivity is dominated by the partial sensitivities involving the temperature analysis sensitivity gradient. Thus, the total sensitivity to a temperature observation is largest where the temperature analysis sensitivity gradient is also largest,

and the total sensitivities to the u- and v-wind observations tend to be phase shifted relative to the temperature analysis sensitivity gradient extrema. One consequence of the multivariate phase shifts is that the maximum sensitivity to a temperature observation does not occur where the sensitivity to a u- or v-wind observation is a maximum, and suggests that targeting exercises may wish to consider placing adaptive observations accordingly.

Overall, the greatest observation sensitivity occurs for large amplitude analysis sensitivity gradients when the spatial scales of $\mathbf{K}^T$ and the analysis sensitivity gradient are similar. The observation sensitivity is much less when the analysis sensitivity gradient is small scale, even though the amplitude may be large. If the observation is located near analysis sensitivity gradient sub-structures with opposing sign, the contributions to the observation sensitivity may also be of opposing sign, so that a large degree of cancellation occurs and the observation sensitivity is very small. Large values of observation sensitivity tend to occur when the observations are relatively isolated or there is an abrupt discontinuity in the density of the observations, even if the analysis sensitivity gradient is relatively weak at the observation location. Similar phenomena occurred at the coastline for the one-dimensional examples (Chapters III.C.1 and Chapter III.D.2), and for the two-dimensional multiple observation examples (Chapter III.E.3.a). The results imply that, for adaptive targeting, one may wish to sample both the large-spatial scale analysis sensitivity patterns and the large amplitude, small-scale analysis sensitivity sub-structures. The results also suggest that it may be necessary to sample larger areas of the analysis sensitivity gradient pattern to avoid abrupt observation density discontinuities in highly sensitive areas.

This section also discussed the point that limited area calculations may not agree with global observation sensitivity calculations if the grid boundaries for the limited domain problem intersect significant values of analysis sensitivity. Therefore, any limited area targeting applications should have sufficient horizontal extent so that large analysis sensitivity gradients are well contained within the grid boundaries.

The marginal observation sensitivity vector, which determines the sensitivity to a single observation given the presence of pre-existing observations, shows that the sensitivity to a single observation is considerably reduced when the pre-existing observations are taken into account. This result clearly demonstrates that targeting applications must consider the entire suite of observations, and not just the adaptive observations.

THIS PAGE INTENTIONALLY LEFT BLANK

IV. EXPLORATION OF NAVDAS OBSERVATION ADJOINT SENSITIVITY FOR THE NORTH PACIFIC OCEAN ON 7 FEBRUARY 1999

Observation sensitivity using simplified one- and two-dimensional analysis systems and idealized analysis sensitivity gradients was examined in Chapter III. In this chapter, the full three-dimensional multivariate observation sensitivity problem is investigated using the adjoint of NAVDAS with three-dimensional analysis sensitivity gradients computed using the NOGAPS adjoint.

A. A BRIEF DESCRIPTION OF NAVDAS

NAVDAS (NRL Atmospheric Variational Data Assimilation System) is a three-dimensional variational data assimilation system used to generate atmospheric analyses for naval applications (Daley and Barker 2000a, 2000b). It has been designed as a replacement for the current operational multivariate optimum interpolation (MVOI) analysis at Fleet Numerical Meteorology and Oceanography Center (FNMOC). The operational analyses are primarily used to specify the global and regional initial conditions for weather prediction using the Navy Operational Global Atmospheric Prediction System (NOGAPS; Hogan and Rosmond 1991) and the Coupled Ocean and Atmospheric Mesoscale Prediction System (COAMPS; Hodur 1997). The analyses (and forecasts) are used as environmental inputs to various naval applications, such as tropical storm motion forecasts, optimum ship and aircraft route planning, and electro-magnetic/electro-optical tactical decision aids to determine the index of refraction and duct locations. The meteorological analyses and forecasts are also used as input for military operations and missile flight tests.

Three-dimensional variational data assimilation systems (3DVAR) have several advantages over the MVOI algorithm. The solution is obtained globally so that data selection is not required and a seamless analysis is produced. Second, the 3DVAR algorithm can incorporate non-standard observations such as satellite radiances, total precipitable water or wind speed in a rigorous and physically consistent manner. Finally, 3DVAR algorithms allow greater flexibility in specifying the background error covariances.

The NAVDAS background error covariance formulation is based on a vertical eigenvector modal decomposition. This formulation permits considerable local anisotropy, such as vertical and modal variation of the horizontal correlation scales, horizontal variation of the vertical correlation lengths, and vertical variation of the mass/divergent wind coupling.

NAVDAS has been designed to be flexible in several respects. The computer codes are essentially the same for the global and mesoscale forecast models. The mesoscale analysis system is quickly relocatable to different areas of naval interest. Moreover, the code is designed to run on either massively-parallel central site computers, or local site workstations (such as shipboard). NAVDAS has also been designed to work in regions where conventional observations may be denied, and to utilize classified observations.

NAVDAS contains a number of diagnostic features for assessing the system performance and for observation quality control, including the adjoint of the analysis system. Finally, one of the most important features of NAVDAS is that it is well documented (Daley and Barker 2000a). A summary of NAVDAS may be found in Daley and Barker (2000b).

The analysis problem to be solved is given by (2.2) and (2.3), or

$$\mathbf{x_a} - \mathbf{x_b} = \mathbf{P}_b\mathbf{H}^T(\mathbf{H}\mathbf{P}_b\mathbf{H}^T + \mathbf{R})^{-1}\left(\mathbf{y} - \mathbf{H}\mathbf{x_b}\right). \tag{4.1}$$

The numerical solution may be broken into two steps. First, define the vector

$$\mathbf{d} = \mathbf{y} - \mathbf{H}\mathbf{x_b}, \tag{4.2}$$

and solve the linear system

$$(\mathbf{H}\mathbf{P}_b\mathbf{H}^T + \mathbf{R})\mathbf{z} = \mathbf{d}, \tag{4.3}$$

where **z** is the vector to be determined. Next, perform the post-multiplication step,

$$\mathbf{x_a} - \mathbf{x_b} = \mathbf{P}_b\mathbf{H}^T\mathbf{z}. \tag{4.4}$$

When (4.1) is posed following (4.2) – (4.4), the matrix

$$\mathbf{A} = (\mathbf{H}\mathbf{P}_b\mathbf{H}^T + \mathbf{R}) \tag{4.5}$$

does not need to be inverted, and the solution of (4.1) instead requires solving the linear system

$$\mathbf{A}\mathbf{z} = \mathbf{d}. \tag{4.6}$$

The major computational difficulty then becomes solving the linear system (4.6).

B. THE NAVDAS ADJOINT

Strictly speaking, only the observation locations and observation and background error covariances are required to compute the observation and background sensitivity. The NAVDAS adjoint uses the observations and background fields so that the NAVDAS quality control and data selection procedures are used. This way, the sensitivity of J to the actual observations used in the NAVDAS analysis is computed. The NAVDAS adjoint uses most of the same computer code as the NAVDAS system, and relatively simple modifications were required to compute the observation sensitivity. These differences include reading in the analysis sensitivity gradient, redefining the post-multiplication matrix, and changing the order of the post-multiplication and linear system solver steps. The NAVDAS solution method is outlined in the next sub-section.

1. The NAVDAS Adjoint Solution Method

The observation sensitivity problem to be solved is given by (2.8a), or

$$\partial J/\partial \mathbf{y} = (\mathbf{HP}_b\mathbf{H}^T + \mathbf{R})^{-1}\mathbf{HP}_b\,\partial J/\partial \mathbf{x}_a.$$

The numerical solution may be broken into two steps, following the NAVDAS solution method described in Chapter IV.A. First, perform the pre-multiplication step that is analogous to the forward analysis "post-multiplication step"

$$\mathbf{d} = \mathbf{HP}_b\,\partial J/\partial \mathbf{x}_a. \tag{4.7}$$

Next, solve the linear system

$$(\mathbf{HP}_b\mathbf{H}^T + \mathbf{R})\,\partial J/\partial \mathbf{y} = \mathbf{d}, \tag{4.8}$$

where $\partial J/\partial \mathbf{y}$ is the vector to be determined. The matrix $(\mathbf{HP}_b\mathbf{H}^T + \mathbf{R})^{-1}$ is symmetric and therefore self-adjoint (i.e., operates in the same way in the forward and adjoint directions). The main difference between the forward and adjoint code is with the post-multiplier (4.4) versus (4.7).

The vertical eigenvector decomposition used to define the background error covariance matrices in the post-multiplier $\mathbf{HP}_b$ introduces a minor complication, which is handled as follows. Consider a single vertical column of the analysis sensitivity gradient **r** and a single observation profile **q**. Then, the adjoint post-multiplication step may be written as

$$\mathbf{q} = \mathbf{HP}_b\mathbf{r} = \mathbf{E}_2\mathbf{D}_{12}\mathbf{E}_1^T\mathbf{r}, \tag{4.9}$$

where the subscripts "1" and "2" denote the locations of elements of the vectors **r** and **q**, respectively, and the forward operator **H** has been incorporated into $\mathbf{E}_2$. The eigenvector matrices are given by $\mathbf{E}_1$ and $\mathbf{E}_2$, and $\mathbf{D}_{12}$ is a diagonal matrix that is a function of the vertical mode number and the horizontal background error correlations between the two vectors, **r** and **q**.[1] Equation (4.9) is the transpose of the forward post-multiplication operation (4.4). The matrix $\mathbf{D}_{12}$ is symmetric and therefore self-adjoint. The operators $\mathbf{E}_2$ and $\mathbf{E}_1$ (and their transposes) already exist in the forward code, so the adjoint code simply requires that they be applied in a different order.

2. The Comparability between the Two-Dimensional Observation Sensitivity and the NAVDAS Adjoint Sensitivity Problems

The purpose of this section is to determine whether the observation sensitivity computed using the NAVDAS adjoint behaves as expected from the theory developed in Chapters II and III. For a single observation, the sensitivity was shown to vary as a function of the background error correlation length scale, the analysis sensitivity gradient length scale, and of the ratio of the observation error variance to the background error variance. The two-dimensional observation sensitivity and the three-dimensional NAVDAS adjoint observation sensitivity are fundamentally different problems in several important respects that limit comparisons between the two systems.

---

[1] See Daley and Barker (2000a) for a complete description of the vertical eigenvector decomposition of the background error covariance matrices.

For the two-dimensional multivariate examples in Chapter III.F.3, the NOGAPS 850-hPa temperature analysis sensitivity gradient is used as a proxy for the height analysis sensitivity gradient, and the analysis variable is temperature rather than height. As discussed in Chapter III.F.3, the geostrophic relationship relates the horizontal geopotential height field (not temperature field) to the u- and v-wind fields. The physical link between the temperature and wind fields is through the thermal wind equation, which cannot be properly represented with a two-dimensional horizontal problem, so that resulting analysis problem is instructive, but physically inconsistent.

Other major differences between the NAVDAS adjoint and the two-dimensional analysis system are that the NAVDAS adjoint analysis sensitivity gradients and background error covariances are three-dimensional, so that the sensitivity to a single observation will be affected by the analysis sensitivity gradients above and below the level of the observation (through the vertical background error covariances). Consequently, the two-dimensional and the NAVDAS adjoint observation sensitivity are not likely to exhibit the same behavior as a function of L_b and L_s. Note that this does not imply that the theory developed in Chapter III does not apply to the NAVDAS adjoint, only that direct comparisons between the two-dimensional analysis adjoint and the NAVDAS adjoint must be made carefully.

From (3.9) and (3.11), the single observation sensitivity is given by

$$\partial J/\partial \mathbf{y} = \varepsilon_b^2\left(\varepsilon_b^2+\varepsilon_r^2\right)^{-1}\sum_{n=-\infty}^{+\infty}\rho_b(x_r,x_n)\left(\partial J/\partial \mathbf{x}_a\right)_{x_n}, \tag{4.10}$$

so that the *change* of the observation sensitivity as a function of $\varepsilon_r/\varepsilon_b$ is proportional to the ratio of the background error variance to the total error variance, or

$$E = \varepsilon_b^2\big/\left(\varepsilon_b^2+\varepsilon_r^2\right) = 1/(1+\varepsilon_r^2/\varepsilon_b^2), \tag{4.11}$$

which is independent of the specified analysis sensitivity vector and the background error covariance functions. Therefore, this aspect of observation sensitivity was selected to compare the NAVDAS adjoint observation sensitivity to the two-dimensional observation sensitivity.

A single temperature observation is placed at the center (43.0°N, 154.0°W) of the large amplitude, small-scale 850-hPa temperature analysis sensitivity gradient maxima (Fig. 4.1c). The observation error is set to the NAVDAS value of $\varepsilon_r = 1.3\,^{\circ}\mathrm{K}$, which is appropriate for an automated aircraft temperature observation. The background temperature error variance is set to the NAVDAS value at the observation location, or $\varepsilon_b = 2.67\,^{\circ}\mathrm{K}$. The background errors are homogeneous for the two-dimensional univariate problem, but vary spatially for the NAVDAS adjoint (see Daley and Barker 2000a). The NAVDAS adjoint univariate temperature observation sensitivity is simulated using the NOGAPS three-dimensional temperature analysis sensitivity gradients, while the u- and v-wind analysis sensitivity gradients are set to zero.

Three sets of experiments are conducted. For the first experiment (EXP1), the observation error is set to 10% of the observation error or $\varepsilon_r = 0.13$ °K. The observation error equals 1.3 °K (or 100%) for the second experiment (EXP2), and is doubled (to 2.6 °K or 200%) for the third experiment (EXP3).

The univariate temperature single observation sensitivity results using the NAVDAS adjoint are summarized in Table 4.1, and the two-dimensional univariate temperature single observation sensitivity results are summarized in Table 4.2. In both cases, the observation sensitivity is largest when the observations are assumed to be accurate (EXP1) and decreases as the observation error increases (EXP2 and EXP3). The changes in the observation sensitivities (column 4) for the NAVDAS adjoint (Table 4.1) and the two-dimensional system (Table 4.2) are in excellent agreement with the changes predicted by (4.10) and given in column 6. Moreover, the variations of the observation sensitivity as a function of observation error for the NAVDAS adjoint and the two-dimensional observation sensitivity are in excellent agreement with each other. These results agree well with the one-dimensional univariate observation sensitivity results presented in Fig. 3.7, which is a further indication that the NAVDAS adjoint is performing as anticipated.

The total observation sensitivity for a single temperature observation (3.52a) was computed for the NAVDAS adjoint and the two-dimensional analysis system. The experimental design is the same, except that the u- and v-wind analysis sensitivity gradients from NOGAPS are used. The results, which are summarized in Table 4.3 for the NAVDAS adjoint and Table 4.4 for the two-dimensional system, show that the variations of the total temperature observation sensitivities agree well with the univariate observation sensitivity variations, which implies that the multivariate observation sensitivity components agree between the two systems.

Table 4.1. Change in the univariate sensitivity to a single temperature observation for a specified change in the observation error for the NAVDAS adjoint. Values in columns 2-4 are, respectively, the observation error standard deviations (ε_r), E from (3.11), and the changes in E, expressed as a ratio, from EXP1. Values in column 5 are the observation sensitivities and values in column 6 are the changes in the observation sensitivity, expressed as a ratio, from EXP1.

	ε_r	E	ΔE from EXP1	$\partial J/\partial y$	$\Delta \partial J/\partial y$ from EXP1
EXP1	0.13°K	0.998	1.0	0.223	1.0
EXP2	1.3°K	0.808	0.810	0.180	0.810
EXP3	2.6°K	0.513	0.514	0.114	0.511

Table 4.2. As in Table 4.1, except for the change in the univariate sensitivity to a single temperature observation for a specified change in the observation error for the two-dimensional analysis system.

	ε_r	E	ΔE from EXP1	$\partial J/\partial y$	$\Delta \partial J/\partial y$ from EXP1
EXP1	0.13°K	0.998	1.0	9.611	1.0
EXP2	1.3°K	0.808	0.810	7.782	0.810
EXP3	2.6°K	0.513	0.514	4.936	0.514

Table 4.3. As in Table 4.1, except for the change in the total sensitivity to a single temperature observation for a specified change in the observation error for the NAVDAS adjoint.

	ε_r	E	ΔE from EXP1	$\partial J/\partial y$	$\Delta\partial J/\partial y$ from EXP1
EXP1	0.13°K	0.998	1.0	0.216	1.0
EXP2	1.3°K	0.808	0.810	0.175	0.810
EXP3	2.6°K	0.513	0.514	0.111	0.514

Table 4.4. As in Table 4.3, except for the change in the total sensitivity to a single temperature observation for a specified change in the observation error for the two-dimensional analysis system.

	ε_r	E	ΔE from EXP1	$\partial J/\partial y$	$\Delta\partial J/\partial y$ from EXP1
EXP1	0.13°K	0.998	1.0	5.789	1.0
EXP2	1.3°K	0.808	0.810	4.688	0.810
EXP3	2.6°K	0.513	0.514	2.973	0.514

The observation sensitivity values for the two cases differ by more than an order of magnitude. Several experiments were conducted to understand the reasons for this difference, and it was concluded that the differences are most likely due to the contributions (through the background error correlation) to the NAVDAS adjoint observation sensitivities from the analysis sensitivity gradients at the other pressure levels. It is interesting to note that the ratio of the NAVDAS adjoint observation sensitivity to the corresponding two-dimensional observation sensitivity is the same for all three experiments. Likewise, the ratio of the NAVDAS adjoint total temperature sensitivity to the two-dimensional total temperature sensitivity is constant for all three experiments.

The results from this section indicate that the NAVDAS adjoint observation sensitivity results are consistent with the one- and two-dimensional observation sensitivity experiments in Chapter III.

C. MEASURES OF POTENTIAL OBSERVATION FORECAST IMPACT

The purpose of this subsection is to define a measure that estimates the potential contribution of an observing platform to the change in the forecast aspect J. Such information could be used to assess the relative efficiency of various adaptive observation deployments, to evaluate the existing observing network, or to design new observing systems.

The change in the forecast aspect J is defined as the projection of the analysis error (ε_a) onto the analysis sensitivity gradient, or

$$\delta J = \varepsilon_a^T \frac{\partial J}{\partial \mathbf{x}_a}. \tag{4.12}$$

The expected change in J may be written as

$$\langle \delta J \rangle = \left\langle \varepsilon_a^T \frac{\partial J}{\partial \mathbf{x}_a} \right\rangle = \left\langle \varepsilon_a^T \right\rangle \frac{\partial J}{\partial \mathbf{x}_a}, \tag{4.13}$$

while the expected variance of the change in the forecast aspect J is

$$\left\langle (\delta J)^2 \right\rangle = \left(\frac{\partial J}{\partial \mathbf{x}_\mathbf{a}} \right)^T \left\langle \varepsilon_a \varepsilon_a^T \right\rangle \frac{\partial J}{\partial \mathbf{x}_\mathbf{a}}, \tag{4.14}$$

where $\left\langle \varepsilon_a \varepsilon_a^T \right\rangle$ is the analysis error covariance matrix given by

$$\mathbf{P}_a = \mathbf{P}_b - \mathbf{P}_b \mathbf{H}^T (\mathbf{H}\mathbf{P}_b\mathbf{H}^T + \mathbf{R})^{-1} \mathbf{H}\mathbf{P}_b. \tag{4.15}$$

The second term in (4.15) represents the reduction to the background error covariances due to the presence of the observations. Combining (4.14) with (4.15) gives

$$\left\langle (\delta J)^2 \right\rangle = \left(\frac{\partial J}{\partial \mathbf{x_a}} \right)^T \mathbf{P}_b \frac{\partial J}{\partial \mathbf{x_a}} - \left(\frac{\partial J}{\partial \mathbf{x_a}} \right)^T \mathbf{P}_b \mathbf{H}^T (\mathbf{H}\mathbf{P}_b \mathbf{H}^T + \mathbf{R})^{-1} \mathbf{H}\mathbf{P}_b \frac{\partial J}{\partial \mathbf{x_a}}, \qquad (4.16)$$

which may be expanded as

$$\begin{aligned} \left\langle (\delta J)^2 \right\rangle &= \left(\frac{\partial J}{\partial \mathbf{x_a}} \right)^T \mathbf{P}_b \frac{\partial J}{\partial \mathbf{x_a}} \\ &\quad - \left(\frac{\partial J}{\partial \mathbf{x_a}} \right)^T \mathbf{P}_b \mathbf{H}^T (\mathbf{H}\mathbf{P}_b \mathbf{H}^T + \mathbf{R})^{-1} (\mathbf{H}\mathbf{P}_b \mathbf{H}^T + \mathbf{R}) (\mathbf{H}\mathbf{P}_b \mathbf{H}^T + \mathbf{R})^{-1} \mathbf{H}\mathbf{P}_b \frac{\partial J}{\partial \mathbf{x_a}}. \end{aligned} \qquad (4.17)$$

Substituting the observation sensitivity definition (2.8a) into (4.17) gives

$$\left\langle (\delta J)^2 \right\rangle = \left(\frac{\partial J}{\partial \mathbf{x_a}} \right)^T \mathbf{P}_b \frac{\partial J}{\partial \mathbf{x_a}} - \left(\frac{\partial J}{\partial \mathbf{y}} \right)^T (\mathbf{H}\mathbf{P}_b \mathbf{H}^T + \mathbf{R}) \frac{\partial J}{\partial \mathbf{y}}, \qquad (4.18)$$

which may be interpreted as the expected variance of the change in the forecast aspect due to the background and the observations. Equation (4.18) may be divided into separate contributions from the background and the observations, or

$$\left\langle (\delta J)^2 \right\rangle = \left\langle (\delta J)^2 \right\rangle_b - \left\langle (\delta J)^2 \right\rangle_o, \qquad (4.19)$$

where

$$\left\langle (\delta J)^2 \right\rangle_b = \left(\frac{\partial J}{\partial \mathbf{x_a}} \right)^T \mathbf{P}_b \frac{\partial J}{\partial \mathbf{x_a}}, \qquad (4.20)$$

and

$$\left\langle (\delta J)^2 \right\rangle_o = \left(\frac{\partial J}{\partial \mathbf{y}}\right)^T (\mathbf{HP}_b\mathbf{H}^T + \mathbf{R})\frac{\partial J}{\partial \mathbf{y}}, \tag{4.21}$$

where the subscripts (b) and (o) refer to the background and observations, respectively. Equation (4.21) may be interpreted as the reduction in the expected variance of the change in J due to the observations.

The reduction of the expected variance of δJ computed from (4.21) is a scalar number corresponding to the entire set of observations. It may also be computed for specified subsets of observations, such as radiosondes, cloud-drift winds, or different adaptive observation configurations, so that their relative contributions can be assessed. For targeting applications, $\left\langle (\delta J)^2 \right\rangle_o$ can be used to rank different adaptive observation configurations according to their potential impact on J. It is important to note that the scalar numbers given by (4.18) or (4.21) are always positive, and that the actual impact (i.e., sign of δJ) cannot be determined except by assimilating the observations and computing the forecast. It is also important to realize that the term $(\mathbf{HP}_b\mathbf{H}^T + \mathbf{R})$ in (4.18) and (4.21) always involves the entire set of observations, so that changing the properties (location or assumed error variance) of even one observation will change the scalar measure for all other observations.

Doerenbecher and Bergot (2000) define an impact function

$$\delta J = \left(\frac{\partial J}{\partial \mathbf{y}_o}\right)^T \left(\mathbf{y}_o - \mathbf{H}_o(\mathbf{x}_\mathbf{b})\right), \tag{4.22}$$

where the subscript (o) refers to the selected observation platform. The impact function gives an estimate of the influence of a specified observation type on the forecast aspect J. Strictly speaking, this measure can only be computed after the observations have been taken, as the sign of δJ cannot be known in advance.

D. OBSERVATION ADJOINT SENSITIVITY RESULTS

The analysis sensitivity gradients were computed in an *a posteriori* sense in that the cost function J is the energy-weighted forecast error for the NOGAPS forecast starting from the FNMOC/NOGAPS operational initial conditions valid at the target time of 00 UTC 7 February 1999 and verifying 72 hours later at 00 UTC 10 February 1999. This case corresponds to the largest 72-h forecast error in a forecast verification area centered over the western United States and Canada and given by (30°N – 60°N and 150°W – 100°W) for a three-year period from 1997 – 1999 (R. Langland, NRL – Monterey, personal communication). The analysis sensitivity gradients for the 850-, 700-, 500-, and 400-hPa levels are shown in Figs. 4.1 through 4.4, respectively. The amplitudes of the analysis sensitivity gradients are largest at these levels, and decrease above and below these levels.

The high amplitude, small-scale temperature analysis sensitivity gradient sub-structure centered about 43°N and 155°W in Fig. 4.1c has maximum amplitude near 850 hPa and weakens as it tilts westward with increasing height (Figs. 4.2c – 4.4c). In contrast, the moderate amplitude, large-scale temperature analysis sensitivity gradient sub-structure centered about 40°N and 175°W in Fig. 4.1c has maximum amplitude near

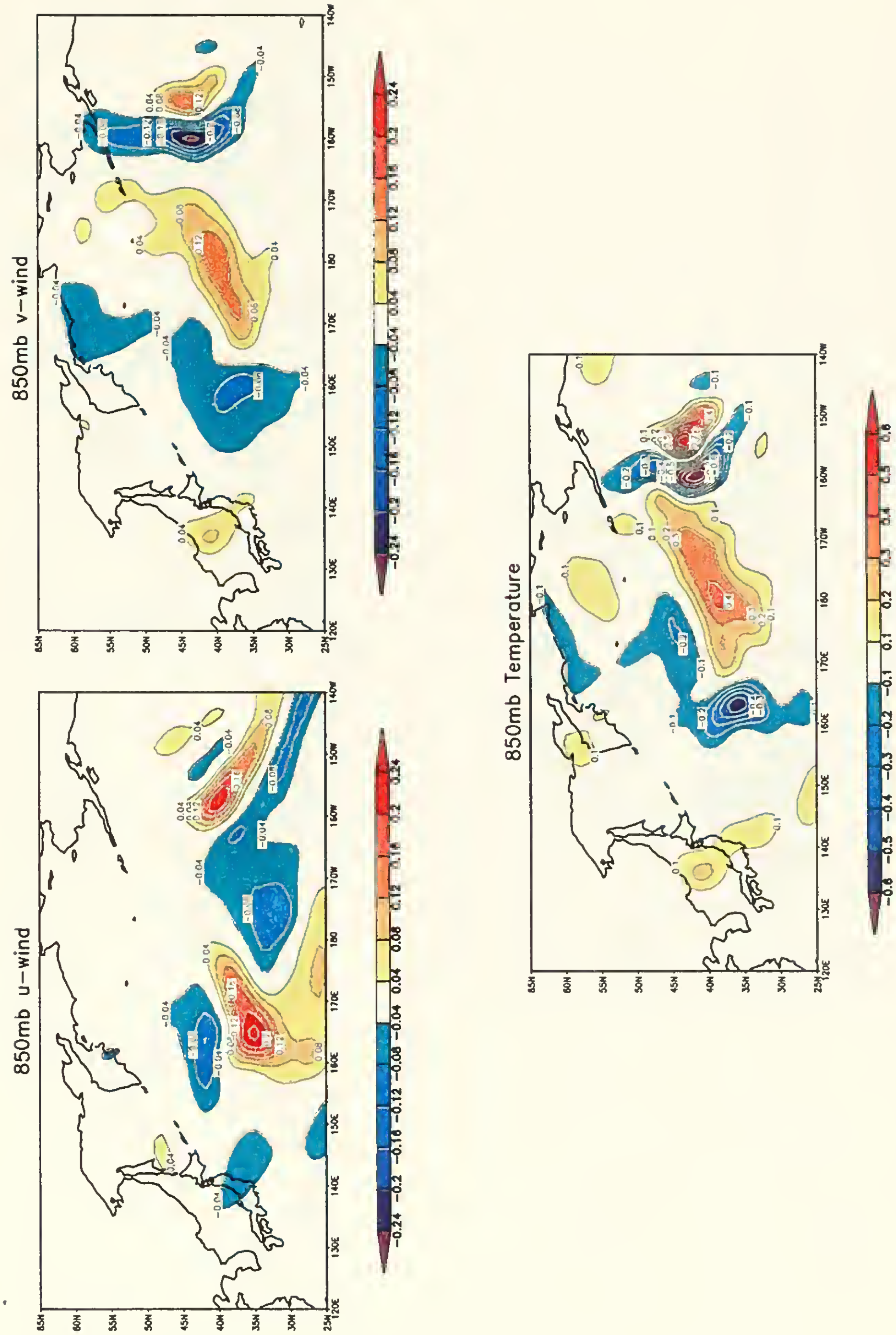

850mb u-wind
850mb v-wind
850mb Temperature
65N
60N
55N
50N
45N
40N
35N
30N
25N
120E
130E
140E
150E
160E
170E
180
170W
160W
150W
140W
-0.24 -0.2 -0.16 -0.12 -0.08 -0.04 0.04 0.08 0.12 0.16 0.2 0.24
-0.6 -0.5 -0.4 -0.3 -0.2 -0.1 0.1 0.2 0.3 0.4 0.5 0.6

Figure 4.1. Sensitivity of the 72-h NOGAPS energy-weighted forecast error with respect to the FNMOC/NOGAPS 850-hPa initial (a) u-wind component, (b) v-wind component, and (c) temperature fields valid at the target time of 00 UTC 7 February 1999. The forecast verification area (not shown) is centered over the western United States and Canada (30 °N – 60°N and 150°W – 100°W).

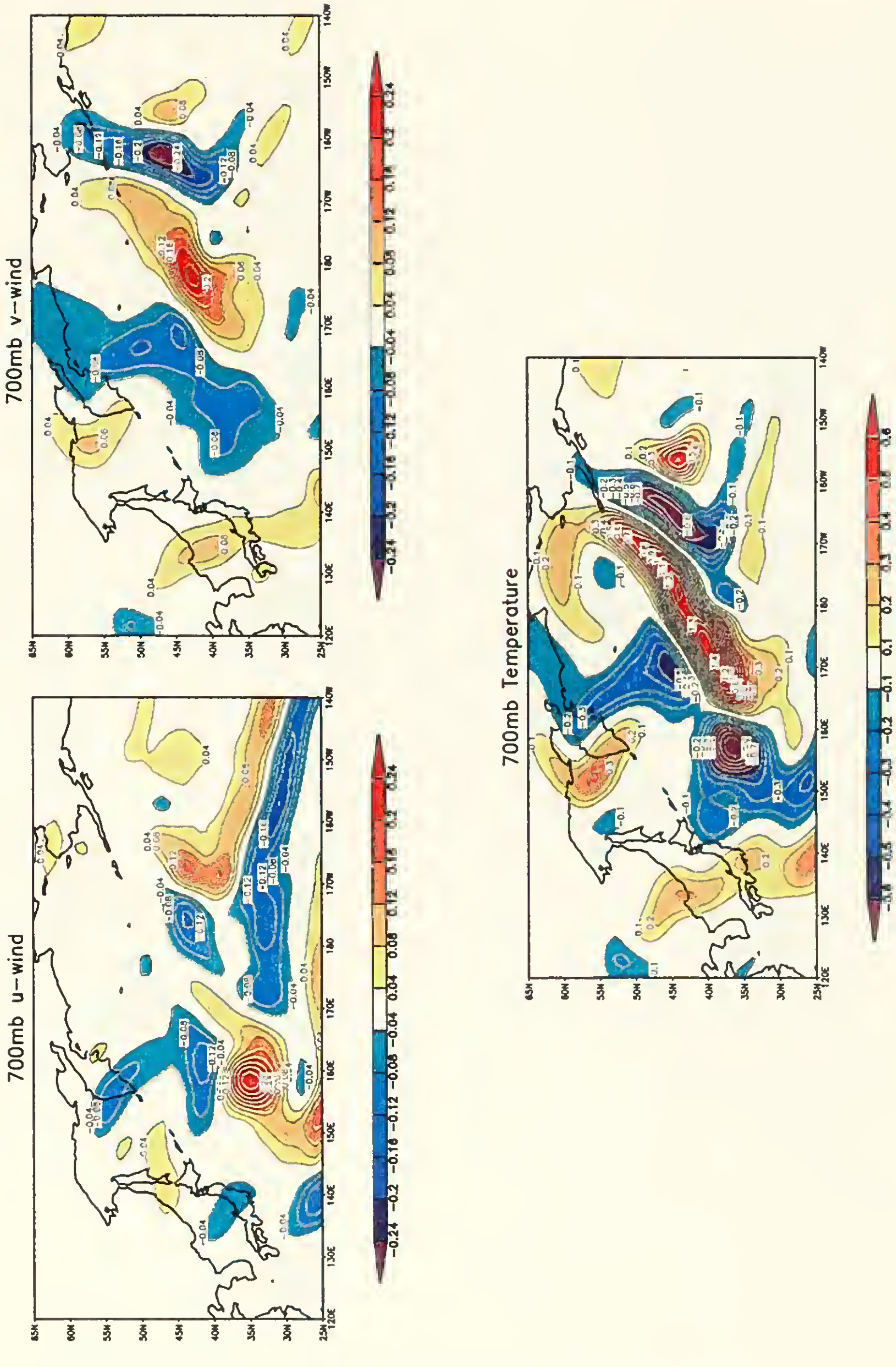
700mb u-wind
700mb v-wind
700mb Temperature

Figure 4.2. As in Fig. 4.1, except for the sensitivity of the 72-h NOGAPS energy-weighted forecast error with respect to the FNMOC/NOGAPS 700-hPa initial (a) u-wind component, (b) v-wind component, and (c) temperature fields valid at the target time of 00 UTC 7 February 1999.

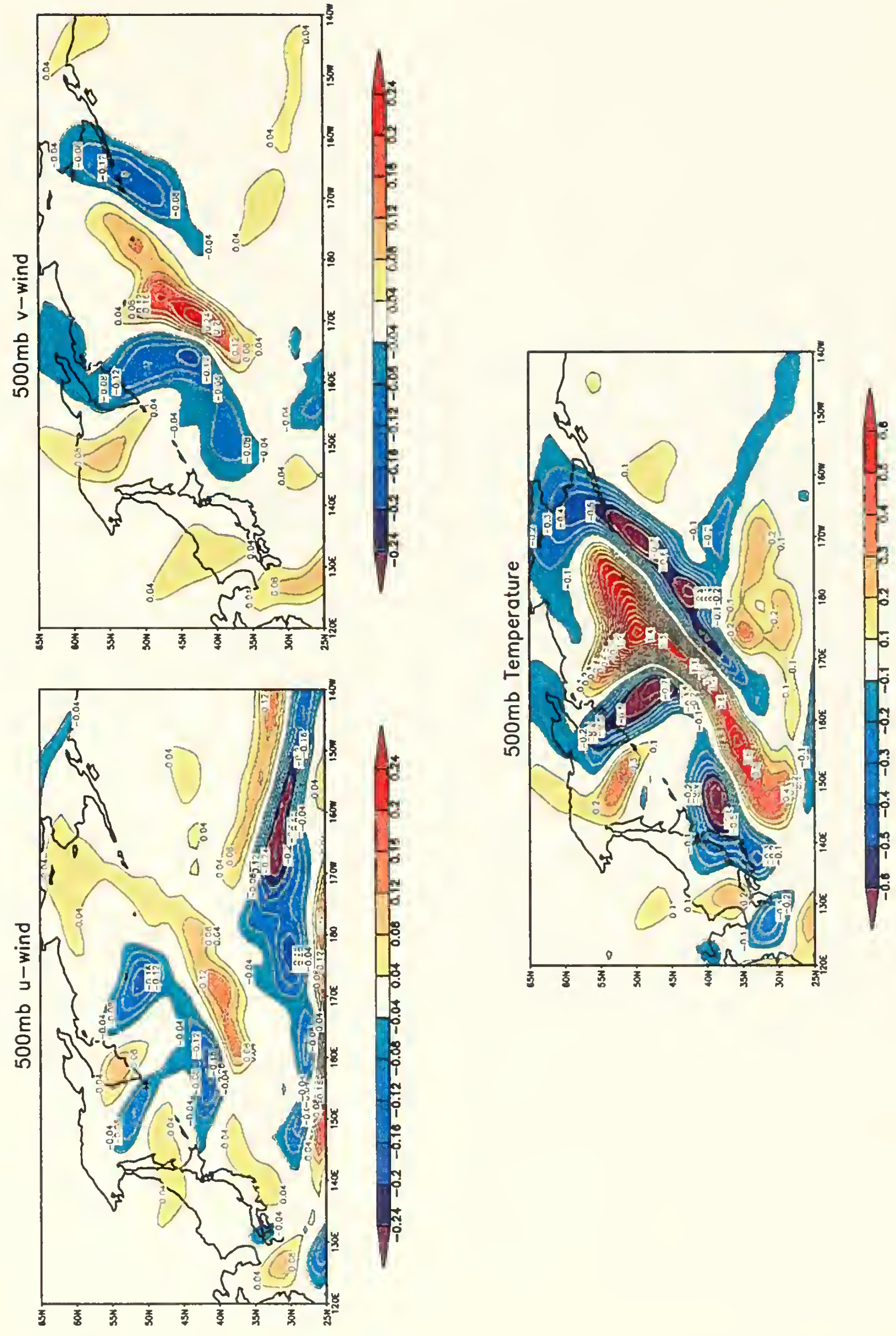
500mb v-wind
500mb u-wind
500mb Temperature
-0.24 -0.2 -0.16 -0.12 -0.08 -0.04 0.04 0.08 0.12 0.16 0.2 0.24
-0.6 -0.5 -0.4 -0.3 -0.2 -0.1 0.1 0.2 0.3 0.4 0.5 0.6
65N 60N 55N 50N 45N 40N 35N 30N 25N
120E 130E 140E 150E 160E 170E 180 170W 160W 150W 140W

Figure 4.3. As in Fig. 4.1, except for the sensitivity of the 72-h NOGAPS energy-weighted forecast error with respect to the FNMOC/NOGAPS 500-hPa initial (a) u-wind component, (b) v-wind component, and (c) temperature fields valid at the target time of 00 UTC 7 February 1999.

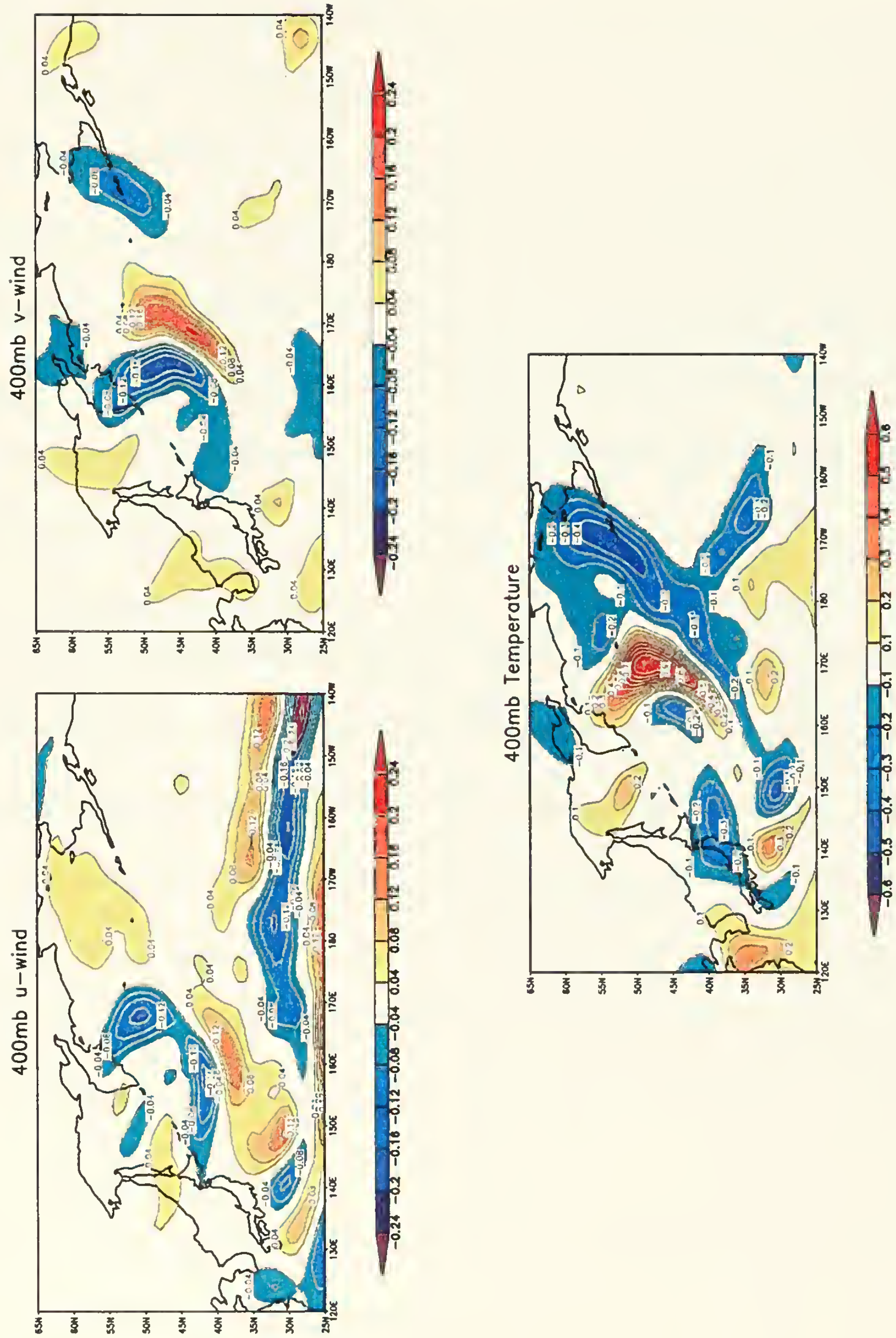
400mb v-wind
400mb u-wind
400mb Temperature
65N
60N
55N
50N
45N
40N
35N
30N
25N
120E
130E
140E
150E
160E
170E
180
170W
160W
150W
140W
-0.24 -0.2 -0.16 -0.12 -0.08 -0.04 0.04 0.08 0.12 0.16 0.2 0.24
-0.6 -0.5 -0.4 -0.3 -0.2 -0.1 0.1 0.2 0.3 0.4 0.5 0.6

Figure 4.4. As in Fig. 4.1, except for the sensitivity of the 72-h NOGAPS energy-weighted forecast error with respect to the FNMOC/NOGAPS 400-hPa (a) initial temperature, (b) u-wind component, and (c) v-wind component fields valid at the target time of 00 UTC 7 February 1999.

500 hPa and strong westward (baroclinic) vertical tilt. The spatial scale of the large-scale temperature analysis sensitivity sub-structure increases with increasing height (up to near 500 hPa). The v-wind analysis sensitivity gradient extrema have similar amplitude for the four pressure levels and tend to shift farther west with increasing height. The largest amplitudes for the 850 hPa and 700 hPa u-wind analysis sensitivity gradient are associated with the temperature and v-wind analysis sensitivity gradient extrema, while the largest amplitudes at 500 and 400 hPa are associated with the northern branch of the subtropical jet south of 40°N.

1. Experimental Design

The observations are derived from the global meteorological reports available operationally at FNMOC and valid for a six-hour window centered on the target time. While the actual observed values and background fields are not required to compute the observation and background sensitivities, the observed values and background fields are required for the NAVDAS analysis pre-processing and observation quality control (QC) algorithms. In this way, the NAVDAS adjoint computes the sensitivities to the observations and background taking into account the actual observations used by the NAVDAS assimilation cycle (with the exception of any hypothetical targeted observations). The NAVDAS global configuration with one-degree lat./long. grid spacing and 16 mandatory[2] pressure levels from 1000 hPa to 10 hPa is used, although the input NOGAPS adjoint temperature, u- and v-wind analysis sensitivity gradients are available only for the mandatory pressure levels up to 100 hPa. The analysis sensitivity gradients are assumed to be zero above 100 hPa, which is appropriate since the analysis sensitivity gradients for this case are maximized in the lower to mid-troposphere and are small in the upper troposphere.

---

[2] The mandatory or standard pressure levels are 1000, 925, 850, 700, 500, 400, 300, 250, 200, 150, 100, 70, 50, 30, 20, and 10 hPa.

The observations are subjected to extensive QC, particularly for radiosondes, TOVS brightness temperatures, and aircraft temperatures and winds. In addition, observations with high spatial density are thinned to remove data redundancy and to lessen the computational expense. For example, every third DMSP (Defense Meteorological Satellite Program) SSM/I (Special Sensor Microwave Imager) wind speed retrieval is used, which corresponds roughly to a spacing of one degree between the observations. The SSM/I total precipitable water retrievals are not used since the sensitivity of J with respect to moisture observations is not considered. The infrared and visible cloud-drift winds, and the water vapor winds, have high spatial and temporal density with non-uniform spatial coverage. In the future, sophisticated algorithms will be implemented to thin these observations. For the present, every third cloud or water vapor wind is used. The aircraft winds are thinned by specialized aircraft QC algorithms.

During the winter months of 1999, numerous WSR flights sampled targets defined by NCEP for the eastern North Pacific Ocean (Szunyogh *et al.* 2000). One of the targeting sorties coincides with the period of interest (00 UTC 7 February 1999). The G-IV aircraft deployed out of Hickam AFB, Honolulu, Hawaii, released 11 dropsondes. These observations are included in the observation sensitivity calculations.

A summary of the observations valid for the 3-h time window centered on 00 UTC 7 February 1999 is given in Table 4.5. Many observations are rejected because they do not fall within the 3-h analysis time window. The large numbers of rejected and thinned radiosonde observations are because temperatures rather than geopotential heights are used by NAVDAS, and removal of redundant radiosonde/ pilot balloon reports. The large number of rejected and thinned TIROS[3] Operational Vertical Sounder (TOVS) brightness temperatures are due to unused TOVS channels, or QC rejected observations over snow, ice or land. Of the nearly one million global available observations, 208242 are used by the NAVDAS adjoint.

Table 4.5. Summary of the observations valid for the 6-h time window centered on 00 UTC 7 February 1999. Column 1 denotes the observing platform; column 2 is the number of observations; column 3 is the number of rejected or thinned observations, and column 4 gives the total number of observations.

Observation type	Accepted	Rejected or Thinned	Total
Surface land	33872	38022	71894
Surface marine	6222	5233	11455
Aircraft reports	11799	25382	37181
Cloud and water vapor winds	11124	38123	49247
SSM/I windspeed	2698	17200	19898
Radiosonde and pilot balloons	73852	28567	102419
Automated aircraft ascent and descent	5910	6940	12850
TOVS brightness temperatures	62765	589852	652617
SSM/I total precipitable water	0	19903	19903
Total	208242	707250	977464

---

[3] Television Infra-Red Observation Satellite

2. Discussion of NAVDAS Observation Sensitivity Results

The magnitudes of the observation sensitivities for temperature, u- and v-wind observations from 450 – 550 hPa (for all instruments except TOVS) are in Fig. 4.5. The inverted "V" pattern of observations corresponds to the G-IV flight. Overall, the observation sensitivity is largest for observations that are relatively isolated, although considerable variation occurs. In Chapter III, the row of the transposed Kalman gain matrix corresponding to an observation of interest was plotted to help understand observation sensitivity. Even though $\mathbf{K}^T$ is not available explicitly for the NAVDAS adjoint (see Chapter IV.B), the behavior of the observation sensitivity can be inferred based on the results of Chapter III. The NAVDAS adjoint observation sensitivity is illustrated by considering several observations in detail.

The largest sensitivity (red circle) to a u-wind observation for the 450 – 500-hPa layer (Fig. 4.5a) occurs for the water vapor wind observation near 35°N, 178°W, and appears to be associated with the high-amplitude, large-scale u-wind analysis sensitivity gradients at 500 and 400 hPa (Figs. 4.3a and 4.4a) that are related to the northern branch of the subtropical jet. The corresponding v-wind observation sensitivity is very weak, largely because the v-wind analysis sensitivity gradients near the observation are also weak.

The largest sensitivities (red circle) to v-wind observations (Fig. 4.5b) occur for the water vapor winds near 45°N, 169°E, and 43°N, 178°E. These observations are located near the extrema of the high-amplitude, large-scale temperature analysis

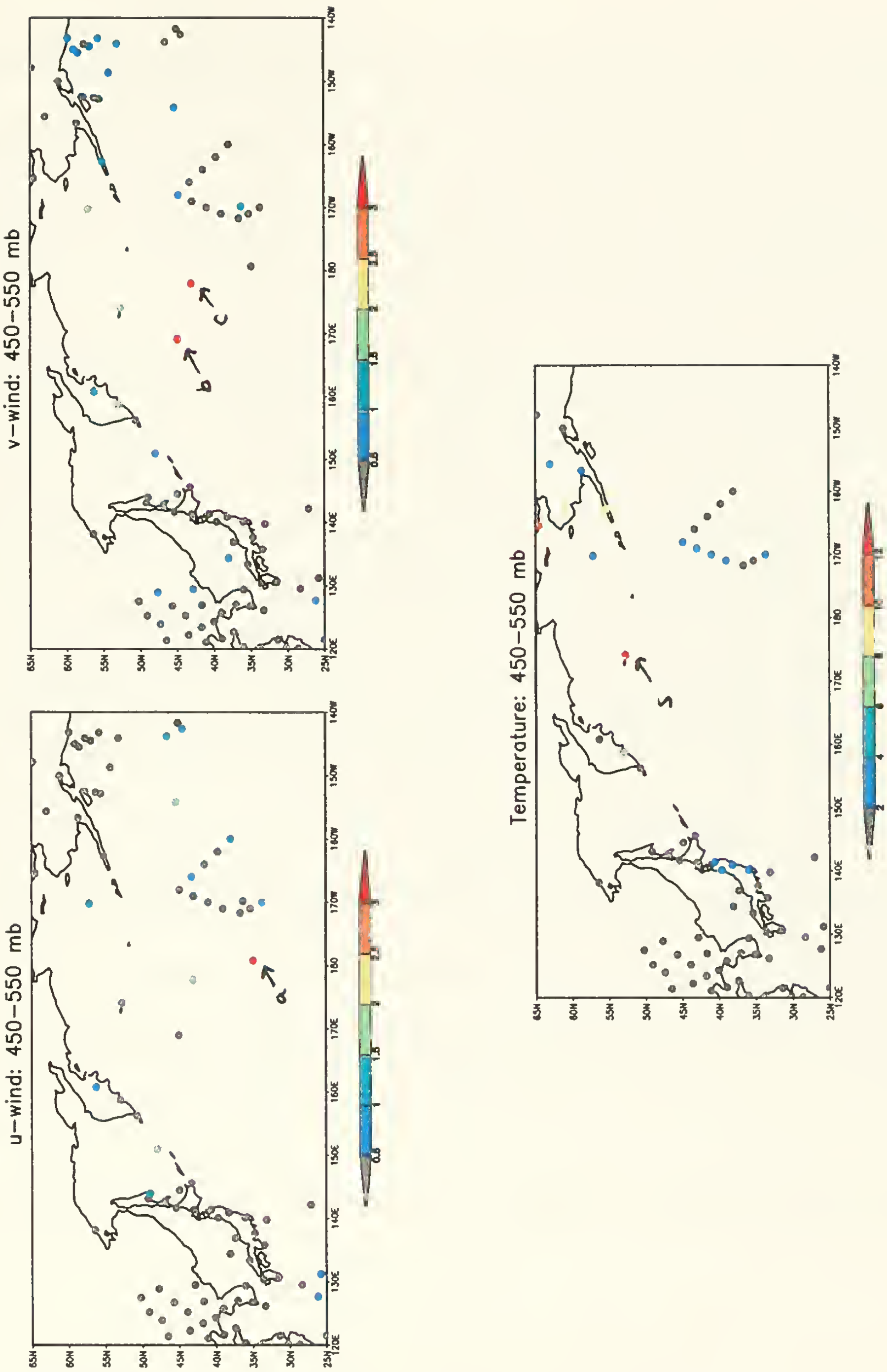

v-wind: 450-550 mb
b
c
u-wind: 450-550 mb
a
Temperature: 450-550 mb
s
65N
60N
55N
50N
45N
40N
35N
30N
25N
120E
130E
140E
150E
160E
170E
180
170W
160W
150W
140W

Figure 4.5. Magnitude of the sensitivity of the forecast aspect J to the (a) u-wind observation components, (b) v-wind observation components, and (c) temperature observations between 450 and 550 hPa valid at 00 UTC 7 February 1999 for the control plus G-IV adaptive observations (CTL+G-IV) case. The letter "a" indicates the largest u-wind observation sensitivity, while the "b" and "c" indicate the largest v-wind observation sensitivities, and the "s" indicates the Shemya radiosonde station.

sensitivity gradients at 700, 500, and 400 hPa (Figs. 4.2c, 4.3c, 4.4c). The 500-hPa v-wind analysis sensitivity gradients are large in amplitude and scale near the observation at 45°N, 169°E, but not near the observation at 43°N, 178°E. The results from Chapter III.F.3 suggest that the wind observation sensitivities are dominated by the projection of $\mathbf{K}^T$ onto the temperature analysis sensitivity gradient, with weaker contributions from the univariate wind components (e.g., the projection of $\mathbf{K}^T$ onto the v-wind analysis sensitivity gradient). Therefore, the large v-wind observation sensitivities are probably due to the large temperature analysis sensitivity gradients with lesser contributions from the v-wind analysis sensitivity gradients. The observation sensitivity is also a function of the analysis sensitivity gradients at adjacent levels through the background error covariances. The results in Chapter III suggest that the largest wind observation sensitivities are phase-shifted with the extrema of the temperature analysis sensitivity gradient. However, it is not possible to ascertain whether this phase shift occurs for the NAVDAS adjoint observation sensitivity results because of the westward tilt with height of the temperature analysis sensitivity gradients and the effects of the vertical background error correlations on the observation sensitivities. Higher observation density may also be needed to determine whether the phase shift exists.

The sensitivity to the 500-hPa temperature observation (Fig. 4.5c) from the conventional radiosonde launched from Eareckson Air Station on Shemya Island (located at the westernmost point (52.72°N, 174.10°E) in the Aleutian Island chain approximately 2400 km southwest of Anchorage, AK) is more than three times greater than the next

largest 500-hPa temperature observation sensitivities for Nome (64.50°N, 165.43°W), Bethel (60.78°N, 161.80°W), and Sand Point (55.20°N, 167.72°W), and is approximately ten times larger than the maximum sensitivity to a G-IV dropsonde temperature. The results from Chapter III.F demonstrated that the observation sensitivity is maximized when an accurate temperature observation is placed near the center of a large amplitude temperature analysis sensitivity gradient with a spatial scale similar to the background error correlation length scale. The 500-hPa temperature analysis sensitivity gradient near Shemya (Fig. 4.3c) is large in amplitude and has a spatial scale similar to that of the NAVDAS background error correlation length scale of 385 km, and these factors contribute to the large sensitivity to the 500-hPa temperature observation. Two additional factors that further enhance the temperature observation sensitivity are that the observation is relatively isolated and that the observation is assumed to be much more accurate than the background temperature error (0.90 °K versus 1.73 °K).

These results support the conclusions from Chapter III that the observation sensitivity is largest for relatively isolated, accurate observations near large-scale analysis sensitivity gradients. The relatively weak observation sensitivities noted for the G-IV adaptive observations occur because the G-IV flight did not sample the large-scale analysis sensitivity gradients.

The magnitudes of the sensitivities of J to the TOVS Microwave Sounding Unit (MSU) channel 2 brightness temperatures, which have a broad vertical weighting function that peaks near 700 hPa (Smith *et al.* 1979), are shown in Fig. 4.6. The

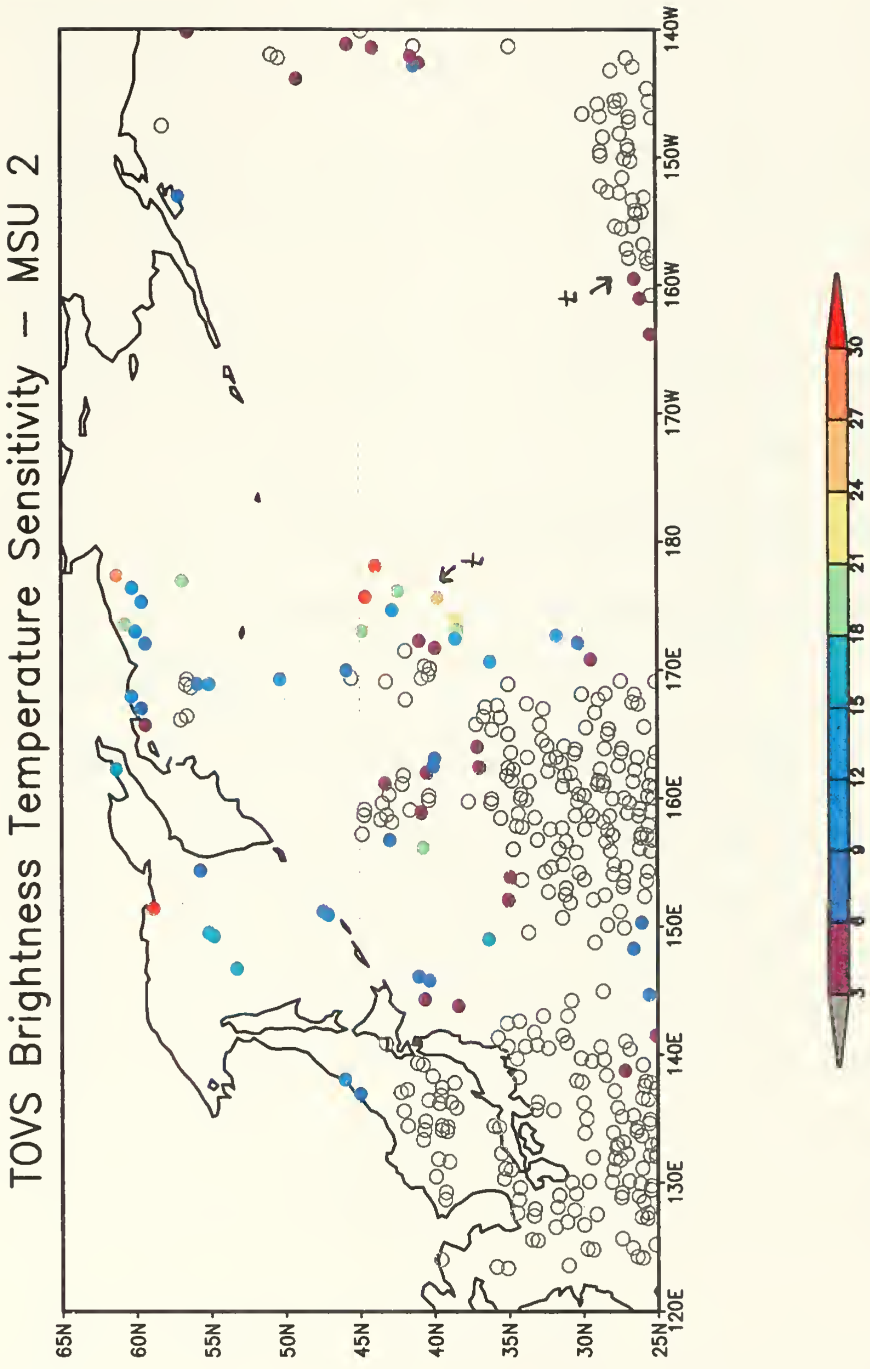
TOVS Brightness Temperature Sensitivity – MSU 2
65N
60N
55N
50N
45N
40N
35N
30N
25N
120E
130E
140E
150E
160E
170E
180
170W
160W
150W
140W
t
t
3
6
9
12
15
18
21
24
27
30

Figure 4.6. Magnitude of the sensitivity of the forecast aspect *J* to the TOVS MSU Channel 2 brightness temperatures valid at 00 UTC 7 February 1999 for the control plus G-IV adaptive observations (CTL+G-IV) case. The time-window data discontinuities are indicated by the letter "t" (see text for more details). The open circles correspond to magnitudes less than 3.0.

maximum observation sensitivities occur where large analysis sensitivity gradients (amplitude and scale) coincide either with an abrupt discontinuity in the observation density, or with a relatively isolated observation. Observation discontinuities frequently occur with TOVS brightness temperatures for a variety of reasons. For example, polar-orbiting satellite instruments such as TOVS observe the atmosphere continuously, and the observations are selected or rejected according to the time difference between the observations and analysis. Two instances of time-window data discontinuities are indicated by the letter "t" in Fig. 4.6. The data discontinuity near 45°N, 175°E that occurs in the middle of the large 700-hPa temperature analysis sensitivity gradient is associated with large observation sensitivities.

Other discontinuities in the TOVS brightness temperatures are associated with larger observation errors, and these have important implications for data assimilation systems. For example, the TOVS brightness temperatures over land and ice are more difficult to assimilate properly and are eliminated in the present NAVDAS configuration, which creates a discontinuity in the brightness temperature observation density along the coastlines and ice-edge boundaries. The brightness temperatures along these boundaries contain contributions from the different surface types and have larger representativeness errors than the brightness temperatures over the open oceans. Abrupt changes in the data density also occur for the less accurate observations along the edges of the satellite scan (*cf.*, Chapter III.F.3.d). If the MSU observation errors are incorrectly assumed to be spatially homogeneous, and the data discontinuities coincide with large-scale analysis sensitivity gradients, the sensitivity to the relatively inaccurate observations along the data discontinuity will be larger than the sensitivity to the more accurate (data dense) observations. This implies that the less accurate observations have greater potential to change the forecast aspect J, and influence the analysis. As demonstrated in Chapter III.C.4.b and Chapter III.E.3.c, increasing the assumed observation error variance decreases both the observation sensitivity and the influence of the observation on the analysis. These results, which illustrate a non-targeting application of the data assimilation adjoint theory, highlight the importance of properly specifying the observation errors.

E. TARGETING STRATEGIES WITH THE NAVDAS ADJOINT

A hypothetical flight path that can be achieved by the NOAA (National Oceanic and Atmospheric Administration) Gulfstream (G-IV) (M. Shapiro, NCAR, personal communication) is defined with the outbound and return flight legs that are approximately 1950 km and the two shorter flight legs that are around 450 km. One dropsonde is placed near the take-off/landing site and at each point where the flight track changes direction. Four dropsondes are evenly spaced along each flight leg for a total of 20 dropsondes per flight. Each dropsonde is assumed to measure temperature, wind speed and direction at 50 hPa increments from 200 and 1000 hPa. The dropsonde observation errors are assigned the values assumed by NAVDAS for a conventional radiosonde.

Although three airfields have been selected for the hypothetical aircraft deployment, their selection is not intended to imply that these locations would be used for actual targeting experiments. Elmendorf AFB near Anchorage, Alaska, which was used for NORPEX and subsequent WSR missions, gives access to the eastern North Pacific Ocean. Tokyo International Airport in Japan allows sampling of the western Pacific Ocean. Finally, Eareckson Air Station on Shemya Island allows for sampling of the mid-Pacific Ocean. The results from Chapter III.F.3.d demonstrate that the total temperature, u- and v-wind observation sensitivities tend to be dominated by the contribution from the temperature analysis sensitivity gradient. Accordingly, the flight path from each airfield is defined so that the temperature analysis sensitivity gradients are most thoroughly surveyed with the pre-defined flight track.

An additional hypothetical flight track corresponds to the backwards "N" pattern from Chapter III.F.3.c. The two observations at the southeast corner are not used so that the total number of dropsondes (20) is consistent with the other hypothetical flight tracks.

The G-IV targeting flight in Fig. 4.5 is included as an alternate targeting configuration. The mandatory and significant pressure level temperature and wind observations were included so that the total number of adaptive observations from the 11 dropsondes is slightly larger than for the hypothetical flight tracks (see Table 4.6).

Another hypothetical targeting strategy utilizes the new driftsonde observing system that is being developed by the National Center for Atmospheric Research (NCAR) Atmospheric Technology Division as a candidate observing system for the (proposed) The Hemispheric Observing system Research and Predictability Experiment (THORPEX)(M. Shapiro, NCAR, personal communication). The driftsonde observing system consists of a large polyethylene balloon with an attached gondola that can carry up to 24 Global Positioning Satellite (GPS) dropsondes. The carrier balloon ascends to between 50 and 100 hPa and drifts with the prevailing stratospheric winds at a constant pressure level for up to five days. Dropsondes may be released at specified intervals (e.g., every 6 hours). The dropsonde observations are collected and sent via a low-earth-orbiting satellite (LEO) to ground processing stations for real-time dissemination on the Global Telecommunication System (GTS).

Table 4.6. Observation counts for the different observing platforms for the hypothetical targeting experiments for a 3-h time window centered on 00 UTC 7 February 1999. CTL: control or conventional observing networks; CTL+GIV: control plus G-IV flight track; CTL+e1: control plus Elmendorf flight track; CTL+s1: control plus Shemya flight track; CTL+t1: control plus Tokyo flight track; CTL+c4: control plus Chapter III.F.3.c flight path; and CTL+d1: control plus driftsonde network.

Observing Platform	CTL	CTL +GIV	CTL +e1	CTL +s1	CTL +t1	CTL +c4	CTL +d1
Surface land	33872	33872	33872	33872	33872	33872	33872
Surface marine	6222	6222	6222	6222	6222	6222	6222
Aircraft	17709	17709	17709	17709	17709	17709	17709
Cloud winds – infrared	4812	4812	4812	4812	4812	4812	4812
Cloud winds – visible	126	126	126	126	126	126	126
Water vapor winds	6186	6186	6186	6186	6186	6186	6186
SSM/I windspeed	2698	2698	2698	2698	2698	2698	2698
TOVS brightness temperatures	62765	62765	62765	62765	62765	62765	62765
Adaptive dropsondes	0	1253	1020	1020	1020	1020	2295
Conventional radiosondes	72599	72599	72599	72599	72599	72599	72599
Total	206996	208249	20816	20816	20816	20816	209291

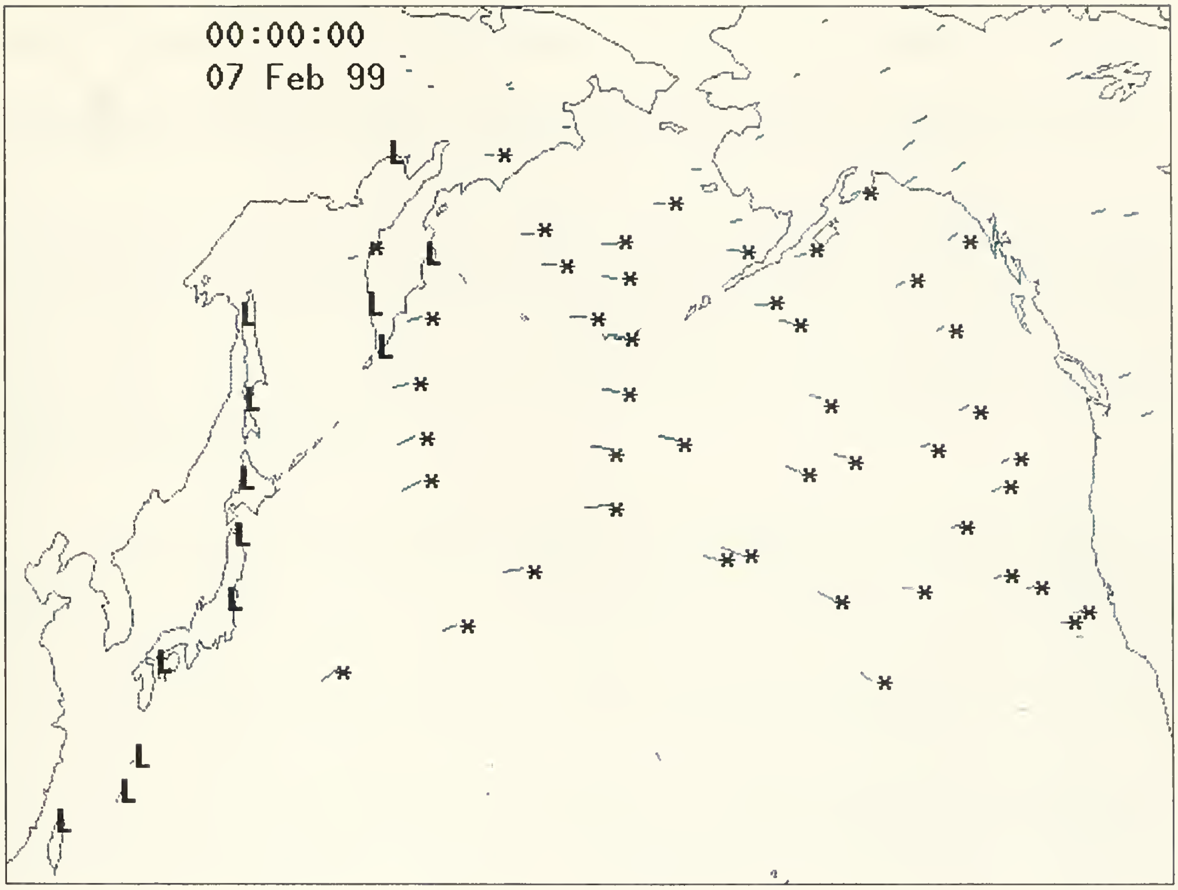

Figure 4.7. Hypothetical driftsonde locations, denoted by the flag and "*", and valid for 00 UTC 7 February 1999. The approximate locations of the 13 launch sites are indicated by a "L". The driftsonde carrier balloons were assumed to be launched at 12-h intervals beginning with 00 UTC 2 February 1999, and the 50-hPa FNMOC operational wind analyses were used to advect the carrier balloons. The driftsonde locations over the oceans are assumed to correspond to dropsonde releases.

An example of the hypothetical driftsonde locations valid for 00 UTC 7 February 1999 is shown in Fig. 4.7. The driftsonde locations were computed by R. Langland of NRL-Monterey using the atmospheric tracer capabilities associated with the Vis5d software package. The driftsonde carrier balloons were assumed to be launched at 12-h intervals beginning with 00 UTC 2 February 1999 from 13 launch sites (Fig. 4.7) along the east coast of Asia. The 50-hPa FNMOC operational wind analyses were used to to 24 Global Positioning Satellite (GPS) dropsondes. The carrier balloon ascends to between 50 and 100 hPa and drifts with the prevailing stratospheric winds at a constant pressure level for up to five days. Dropsondes may be released at specified intervals (e.g., every 6 hours). The dropsonde observations are collected and sent via a low-earth-orbiting satellite (LEO) to ground processing stations for real-time dissemination on the Global Telecommunication System (GTS).

Table 4.6. Observation counts for the different observing platforms for the hypothetical targeting experiments for a 3-h time window centered on 00 UTC 7 February 1999. CTL: control or conventional observing networks; CTL+GIV: control plus G-IV flight track; CTL+e1: control plus Elmendorf flight track; CTL+s1: control plus Shemya flight track; CTL+t1: control plus Tokyo flight track; CTL+c4: control plus Chapter III.F.3.c flight path; and CTL+d1: control plus driftsonde network.

Observing Platform	CTL	CTL +GIV	CTL +e1	CTL +s1	CTL +t1	CTL +c4	CTL +d1
Surface land	33872	33872	33872	33872	33872	33872	33872
Surface marine	6222	6222	6222	6222	6222	6222	6222
Aircraft	17709	17709	17709	17709	17709	17709	17709
Cloud winds – infrared	4812	4812	4812	4812	4812	4812	4812
Cloud winds – visible	126	126	126	126	126	126	126
Water vapor winds	6186	6186	6186	6186	6186	6186	6186
SSM/I windspeed	2698	2698	2698	2698	2698	2698	2698
TOVS brightness temperatures	62765	62765	62765	62765	62765	62765	62765
Adaptive dropsondes	0	1253	1020	1020	1020	1020	2295
Conventional radiosondes	72599	72599	72599	72599	72599	72599	72599
Total	206996	208249	20816	20816	20816	20816	209291

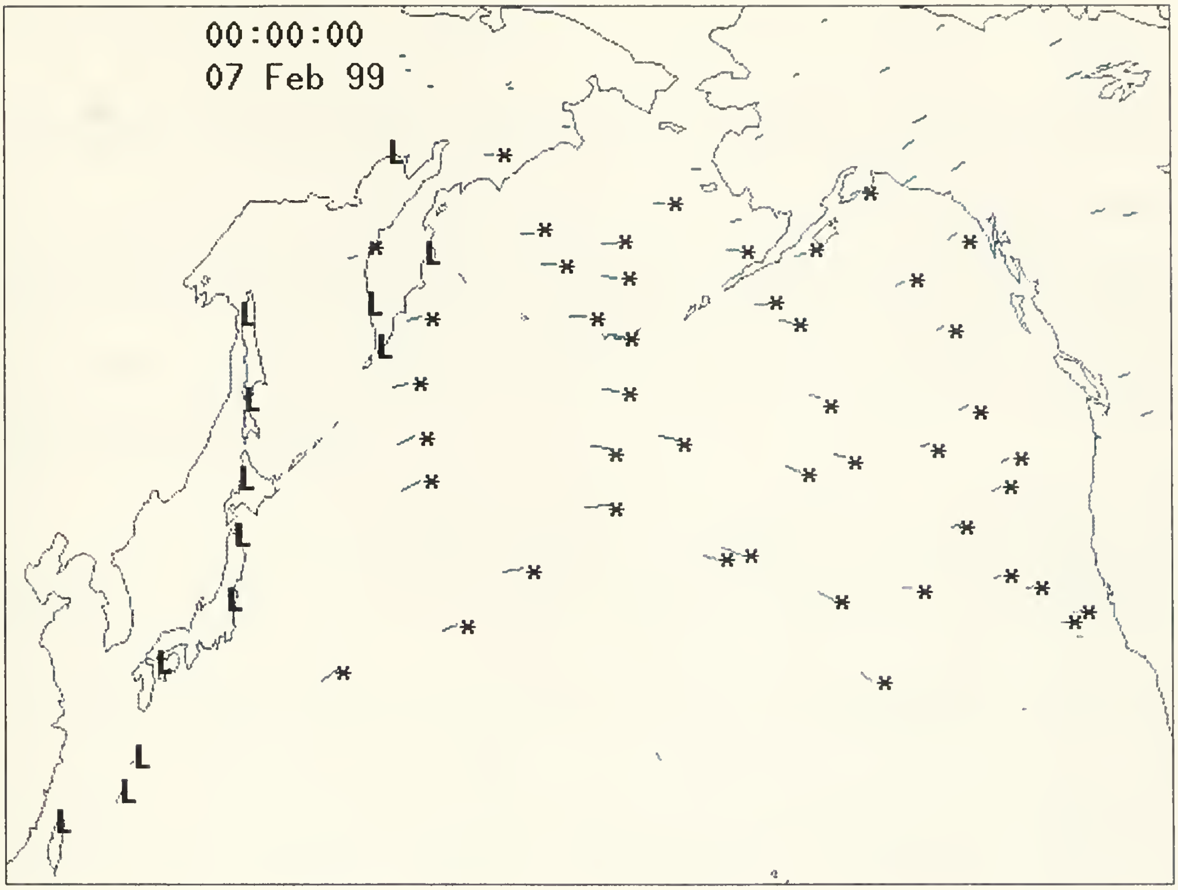

Figure 4.7. Hypothetical driftsonde locations, denoted by the flag and "*", and valid for 00 UTC 7 February 1999. The approximate locations of the 13 launch sites are indicated by a "L". The driftsonde carrier balloons were assumed to be launched at 12-h intervals beginning with 00 UTC 2 February 1999, and the 50-hPa FNMOC operational wind analyses were used to advect the carrier balloons. The driftsonde locations over the oceans are assumed to correspond to dropsonde releases.

An example of the hypothetical driftsonde locations valid for 00 UTC 7 February 1999 is shown in Fig. 4.7. The driftsonde locations were computed by R. Langland of NRL-Monterey using the atmospheric tracer capabilities associated with the Vis5d software package. The driftsonde carrier balloons were assumed to be launched at 12-h intervals beginning with 00 UTC 2 February 1999 from 13 launch sites (Fig. 4.7) along the east coast of Asia. The 50-hPa FNMOC operational wind analyses were used to

advect the carrier balloons. The driftsonde locations over the oceans are assumed to correspond to dropsonde releases. Each dropsonde is assumed to measure temperature, wind speed and direction at 50 hPa increments from 100 and 1000 hPa with an accuracy equivalent to a conventional radiosonde in NAVDAS. More than twice as many adaptive observations are available from the driftsonde network as from the hypothetical or G-IV flight tracks (see Table 4.6).

The reduction in the expected variance of the change in the forecast aspect, or $\left\langle (\delta J)^2 \right\rangle_o$, computed from (4.21) for each radiosonde profile (but using observation sensitivities computed using the entire set of conventional observations) is in Fig. 4.8. According to (4.21), the values in Fig. 4.8 represent a vertical summation of the (squared) error-weighted observation sensitivity contributions for temperature and wind observations at each pressure level. The contribution to $\left\langle (\delta J)^2 \right\rangle_o$ is largest for the three Alaskan radiosonde stations of Shemya/Eareckson Air Station, St. Paul Island (57.15°N, 170.22°W), and Sand Point. By comparison, the contributions to $\left\langle (\delta J)^2 \right\rangle_o$ are much smaller for the other radiosonde stations (green and gray circles). The large observation sensitivities and subsequent large contributions to $\left\langle (\delta J)^2 \right\rangle_o$ from the three Alaskan radiosonde stations arise because these radiosonde stations are relatively isolated and are in regions where the analysis sensitivity gradients are strong.

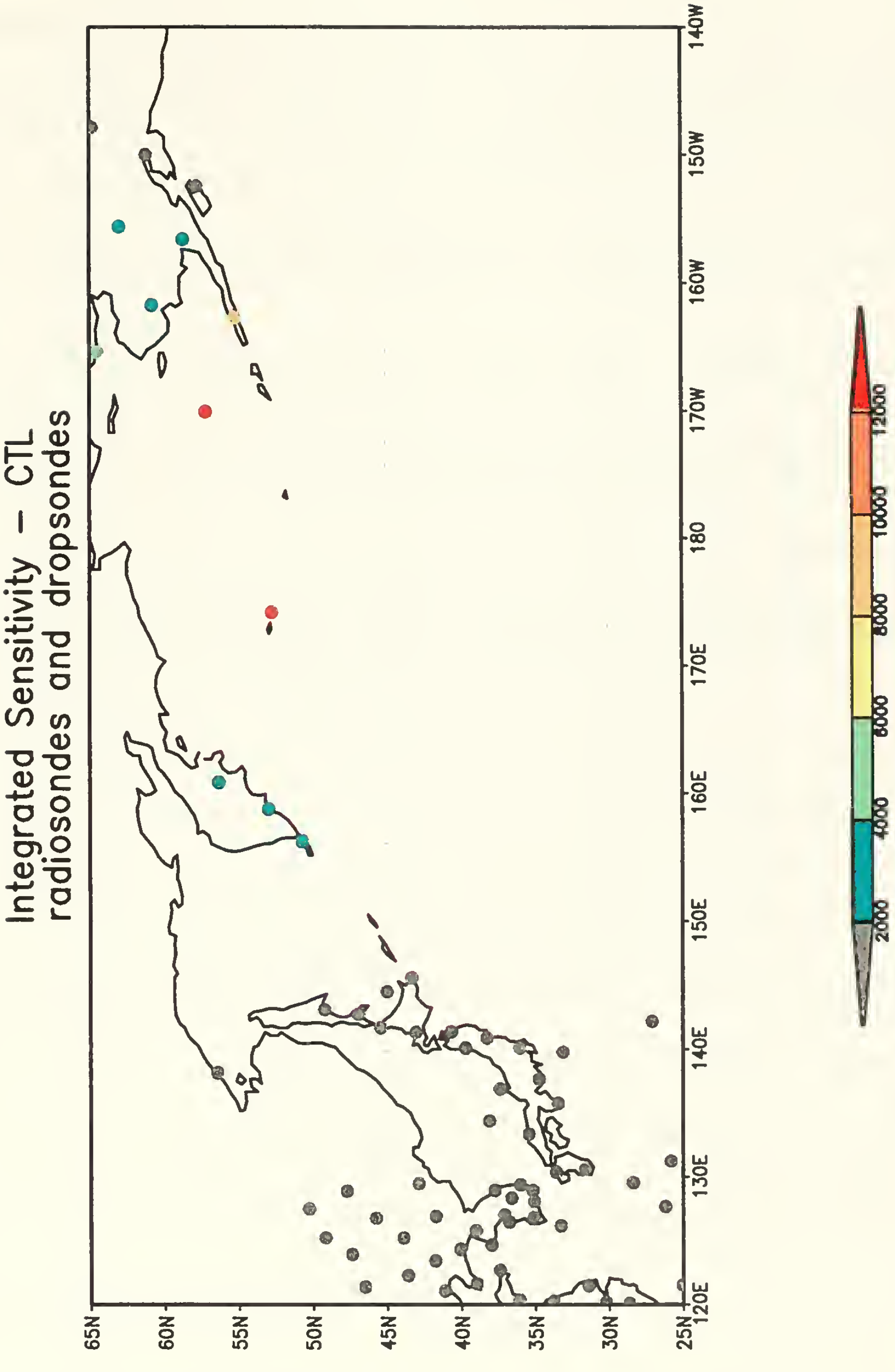
Integrated Sensitivity – CTL
radiosondes and dropsondes
65N
60N
55N
50N
45N
40N
35N
30N
25N
120E
130E
140E
150E
160E
170E
180
170W
160W
150W
140W
2000
4000
6000
8000
10000
12000

Figure 4.8. Reduction in the expected variance of the change in the 72-h forecast error $\left\langle (\delta J)^2 \right\rangle_o$ computed for all observations for the control (CTL) case, and plotted for the radiosonde observations.

The contributions to $\left\langle (\delta J)^2 \right\rangle_o$ for the G-IV flight, the three hypothetical targeting flights, the backwards "N" deployment from Chapter III.F.3.c, and the driftsonde network are shown in Figs. 4.9 to 4.14, respectively. For most dropsonde deployments, the radiosondes from Shemya, St. Paul Island, and Sand Point continue to dominate the contributions to $\left\langle (\delta J)^2 \right\rangle_o$, and these contributions are reduced only when adaptive dropsondes are nearby (e.g., Figs. 4.10, 4.11, and 4.14). Overall, the largest contributions to $\left\langle (\delta J)^2 \right\rangle_o$ occur for the hypothetical Shemya flight path dropsondes (Fig. 4.11) and for the driftsonde-deployed dropsonde network (Fig. 4.14). Both of these dropsonde networks sample the large amplitude, large-scale analysis temperature and wind sensitivity gradients in the mid-Pacific Ocean in Figs. 4.1-4.4.

The contributions to $\left\langle (\delta J)^2 \right\rangle_o$ from the G-IV flight path dropsondes (Fig. 4.9) are modest compared to Shemya and St. Paul Island, with the largest contribution occurring for the more isolated dropsonde at the apex of the inverted "V" where the temperature and wind analysis sensitivity gradients are relatively large in amplitude and scale. In general, the dropsondes along the western flight leg coincide with stronger temperature and wind analysis sensitivity gradients than the dropsondes along the eastern flight leg and have correspondingly larger contributions to $\left\langle (\delta J)^2 \right\rangle_o$.

The contributions to $\left\langle (\delta J)^2 \right\rangle_o$ from the Elmendorf flight path dropsondes (Fig. 4.10), which sample the small-scale low-level temperature and v-wind analysis sensitivity

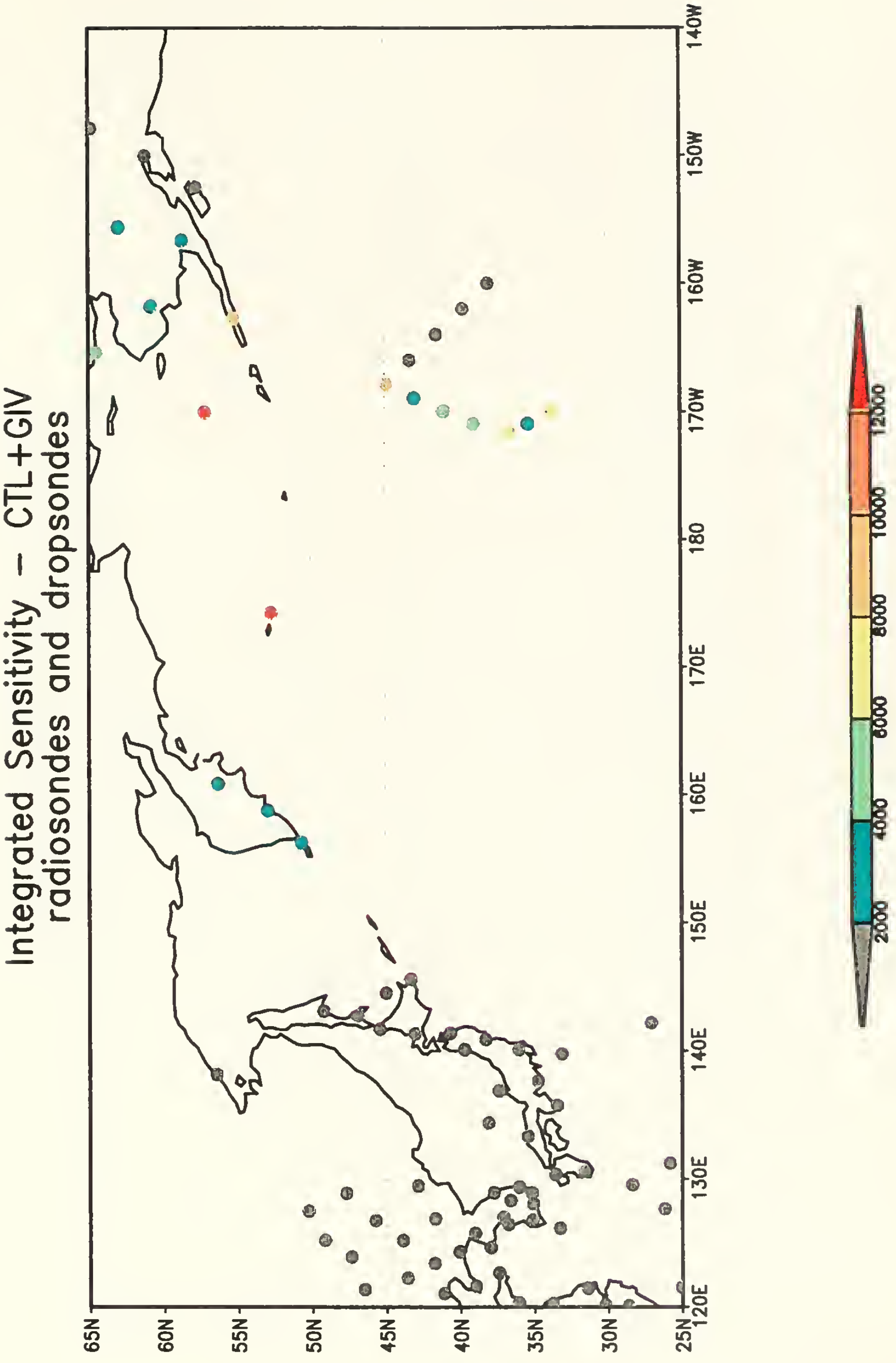

Integrated Sensitivity - CTL+GIV
radiosondes and dropsondes
65N
60N
55N
50N
45N
40N
35N
30N
25N
120E
130E
140E
150E
160E
170E
180
170W
160W
150W
140W
2000
4000
6000
8000
10000
12000

Figure 4.9. As in Fig. 4.8, except for the reduction in the expected variance of the change in the 72-h forecast error $\left\langle (\delta J)^2 \right\rangle_o$ computed for all observations for the control plus G-IV targeting (CTL+GIV) case, and plotted for the radiosonde and dropsonde observations.

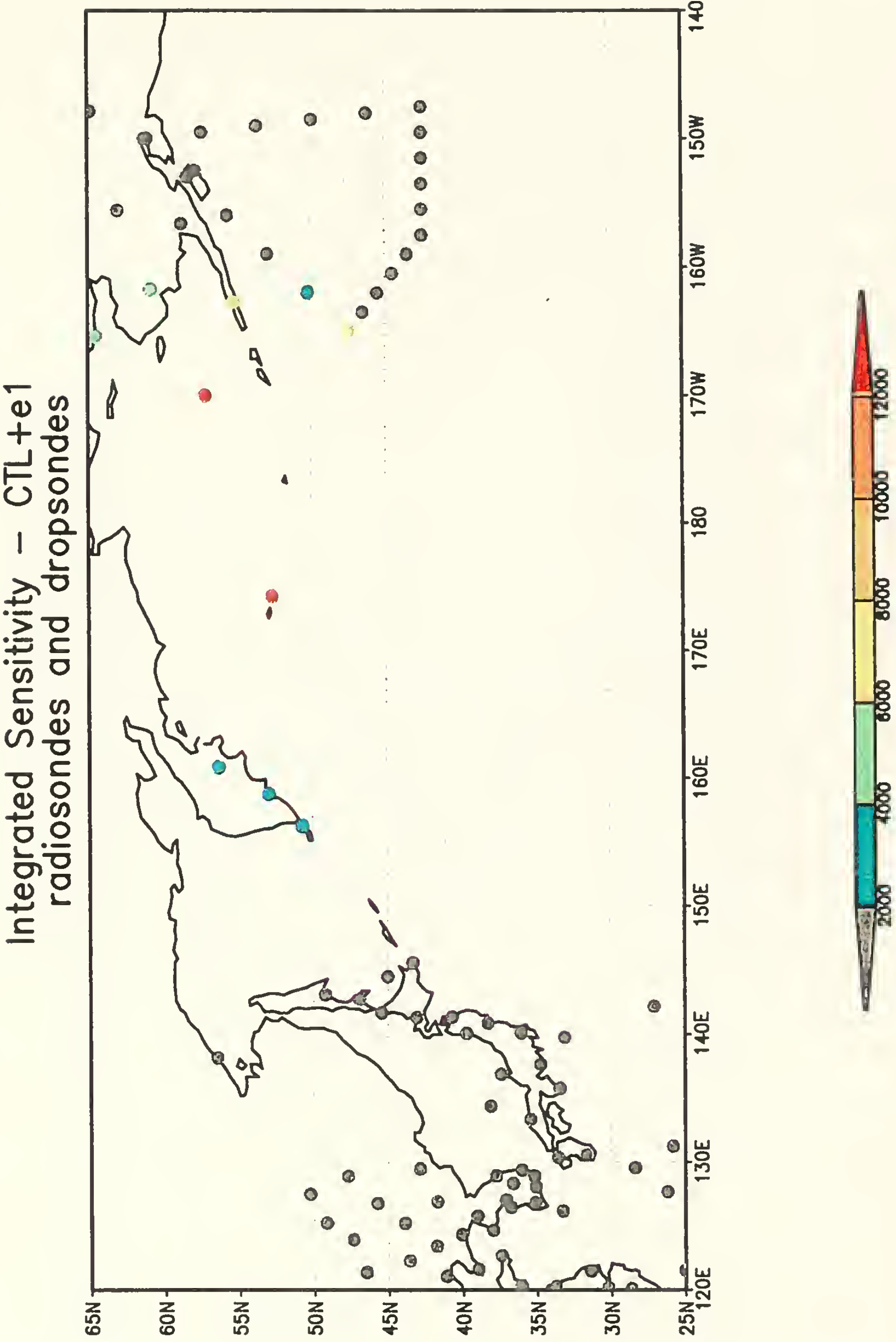
Integrated Sensitivity – CTL+e1
radiosondes and dropsondes
65N
60N
55N
50N
45N
40N
35N
30N
25N
120E
130E
140E
150E
160E
170E
180
170W
160W
150W
140W
2000
4000
6000
8000
10000
12000

Figure 4.10. As in Fig. 4.8, except for the reduction in the expected variance of the change in the 72-h forecast error $\left\langle (\delta J)^2 \right\rangle_o$ computed for all observations for the control plus hypothetical targeting deployment from Elmendorf AFB (CTL+e1) case, and plotted for the radiosonde and dropsonde observations.

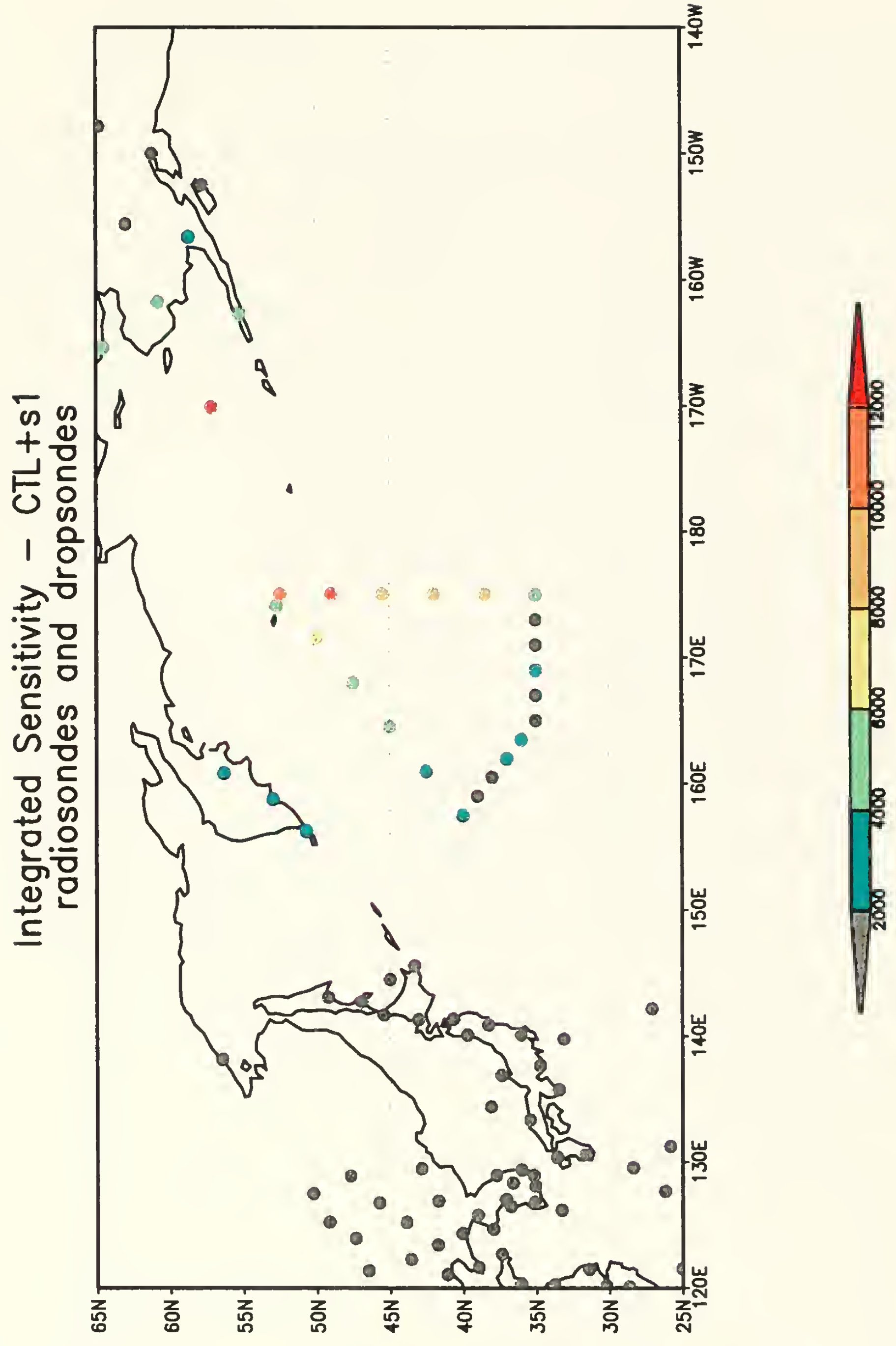
Integrated Sensitivity – CTL+s1
radiosondes and dropsondes
65N
60N
55N
50N
45N
40N
35N
30N
25N
120E
130E
140E
150E
160E
170E
180
170W
160W
150W
140W
2000
4000
6000
8000
10000
12000

Figure 4.11. As in Fig. 4.8, except for the reduction in the expected variance of the change in the 72-h forecast error $\left\langle (\delta J)^2 \right\rangle_o$ computed for all observations for the control plus hypothetical targeting deployment from Shemya/ Eareckson air station (CTL+s1) case, and plotted for the radiosonde and dropsonde observations.

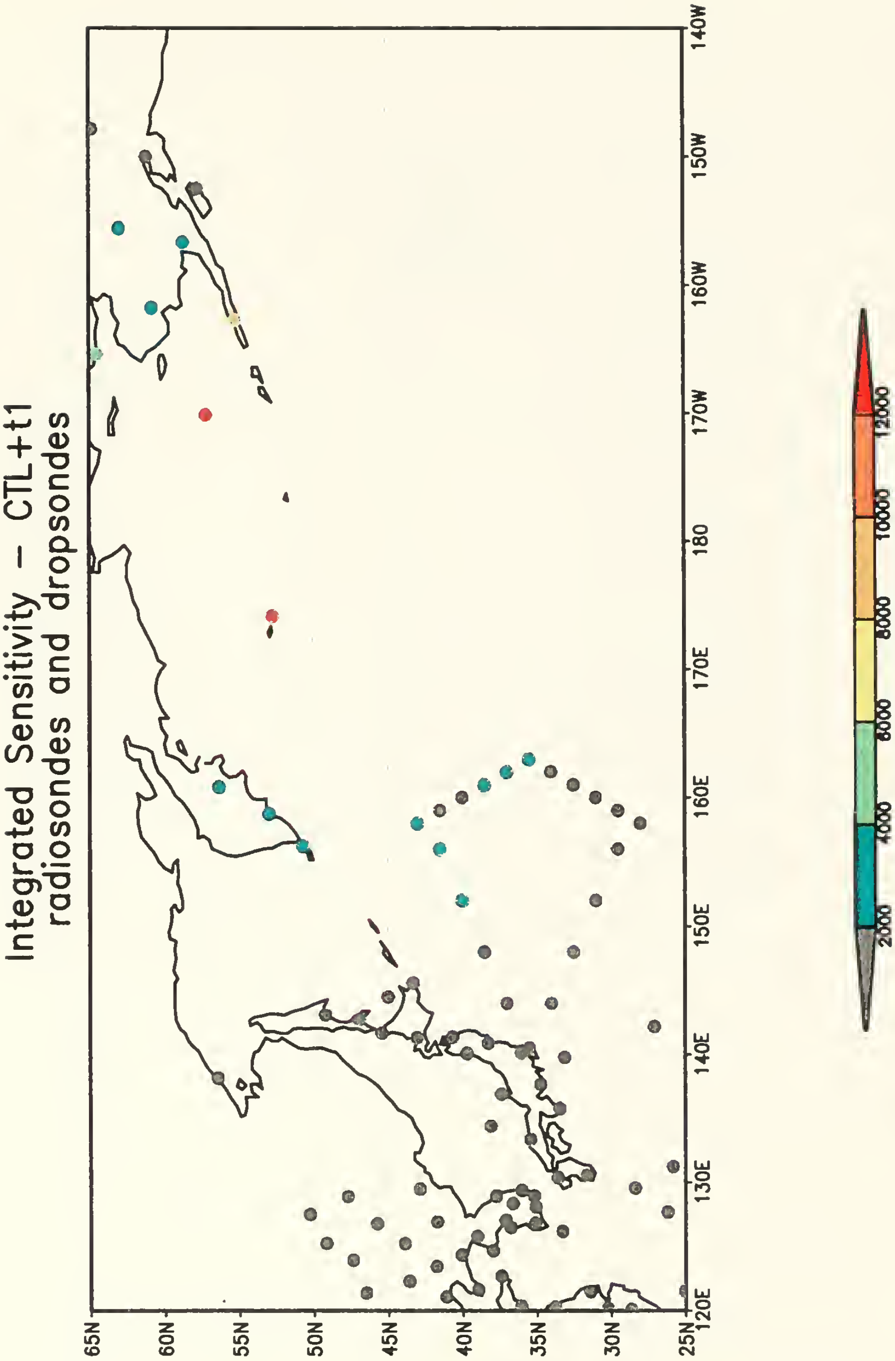
Integrated Sensitivity – CTL+t1
radiosondes and dropsondes
65N
60N
55N
50N
45N
40N
35N
30N
25N
120E
130E
140E
150E
160E
170E
180
170W
160W
150W
140W
2000
4000
6000
8000
10000
12000

Figure 4.12. As in Fig. 4.8, except for the reduction in the expected variance of the change in the 72-h forecast error $\left\langle (\delta J)^2 \right\rangle_o$ computed for all observations for the control plus hypothetical targeting deployment from Tokyo (CTL+t1) case, and plotted for the radiosonde and dropsonde observations.

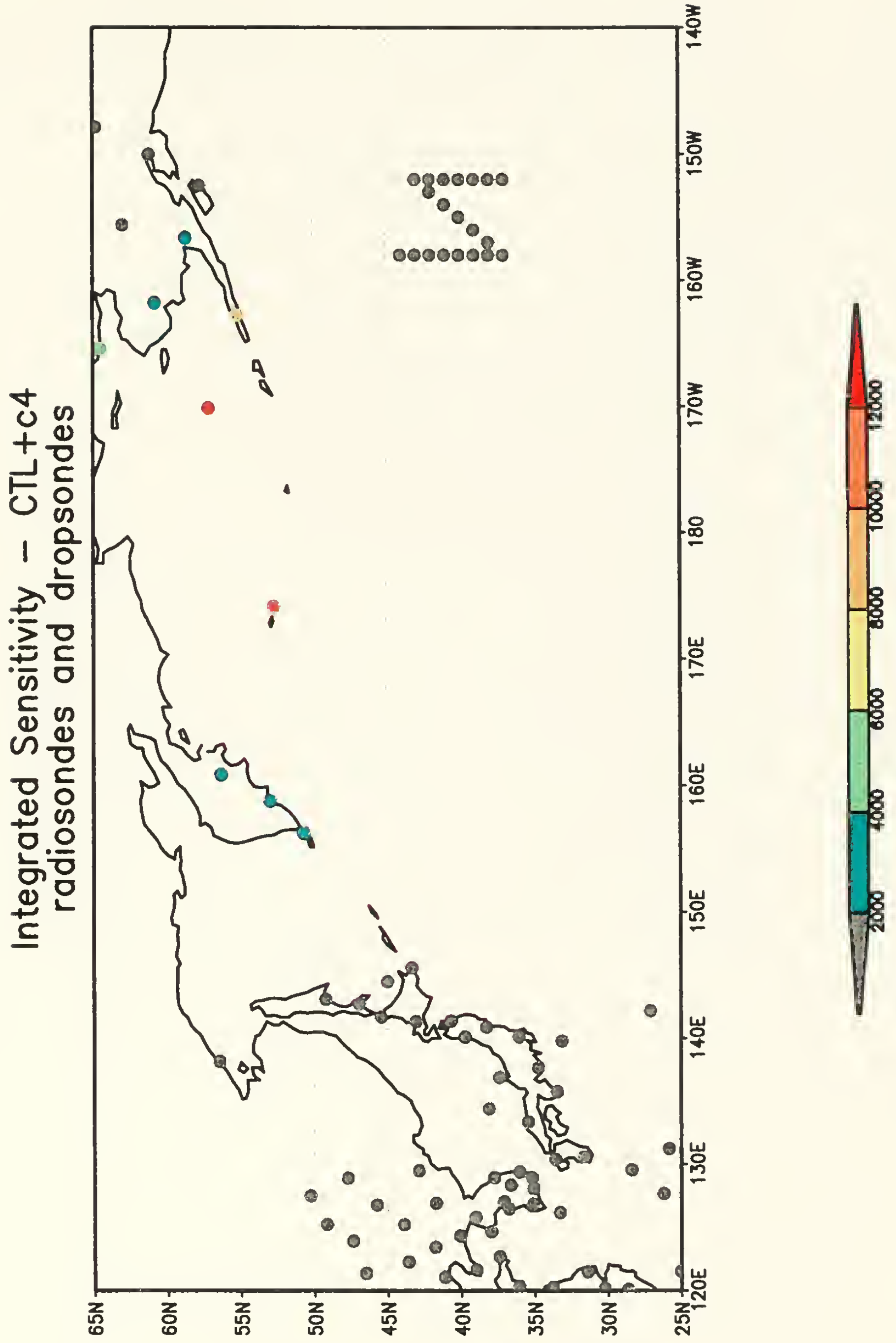
Integrated Sensitivity - CTL+c4
radiosondes and dropsondes
65N
60N
55N
50N
45N
40N
35N
30N
25N
120E
130E
140E
150E
160E
170E
180
170W
160W
150W
140W
2000
4000
6000
8000
10000
12000

Figure 4.13. As in Fig. 4.8, except for the reduction in the expected variance of the change in the 72-h forecast error $\left\langle (\delta J)^2 \right\rangle_o$ computed for all observations for the control plus hypothetical targeting deployment in Chapter III.F.3.c. (CTL+c4) case, and plotted for the radiosonde and dropsonde observations.

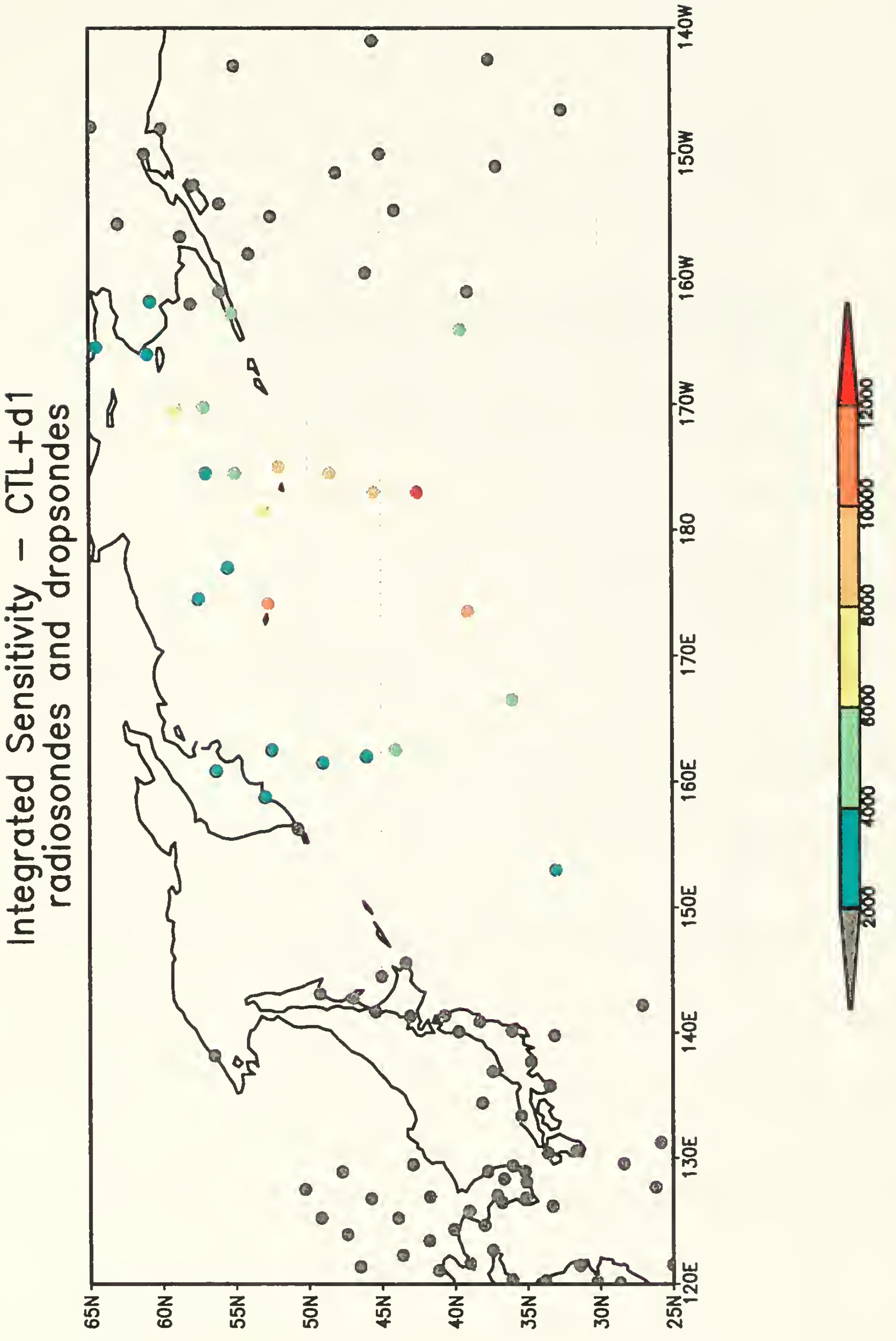
Integrated Sensitivity – CTL+d1
radiosondes and dropsondes
65N
60N
55N
50N
45N
40N
35N
30N
25N
120E
130E
140E
150E
160E
170E
180
170W
160W
150W
140W
2000
4000
6000
8000
10000
12000

Figure 4.14. As in Fig. 4.8, except for the reduction in the expected variance of the change in the 72-h forecast error $\left\langle (\delta J)^2 \right\rangle_o$ computed for all observations for the control plus hypothetical driftsonde-deployed dropsondes (CTL+d1) case, and plotted for the radiosonde and driftsonde-deployed dropsonde observations.

gradients extrema, are even weaker. This result is consistent with the single observation sensitivity maps in Fig. 3.46 that demonstrate that the sensitivity to a single temperature or wind observation near the extrema of the small-scale analysis sensitivity gradients is small. While Fig. 3.46 formally pertains to a single observation, the general conclusions from the single observation experiments are supported by the results from the Shemya flight (Fig. 4.11). The strongest contributions to $\left\langle (\delta J)^2 \right\rangle_o$ are from the dropsondes on the southbound flight leg that sample the larger amplitude and spatial scale analysis sensitivity gradients. In contrast, the contributions to $\left\langle (\delta J)^2 \right\rangle_o$ from the Tokyo flight path dropsondes (Fig. 4.12) are moderately weak since the flight track barely intersects significant analysis sensitivity gradient features.

Similar results are obtained for the driftsonde-deployed dropsonde network (Fig. 4.14), where the strongest contributions to $\left\langle (\delta J)^2 \right\rangle_o$ occur for the dropsondes in the mid-Pacific Ocean near large horizontal scale and amplitude analysis sensitivity gradients. When driftsonde observations are combined with the conventional observations (Fig. 4.14), the relative contributions to $\left\langle (\delta J)^2 \right\rangle_o$ from the three Alaskan radiosonde stations decrease (*cf.* Fig. 4.8), which suggests both the forecast aspect and the analysis are less dependent on these radiosondes when nearby driftsonde observations are present.

Perhaps the most interesting results are for the backwards "N" deployment (Fig. 4.13) from Chapter III.F.3.c. Since features similar to the high-amplitude, small-scale temperature analysis sensitivity gradient sub-structures (Fig. 4.1c) were often selected as targets during FASTEX and NORPEX, the flight path in Fig. 4.13 was designed to sample both the extrema and the gradients, with the *a priori* expectation that such a deployment would maximize the observation sensitivity. However, the adaptive dropsonde contributions to $\left\langle (\delta J)^2 \right\rangle_o$ are quite small, which indicates that the sensitivity to these observations is also small. These results support the conclusions from Chapter III.F.3 that the data assimilation system is comparatively insensitive to the observations when the length scale of the analysis sensitivity sub-structures is smaller than the background error correlation length scale. While it is tempting to speculate that the majority of the observations in this deployment are unnecessary and may be eliminated, the results from Chapter III.C.3 suggest that, for small-scale analysis sensitivity gradients, the observation sensitivity increases as the observation density increases. Consequently, more observations may be required to sample this small-scale analysis sensitivity gradient.

The reductions in the variance of the change in the forecast aspect are now computed for ten observing platforms for the seven different targeting configurations (Fig. 4.15). For the control experiment (conventional observations only, red bar), the contributions to $\left\langle (\delta J)^2 \right\rangle_o$ are quite small for surface land, surface marine, and SSM/I windspeed observations, which is not surprising, given that the temperature and wind analysis sensitivity gradients at the lowest pressure levels have small amplitude (not

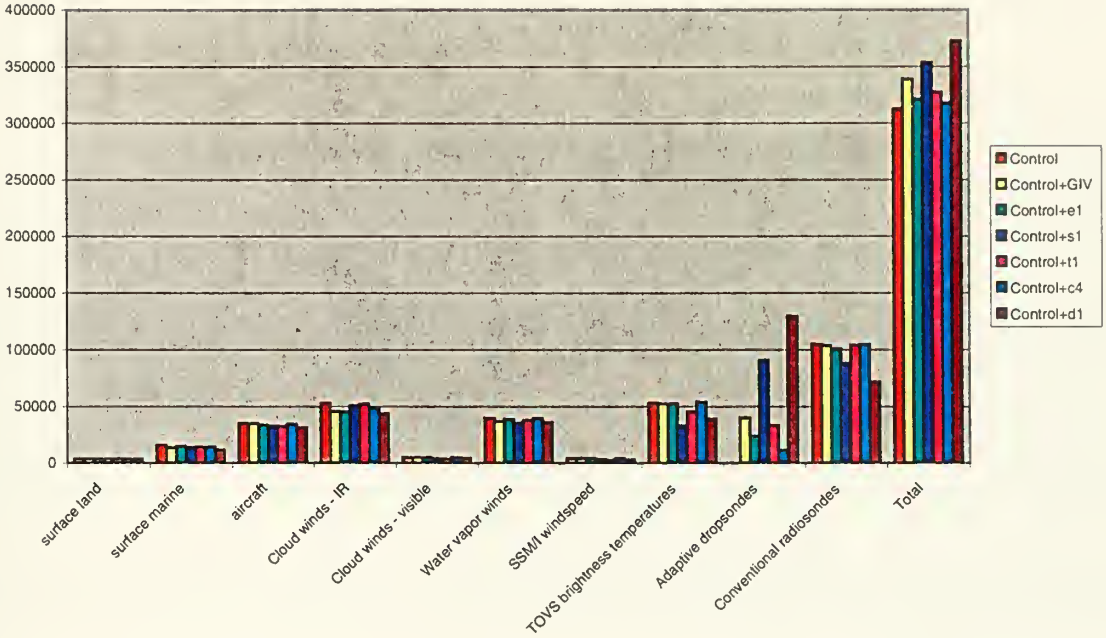

Figure 4.15. Relative contributions to the reduction in the variance of the change in the forecast aspect for ten observing platforms for the seven different targeting deployments corresponding to Figs. 4.8-4.14.

shown), and the vertical coupling through the boundary layer is weak. The contributions from the visible cloud-tracked winds are also small, but this is principally due to the low number of visible cloud-tracked winds (Table 4.6). Larger contributions occur for aircraft winds, infrared cloud-tracked winds, water vapor winds, and TOVS brightness temperatures, with the largest contribution from the conventional radiosondes. When the G-IV adaptive observations are included (yellow bar), their relative contribution to $\left\langle (\delta J)^2 \right\rangle_o$ of 40000 is offset by small decreases from the other observations (primarily infrared and water vapor winds) so that the total $\left\langle (\delta J)^2 \right\rangle_o$ increases by only 26000. This

suggests that some of the information in the G-IV dropsondes is redundant with respect to the conventional observations.

The contributions from the Elmendorf (green bar) and Tokyo (pink bar) deployments are small, and the relative contributions to the total $\left\langle (\delta J)^2 \right\rangle_o$ from the conventional observation platforms are relatively constant, which implies that these dropsonde observations do not contribute very much to the reduction in the variance of the change in J. The backwards "N" deployment (cyan bar) in Fig. 4.13 has the smallest contribution to $\left\langle (\delta J)^2 \right\rangle_o$, despite this deployment thoroughly sampling the large amplitude, small-scale 850-hPa temperature analysis sensitivity gradient (Fig. 4.1c).

The two adaptive observation deployments with the largest relative contributions to $\left\langle (\delta J)^2 \right\rangle_o$ occur for the Shemya flight track (blue bar) and the driftsonde network (purple bar), even though these deployments have led to moderate decreases in the relative contributions from TOVS brightness temperatures and the conventional radiosonde network. It should be noted that the driftsonde contribution to $\left\langle (\delta J)^2 \right\rangle_o$ represents a lower limit since, in an actual driftsonde experiment, the data assimilation cycle would have benefited from driftsonde-deployed dropsondes used in earlier forecast/assimilation cycles. The decrease in the conventional radiosonde network is primarily due to the reduction in $\left\langle (\delta J)^2 \right\rangle_o$ for the radiosonde observations from Shemya, St. Paul, and Sand Point (e.g., Figs. 4.11 and 4.14), which demonstrates that extremely large

observation sensitivities are not necessary to maximize the total reduction in $\left\langle (\delta J)^2 \right\rangle_o$. The decreases in the TOVS brightness temperature contributions occur because the relative weight or importance of these lower quality observations is less in the presence of the additional higher quality dropsonde observations in the highly sensitive regions. Interestingly, the TOVS contribution actually increases for the backwards "N" adaptive observation deployment (Fig. 4.13), which suggests that the adaptive observations have contributed very little useful information to the analysis.

Since the contribution to $\left\langle (\delta J)^2 \right\rangle_o$ from the Shemya aircraft deployment in Fig. 4.11 is only slightly less than for the driftsonde network (which has more than twice as many observations), two slightly varied flight paths from Shemya are also evaluated. The first alternate flight path (Fig. 4.16) is located slightly east of the initial Shemya flight track, and samples more completely the large-scale 850-hPa temperature analysis sensitivity gradient in Fig. 4.1c. The second alternate flight path (Fig. 4.17) directly samples the maxima of the large-scale 850-hPa temperature analysis sensitivity gradient. The total reduction in the variance in the change of J and the relative contributions to $\left\langle (\delta J)^2 \right\rangle_o$ (Fig. 4.18) for the two alternate deployments (the light blue and light yellow bars) are larger than for the initial Shemya flight path (blue bar), but are smaller than for the driftsonde network contribution (purple bar). The largest increase occurs for the flight path (Fig. 4.16) that samples the 850-hPa large-scale temperature analysis

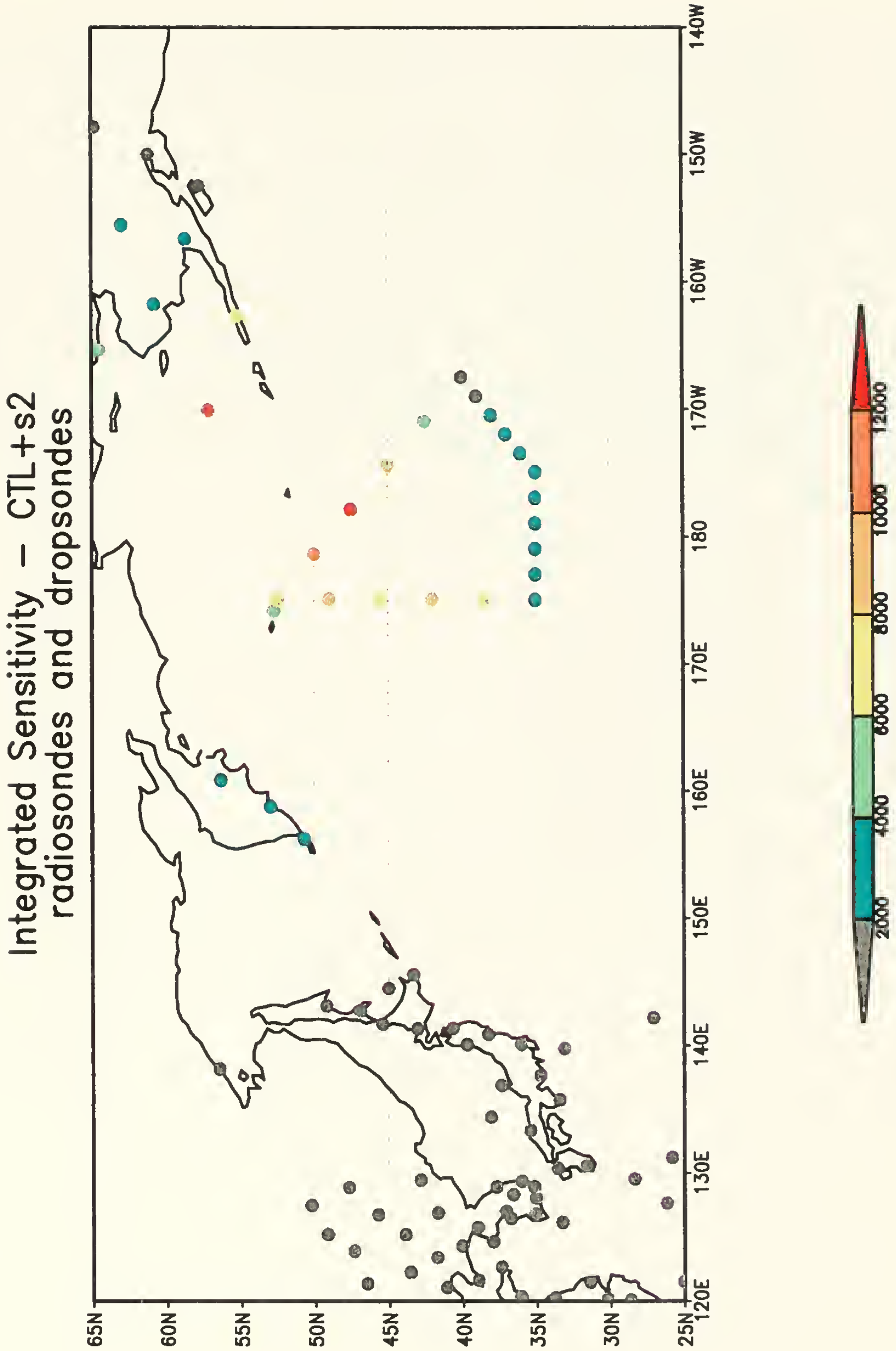
Integrated Sensitivity – CTL+s2
radiosondes and dropsondes
65N
60N
55N
50N
45N
40N
35N
30N
25N
120E
130E
140E
150E
160E
170E
180
170W
160W
150W
140W
2000
4000
6000
8000
10000
12000

Figure 4.16. As in Fig. 4.8, except for the reduction in the expected variance of the change in the 72-h forecast error $\left\langle (\delta J)^2 \right\rangle_o$ computed for all observations for the control plus hypothetical first alternate targeting deployment from Shemya/ Eareckson air station (CTL+s2) case, and plotted for the radiosonde and dropsonde observations.

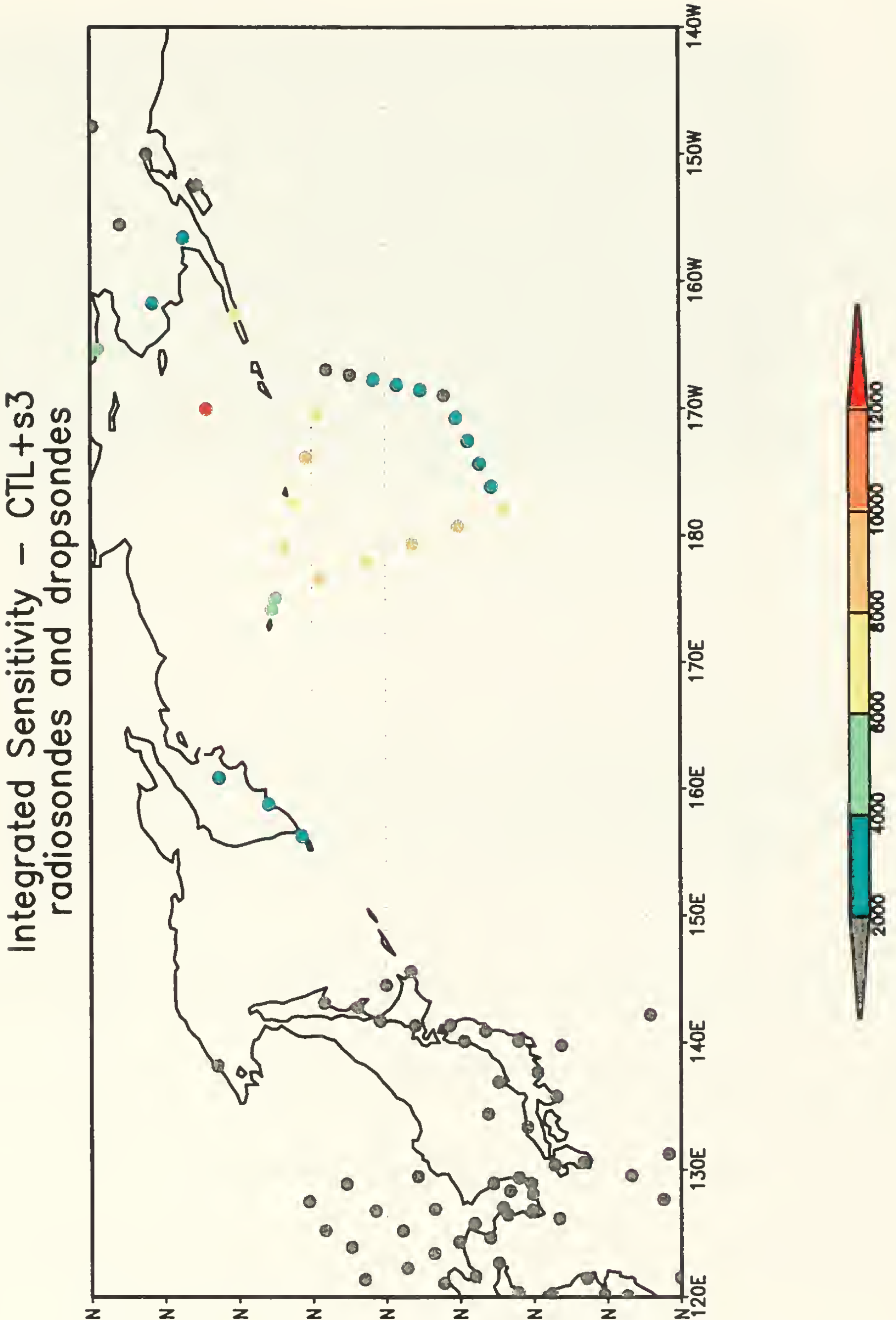
Integrated Sensitivity – CTL+s3
radiosondes and dropsondes
65N
60N
55N
50N
45N
40N
35N
30N
25N
120E
130E
140E
150E
160E
170E
180
170W
160W
150W
140W
2000
4000
6000
8000
10000
12000

Figure 4.17. As in Fig. 4.8, except for the reduction in the expected variance of the change in the 72-h forecast error $\left\langle (\delta J)^2 \right\rangle_o$ computed for all observations for the control plus hypothetical second alternate targeting deployment from Shemya/ Eareckson air station (CTL+s3) case, and plotted for the radiosonde and dropsonde observations.

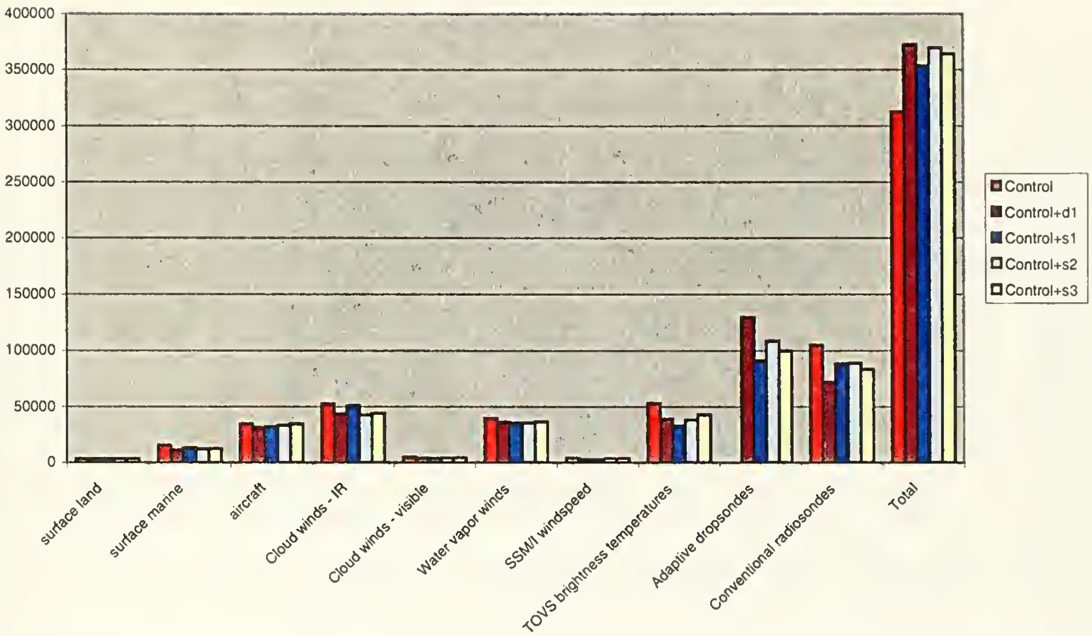

Figure 4.18. As in Fig. 4.15, except for relative contributions to the reduction in the variance of the change in the forecast aspect for ten observing platforms for the control plus driftsonde (CTL+d1) in Fig. 4.14 and three Shemya/Eareckson hypothetical targeting deployments labeled s1, s2, and s3 corresponding to Figs. 4.11, 4.16, and 4.17.

sensitivity gradient most completely (light blue bar). The relative TOVS contribution to $\left\langle (\delta J)^2 \right\rangle_o$ in Fig. 4.18 from the two alternate Shemya deployments (light blue and yellow bars) are larger than for the initial Shemya flight path (blue bar), which indicates that the two alternate Shemya deployments represent a more efficient mix of observations for the analysis. Comparison of Figs. 4.11 and 4.16 indicates that, even though the hypothetical observations for the southbound flight leg from Shemya are the same, the relative

contributions to $\left\langle (\delta J)^2 \right\rangle_o$ are not the same, which demonstrates the dependence of the observation sensitivity on the distribution of the neighboring observations.

Finally, two additional adaptive observation deployment strategies are considered. Suppose that an aircraft with dropsonde capabilities was available along with the driftsonde system. Is it worthwhile to deploy the aircraft to supplement the driftsonde network? The first experiment combines the conventional observations and the driftsonde-deployed dropsondes with the "best" (Fig. 4.16) hypothetical flight track from Shemya, and adds additional dropsondes to the highly sensitive mid-Pacific Ocean area. The second experiment combines the conventional and driftsonde observations with the hypothetical flight track from Tokyo in Fig. 4.12, and thereby supplements a region with few driftsonde-deployed dropsondes, and with weak temperature analysis sensitivity (panels (C) of Figs. 4.1-4.4). The contributions to $\left\langle (\delta J)^2 \right\rangle_o$ are shown in Fig. 4.19. Whereas the additional dropsondes from the Tokyo flight path add only slightly to the total $\left\langle (\delta J)^2 \right\rangle_o$, the Shemya flight path dropsondes have a somewhat larger contribution. The increase in the total $\left\langle (\delta J)^2 \right\rangle_o$ is largely due to the adaptive dropsondes, with net decreases in $\left\langle (\delta J)^2 \right\rangle_o$ noted for the other observing platforms, and particularly for the TOVS brightness temperatures and the conventional radiosondes, which indicates that the adaptive observations do not exclusively add unique information to the data assimilation system. These results also suggest that the observation density in the highly sensitive

regions is not sufficient, and that the additional observations should be placed in regions with stronger analysis sensitivity.

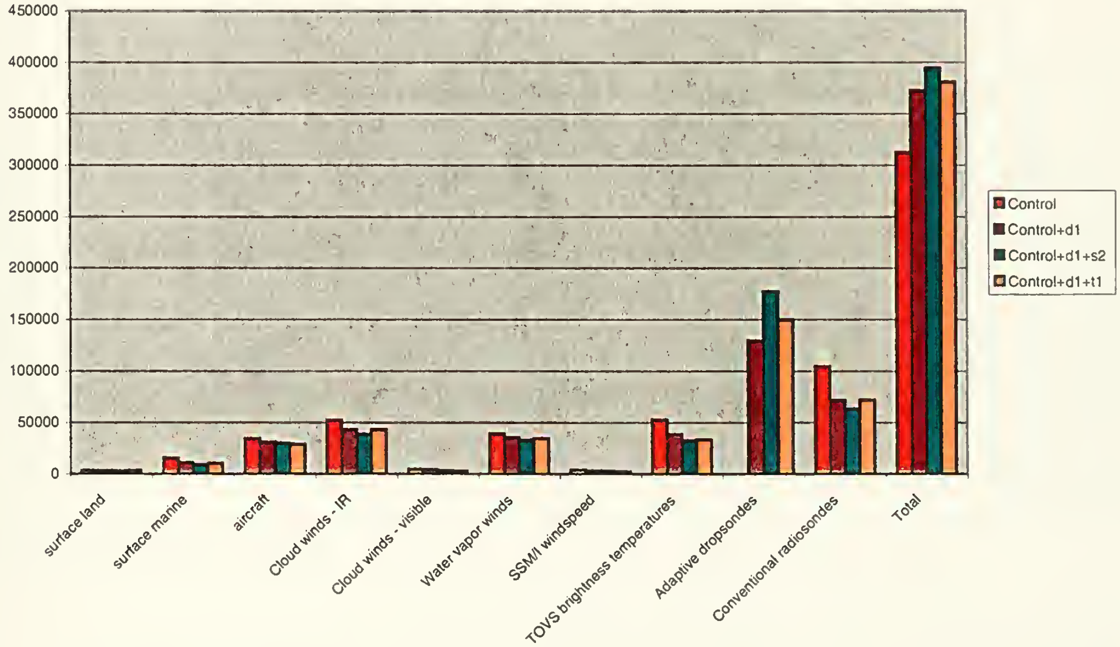

Figure 4.19. As in Fig. 4.15, except for relative contributions to the reduction in the variance of the change in the forecast aspect for ten observing platforms for the control (CTL) in Fig. 4.8, control plus driftsonde (CTL+d1) in Fig. 4.14, and hypothetical targeting deployments combining the driftsonde network with the second Shemya and the Tokyo hypothetical deployments labeled (d1+s2) and (d1+t1) corresponding to Figs. 4.16 and 4.12.

F. CHAPTER SUMMARY

The adjoint of the NAVDAS data assimilation system is used to compute the sensitivity of J to the observations available for an analysis valid at 00 UTC 7 February 1999. This case corresponds to the largest 72-h NOGAPS forecast error verifying over the western United States and Canada during a three-year period from 1997 – 1999. The analysis sensitivity gradients were computed using an energy-weighted forecast error cost

function J for the NOGAPS forecast starting from the FNMOC/NOGAPS operational initial conditions valid at the target time of 00 UTC 7 February 1999 and verifying 72 h later at 00 UTC 10 February 1999.

Overall, the largest observation sensitivities occur for observations that are relatively isolated and near high-amplitude, large-scale analysis sensitivity gradients. In general, the largest sensitivities to the temperature or u- or v-wind observations do not occur at the same location. The largest sensitivity to a temperature observation occurs for the Shemya radiosonde, and probably occurs because the observation is isolated, assumed to be accurate, and is located near the center of a high-amplitude, large-scale temperature analysis sensitivity gradient.

The largest sensitivity to a u-wind observation occurred for a water vapor wind near the high-amplitude, large-scale u-wind analysis sensitivity gradient associated with the northern branch of the subtropical jet. The largest v-wind observation sensitivities appear to be associated with the high-amplitude, large-scale temperature analysis sensitivity gradients, with weaker contributions (through the background error covariances) from the v-wind analysis sensitivity gradients at adjacent levels. These results are consistent with the two-dimensional results in Chapter III.F.3 that the wind observation sensitivities may be dominated by the projection of $\mathbf{K}^T$ onto the temperature analysis sensitivity gradient, with weaker contributions from the univariate wind components (e.g., the projection of $\mathbf{K}^T$ onto the v-wind analysis sensitivity gradient). While the results from Chapter III suggest that the largest wind observation sensitivities are phase-shifted with the extrema of the temperature analysis sensitivity gradient, it is not possible to unambiguously state that this phase shift occurs for the NAVDAS adjoint observation sensitivity results because of the westward tilt with height of the temperature analysis sensitivity gradients and the effects of the vertical background error correlations. Higher density observations may also be needed to determine whether the phase shift exists.

An important, non-targeting application of the data assimilation adjoint theory was illustrated with the TOVS brightness temperature observation sensitivities. Chapter III demonstrated that large observation sensitivities occur when high-amplitude, large-scale analysis sensitivities coincide with an abrupt discontinuity in the observation density. Such observation density discontinuities occur for TOVS brightness temperatures along the edges of the satellite swath, or between ocean and land or sea-ice observations when the land and sea-ice observations are not used. The observations along these boundaries are less accurate for a variety of reasons. Since the observation sensitivity is larger for observations that are assumed to be accurate, the data assimilation systems should properly account for these sensitivity and accuracy factors when assigning the observation error so that the analyses and forecasts are not highly sensitive to the less accurate observations.

A scalar measure of the reduction in the expected variance in the change of the forecast aspect J, which uses the observation sensitivities computed for the entire global set of observations, was introduced. This measure, $\left\langle (\delta J)^2 \right\rangle_o$ may be computed for the entire global set of observations, or a specified subset, such as the adaptive observing network. As such, it can be used to assess the relative efficiency of various adaptive observation deployments, to evaluate the existing observing network, or to design new observing systems.

In this chapter, $\left\langle (\delta J)^2 \right\rangle_o$ was used to evaluate the relative contributions for different hypothetical adaptive observation-targeting strategies. The two hypothetical targeting deployments with the largest contributions are the Shemya-based targeting flight and the driftsonde-deployed dropsonde network that sample the large-amplitude, large-scale analysis temperature and wind sensitivity gradients in the mid-Pacific Ocean. Large contributions also occur for several of the Alaskan radiosonde reports. When a hypothetical targeting flight is added to supplement the driftsonde network, a larger increase in $\left\langle (\delta J)^2 \right\rangle_o$ occurs when the dropsondes are added to highly sensitive regions than when the same number of observations is added to comparatively data-void areas with weak sensitivity, which implies that sufficient data density has not been achieved in the sensitive regions.

Perhaps the most remarkable result occurs for the targeting deployment designed to sample both the extrema and the gradients of the high-amplitude, small-scale temperature analysis sensitivity gradient sub-structure. Such features were often selected as targets based on adjoint-based targeting methods during FASTEX and NORPEX. However, the adaptive dropsonde contributions $\left\langle (\delta J)^2 \right\rangle_o$ from this deployment are much smaller than the contributions from the hypothetical adaptive dropsonde networks that sample the large amplitude, large-scale analysis temperature and wind sensitivity gradients in the mid-Pacific Ocean. These results suggest that targeting decisions based solely on the analysis sensitivity gradients or associated singular vectors may be substantially different from targeting decisions that also consider the adjoint of the data assimilation system.

V. SUMMARY AND CONCLUSIONS

Despite ongoing improvements to observing systems, data assimilation systems, and numerical weather forecast models, it is clear that a significant component of the forecast error is due to analysis error in sparsely observed regions. However, if the regions where additional observations would have the largest potential positive impact on the forecast can be identified in advance, then these regions could be sampled with supplemental observations. This adaptive observation concept has generated a great deal of interest recently, and several objective targeting techniques have been developed.

For the classical adjoint-based targeting methods, some aspect of interest of the forecast output is chosen as the cost function J, and the sensitivity or gradient of J with respect to the initial conditions is determined using the adjoint of the linearized forecast model. Numerous studies have demonstrated that regions with large sensitivity correspond to synoptic features where small errors in the initial conditions amplify rapidly during the ensuing numerical forecast and dominate the short- and medium-range forecast error. These analysis sensitivity gradients (and closely related singular vectors) were used by scientists from NRL – Monterey during the recent FASTEX and NORPEX field experiments to identify sensitive regions (or targets) for adaptive sampling using aircraft-deployed dropsondes. The expectation is that the additional observations would decrease the analysis error in these data-sparse sensitive regions, and thus improve the subsequent weather forecast. While assimilations of the aircraft-deployed dropsondes from some of the FASTEX and NORPEX targeting sorties were associated with decreased forecast error in the verification area, the assimilation of adaptive dropsondes from other targeting deployments led to forecast degradation.

The classical adjoint sensitivity gradient represents only the first part of the complete numerical forecast adjoint sensitivity problem. In the same way that the numerical weather forecast problem includes the data assimilation step, the complete numerical forecast adjoint sensitivity problem must include the adjoint of the data assimilation system. Thus, the complete forecast adjoint sensitivity includes two complementary components. The first step, which uses the adjoint of the linearized forecast model to compute the sensitivity of J to the initial conditions or analysis, corresponds to the classical adjoint sensitivity problem. In the second step, the adjoint of the data assimilation system is used to determine the sensitivity of the initial conditions to the observations and the background. Combining the classical sensitivity gradient, which is defined in analysis or grid space, with the adjoint of the data assimilation system gives the sensitivity of the forecast aspect to the observations and background that is defined in observation space.

In this study, the adjoint of the data assimilation systems is used to explore the sensitivity of the forecast aspect J to the observations and background for progressively more complex idealized one- and two-dimensional data assimilation systems. The key results are briefly summarized in this chapter, with an emphasis on those relevant to the adaptive observation-targeting problem.

The observation sensitivity is largest when the observation is strongly projected onto the analysis sensitivity gradients by the adjoint of the assimilation system (e.g., $\mathbf{K}^T$). This occurs when the spatial structures and length scales of $\mathbf{K}^T$ are similar to the analysis sensitivity gradient. In turn, the spatial structures and length scales of $\mathbf{K}^T$ are determined by the background error variances, the correlation length scale (L_b) and type (i.e., temperature and wind autocorrelations versus cross-correlations), the forward observation operators, and the distribution and properties of the observations. Because of the highly complex nature of these interactions, the observation sensitivity is far from intuitive, and it is difficult to draw general conclusions that are applicable under all conditions. Therefore, for the purposes of this discussion, the background error correlation length scale is assumed to be similar to the NAVDAS adjoint value of 385 km. An analysis sensitivity gradient is defined to be small scale when its characteristic length (L_s) is less than the background error correlation length scale (L_b), and is defined to be large scale when L_s is similar to L_b.

The simplest problem corresponding to the one-dimensional univariate height analysis was considered first. The largest observation sensitivity occurs when an isolated height observation that is assumed to be accurate relative to the background is placed near the extrema of a large-scale height analysis sensitivity gradient. The observation sensitivity is much weaker when the analysis sensitivity gradients are either small-scale or weak, the observations are relatively inaccurate, or the observation density is high. Large observation sensitivity also occurs along hypothetical coastlines when large-scale analysis sensitivity gradients coincide with the abrupt change in the density of the observations. The observation sensitivity results were explained as follows. When the observations are relatively isolated or associated with changes in the observation density, $\mathbf{K}^T$ is large in amplitude and spatial scale, and projects strongly on large-scale analysis sensitivity gradients. However, when the observations are dense, $\mathbf{K}^T$ is small in amplitude and spatial scale, so that its projection onto either large- or small-scale analysis sensitivity gradients is weak. Similarly, since $\mathbf{K}^T$ is larger in amplitude and spatial scale for relatively accurate observations than for relatively inaccurate observations, the observation sensitivity is larger.

While the one-dimensional univariate wind observation sensitivity results differ in detail from the one-dimensional height observation sensitivity results, the same general conclusions can be drawn. The main difference is that the univariate height observation sensitivity increases as L_s increases, while the univariate wind observation sensitivity decreases when L_s is much larger than L_b because of the negative side lobes on the background wind error correlation function.

Whereas the maximum univariate one-dimensional observation sensitivity coincides with the extrema of the analysis sensitivity gradient, the maximum one-dimensional multivariate observation sensitivities involving the height-wind and wind-height background error correlations occur where the analysis sensitivity gradient is zero. This difference is due to the positive and negative side lobes of the height-wind and wind-height background error covariances.

A hypothetical flight path was designed to sample the extrema and gradients of an idealized two-dimensional height analysis sensitivity pattern composed of large- and small-scale sub-structures. The largest sensitivity occurs for the height observation at the end of the flight path that coincides with the large-scale height analysis sensitivity gradient sub-structure, and arises because of the change in the observation density. Consequently, $\mathbf{K}^T$ is large in amplitude and spatial scale and projects strongly onto the large-scale analysis sensitivity gradient. This result suggests that the large-scale analysis sensitivity gradient should be more thoroughly sampled to avoid very large observation sensitivity in sensitive regions. Overall, the general conclusions obtained for the one-dimensional univariate height observation sensitivity are supported by the two-dimensional univariate height observation sensitivity problem.

The two-dimensional multivariate temperature, u- and v-wind observation sensitivities tend to be largest when an isolated observation is near the center of a large-amplitude, large-scale temperature analysis sensitivity gradient, and are considerably weaker for small-scale analysis sensitivity gradients. The multivariate contributions to the observation sensitivity, which are most apparent for wind observations, tend to shift the maximum observation sensitivity away from the extrema of the analysis sensitivity gradients.

When an isolated temperature or wind observation is near the center of a small-scale temperature analysis sensitivity gradient sub-structure with nearby sub-structures of the opposing sign, the observation sensitivity is very weak. Under these conditions, the contributions to the observation sensitivity from the projection of $\mathbf{K}^T$ onto the analysis sensitivity gradient sub-structures are of opposing sign and a large degree of cancellation occurs. The observation sensitivity increases slightly when more observations are included, and attains an appreciable value only when the observations density is large, which implies that the two-dimensional data assimilation system requires a higher density of observations to analyze features such as the small-scale analysis sensitivity gradients than it does for large-scale analysis sensitivity gradients. Since L_b for the two-dimensional problem was selected to correspond to the NAVDAS value, this result is likely to also apply to NAVDAS.

However, the high observation density may introduce another potential complication, and this was illustrated with a hypothetical swath of satellite observations. When the edges of the swath coincide with large-scale analysis sensitivity gradients, the sensitivities to the observations at the edge of the swath may be significantly larger than the sensitivities to the observations in the observation-dense center of the swath. In this respect, the data discontinuities along the edges of the swath are analogous to the coastline in the one-dimensional examples. This example has important implications for satellite observations since the observations along the edges of the satellite swaths tend to be less accurate than the observations in the center of the swath for a variety of reasons. The large observation sensitivities imply that the less accurate observations along the swath edge have greater potential to change the forecast aspect. One way to compensate for this effect is to increase the expected observation error for the observations along the edge of the swath since this decreases the observation sensitivity and the potential impact of the less accurate observations.

Finally, it was noted that limited area and global observation sensitivity calculations may differ considerably if the regions with significant analysis sensitivity are near the limited domain boundaries.

Together, the one- and two-dimensional observation sensitivity examples provide the background needed to help interpret the NAVDAS adjoint observation sensitivity results. Even with this background, the three-dimensional NAVDAS adjoint observation sensitivity is difficult to understand because the three-dimensional analysis sensitivity gradients and background error covariances add considerably to the complexity of the problem. Nevertheless, many of the general results from the idealized examples appear to apply to the NAVDAS adjoint observation sensitivities.

The NAVDAS adjoint observation sensitivities were computed for a case in February 1999 that corresponds to unusually large 72-h forecast errors over the western United States. The largest u-wind observation sensitivities correspond to the large-scale u-wind analysis sensitivity gradients associated with the northern branch of the subtropical jet, while the largest v-wind observation sensitivities appeared to be primarily connected to the large-scale temperature analysis sensitivity gradients at 500 hPa, with lesser contributions from the v-wind analysis sensitivity gradients at lower levels. These v-wind observation sensitivities for the NAVDAS adjoint are consistent with the multivariate phase-shifts in the multivariate results discussed above, although it is difficult to separate the phase-shift contributions from the contributions due to the vertical coupling of the analysis sensitivity gradients through the background error covariances. The largest temperature observation sensitivities occur for several isolated Alaskan radiosonde stations in a region with a large-scale temperature analysis sensitivity gradient. For all of these examples, the density of the observations is low in the vicinity and this enhances the observation sensitivity of the radiosonde stations.

The observation density is higher for areas sampled by the TOVS satellite, and the largest brightness temperature sensitivities correspond to the less accurate observations along data discontinuities such as the edges of the satellite swath, and between open ocean and land or sea ice where the brightness temperatures are not used. Since the present NAVDAS configuration does not adjust the expected observation errors to account for these less accurate observations, the observation sensitivities are inappropriately large. This example highlights an important, non-targeting application of the data assimilation adjoint theory.

What are the implications of the observation sensitivity? For a given observation, the row of $\mathbf{K}^T$ corresponds to the column of the analysis weight matrix $\mathbf{K}$, and the contribution to the analysis from that observation equals the matrix-vector multiplication of that column of $\mathbf{K}$ and the innovation. When $\mathbf{K}$ is large in spatial scale, the potential influence of the observation on the analysis is spread to more distant gridpoints, and when the amplitude of $\mathbf{K}$ is strong, the potential change to the analysis is large. Conversely, when $\mathbf{K}$ is small in spatial scale, any changes to the analysis will be localized, and when the amplitude of **K** is weak, the potential change to the analysis is small. It is important to note that since the observation sensitivity calculations do not explicitly require the observed and background values, the actual impact of the observations on the analysis or forecast cannot be determined until the observations have been taken. Therefore, the observation sensitivity gives an estimate of the *potential* for an observation to change the analysis and the forecast aspect.

Weak observation sensitivity occurs when one or more of the following conditions are met: the observations are assumed to be less accurate than the background, the analysis sensitivity is weak in the vicinity of the observations, the observation density is high, and the analysis sensitivity gradient is small-scale. When the expected observation error is greater than the expected background error, the observation is given less weight in the analysis, and when the observation density is high, the influence of the observation on the analysis is relatively localized. Under these conditions, the spatial structures and scales of $\mathbf{K}^T$ (which are largely determined by the background error covariances) do not coincide with the sub-structures of the analysis sensitivity gradient, and $\mathbf{K}^T$ projects weakly onto the analysis sensitivity gradient. Consequently, weak observation sensitivity implies that the analysis changes associated with the observation will not have the proper amplitude and structure to effectively change the analysis and forecast aspect. This reasoning provides a possible explanation for the lack of forecast improvement associated with the assimilation of the FASTEX and NORPEX adaptive observations.

Conversely, strong observation sensitivity occurs when the analysis sensitivity gradients are large scale and relatively strong, the observation density is low or there is an abrupt discontinuity in the density, and the expected error variances of the observations are less than the expected background error variances. When the observations are assumed to be accurate relative to the background, the observations are given more weight by the analysis, and when the observation density is low, the observation influence extends to farther away gridpoints. Under these conditions, the spatial structures and scales of $\mathbf{K}^T$ may coincide with the analysis sensitivity gradient sub-structures and $\mathbf{K}^T$ projects strongly onto the analysis sensitivity gradient. Therefore, strong observation sensitivity implies that the changes to the analysis may have both significant amplitude and the proper structure to effectively change the forecast aspect.

Intuitively, it might be assumed that very large observation sensitivities are desirable. However, extremely large values of observation sensitivity imply that the analysis is very dependent upon a few observations in highly sensitive regions. Under these conditions, even small errors in the observations may contribute to large forecast errors. Large values of observation sensitivity are also associated with large background sensitivities, and indicate that the forecast aspect is highly sensitive to the background as well. When the analysis must rely on a few sparsely placed observations, it is unlikely that the observations can adequately correct the background errors, and the remaining background errors will contribute strongly to the forecast error. For these reasons, extremely large values of observation sensitivity are undesirable. As more observations are added to the system, the analysis becomes less dependent upon the individual observations or the background, and the observation and background sensitivities decrease, which implies that intermediate values of observation sensitivity are desirable. This provides a possible explanation for the forecast degradation that occurred for several of the FASTEX and NORPEX cases with insufficient dropsondes properly distributed relative to the sensitive area.

The data assimilation adjoint theory has also been used to illustrate how the observation sensitivity may be used to supplement the classical adaptive observation-targeting strategies. For example, the FASTEX and NORPEX adjoint-based targeting strategies tended to focus on the high-amplitude, small-scale analysis sensitivity gradient or singular vector sub-structures. These targeting decisions were founded on dynamical theory, as these features are frequently associated with rapidly intensifying baroclinic features that are highly sensitive to small errors in the initial conditions. However, dynamical reasoning does not take into account how the data assimilation system will use the adaptive observations, or the impact of the distribution and properties of the other observations in the area. As such, neither adjoint-based targeting method provides complete guidance as to where to place the additional observations in the sensitive areas. By comparison, the observation adjoint sensitivity, which specifically accounts for these factors, indicates that the sensitivity of the forecast aspect to observations placed near high-amplitude, small-scale analysis sensitivity gradients may be weak or even negligible, and suggests that targeting large-scale moderate to strong amplitude analysis sensitivity gradients is more advantageous.

The observation sensitivities were used to compute an estimate of reduction in the expected variance of the change in the forecast aspect J due to the observations. This scalar number may be computed for the entire suite of observations, for a specified observing platform or targeting deployment, or for a given dropsonde report. This measure has been used to assess the efficiency of different hypothetical targeting deployments. Since the sign and the amplitude of the change of the forecast aspect cannot be determined until the observations are taken, this measure alone cannot indicate whether, or how much, the forecast error will be reduced.

The largest relative contributions were from the driftsonde-deployed dropsonde network and the hypothetical targeting flight from Shemya, both of which sampled the high-amplitude, large-scale temperature and v-wind analysis sensitivity gradients. The contributions to the total reduction in the expected variance of the change in J due to these two adaptive-observation deployments are also associated with decreases in the relative contributions from the other observation platforms (particularly the satellite winds and brightness temperatures), which suggest a certain amount of redundancy in the information among the different observing systems. The adaptive observations also reduce the extremely large observation sensitivities for the conventional Alaskan radiosondes, which indicates that the analysis has become less dependent upon these relatively isolated observations. In contrast, the hypothetical targeting deployment that was specifically designed to sample the gradients and extrema of the 850-hPa temperature analysis sensitivity pattern contributed very little to the total reduction in the expected variance of the change in the forecast aspect.

These results confirm that, for NAVDAS, targeting the large-scale, moderate-amplitude analysis sensitivity gradients is more advantageous than targeting the small-scale, high-amplitude sub-structures, and demonstrate that adaptive observation-targeting decisions based on the adjoint of the data assimilation system can be significantly different from targeting decisions based solely on analysis sensitivity gradients or singular vectors. The results also emphasize the importance of accounting for the data assimilation procedures in the adaptive observation-targeting problem.

While this research was primarily concerned with the adaptive observation-targeting problem, the potential applicability of the data assimilation adjoint theory is much broader in that it illustrates how the data assimilation system works, and gives insight into how the observations are used by the data assimilation system. For example, the reduction in the expected variance of the change in the forecast aspect, which is computed using all observations, may be used to modify the data selection and screening procedures to obtain the most efficient mix of observations for the analysis. As illustrated with the TOVS brightness temperature example, the observation sensitivities may also be used as guidelines to adjust the observation error variances in the data assimilation system according to known factors.

Because the NAVDAS adjoint observation sensitivities follow the same general principles as the idealized one- and two-dimensional observation sensitivity examples, certain behavior (e.g., the observation sensitivity is large when an accurate observation is near a large-scale analysis sensitivity gradient) may be expected with confidence. Several errors in the assignment of the observation errors in NAVDAS were identified during the course of this research because the observation sensitivities were unexpectedly weak. These diagnostic applications of the NAVDAS adjoint observation sensitivity will be used in the near future as an additional NAVDAS evaluation tool prior to NAVDAS' operational implementation at FNMOC.

A completely different application of the data assimilation adjoint theory is the *a posteriori* forensic assessment of the sources of forecast error attributable to the errors in the analysis, and how these are related to the observation distributions, types or accuracies. Traditional methods of locating such errors usually require a brute force approach, where several analyses are generated using different sets of observations and the resulting forecasts are compared to estimate the forecast aspect. Many such calculations may be required and it can be difficult or impossible to trace the forecast error back to its source. In contrast, the adjoint of the data assimilation system locates those observations with the greatest sensitivity to the forecast aspect. Observations with both large sensitivities and large innovations are those most likely to have changed the forecast aspect.

The next phase of the targeting application of the observation sensitivity will be to investigate the potential of the driftsonde network for THORPEX. The adjoint of the data assimilation system will be used to answer fundamental questions concerning the locations and frequency of the carrier balloon launches and deployed dropsondes. The NAVDAS adjoint will also be used to evaluate whether the driftsonde network should be supplemented with additional aircraft targeting flights, and if so, how best to sample the sensitive regions.

Finally, the NAVDAS adjoint along with NAVDAS will be used to evaluate how well the FASTEX targeting flights sampled the sensitive areas given the characteristics of NAVDAS, and to relate the observation sensitivities to the changes made to the analysis by the observations.

THIS PAGE INTENTIONALLY LEFT BLANK

LIST OF REFERENCES

Baker, N.L., and R. Daley, 1999: Observation and background adjoint sensitivity in the adaptive observation targeting problem. Preprints, *13th Conf. Num. Wea. Pred.*, Denver, CO, Amer. Meteor. Soc., 20-22.

Baker, N.L, and R. Daley, 2000: Observation and background adjoint sensitivity in the adaptive observation-targeting problem. *Quart. J. Roy. Meteor. Soc.*, **126**, 1431-1454.

Bergot, T., 1999: Adaptive observations during FASTEX: A systematic survey of upstream flights. *Quart. J. Roy. Meteor. Soc.*, **125**, 3271-3298.

Bergot, T., 2000: Influence of the assimilation scheme on the efficiency of adaptive observations. *Quart. J. Roy. Meteor. Soc.*, in press.

Bergot, T., G. Hello, A. Joly, and S. Malardel, 1999: Adaptive observations: A feasibility study. *Mon. Wea. Rev.*, **127**, 743-765.

Berliner, L.M., Z.-Q. Lu, and C. Snyder, 1999: Statistical design for adaptive weather observations. *J. Atmos. Sci.*, **56**, 2536-2552.

Bishop, C.H., and Z. Toth, 1999: Ensemble transformations and adaptive observations. *J. Atmos. Sci.,* **56,** 1748-1765.

Bishop, C.H., B.J. Etherton, and S. Majumdar, 2000: Adaptive sampling with the ensemble transform Kalman filter. Part I: Theoretical aspects. *Mon. Wea. Rev.*, in press.

Buizza, R, and T. N. Palmer, 1995: The singular vector structure of the atmospheric general circulation. *J. Atmos. Sci.,* **52**, 1434-1456.

Buizza, R., and A. Montani, 1999: Targeting observations using singular vectors. *J. Atmos. Sci.*, **56**, 2965-2985.

Buizza, R., R. Gelaro, F. Molteni, and T.N. Palmer, 1997: The impact of increased resolution on predictability studies with singular vectors. *Quart. J. Roy. Meteor. Soc.,* **123**, 1007-1033.

Daley, R., 1991: *Atmospheric Data Assimilation*, Cambridge University Press, 457 pp.

Daley, R., and E. Barker, 2000a: NAVDAS Source Book 2000. Tech. Rep. NRL/PU/7530-00-418, Naval Research Laboratory, Monterey, CA 93943-5502, 153 pp.

Daley, R., and E. Barker, 2000b: NAVDAS – formulation and diagnostics. *Mon. Wea. Rev.*, accepted.

Doerenbecher, A. and T. Bergot, 2000: Sensitivity to observations applied to FASTEX cases. Manuscript submitted to *Nonlin. Process. in Geophy.*

Doerenbecher, A., T. Bergot, and F. Bouttier, 2000: Sensitivity to observations and targeted observations. Preprints, *4th Symposium on Integrated Observing Systems,* Long Beach, CA, Amer. Meteor. Soc., 200-203.

ECMWF, 2000: Improvements in the accuracy of forecasts. In *The first twenty-five years*, European Centre for Medium-Range Weather Forecasts, Shinfield Park, Reading RG2 9AX, United Kingdom, 100 pp.

Fischer, C., A. Joly, and F. Lalaurette, 1998: Error growth and Kalman filtering within an idealized baroclinic flow. *Tellus*, **50A**, 596-615.

Gelaro, R., R. Buizza, T.N. Palmer, and E. Klinker, 1998: Sensitivity analysis of forecast errors and the construction of optimal perturbations using singular vectors. *J. Atmos. Sci.*, **55**, 1012-1037.

Gelaro, R., R.H. Langland, G.D. Rohaly, and T.E. Rosmond, 1999: An assessment of the singular vector approach to targeted observing using the FASTEX data set. *Quart. J. Roy. Meteor. Soc.,* **125**, 3299-3327.

Gelb, A., 1974: *Applied optimal estimation.* MIT Press, 374 pp.

Harrison, M.S.J, T.N. Palmer, D.S. Richardson, and R. Buizza, 1999: Analysis and model dependencies in medium-range ensembles: Two transplant case studies. *Quart. J. Roy. Meteor. Soc.,* **125**, 2487-2515.

Hodur, R.M., 1997: The Naval Research Laboratory's coupled ocean/atmosphere mesoscale prediction system (COAMPS). *Mon. Wea. Rev.*, **125**, 1414-1430.

Hogan, T.F., and T.E. Rosmond, 1991: The description of the navy operational global atmospheric prediction system spectral forecast model. *Mon. Wea. Rev.*, **119**, 1786-1815.

Hogan, T.F., T.E. Rosmond, and R.L. Pauley, 1999: The navy operational global atmospheric prediction system: Recent changes and testing of gravity wave and cumulus parameterizations. Preprints, *13th Conf. Num. Wea. Pred.*, Denver, CO, Amer. Meteor. Soc., 60-65.

Hollingsworth, A., and P. Lönnberg, 1986: The statistical structure of short-range forecast errors as determined from radiosonde data. Part I: The wind field. *Tellus*, **38A**, 111-136.

Joly, A, D. Jorgensen, M.A. Shapiro, A. Thorpe, P. Bessemoulin, K.A. Browning, J.-P. Chalon, S.A. Clough, K.A. Emanuel, L. Eymard, R. Gall, P.H. Hildebrand, R.H. Langland, Y. Lemaitre, P. Lynch, J.A. Moore, P.O.G. Persson, C. Snyder, and R. Wakimoto, 1997: The Fronts and Atlantic Storm-track Experiment (FASTEX): Scientific objectives and experimental design. *Bull. Amer. Meteor. Soc.*, **78**, 1917-1940.

Langland, R.H., and G.D. Rohaly, 1996: Adjoint-based targeting of observations for FASTEX cyclones. Preprints, *Seventh Conf. Mesoscale Processes*, Reading, United Kingdom, Amer. Meteor. Soc., 369-371.

Langland, R.H., R. Gelaro, G.D. Rohaly, and M.A. Shapiro, 1999a: Targeted observations in FASTEX: Adjoint-based targeting procedures and data impact experiments in IOPs-17 and 18. *Quart. J. Roy. Meteor. Soc.*, **125**, 3241-3270.

Langland, R.H., Z. Toth, R. Gelaro, I. Szunyogh, M.A. Shapiro, S.J. Majumdar, R.E. Morss, G.D. Rohaly, C. Velden, N. Bond, and C.H. Bishop, 1999b: The North Pacific Experiment (NORPEX-98): Targeted observations for improved North American weather forecasts. *Bull. Amer. Meteor. Soc.*, **80**, 1363-1384.

Le Dimet, F.-X., H.E. Ngodock, and J. Vernon, 1995: Sensitivity analysis in variational data assimilation. *Second International Symposium on Assimilation of Observations in Meteorology and Oceanography*, Tokyo, **WMO/TD- No. 651, Vol. 1**, 99-104.

Lönnberg, P., and A. Hollingsworth, 1986: The statistical structure of short-range forecast errors as determined from radiosonde data. Part II: The covariance of height and wind errors. *Tellus*, **38A**, 137-161.

Lorenz, E.N., and K.A. Emanuel, 1998: Optimal sites for supplementary observation sites: Simulation with a small model. *J. Atmos. Sci.*, **55**, 399-414.

Palmer, T.N., R. Gelaro, J. Barkmeijer, and R. Buizza, 1998: Singular vectors, metrics and adaptive observations. *J. Atmos. Sci.*, **55**, 633-653.

Pu, Z.-X., and E Kalnay, 1999: Targeting observations with the quasi-inverse linear and adjoint NCEP global models. *Quart. J. Roy. Meteor. Soc.*, **125**, 3329-3338.

Pu, Z.-X., S.J. Lord, and E. Kalnay, 1998: Forecast sensitivity with dropwindsonde data and targeted observations. *Tellus*, **50**, 391-410.

Rabier, F., E. Klinker, P. Courtier, and A. Hollingsworth, 1994: Sensitivity of two-day forecast errors over the Northern Hemisphere to initial conditions. *ECMWF Tech. Mem.*, **203**, 38 pp.

Rabier, F., E. Klinker, P. Courtier, and A. Hollingsworth, 1996: Sensitivity of forecast errors to initial conditions. *Quart. J. Roy. Meteor. Soc.*, **122**, 121-150.

Rabier, F., H. Jarvinen, E. Klinker, J.-F. Mahfouf, and A. Simmons, 2000: The ECMWF operational implementation of four-dimensional variational assimilation. I: Experimental results with simplified physics. *Quart. J. Roy. Meteor. Soc.*, **126**, 1143-1170.

Rosmond, T.E., 1997: A technical description of the NRL Adjoint Modeling System, Tech. Rep. NRL/MR/7532/97/7230, Naval Research Laboratory, Monterey, CA 93943-5502, 55 pp.

Smith, W.L., H.M. Woolf, C.M. Hayden, D.Q. Wark, and L.M. McMillin, 1979: The TIROS-N operational vertical sounder. *Bull. Amer. Meteor. Soc.*, 60, 1177-1187.

Snyder, C., 1996: Summary of an informal workshop on adaptive observations and FASTEX. *Bull. Amer. Meteor. Soc.*, **77**, 953-961.

Szunyogh, I., Z. Toth, K.A. Emanuel, C.H. Bishop, C. Snyder, R.E. Morss, J. Woolen, and T. Marchok, 1999: Ensemble-based targeting experiments during FASTEX: The impact of dropsonde data from the LEAR jet. *Quart. J. Roy. Meteor. Soc.*, **125**, 3189-3218.

Szunyogh, I., Z. Toth, R.E. Morss, S. Majumdar, B.J. Etherton, and C.H. Bishop, 2000: The effect of targeted dropsonde observations during the 1999 Winter Storm Reconnaissance Program. *Mon. Wea. Rev.*, **128**, 3520-3537.

INITIAL DISTRIBUTION LIST

1. Defense Technical Information Center 2
8725 John J. Kingman Road, Suite 0944
Ft. Belvoir, VA 22060-6218

2. Dudley Knox Library 2
Naval Postgraduate School
411 Dyer Road
Monterey, CA 93943-5101

3. Chairman, Code MR 1
Department of Meteorology
Naval Postgraduate School
Monterey, CA 93943-5101

4. Prof. Russell L. Elsberry 1
Department of Meteorology
Naval Postgraduate School
Monterey, CA 93943-5101

5. Prof. R. Terry Williams 1
Department of Meteorology
Naval Postgraduate School
Monterey, CA 93943-5101

6. Prof. Carlyle H. Wash 1
Department of Meteorology
Naval Postgraduate School
Monterey, CA 93943-5101

7. Prof. Richard Franke 1
Department of Mathematics
Naval Postgraduate School
Monterey, CA 93943-5101

8. Dr. Roger Daley 1
Naval Research Laboratory
Marine Meteorology Division
Monterey, CA 93943-5502

9. Dr. Ronald M. Errico 1
National Center for Atmospheric Research
P.O. Box 3000
Boulder, CO 80303-3000

10. Dr. Nancy L. Baker 1
Naval Research Laboratory
Marine Meteorology Division
Monterey, CA 93943-5502

11. Dr. Phillip Merilees 1
Naval Research Laboratory
Marine Meteorology Division
Monterey, CA 93943-5502

12. Dr. Richard M. Hodur 1
Naval Research Laboratory
Marine Meteorology Division
Monterey, CA 93943-5502

13. Dr. Rolf H. Langland 1
Naval Research Laboratory
Marine Meteorology Division
Monterey, CA 93943-5502

14. Dr. Ronald Gelaro 1
Naval Research Laboratory
Marine Meteorology Division
Monterey, CA 93943-5502

15. Dr. Eric O. Hartwig 1
Code 7000
Naval Research Laboratory
Washington, D.C. 20375-5320

16. Dr. Scott Sandgathe 1
Office of Naval Research
800 North Quincy St.
Arlington, VA 22217-5660

17. Ms. Joanne May 1
Library, Code 84
Fleet Numerical Meteorology and Oceanography Center
Monterey, CA 93943-5502

18. Naval Research Laboratory 1
Ruth H. Hooker Research Library
4555 Overlook Ave. S.W.
Washington, D.C. 20375-5000

19. Dr. John Derber 1
NOAA
World Weather Building, W/NP23
5200 Auth Road
Washington, D.C. 20746-4304

20. Dr. Thierry Bergot 1
Meteo-France
CNRM/GMME
42, Avenue Corolios
F-31057 Toulouse Cedex, France

21. Dr. Francois Bouttier 1
Meteo-France
CNRM/GMME
42, Avenue Corolios
F-31057 Toulouse Cedex, France

22. Dr. William Bourke 1
Bureau of Meteorology Research Centre
150 Lonsdale Street
Melbourne, Victoria 3000 AUS

23. Dr. T.N. Palmer 1
ECMWF
Shinfield Park
Reading RG2 9AX UK

24. Dr. Eric Andersson 1
ECMWF
Shinfield Park
Reading RG2 9AX UK

63 290NPG 2560
TH
6/02 22527-200 NLB
HF BINDING

DUDLEY KNOX LIBRARY
3 2768 00402777 1